Electronic and Magnetic Structure of Few Strongly Correlated Spinel Oxides

A Thesis Submitted to
Indian Institute of Technology Guwahati
for the degree of

Doctor of Philosophy

By

Sayandeep Ghosh

Roll. No: 166121011

Department of Physics
Indian Institute of Technology Guwahati
Guwahati-781039, Assam (India)

Dedicated To: My beloved parents, my brother and Saptaparna

INDIAN INSTITUTE OF TECHNOLOGY GUWAHATI

Department of Physics

Guwahati – 781039

Declaration

"Electronic and Magnetic Structure of Few Strongly Correlated Oxides" is the result of my own doctoral research work. This work was carried out under the supervisions of Dr. Subhash Thota and Dr. Pankaj Kumar Mishra at the Department of Physics, Indian Institute of Technology Guwahati. To the best of my knowledge, the work presented in this thesis has not been submitted to any other Institute/University for the award of any degree.

Sayandeep Ghosh

Sayandeep Ghosh
Research Scholar
Roll No: 166121011
Department of Physics
Indian Institute of Technology Guwahati
Guwahati-781039, India

INDIAN INSTITUTE OF TECHNOLOGY GUWAHATI

Department of Physics

Guwahati – 781039

Certificate

It is certified that the work described in this thesis, entitled "Electronic and Magnetic Structure of Few Strongly Correlated Oxides", done by Ms. Sayandeep Ghosh, a Ph.D. student of Department of Physics, Indian Institute of Technology Guwahati, for the award of degree of Doctor of Philosophy has been carried out under my supervision. This work has not been submitted elsewhere for the award of any degree.

Dr. Subhash Thota
Associate Professor
Department of Physics
Indian Institute of Technology Guwahati
Guwahati-781039, India

Dr. Pankaj Kumar Mishra
Assistant Professor
Department of Physics
Indian Institute of Technology Guwahati
Guwahati-781039, India

Synopsis Report

Spinel oxides (AB_2O_4-Type of crystal structure) with transition metals as cations at A and B sites are considered as important class of solid-state materials due to their wide-range of industrial applications. The family of Cobalt (Co) spinels such as Co_3O_4, Co_2TiO_4, Co_2AlO_4, Co_2SnO_4, etc. exhibit excellent catalytic behvoiur which are useful in many of the fuel-cells. In addition, they have unique magnetic, semiconducting, and optical properties as compared to other binary oxides like CoO, MnO, NiO, TiO_2, SnO_2 etc. Such spinel oxides have drawn immense attention of the scientific community primarily due to two important reasons: (*i*) A variety of magnetic and nonmagnetic ions can be accommodated on the eight tetrahedral A sites and 16 octahedral B sites leading to the discovery of new compounds with novel functionalities. These particular features have opened up garden variety of fundamental research problems related to the magneto-structural and magneto-electric properties of spinals, (*ii*) Unlike metallic ferromagnets (FM) such as Fe, Co, and Ni, the magnetic spinels generally have very low electrical conductivity that leads the applications of these spinels in telecommunications, in particular microwave communication devices, where, reduction in eddy current loss is considered as vital parameter for the system. In recent years, among the spinels, the normal spinel Co_3O_4 have gained potential interests owning to their wide range of applications in many of the renewable energy system such as solar energy reflectors, gas-sensors, electro-chromic devices, electrode material for thin film super-capacitor, magneto-electronic devices, and photo-voltaic cells and catalyst. On the other hand, incorporation of nonmagnetic elements (Al, Ti, Sn, Ge etc.) in the Co_3O_4 lattice bring a remarkable change in the magnetic properties of the spinels which further affect different functionalities of the compounds. Our current doctoral thesis work revolves around to investigate and further understand these peculiar features of the spinels using experiments complimented by theoretical calculations done from the first principle. Such dilution essentially alters the crystal and electronic structure, as well as magnetic exchange interaction between the cations that further lead to anomalous magnetic behavior. By keeping our main focus on these issues, we have performed detailed computational and experimental studies on a variety of Cobalt-spinels and their derivatives. In the below we present a detailed structure of our thesis which is mainly divided into seven Chapters.

Chapter 1 brings with a brief introduction of the spinel compounds and their classifications along with their potential applications in solid-state-technology with main emphasis over the underlying Physics. Further we present various basic concepts required to understand the effect of structure on the overall electronic and magnetic behavior. In particular, few key concepts like density-of-states, exchange-splitting, crystal-field-splitting, Jahn-Teller distortion, magnetic exchange interactions and exchange are discussed. We also outline the main motivation for choosing this particular set of spinels for our work.

Chapter 2 renders details of numerical methodology and various experimental techniques employed including the synthesis procedure as well as characterization details used for our work. It begins with a brief description of the first-principles density functional theory (DFT) formalism, which we have extensively used to investigate the electronic and magnetic structure of the spinels. In order to consider the electron-electron

correlations we resort on DFT+U formalism, where U being the strength of Coulomb Interaction. We have extensively presented the kind of pseudo potentials that we considered for our work. Further we present the details of various experimental techniques used for our work that includes the low-temperature magnetization measurements, magneto-transport, neutron diffraction and the electron spin resonance.

Chapter 3 presents the results obtained from DFT+U calculations and the experimental data on different spinels $Co_2\Sigma O_4$ (Σ = Ti, Ru, Ge, Al, and Sn). Here we mainly focus on the electronic and magnetic structure of these compounds along with the energy band-structure which are complimented by the experimental results. A substantial increase in the size of the unit cell along with collapse of the long-range antiferromagnetic (AFM) ordering with spin-orbit compensation effect are the key features noticed as the octahedral Co site is diluted with non-magnetic cations. The extent of exchange splitting, $\Delta_{EX}^{e_g}$ of tetrahedral Co^{2+} varies between 1.8 eV and 1.3 eV for Co_3O_4 and Co_2AlO_4 (CAO) respectively. Conversely, $\Delta_{EX}^{t_{2g}}$ exhibits decreasing trend (5.2 eV→3.6 eV for Co_3O_4→Co_2SnO_4) with increasing the lattice parameter, except normal spinel Co_2GeO_4 (CGO). In case of the inverse spinels Co_2SnO_4 (CSO) and Co_2TiO_4 (CTO), weak ferrimagnetic (FiM) behavior emerges due to unequal magnetic moments at the two-sublattices A ($3.87\mu_B$) and B ($4.16\mu_B$ and $5.19\mu_B$ for CSO and CTO, respectively). Experiments and DFT calculations indicate that AFM configuration is stable in Co_3O_4 and CAO with an equal and opposite moment (~ $2.60\mu_B$) at the tetrahedral sites of divalent Co ions and negligible contribution from the trivalent B-site Co. This happens due to complete filling of the t_{2g} levels having giant crystal field ~ 2.5 eV and 1.8 eV, respectively. Interestingly, the AFM ordering remains intact in the normal spinel CGO due to the opposite spins at octahedral sites of divalent Co ions. However, the remaining spinels CTO (T_N ~ 47.8 K) and CSO (T_N ~ 41 K) are more favorable to FiM structure because of different temperature dependence of magnetic moments A(T) and B(T) at tetrahedral-A and octahedral-B sites, respectively. This chapter also deals with the variation in the energy band-gap obtained from DFT+U calculations which are compared with the experimental results obtained from the diffusive reflectance spectroscopy.

Chapter 4 deals with the static and dynamic magnetic behavior of normal spinel Co_2RuO_4 (CRO) which exhibits AFM transition at Néel temperature (T_N) ~ 15.2 K, along with a spin-glass state below T_N. In this system, T_N is mainly governed by ordering of the spins of Co^{2+} ions occupying the A-site. However, the exchange interaction between the Co^{2+} ions on the A-site and randomly distributed Ru^{3+} on the B-site triggers the spin-glass phase. Further we provide the Field-Temperature (H-T) phase diagram obtained from the analysis of M-T measurements at different H for $T < T_N$. The remaining sections of this chapter deals with the spin-glass state with freezing temperature T_{SG} (=14.2K) and the analysis of the paramagnetic susceptibility (χ) vs. T and exchange interactions in CRO. We employed the high-temperature-series (HTS) technique along with the experimentally obtained parameters to determine the exchange constant J_1/k_B (~ 6 K) between the Co^{2+} on the A-sites. The last section of this chapter deals with the M-H loop asymmetry at low temperatures and magnetocaloric effect (MCE) in CRO. Accordingly, we noticed giant exchange bias effect (H_{EB} ~ 1.8 kOe) and coercivity (H_C ~7 kOe) for a field cooled sample which further support the mixed magnetic phase of CRO. This

chapter ends with the discussion on the zero crossover of the magnetic entropy change for $T > T_N$ ad its correlation with the change in sign of differential magnetic susceptibility data.

In Chapter 5 we focus our study in probing the low temperature structural distortion, magnetic ground state, and spin structures of single-crystal and powder samples of CTO and CSO using the neutron diffraction technique performed between 1.6 K and 80 K. Both these compounds exhibit highest magnetic intensity from the $(111)_M$ reflection due to FiM ordering, which sets in below T_N = 48.6 K and 41 K for CTO and CSO, respectively. An additional low intensity $(200)_M$ magnetic reflection is evident in CTO due to the presence of an additional weak AFM component. Interestingly, from both the powder and the single-crystal neutron data of CTO and CSO a significant broadening of the $(111)_M$ magnetic reflection was noticed due to the disorderly distributed Ti and Co atoms on the *B* site. On the other hand, from our single-crystal neutron diffraction data of CTO we found a spontaneous increase of particular nuclear Bragg reflections below the magnetic ordering temperature which is ascribed to the presence of anisotropic extinction and change of the mosaicity of the crystal. In this case it can be expected that competing Jahn-Teller effects act along different crystallographic axes can induce anisotropic local strain that further brings a splitting in t_{2g} levels for both Ti^{3+} and Co^{3+} resulting yielding of lower d_{xy} level and higher two-fold degenerate d_{xz}/d_{yz} levels. As a consequence, one can expect a tetragonal distortion in CTO with $c/a < 1$, which could not significantly detect in the present work.

Chapter 6 focuses on the electronic structure and magnetic properties of Ge diluted CTO spinel (i.e. $Co_2Ti_{1-x}Ge_xO_4$ (CTGO)) over a wide composition range ($0 \leq x \leq 1$) by means of the first-principles methods of DFT+U calculations. Special emphasis has been given to explore the site occupancy of Ge atoms in the lattice by introducing the cationic disorder parameter (y) which is done in such a way that one can tailor the Pyrochlore geometry and determine the electronic and magnetic structure quantitatively. For all the x, the system exhibits weak tetragonal distortion ($c/a \neq 1$) due to the non-degenerate d_{z^2} and $d_{x^2-y^2}$ states (e_g orbitals) of the B-site Co. We observe large exchange splitting (Δ_{EX} ~ 9 eV) between the up and down spin bands of t_{2g} and e_g states, respectively, of tetrahedral and octahedral Co^{+2} ($^4A_{2(g)}$(F)) and moderate crystal-field splitting (Δ_{CF} ~ 4 eV) and the Jahn-Teller distortion (Δ_{JT} ~ 0.9 eV). These features indicate the strong intra-atomic interaction of CTGO system which is also responsible for the large variation of energy band-gap (1.7 eV $\leq E_g \leq$ 3.3 eV). On the other hand, the exchange interaction (J_{BB} ~-4.8 meV, for (x,y) = (0.25, 0)) between the Co^{2+} dominates the overall AFM behavior of the system for all 'x' as compared to interactions J_{AA} (~-2.2 meV, for (x,y) = (0.25, 0)) and J_{AB} (~-1.8 meV, for (x,y) = (0.25, 0)). For all the values of 'x' without any disoderness in the system, net FiM moment ($\Delta\mu$) remains constant, however, $\Delta\mu$ increases progressively with composition due to the imbalance of Co spins between the A- and B-sites ($\Delta\mu_{MAX}$ ~ -4.4μ_B for x = 0.75 and y = 1.0).

Chapter 7 presents a brief summary of important findings of our experimental results. In this chapter we also identify some open issues which are potentially interesting for the future studies.

List of Publications:

Peer Reviewed Journals:

[1] "Tailoring the Electronic Structure and Magnetic Properties of Pyrochlore $Co_2Ti_{1-x}Ge_xO_4$: A GGA+U *Ab initio* Study",
S. Ghosh, S. Singh, D. Das, S. Ghosh, P. K. Mishra, and S. Thota,
Journal of Physics: Condensed Matter **33**, 145504 (2021).

[2] "Antiferromagnetism, spin-glass state, H-T phase diagram, and inverse magnetocaloric effect in Co_2RuO_4",
S. Ghosh, D. C. Joshi, P. Pramanik, S. K. Jena, S. Pittala, T. Sarkar, M. S. Seehra, S. Thota
Journal of Physics: Condensed Matter **32**, 485806 (2020).

[3] "Low-temperature anomalous spin correlations and Kondo effect in ferromagnetic $SrRuO_3/LaNiO_3/La_{0.7}Sr_{0.3}MnO_3$ trilayers",
S. Ghosh, R. G. Tanguturi, P. Pramanik, D. C. Joshi, P. K. Mishra, S. Das, S. Thota
Physical Review B **99**, 115135 (2019).

[4] "Role of dilution on the electronic structure and magnetic ordering of spinel cobaltites",
S. Ghosh, S. Singh, D. C. Joshi, P. Pramanik, S. Ghosh, P. K. Mishra, S. Thota
Physical Review B **98**, 235119 (2018).

[5] "Neutron diffraction study of the inverse spinels Co_2TiO_4 and Co_2SnO_4",
S. Thota, M. Reehuis, A. Maljuk, A. Hoser, J. -U. Hoffmann, B. Weise, A. Waske, M. Krautz, D. C. Joshi, S. Nayak, **S. Ghosh**, P. Suresh, K. Dasari, S. Wurmehl, O. Prokhnenko, B. Büchner
Physical Review B **96**, 144104 (2017).

[6] "Magnetic exchange interactions and band gap bowing in $Ni_xMg_{1-x}O$ ($0.0 \leq x \leq 1.0$): A GGA+U density functional study",
S. Ghosh, S. K. Jena, P. K. Mishra, M. S. Seehra, S. Thota
Journal of Applied Physics **126**, 233904 (2019).

Work presented in international/national conferences and workshops:

[1] "Magnetic Exchange Bias and Spin-glass state in Cobaltorthoruthanate"
S. Ghosh, A. V. Singh, S. Sharma, T. Sarkar, S. Thota
National Conference on Progresses in Material Science Research (PMSR-2020), February 4-6, 2020, Dibrugarh University, India.

[2] "First-Principle Density Functional Theory (DFT) study of Ge diluted Cobalt orthotitanate",
S. Ghosh, S. K. Jena, P. K. Mishra, S. Thota
International Conference on Nanoscience and Nanotechnology (ICNAN-2019), November 29 – December 1, 2019, Vellore Institute of Technology, Vellore, India.

[3] "Density Functional Theory Studies of Mg doped NiO"
S. Ghosh, S. K. Jena, D. C. Joshi, P. Pramanik, P. K. Mishra and S. Thota
International Conference on Nano-structured Materials & Devices (ICNSMD-2018), December 17-20, 2018, University of Delhi, New Delhi, India.

[4] "Density Functional Theory Studies of Co-based Spinels"
S. Ghosh, S. Singh, P.K. Mishra, S. Thota
International Conference on Systems and Processes in Physics, Chemistry and Biology (ICSPPCB- 2018), 1-3 March, 2018, Silchar, Assam, India.

[5] "Structural and Magnetic properties of Cobalt Aluminate"
S. Ghosh, S. Nayak, P. K. Mishra and S. Thota, *International Conference on Advanced Nanomaterials and Nanotechnology (ICANN-2017), December 18-21, 2017, IIT Guwahati, Assam, India.*

Acknowledgements

First and foremost, I would like to thank Dr. Subhash Thota and Dr. Pankaj Kumar Mishra for giving me the opportunity to work under their guidance. I would like to express a deep sense of gratitude to my research supervisors. I am very thankful to them for their mentorship, friendship, and supervision. Additionally, I would also like to thank them for being so patient and for listening to all my thoughts/idea and guiding me accordingly to achieve the research goals which eventually helped me to complete the thesis work successfully. I would like to express my gratitude towards my doctoral committee members, Dr. Uday Narayan Maiti (DC chairman), Dr. Tapan Kumar Mishra and Dr. Anki Reddy Katha for reviewing the research work and providing their valuable suggestions for the improvement of the thesis. I am also thankful to the present HoD, Prof. Subhradip Ghosh and the former HoD, Prof. P. Poulose for their immense support and for providing me with all the necessary facilities to carry forward the research work.

I am very much thankful to Prof. Mohindar Singh Seehra, Eberly distinguished Professor Emeritus, Department of Physics & Astronomy, West Virginia University, USA for his most priceless opinions, guidance and for interesting discussions related to Physics which helped me to tackle any scientific problem efficiently. I thank him for giving me so much of his valuable time and for rectifying all my mistakes so patiently. I was very much fortunate to be able to work with him and it was truly a great learning experience for me. I am grateful to Dr. Tapati Sarkar for performing all the SQUID magnetic measurements which were very important for the completion of this doctoral thesis. I take this opportunity to thank Dr. Manfred Reehuis from Helmholtz-Zentrum Berlin, Germany for performing the neutron diffraction measurements which are reported in this thesis. I also express my gratitude and sincere thanks to Dr. R. Rawat, UGC DAE Indore for helping with the electrical measurements, and Dr. R. J. Choudhary, UGC DAE Indore for the support in performing magnetic measurements. I am thankful to IIT Guwahati, for providing the PARAM-ISHAN supercomputing facility. This really made my research experience easier. I also acknowledge the funding program DST FIST-I (XRD and Newton cluster), DST FIST-II (PPMS) and the Central Instruments Facility (CIF) for supporting my research work. I am grateful to IIT Guwahati, and Govt. of India, Ministry of Education for the financial support.

I am fortunate enough to have had seniors like Dr. Deep Chandra Joshi and Dr. Prativa Pramanik, who helped me in various ways throughout my research work. I sincerely thank them for their selfless assistance and constant support. I would like to especially thank Suchit for always being there beside me whenever I required help and support. I am thankful to my juniors Shaona, Ravi, and Maruthi for their help and pleasant company. I am thankful to Mouli with whom I established a wonderful relation in a short span of time. I would sincerely like to thank Dr. Sobhit Singh for helping me out whenever I encountered any problem during my research especially in DFT calculations. The discussions with him were very fruitful and it helped me a lot in theoretical analysis. I would also like to thank Dr. Debashish Das, for helping me to perform the DFT calculations at the initial stages of my PhD life. I would like to acknowledge Dr. Ranganadha Tanguturi for guiding me during different analyses of the experimental data. I acknowledge all my present and former lab members along with the intern students: Anshul, Tanveer Bhaiya, Ayush, Joya, Rohan, Ameer, Bhupesh, Mahendar, Swati, Kamal, Soumya, Atyant, Shweta, Shalini and Shourya. I thank them all for the wonderful memories we shared at IITG.

I would also like to thank the family members of my guide, Dr. Subhash Thota for their love and affection at all times. I had many memorable times with Sir, Revathi Mam, Samitha, Avantika and Sir's father. The late-night dinners will be dearly missed.

I shared my workspace with plenty of wonderful people: Kallol da, Ramiz da, Srimoy da, Rishav da, Tapo da, Arghya, Madhurima, Ipsita, Devabrat, Rony, Suruj, Prantik, Esha, Sumit, Danny, Shafeeque. They made the working atmosphere lively and enjoyable.

I am extremely fortunate to have some amazing friends who are very close to me. Lopamudra, Kajal, Dibyendu, Suman, Abhishek and I had a wonderful time in IITG right from the day we landed here and hopefully it will continue further. I thank them for being there always for me. I was also lucky to have Dibyendu, Niloy and Briti, who were like my younger brothers. A heartful thanks to Motor and KC da for being there always and for all the advice, support and affection you guys showed towards me. I thank my friends Anirban, Praloy, Guju, Haru, Lokesh, Guha and Sayak for being a part of my life. They will always remain very special. I thank Lina and boudi (Rumi) very much for treating me as their brother. Suna is always there to lend his support and I really adore our brotherhood from the very day we met. Ranita deserves a special mention for being there for me at all times ever since the eighth standard.

I am grateful to all my teachers who taught me at various stages of my life since childhood. I would never have been able to come this far without their support. Special thanks to Chorda Kaku (my uncle) who taught me physics during my tenth standard. I was influenced by his teaching and fell in love with Physics because of his teachings and it all started from there.

I owe everything to my beloved parents. Without their support and infinite motivation, I would never have been ever able to complete my PhD. Ma and Baba, I thank you for all the sacrifices you made to make my life a lot easier. Dada, you are one of the main reasons behind whatever success I have achieved in my life. You have taken care of all the necessary things and never let any problem come to me. Thank you as you will be the main source of motivation for me till the last day of my life. I sincere thank Masi and Mammam for their moral support and encouragement. I am thankful to my in-laws for understanding my conditions and for accepting as I am, which helped me in continuing my research work peacefully. Saptaparna, who is my life partner, deserves the most special mention for being my rock throughout my PhD. I thank you for being so patient and for tolerating me on my bad days. You were there for me through all the ups and downs in my life and had absolute faith in me. Thank you for your unconditional love and support. Finally, my sincere thanks to all those persons who helped me in all the means to bring me to this position, some of them whom I may unintentionally forgotten to mention in this acknowledgement.

Sayandeep Ghosh

Contents

List of Figures

Chapter-2

Chapter-3

Chapter-4

Chapter-5

Chapter-6

List of Tables

Chapter-5

Chapter-6

List of Abbreviations and Symbols

XRD — X-ray diffraction
DOS — Density of states
GGA — Generalized gradient approximation
E_g — band gap energy
T_N — Néel temperature
T_{SG} — Spin-Glass temperature
h — hours
ZFC — Zero-Field Cooled
FC — Field Cooled
FM — Ferromagnet
AFM — Anti-ferromagnet
FiM — Ferrimagnet
Å — Angstrom
χ — Magnetic susceptibility
K — Kelvin
M — Magnetization
H — Magnetic field
T — Temperature
U — Coulombic parameter
μ_B — Bohr magnetron
K-M — Kubelka-Munk
XPS — X-ray Photoelectron spectroscopy
MCE — magnetocaloric effect

Chapter 1
Introduction

Since 1950's, the magnetic spinel oxides are well studied due their unique magnetic properties and potential applications in the low-loss transformer cores, magnetic recording, microwave devices, magnetic read-write heads, magnetically tuneable capacitor and magnetic field sensors [1-8]. Among the magnetic spinel oxides, cobalt oxide (Co_3O_4) in the form of bulk and nanostructure draws immense attention due to its strong catalytic activity and potential application in renewable energy sector [9-12]. Due to its low cost, simple fabrication process and wide range of application, extensive investigation has been done in last few decades on Co_3O_4 and related nanostructures [13-20]. In recent times, more attention has been focused on nano-structured Co_3O_4 due to its ability to exhibit different behaviour than its bulk counterpart in terms of both super-paramagnetism and ferrimagnetism. Additionally, while incorporating non-magnetic elements like Ti, Sn, Ru, Ge in Co_3O_4 matrix (popularly known as magnetic-dilution), the resultant compounds also exhibit promising candidates for fuel cell and renewable energy. Besides the technological applications, these diluted spinels have unique magnetic properties such as exchange bias, geometrical frustration, spin-glass state, negative magnetization, magnetic compensation, magnetic field induced transitions etc. [20-24]. In this thesis, we have investigated the structure, magnetic, electronic behaviour of these spinels.

In this chapter, first we discuss the structure details of different spinel compounds that we have considered for this doctoral thesis. It is followed by a brief presentation on different magnetic behaviour (like ferromagnetism, antiferromagnetism, ferrimagnetism, paramagnetism) exhibited by the investigated materials. Also, the relevant theories like Hund's rule, Weiss molecular field theory, magnetic exchange interactions, etc are outlined. Further, we discuss the underlying concepts and theories behind interesting complex magnetic phenomena, like negative magnetization, magnetic compensation, spin glass, shown by the magnetic spinels. Next, the crystal field theory and Jahn Teller distortions have been presented. At the end we give a description of the problems presented in different chapters.

1.1 Spinel oxides:

Spinels are special class of minerals, represented with general formula AB_2X_4 (A, B ≡ cations and X ≡ anions (O, S, Se, Te)). The crystal structure was first determined by Bragg [25] and Nishikawa [26] which is similar to the mineral $MgAl_2O_4$ (belongs to the space group *Fd3m* ($F^4_{1/d}\bar{3}_{2/m}$; O^7_h; No. 227) [27]. Figure 1.1 shows the primitive tetrahedral unit cell of the spinel, consisting of two molecular units and represented as two octants consisting of eight effective formula units per unit cell with 24 cations and 32 anions, out of total 56 atoms [28]. Generally, the anion sublattices are arranged in pseudo-cubic closed packed spatial arrangements with 96 interstices (64 tetrahedral and 32 octahedral interstices) between the anions. Among the 64 tetrahedral interstices, 8 are occupied by the cations and remaining 16 cations occupy the half of the octahedral interstices. Depending on the choice of setting of the origin in the unit cell there are two possible cases of the equipoints with point symmetry $\bar{4}3m$ and $\bar{3}m$, where the atoms can occupy the empty sites or

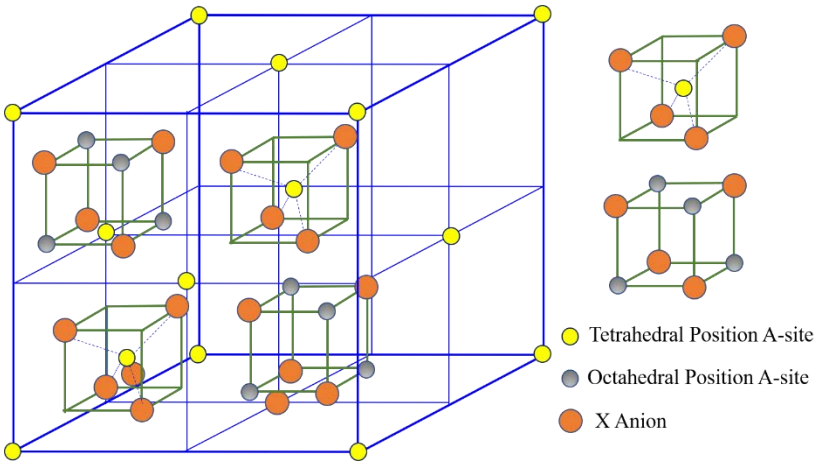

Fig. 1.1: Schematic representation of the primitive tetragonal and conventional cubic unit cells of spinel. The primitive cell consists of two octants of the cubic unit cell in the tetrahedral and octahedral co-ordinates [28].

Table 1.1: Lattice sites along the body diagonal in the ideal conventional unit cell of spinel by considering four possible choices of the origin.

Fractional coordinates along body diagonal of unit cell	Origin at $\bar{4}3m$			Origin at $\bar{3}m$		
	Equipoint (Wycoff notation)	Origin on A-site	Origin on tetrahedral vacancy	Equipoint (Wycoff notation)	Origin on B-site	Origin on octahedral vacancy
0, 0, 0	8a	A-site cation	Tetrahedral vacancy	16c	B-site cation	Octahedral vacancy
1/8, 1/8, 1/8	16c	Octahedral vacancy	B-site cation	8a	Tetrahedral vacancy	A-site cation
1/4, 1/4, 1/4	8a	A-site cation	Tetrahedral vacancy	32e	Anion X	Anion X
3/8, 3/8, 3/8	32e	Anion X	Anion X	8b	A-site cation	Tetrahedral vacancy
1/2, 1/2, 1/2	8b	Tetrahedral vacancy	A-site cation	16d	Octahedral vacancy	B-site cation
5/8, 5/8, 5/8	16d	B-site cation	Octahedral vacancy	8b	A-site cation	Tetrahedral vacancy
3/4, 3/4, 3/4	8b	Tetrahedral vacancy	A-site cation	32e	Anion X	Anion X
7/8, 7/8, 7/8	32e	Anion X	Anion X	8a	Tetrahedral vacancy	A-site cation

already occupied lattice sites. Table 1.1 lists the position of the lattice site along the body diagonal unit cell for four possible choices of the origin. Generally, the tetrahedral A-sites are occupied by the divalent cations and the octahedral B-sites are occupied by trivalent cations. However, other combinations are also possible with divalent, trivalent, and tetravalent cations. Depending upon the cationic distribution ($(A_{1-x}B_x)[B_{2-x}A_x]X_4$, where x is the inversion parameter) spinels are divided into three different categories: (*i*) Normal spinel ($x = 0$) (*ii*) Inverse spinel ($x = 1$), and (iii) Mixed spinel ($0 < x < 1$). The average bond angle of *B*-*X*-*B* and *A*-*X*-*B* is approximately 90° and 125°, respectively. The *A*-*X* bond length is $\sqrt{3}a(u - 1/4)$ and bond length between the *B* and *X* is $a[2(u - 3/8)^2 + (5/8 - u)^2]^{1/2}$, where '$a$' is the lattice parameter and 'u' is the anion parameter. The bond-lengths and bond-angles play a vital role in determining the physical properties of the system. The present thesis deals with the spinel family of Cobalt, in which various non-magnetic elements are incorporated at A/B sites of the spinel lattice which alters the bond-length and bond-angles. Consequently, the magnetic exchange interaction varies leading to interesting magnetic and electronic properties.

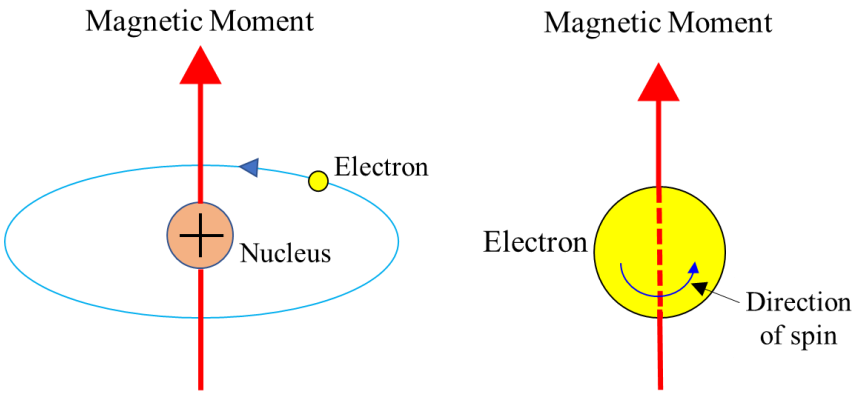

Fig. 1.2: Schematic of the magnetic moment corresponding to (a) an orbiting electron and (b) a spinning electron.

After a brief structural discussion, now we present the underlying concepts behind different magnetic features exhibited by these spinels.

1.2 Magnetic moments:

The magnetic moment appears in the materials due to the presence of the motion of the electrons. There are two reasons for the origin of magnetic moments. Firstly, the electron revolves around the nucleus and the orbital motion generates the magnetic moment along the axis of rotation. Secondly, the electron rotates about its axis, known as electron spin and the magnetic moments originate along the direction of the spin axis (shown in Fig. 1.2). This indicates all the electrons in an atom behaves like tiny magnets due to the orbital and spin magnetic moments, consequently, various macroscopic magnetic properties emerge. For example, if an electron is placed in a magnetic field then its spin aligns parallel to the field along the z-axis with energy $E = g\mu_B B m_S$,where, B is the magnetic flux density, g is Landé g-factor (≈ 2) and $m_S = \pm\frac{1}{2}$ as we consider that the electron spin is along *z*-axis. This implies that if the magnetic field and the electron spin are not parallel to each other, then the energy can be written as vector product $E = g\mu_B \boldsymbol{B}.\boldsymbol{S}$. Along with the spin angular momentum, an electron also exhibits orbital angular momentum $\hat{L} = \sum_i \boldsymbol{r}_i \times \hat{p}_i$. In this expression, $\boldsymbol{r}_i$ is the position of the i^{th} electron in the atom and the corresponding momentum is $\hat{p}_i$. Now for any given atom the Hamiltonian is given by [29]:

$$\hat{H}_0 = \sum_{i=1}^{Z} \left(\frac{\hat{p}_i^2}{2m} + V_i \right) \tag{1.1}$$

where the first term is the kinetic energy and the second term is assigned as the potential energy. The summation is taken over all the Z electrons in the atom. Now we need to add the magnetic field **B** $(= \nabla \times \boldsymbol{A})$ in the Hamiltonian. Here $\boldsymbol{A}$ is the magnetic vector potential and the gauge transformation yields $\boldsymbol{A}(\boldsymbol{r}) = (\boldsymbol{B} \times \boldsymbol{r})/2$. However, in the presence of the external magnetic field the classical momentum should be represented as canonical momentum $\hat{p}_i = (\hat{p}_i + e\boldsymbol{A}(\boldsymbol{r}_i))$ and therefore the perturbed Hamiltonian can be written as:

$$\hat{H} = \sum_{i=1}^{Z} \left(\frac{[\hat{p}_i + e\boldsymbol{A}(\boldsymbol{r}_i)]^2}{2m_e} + V_i \right) + g\mu_B \boldsymbol{B}.\boldsymbol{S} \tag{1.2}$$

where $$\boldsymbol{A}.\boldsymbol{p} = \frac{1}{2}(\boldsymbol{B} \times \boldsymbol{r}).\boldsymbol{p} = \frac{1}{2}(\boldsymbol{r} \times \boldsymbol{p}).\boldsymbol{B} = \frac{1}{2}\hbar \boldsymbol{L}.\boldsymbol{B} \tag{1.3}$$

substituting Eq. (1.3) in Eq. (1.2), leads to

$$\hat{H} = \sum_i \left(\frac{\hat{p}_i^2}{2m_e} + V_i \right) + \mu_B(\boldsymbol{L} + g\boldsymbol{S}).\boldsymbol{B} + \frac{e^2}{8m_e}\sum_i (\boldsymbol{B} \times \boldsymbol{r_i})^2$$

$$= \hat{H}_0 + \mu_B(\boldsymbol{L} + g\boldsymbol{S}).\boldsymbol{B} + \frac{e^2}{8m_e}\sum_i (\boldsymbol{B} \times \boldsymbol{r_i})^2 \tag{1.4}$$

In the above equation, $\mu_B = \frac{e\hbar}{2m}$ is the Bohr Magneton and $\hat{H}_0$ represents the unperturbed Hamiltonian. Second term in Eq. (1.4) represents the paramagnetic contribution and this is a dominant perturbation to the original Hamiltonian. This term corresponds to the positive magnetization where the spin magnets orient parallel to the external magnetic field. The last term represents the diamagnetic contribution in the material and exhibits weak negative magnetization due to the anti-parallel alignment of spins to the external magnetic field.

1.2.1 Hund's rules:

The resultant angular momentum of an atom depends only on electrons in unfilled shells (the net angular momentum of a filled shell is zero). There are two factors to consider when determining the appropriate way to add the momentum of the individual electrons to obtain the overall angular momentum of the atom: (i) electrostatic Coulomb interaction between the atomic electrons leads to an effective coupling between the spin angular momenta, and (ii) Spin-orbit interaction, a relativistic effect which becomes more significant for heavier atoms [30].

For low to intermediate weight elements the electrons' static interactions dominate and the spin-orbit interaction can be treated as a perturbation. The combination of angular momentum quantum numbers which minimize the ground state energy can be obtained by applying Hund's rules. When an atom has orbitals of equal energy, the order in which they are filled by electrons is such that a maximum number of electrons have unpaired spins [31]. The three possibilities are: (i) To maximize the total spin angular momentum S, while, keeping the parallel spins to minimize the coulomb repulsion between electrons, (ii) To maximize the total orbital angular momentum L, while the electron orbits rotating in the same direction minimizes the coulomb repulsion between electrons, and (iii) J = L − S if shell is less than half filled, J = L + S if shell is more than half filled. The rules assume that the repulsion between the outer electrons is much greater than the spin-orbit interaction which is in turn stronger than any other remaining interactions. The last rule arises from the spin-orbit interaction. It works well for rare earth ions but for some systems such as TM ions, the spin orbit energies are not as significant as the crystal field for example and so Hund's third rule is disobeyed [29,30].

1.2.2 Theoretical description of Curie's law:

Let us consider a volume V of gas containing N paramagnetic atoms per unit volume with a permanent magnetic moment **μ**. Due to the thermal excitations of the gas the atoms are randomly distributed with favourable spin orientation such that the net magnetic moment must be zero. If we apply any external magnetic field, then the magnetic spins would tend to orient along the field direction overcoming the effect of thermal excitations. The perfect spin alignment is only possible at absolute temperature. Also, the interaction between the spins is neglected so that in the calculations we consider the response of the magnetic atoms to the applied magnetic field. The determination of the net magnetization is usually dependent on the total angular momentum ***J*** (= Orbital angular momentum **L** ± Spin angular momentum **S**). According to the Hund's rule discussed above, if the orbitals are more than half filled, *J* takes the sum of L and S. However, when the orbitals are less than half filled then we have *J* = L - S. The magnetic orbital quantum number (m_J) varies between $-J$ and $+J$ including zero, therefore total 2*J*+1 number of permanent atomic magnetic moment component ($m_J g\mu_B$) lies parallel to the magnetic field direction. According to statistical mechanics, the total magnetization *M* for N number of atoms with a particular orientation can be expressed as:

$$M = N\frac{\sum_{-J}^{+J} m_J g\mu_B e^{m_J g\mu_B B/KT}}{\sum_{-J}^{+J} e^{m_J g\mu_B B/KT}} \tag{1.5}$$

Let us consider $x = g\mu_B B/KT$, above expression can be simplified as:

$$M = Ng\mu_B \frac{d}{dx} ln \sum_{-J}^{+J} e^{m_J x} \tag{1.6}$$

Expanding the series, we obtain $\sum_{-J}^{+J} e^{m_J x} = e^{-Jx}\left(1 + e^{x} + e^{2x} + \cdots + e^{(2J-1)x} + e^{2Jx}\right)$ and using the geometric progression for the sum, Eq. (1.6) one can rewrite the equation as:

$$M = Ng\mu_B \frac{d}{dx}\left(\ln e^{-Jx}\frac{1 - e^{(2J+1)x}}{1 - e^{x}}\right) \tag{1.7}$$

Using $\sinh x = (e^{x} - e^{-x})/2$ we obtain

$$M = Ng\mu_B \left[\frac{d}{dx}\left(\ln\frac{\sinh[(2J+1)/2]x}{\sinh(x/2)}\right)\right] \tag{1.8}$$

Finally, Eq. (1.8) yeilds

$$M = Ng\mu_B J\left[\frac{2J+1}{2J} coth\left(\frac{2J+1}{2J}y\right) - \frac{1}{2J} coth\frac{y}{2J}\right] = Ng\mu_B J B_J(y) \tag{1.9}$$

where, $y = g\mu_B JB/kT$ and $B_J(y)$ is known as 'Brillouin function'. The saturation magnetization is represented as $M_S = Ng\mu_B J$. The Eq. (1.9) can be written as $\frac{M}{M_S} = B_J(y)$. In Fig. 1.3 we plotted the Brillouin function vs. y for different value of J. For $J = \frac{1}{2}$ and ∞ the magnitude of $B_J(y)$ approaches $\tanh(y)$ and

$\coth(y) - \frac{1}{y}$, respectively. Additionally, near the room temperature T = 300K, for $J = \frac{1}{2}$, $g = 2$ and H = 10kOe, the y values yields ~ 2×10^{-3}. For extremely high magnetic field and/or low temperatures the experimental situation will corresponds to $y << 1$. Using the Maclaurin series expansion for small value of y, the calculated $B_J(y) = \frac{(J+1)y}{3J} + O(y^3)$. Hence, at the low temperature the magnetic susceptibility can be expressed as:

$$\chi = \frac{M}{H} \approx \frac{\mu_0 M}{B} = \frac{\mu_0 N}{3kT} g^2 \mu_B^2 J(J+1) = \frac{C}{T} \tag{1.10}$$

Eq. (1.10) is known as the Curie's Law [29,32], where C is the Curie constant and the effective moment is defined as $\mu_{eff} = g\mu_B\sqrt{J(J+1)}$. However, χ obtained experimentally differs from the Curie law, as we consider that the magnetic atoms are isolated with no magnetic interaction between them. Later, Weiss implemented the molecular field theory to consider the interactions between the magnetic atoms and had rewritten the Eq. (1.10) as follows which is popularly known as Curie-Weiss law [29,32]:

$$\chi = \frac{C}{T - \theta} \tag{1.11}$$

In Eq. (1.11), θ is known as Curie-Weiss temperature. Later we will discuss the θ to determine the nature of exchange interactions present in the magnetic materials. Eq. (1.11) may be written as:

$$\chi = \chi_0 + \frac{C}{T - \theta} \tag{1.12}$$

Here, $\chi_0 = \chi_d + \chi_{vv}$ contains contributions from the (negative diamagnetic susceptibility χ_d and (positive) van Vleck susceptibility χ_{vv}, both of which have only very weak temperature dependence [33-35]. All systems

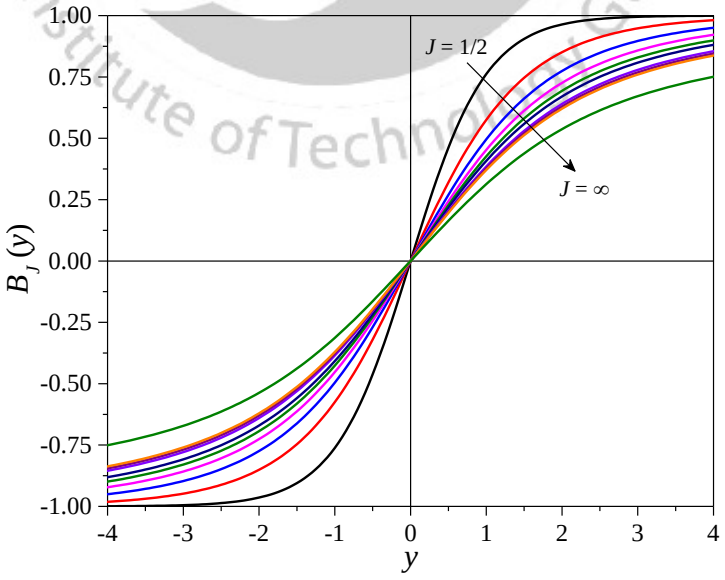

Fig. 1.3: The magnetization of paramagnetic material as a function of the total angular quantum number J. The magnetization follows the Brillouin function $B_J(y) = \frac{2J+1}{2J}coth\left(\frac{2J+1}{2J}y\right) - \frac{1}{2J}coth\frac{y}{2J}$ where, J = 1/2, 1, 3/2, 2, 5/2,…, ∞.

have non-zero χ_d although it may be comparatively negligible. However, χ_{vv} is always present in systems due to the spin-orbit coupling. Since χ_d and χ_{vv} are of opposite signs, $\chi_0 = \chi_d + \chi_{vv}$ is often difficult to calculate accurately. Experimentally, χ_0 is determined from the plot of χ vs. 1/T in the limit of $1/T \rightarrow 0$ with a focus on the high T data where the contribution from the paramagnetic term $C/(T-\theta)$ becomes negligible.

1.2.3 Magnetic exchange interactions:

In this section we provide a brief idea about the interactions between the magnetic atoms based on the quantum mechanical approach. These different types of interactions allow the magnetic constituents to communicate with each other and establish the long-range ordering of the system. Depending upon the energetically favourable structure of the system the spin alignment takes place; i.e. parallel or antiparallel alignment of spins between the neighbouring atoms in which the angle varies between 0 and 90°. There are two main classifications of magnetic interactions: (*i*) Magnetic dipole interaction and (*ii*) Exchange interaction. The magnetic dipole interaction is very weak in nature and account for the ordering of most of the magnetic materials, however this interaction is important to understand the physics of those systems which exhibits milli Kelvin ordering temperature. In most of the magnetic materials exchange coupling or exchange interaction decides the overall magnetic behaviour. To understand this phenomenon let us consider two electrons having spatial co-ordinates $\boldsymbol{r_1}$ and $\boldsymbol{r_2}$. The wavefunctions for the joint state can be represented as the product of individual states $\psi_a(\boldsymbol{r_1})\psi_b(\boldsymbol{r_2})$. Such combination does not necessarily follow the exchange symmetry but the overall wavefunctions of the electrons must be antisymmetric. For two electron system there are only two possibilities: (*a*) For $S = 0$, an antisymmetric singlet spin state (χ_S) with symmetric spatial state, and (*b*) For $S = 1$, a symmetric triplet spin state (χ_T) with an antisymmetric spatial state. Therefore, considering both the spatial and spin part, wavefunctions for the singlet ($\boldsymbol{\Psi}_S$) and triplet ($\boldsymbol{\Psi}_T$) states can be expressed as [29,32]:

$$\boldsymbol{\Psi}_S = \frac{1}{\sqrt{2}}[\psi_a(\boldsymbol{r_1})\psi_b(\boldsymbol{r_2}) + \psi_a(\boldsymbol{r_2})\psi_b(\boldsymbol{r_1})]\chi_S \tag{1.13}$$

$$\boldsymbol{\Psi}_T = \frac{1}{\sqrt{2}}[\psi_a(\boldsymbol{r_1})\psi_b(\boldsymbol{r_2}) - \psi_a(\boldsymbol{r_2})\psi_b(\boldsymbol{r_1})]\chi_T \tag{1.14}$$

If the spin states χ_S and χ_T are normalized then the energies of the two possible states can be expressed as

$$E_S = \int \boldsymbol{\Psi}_S^* \hat{H} \boldsymbol{\Psi}_S \, d\boldsymbol{r_1} d\boldsymbol{r_2} \tag{1.15}$$

$$E_T = \int \boldsymbol{\Psi}_T^* \hat{H} \boldsymbol{\Psi}_T \, d\boldsymbol{r_1} d\boldsymbol{r_2} \tag{1.16}$$

Therefore, the exchange constant can be expressed as

$$J = \frac{E_S - E_T}{2} = \int \psi_a^*(\boldsymbol{r_1})\psi_b^*(\boldsymbol{r_2})\, \hat{H} \psi_a(\boldsymbol{r_2})\psi_b(\boldsymbol{r_1}) d\boldsymbol{r_1} d\boldsymbol{r_2} \tag{1.17}$$

and the effective Hamiltonian is

$$\hat{H} = -2J\, \boldsymbol{S}_1 \cdot \boldsymbol{S}_2 \tag{1.18}$$

If $J > 0$, the triplet state $S = 1$ is favourable because E_S is greater than E_T. Otherwise, for $J < 0$, $E_S < E_T$ and the singlet state $S = 0$ is favoured. Eq. (1.18) can be easily derived for two electron system, but for many body systems generalizing the Eq. (1.18) is far more difficult. However, for many body systems to determine the nearest neighbour exchange constant Heisenberg proposed the Hamiltonian as:

$$\hat{H} = -\sum_{<ij>} J_{ij}\, \boldsymbol{S}_1 \cdot \boldsymbol{S}_2 \tag{1.19}$$

where, J_{ij} is the exchange constant between the i^{th} and j^{th} spins. The magnitude and sign of J_{ij} provides an idea of what type of magnetic ordering the material consists. Positive sign of J_{ij} signifies the ferromagnetic (FM) state where the nearest neighbour (nn) spins are parallel to each other. However, the negative sign of J_{ij} represents the antiparallel spin configuration between the nn spins which corresponds to the antiferromagnetic (AFM) state. While, $J_{ij} = 0$ the system exhibits paramagnetic (PM) state, where the exchange interactions are absent between the magnetic atoms and the spins are randomly orientated. There are two different types of exchange interactions possible: (*i*) direct exchange interaction and (*ii*) indirect exchange interaction. For the first case, coupling between the neighbouring atoms occur without any intermediate atoms as shown in the Fig. 1.4(a). However, this direct exchange does not have any significant impact in controlling the magnetic properties because the direct overlap of localized 3*d* and 4*f* orbitals is quite impossible. Thus, most of the magnetic materials exhibit indirect exchange and depending upon the crystal structure/symmetry different types of indirect exchange interactions are possible. First type of indirect exchange interaction is 'super-exchange' interactions, where, the two magnetic atoms communicate through a non-magnetic atom located between them. Fig. 1.4(b) shows the super exchange interactions which take place through intermediate non-magnetic O^{2-} ions. The AFM interaction is possible when the nearest neighbour orbitals are half-filled. When the overlap happens between the empty and filled orbitals it causes FM coupling [36-40]. However, the FM super exchange interaction is much weaker than AFM case. The second type is first proposed by Rudderman, Kittel, Kasuya and Yosida popularly known as 'RKKY' interaction, where the exchange coupling between the magnetic atoms take places through the conduction electrons [29,32]. The coupling is oscillatory in nature which is the function of the distance between the magnetic atoms and represented as $J_{RKKY}(r) \propto \frac{\sin r - r\cos r}{r^4}$. Depending upon the oscillatory nature the system exhibits either the FM or AFM behaviour as shown in Fig. 1.4(c). The last type of interaction is known as 'double-exchange'. This interaction is noticeable between the magnetic ions which exhibit mixed valency (more than one oxidation state in the compound). For example, in case of $La_{0.7}Sr_{0.3}MnO_3$, both Mn^{3+} and Mn^{4+} coexists and hence the interaction between the Mn^{3+} and Mn^{4+} is FM in nature and this system is a typical example for 'double-exchange' interaction (Fig. 1.4(d)).

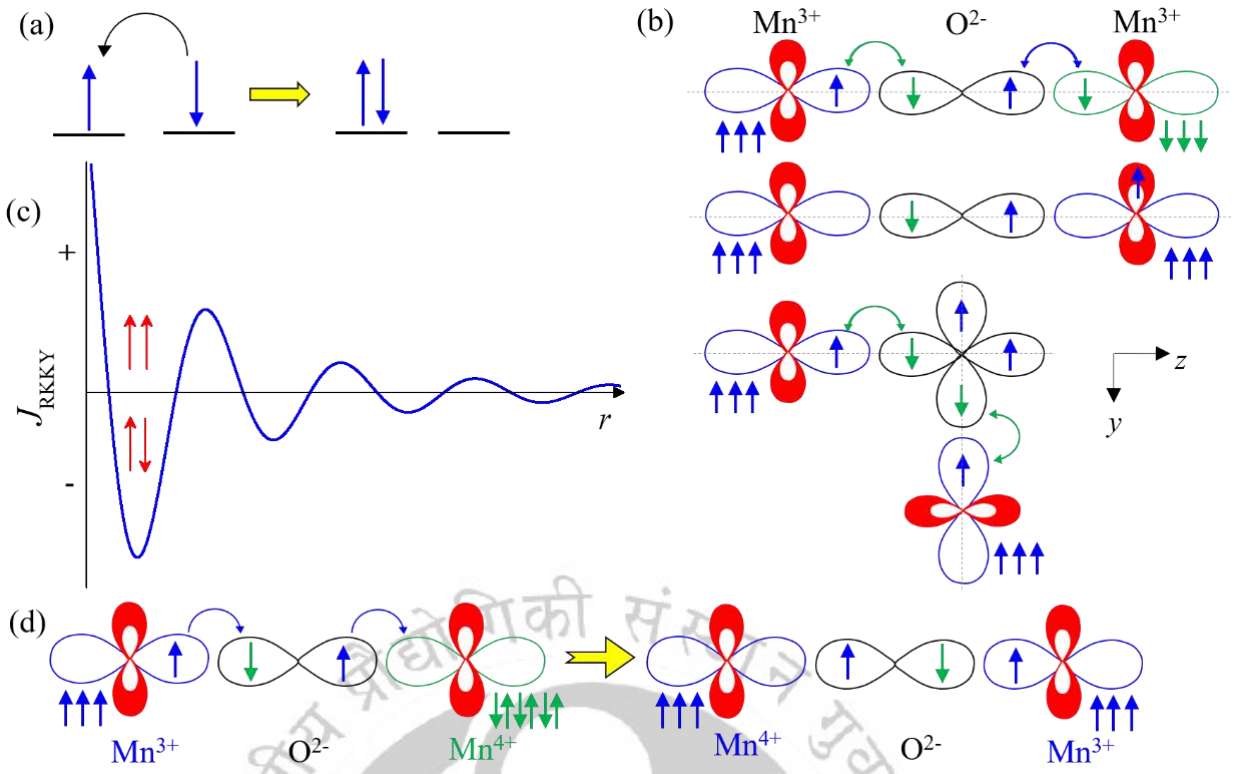

Fig. 1.4: Schematic representation of different types of exchange interactions: (a) direct, (b) indirect, (c) RKKY and (d) double exchange interactions. The indirect and double exchange interactions are shown between Mn cation and O anion in Mn_3O_4 and $La_{0.7}Sr_{0.3}MnO_3$, respectively.

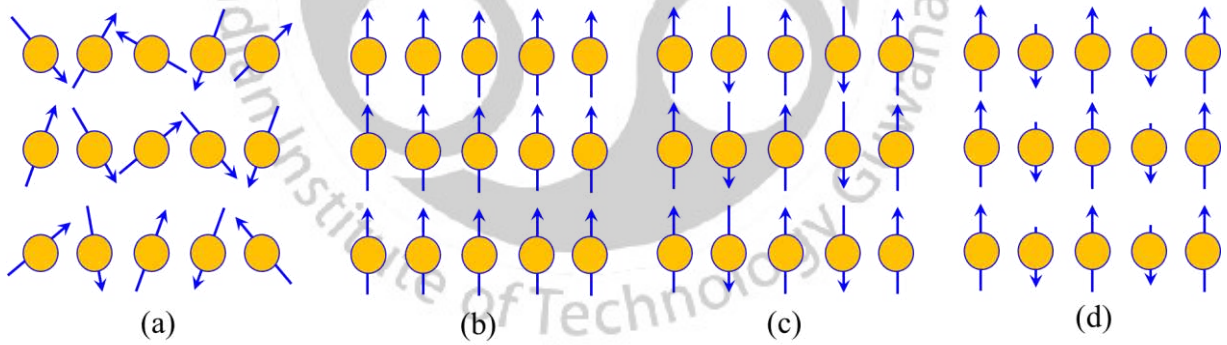

Fig. 1.5: Spin orientation for different magnetic system: (a) Paramagnetism, (b) Ferromagnetism, (c) Anti-ferromagnetism and (d) Ferrimagnetism.

1.2.4 Types of long-range ordering:

As we discussed in the earlier section that depending upon the magnitude of J_{ij} the magnetic ordering can be categorized into three different classes: (i) Paramagnetic ordering ($J_{ij} = 0$), (ii) Ferromagnetic ordering ($J_{ij} > 0$) and (iii) Antiferromagnetic ordering ($J_{ij} < 0$) (shown in Fig. 1.5). Another special class of magnetic ordering, named as Ferrimagnetic ordering (with $J_{ij} < 0$) is also often observed in spinels, which will be discussed later in this section. It is well known that the FM system exhibits non-linear magnetization in the presence of external magnetic field and exhibits spontaneous magnetization after the

removal of the external field. At absolute temperature all the spins get aligned in a particular direction owing to the presence of some internal field. However, while increasing the temperature the thermal excitation resists the spin to align in particular orientation and at certain temperature the atoms acquire thermal energy which destroys the ordered spin state. This critical temperature is known as Curie temperature (T_C) and above T_C the FM substance becomes paramagnetic in nature. According to the Weiss' domains theory of ferromagnetism: (*i*) There are a number of magnetic domains with spontaneous magnetization directed along specific direction and the net magnetization is determined by the vector sum of the individual domains, and (ii) the presence of spontaneous magnetization in each domain is due to internal magnetic field and this energy aligns the spin in parallel direction. The internal magnetic field is proportional to magnetization M, and can be represented as Weiss molecular field $B_E = \lambda M$, where λ is the Weiss field constant [29,32]. Therefore, in the presence of an external magnetic field B, the effective magnetic field is

$$B_{eff} = B + B_E = B + \lambda M \tag{1.20}$$

Now combining Eq. (1.9) and (1.20), we obtain

$$y = \frac{g\mu_B J B_{eff}}{kT} = \frac{g\mu_B J}{kT}(B + \lambda M) \tag{1.21}$$

In the absence of any external field ($B = 0$), Eq. (1.21) becomes

$$y = \frac{g\mu_B J \lambda M}{kT} \tag{1.22}$$

and the magnetization due to spontaneous magnetization is

$$M(T) = \frac{ykT}{\lambda g J \mu_B} \tag{1.23}$$

Now for $T \to 0$ or $y \to \infty$ implies $B_J(y) \to 1$; this signifies that all the moments align parallel to the field direction and the saturation magnetization can be expressed as

$$M_s\,(0) = NgJ\mu_B \tag{1.24}$$

From, Eq. (1.23) and (1.24) we obtain,

$$\frac{M(T)}{M_S(0)} = \frac{ykT}{\lambda N g^2 J^2 \mu_B^2} \tag{1.25}$$

Also, combining Eq. (1.9) and (1.24) gives,

$$\frac{M(T)}{M_S(0)} = B_J(y) \tag{1.26}$$

Since, $\frac{M(T)}{M_S(0)}$ satisfies both the Eqs. (1.25) and (1.26) simultaneously, the magnitude $\frac{M(T)}{M_S(0)}$ at certain temperature can be obtained graphically. The intersection of curves for Eqs. (1.25) and (1.26) gives the value at a given temperature. The graphical representation at different temperatures is shown in Fig. 1.6. The

straight line corresponding to $T = T_C$, is the tangent of the Brillouin function with an intersect at zero. For $T < T_C$, the straight line intersects the curve at two points, one at zero and the other value is non-zero. The non-zero value of $\frac{M(T)}{M_S(0)}$ signifies the stable situation with a spontaneous magnetization. For $T \geq T_C$, there is only one intersection with $\frac{M(T)}{M_S(0)} = 0$ indicating that the spontaneous magnetization vanishes. Thus $T = T_C$ is known as the Curie temperature. Due to the spontaneous magnetization the ferromagnetic samples exhibit hysteresis curve below T_C which is shown in Fig. 1.7(a). This hysteresis curves arise due to the presence of magnetic domains and growth of the size of the magnetic domains with increasing field. Also, complete rotation of these magnetic domains along the applied *H* direction determines the saturation magnetization value.

Moreover, one can easily divide the hysteresis loop in three parts. Firstly, when a small magnetic field is applied across the material the domains gradually increase which are oriented along the field direction. Such displacements are reversible commonly known as 'reversible domain-wall displacement'. If the applied field is increased, larger number of domains grow favourably and the magnetization gradually increases. This process continues until large number of favourable domains attain the maximum extent and the process is known as 'irreversible domain-wall displacement'. Now if one increases the applied field beyond this limit, then 'domain rotation' takes place where the domains rotate from the easy direction to the applied field direction and gradually attain the saturation magnetization M_S. While decreasing the magnetic field, the magnetization does not follow the same path as the random spin orientation cannot be regained easily. Therefore, the magnetization is still observed even when the applied field becomes zero and this is known as 'Remanent magnetization (M_R)'. To reduce this magnetization to zero we need to apply the magnetic field in reverse direction and this field is known as 'Coercivity (H_C)'. Similar behaviour is observed if the reverse magnetic field is increased and sweeps to zero, such a complete cycle is known as 'Hysteresis-loop'.

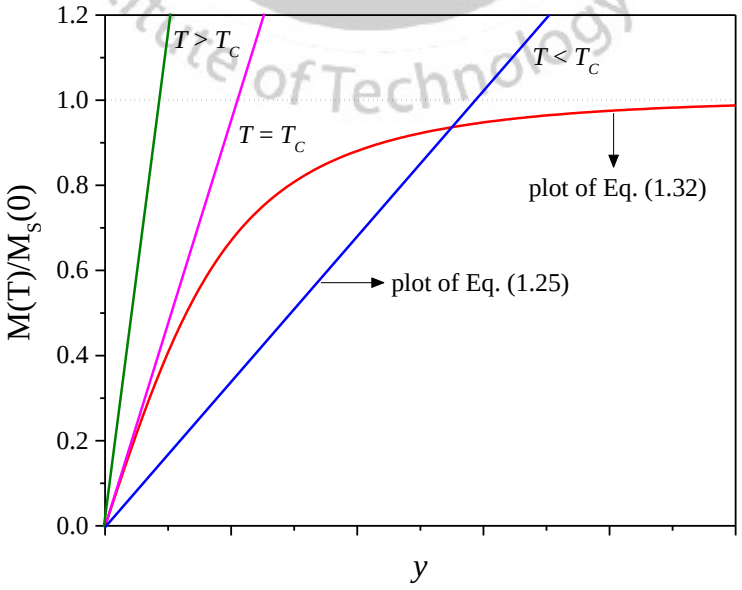

Fig. 1.6: Graphical solution of Eqs. (1.25) and (1.26). The intersection of the two curves give the spontaneous magnetization at temperature $T < T_C$. No solutions are obtained for $T \geq T_C$.

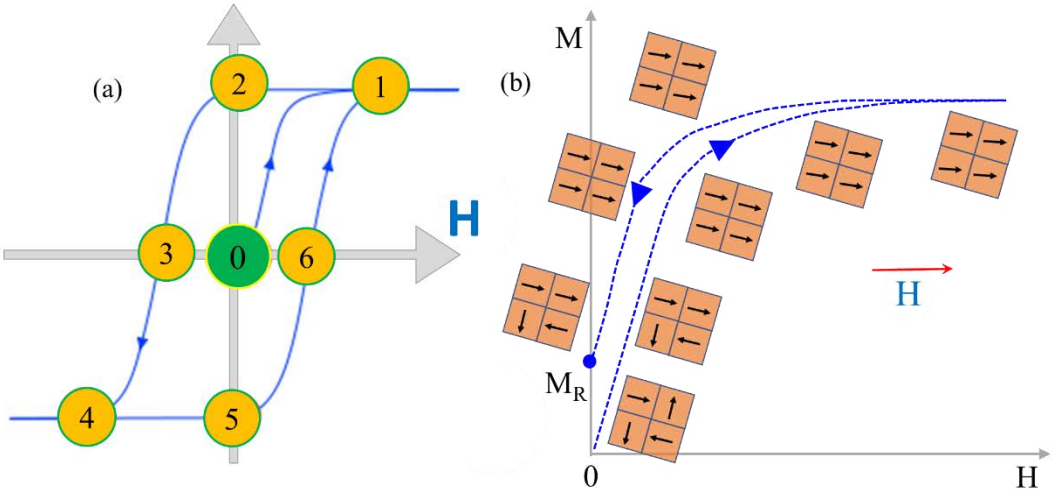

Fig. 1.7: (a) Schematic representation of a Hysteresis loop for a ferromagnetic sample displaying the saturation point (1 and 4), retentivity point (2 and 5) and the coercive point (3 and 6), (b) Schematic diagram for the magnetic domains with increasing and decreasing the magnetic field.

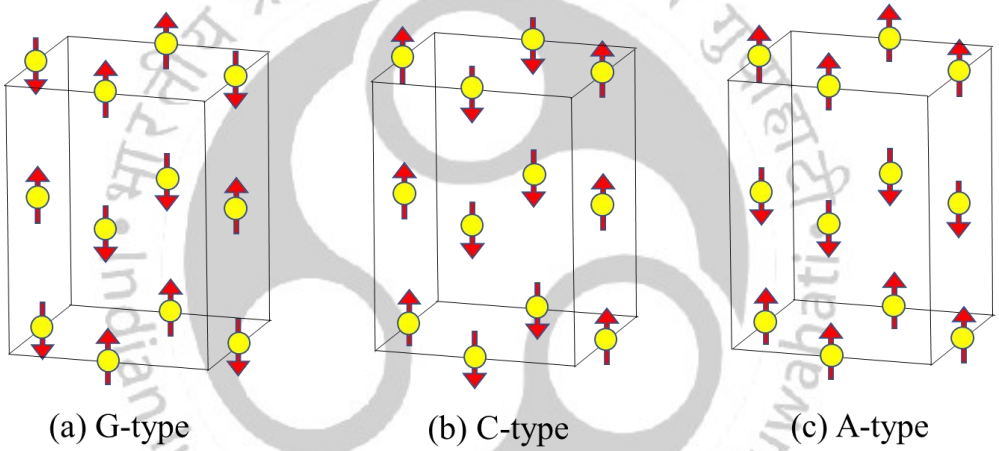

Fig. 1.8: Schematic diagram of different type of antiferromagnetic coupling among the nearest neighbour spins.

Figure 1.7(b) shows the schematic diagram of the magnetic domain orientation with increasing and decreasing of magnetic field (in 1st quadrant). In case of AFM systems spins align antiparallel (↑↓) to each other as shown in the schematic diagram of Fig. 1.8. In the absence of the external magnetic field, the neighbouring magnetic moments cancel out each other's contribution and exhibits a zero net magnetization. Now if an antiferromagnetic material is placed in an external magnetic field, the magnetization (M) appears along the field direction and it gradually increases as we increase the temperature. At certain temperature the M reaches a maximum which is known as Néel temperature (T_N), it is similar to T_C and beyond this T_N magnetization decreases exponentially with increase in temperature following the Curie's behaviour indicating the paramagnetic state. Now let us consider two interpenetrating sublattices A and B, where the one type of atom will have a different type of atom as its nearest neighbour. In case of antiferromagnetic material, the strong negative nearest neighbour interactions (J_{AA}/J_{BB}) is followed by a weak positive next nearest neighbour interaction (J_{AB}/J_{BA}). Following the Weiss theory of molecular field, we consider that α

and β are the interaction parameter or Weiss molecular field constants for AA (or BB) and AB interaction, respectively, then the magnetic flux densities can be written as [29,41]:

$$B_{mA} = -\alpha M_A - \beta M_B \quad (1.27\ a)$$

$$B_{mB} = -\beta M_A - \alpha M_B \quad (1.27\ b)$$

M_A and M_B is the magnetization at A and B sites, respectively. The effective fields at A and B sites in the presence of the external magnetic field can be expressed as:

$$B_A = B - \alpha M_A - \beta M_B \quad (1.28\ a)$$

$$B_B = B - \beta M_A - \alpha M_B \quad (1.28\ b)$$

For T > T_N, using Eq. (1.10) the magnetization at each sublattice can be written as

$$M_A = \frac{N\mu_B^2 g^2 J(J+1)}{6kT} B_A \quad (1.29\ a)$$

$$M_B = \frac{N\mu_B^2 g^2 J(J+1)}{6kT} B_B \quad (1.29\ b)$$

We assumed that A and B atoms are identical and hence the densities are equal $N_A = N_B = N$. Then the net magnetization turns out to be

$$M = M_A + M_B = \frac{N\mu_B^2 g^2 J(J+1)}{6kT}(B_A + B_B)$$

$$= \frac{N\mu_B^2 g^2 J(J+1)}{6kT}[2B - (\alpha+\beta)(M_A + M_B)]$$

$$= \frac{N\mu_B^2 g^2 J(J+1)}{6kT}[2B - (\alpha+\beta)M] \quad (1.30)$$

Hence, the susceptibility is given by,

$$\chi = \frac{\mu_0 M}{B} = \frac{C}{T+\theta} \quad (1.31)$$

where,

$$C = \frac{N\mu_B^2 g^2 J(J+1)}{3k}$$

and

$$\theta = \frac{N\mu_B^2 g^2 J(J+1)(\alpha+\beta)}{6k}$$

Again, T_N and θ can be related as,

$$\frac{T_N}{\theta} = \frac{\beta - \alpha}{\beta + \alpha} \quad (1.32)$$

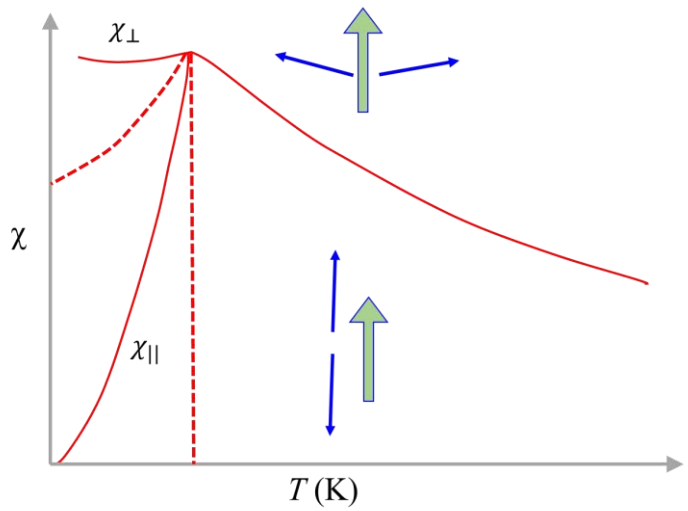

Fig. 1.9: Temperature dependent magnetic susceptibility (χ(T)) of the antiferromagnetic material. The anomaly in the curve represents the Néel temperature T_N. If the magnetic field is applied parallel to the Néel axis, then $\chi_\perp$ and $\chi_{||}$ represents the perpendicular and parallel susceptibility, respectively. The susceptibility of a polycrystalline antiferromagnet will be a combination of both.

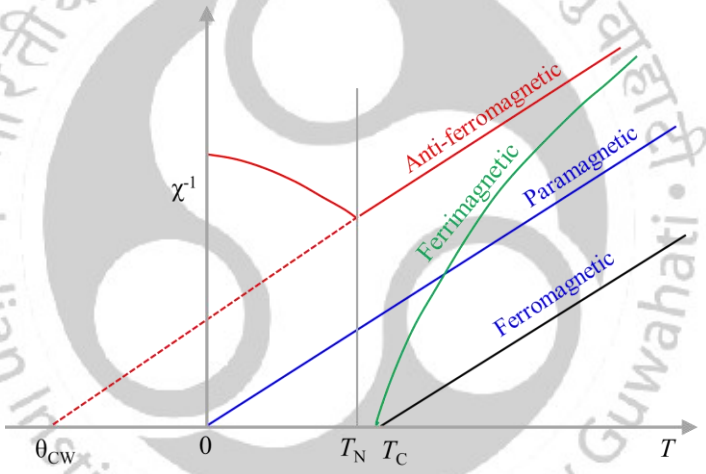

Fig. 1.10: Temperature dependence of inverse susceptibilities (χ^{-1}) of paramagnetic (PM), ferromagnetic (FM), antiferromagnetic (AFM) and ferrimagnetic (FiM) materials.

For $\alpha = 0$, $T_N = \theta$, whereas if $\alpha > 0$, $\theta > T_N$ and if $\alpha \gg \beta$, then the assumed two sublattice configuration become unstable. For $T < T_N$, the net magnetization is zero but the spins of the two sublattices A and B orient along the preferred direction. In the presence of the external magnetic field the system exhibits some net magnetic moment and the magnetization can have two preferred directions, one parallel and another perpendicular to the direction of applied magnetic field. Figure 1.9 shows the dc-magnetic susceptibility (χ = dM/dH) as a function of *T*, along with perpendicular component $\chi_\perp$ and parallel component $\chi_{||}$ below T_N. The $\chi_\perp$ component is independent of temperature and remains constant, whereas, $\chi_{||}$ gradually decreases upon lowering the temperature and approaches to zero. This suggests that at absolute temperature in the presence of external magnetic field, the molecular field is dominating and does not allow the spins of one sublattice to orient along the spins of the other sublattice resulting the net magnetization to zero. In case of

ferrimagnetic (FiM) systems which is a special case of AFM, the spins of the A and B sublattices are in opposite direction but unequal magnitude resulting in a non-zero net magnetic moment ($\Delta M = \uparrow_{\downarrow} \neq 0$). Consequently, the temperature where the transition occurs between ordered spin state to disorder paramagnetic state is known as ferrimagnetic Néel temperature (T_{FN}). The magnetic susceptibility of ferrimagnetic materials can be expressed as: $1/\chi = T/C + 1/\chi_0 - \sigma_0/(T-\theta)$ [8]. Summarizing this section, Fig. 1.10 shows the temperature dependent inverse magnetic susceptibility (χ^{-1}) where the negative θ is obtained for anti/ferri-magnetic and the positive θ is for ferromagnetic materials. In case of paramagnetic sample θ is essentially zero.

1.3 Negative magnetization and magnetic compensation:

This section deals with the concept of negative magnetization/magnetization reversal and magnetic compensation since some of the spinels that we investigated show these phenomena [22-24,42,43]. Usually, all the magnetic compounds (FM, AFM, PM, and FiM) exhibit non-zero spins with positive magnetization, whereas the diamagnetic samples exhibit negative magnetization irrespective of the direction of external magnetic field. However, sometimes when the magnetic material is cooled under the influence of the positive magnetic field, a crossover of the sign of magnetization from a positive value to a negative value takes place which can be seen in the temperature dependence of magnetization. The negative magnetization (with a positive differential susceptibility χ, $\partial M/\partial H$) occurs in the magnetic materials such as FM, AFM, PM, and FiM is completely different from the diamagnetic state (with a negative differential susceptibility) which often occurs in case of superconducting/diamagnetic materials (as shown in Fig. 1.11). Mathematical foundations to these phenomena were first established by Louis Néel in 1948 [44] and two years later, this unique phenomenon was experimentally probed in the spinel ferrites [45]. According to Néel theory this phenomenon mainly arises due to the different temperature dependence of sublattice magnetization. However, it has been observed that the crystal structure, magnetic anisotropy, magnetic exchange interactions can also trigger the magnetization reversal in the system. Negative magnetization is observed in

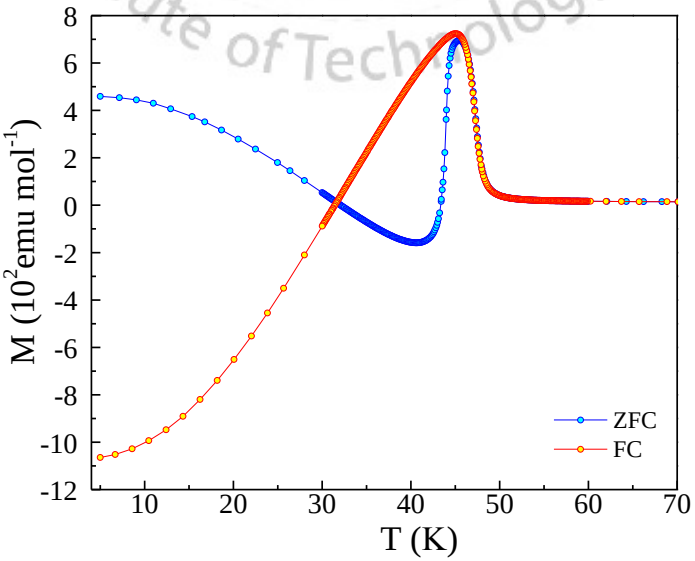

Fig. 1.11: Temperature dependent magnetization of polycrystalline Co_2TiO_4 sample measured under zero field cooled (ZFC) and field cooled (FC) condition at H_{dc} = 500 Oe.

five different conditions such as: (*i*) Negative exchange (NE) coupling among FM sublattices, (*ii*) NE among canted AFM sublattices, (*iii*) NE among FM/Canted-AFM and PM sublattices, (*iv*) Imbalance in the spin and orbital moments, and (*v*) Interfacial exchange coupling between FM and AFM phases [46]. In particular, the unique magnetic behavior of these systems is quite demanding in the field of magnetic recording (as read/write heads), spin-valve devices and applications such as thermally assisted magnetic random-access memory (TAMRAM). Furthermore, the phenomena of negative magnetization and compensation phenomena play a major role in achieving tunable magnetic entropy changes and large relative cooling powers in several magnetic compounds which have practical applications in the field of magnetic refrigeration technologies [46,47].

1.4 Exchange bias:

In this section we focus on the different phenomenological features of exchange bias (EB) effect from both theoretical and experimental point of view along with its importance in modern day technology. In this doctoral thesis we deal with high EB under both ZFC and FC conditions at low temperatures in few spinels. EB effect is also well known as *M-H* hysteresis loop asymmetry. In 1956, Meiklejohn and Bean first observed the magnetic exchange anisotropy in Co(FM)/CoO(AFM) core-shell nano-particles [48,49] under different cooling protocols, the schematic representation is shown in Fig. 1.12. The field cooled hysteresisloops (solid lines) shows a shifted and broadened feature than the zero-field cooled curve (dashed line). The reason for this unique behaviour is due to the unidirectional exchange anisotropy that appears at the interface between FM and AFM spin structures. The discovery of EB effect was a breakthrough discovery, due to which the magnetic materials with FM-AFM exchange interactions have gained immense attention in technological applications such as data storage technology, magnetic recording media, magnetic random-access memories, and magnetic field sensors [50-67]. Although several research works are devoted to develop magnetic nanoparticles which exhibits exchange bias effect, 2D thin film heterostructures become

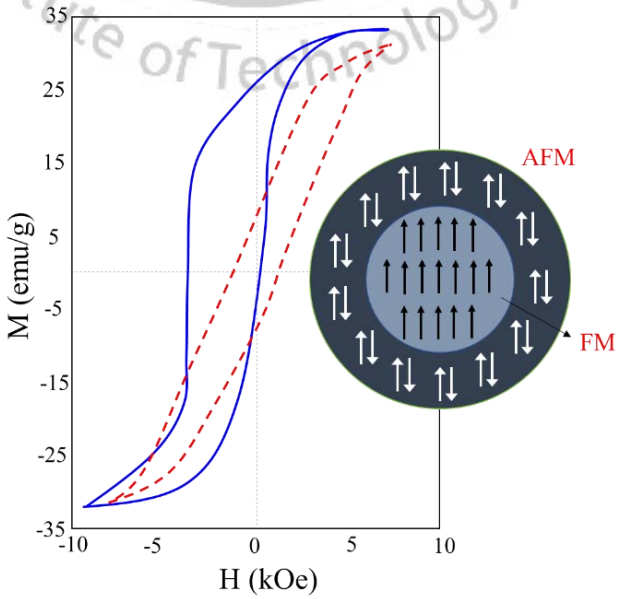

Fig. 1.12: Magnetic loop asymmetry of partially oxidized Co particles measured at 77 K [48].

more interesting due to a greater control of the FM-AFM pinned interface, in which the microstructure of both the constituents play a major role. Such controlled spin-structures across interfaces play a major role in deciding the magnitude of exchange bias field (H_{EB}) which can be used in spin valves and tunnelling devices [50,54,64-68]. To understand the origin of the EB effect let us consider a layer of FM and AFM material with ordering temperatures T_C and T_N, respectively. At any arbitrary temperature T between T_N and T_C, if the applied external field is large enough then all the spins in the FM layer will align parallel to H but spins in the AFM layer will remain random (Fig. 1.13(i)). However, further cooling ($T < T_N$) the system, the anti-ferromagnetic arrangement of spins set up in the AFM layer and at the FM-AFM interface the spins of both layers interact with each other. Therefore, across the interface all the spins in the first monolayer of the AFM layer tends to align parallel to the spins in the FM layers due to the interfacial interactions, while the other residual spins in the AFM layer remain antiparallel to each other which corresponds to zero net magnetization in the AFM layer. The most important aspect in this procedure is to align the AFM interface spins along the field direction and along the FM spins. The magnetic hysteresis loop (measured under FC mode) is shown in Fig. 1.13 which demonstrates the spin configuration in the FM-AFM layers. However, when the field start reversing all the spins, the FM layer start to align along the magnetic field while the large AFM anisotropy tries to keep all the spins pinned in the AFM state. Due to the interface coupling these spins will exert a microscopic torque to the spins in the FM layer and try to keep them in their original position (Fig. 1.13(iii)). Therefore, in order to get complete magnetization reversal, very high magnetic field is required to overcome the microscopic torque exerted by the spins in the AFM layer. As a result, the coercive field value increases in the negative field direction. Quite the reverse, when the magnetic field direction is reversed back to its positive value the rotation of spins in the FM will be easier since the interfacial interaction with the spins in

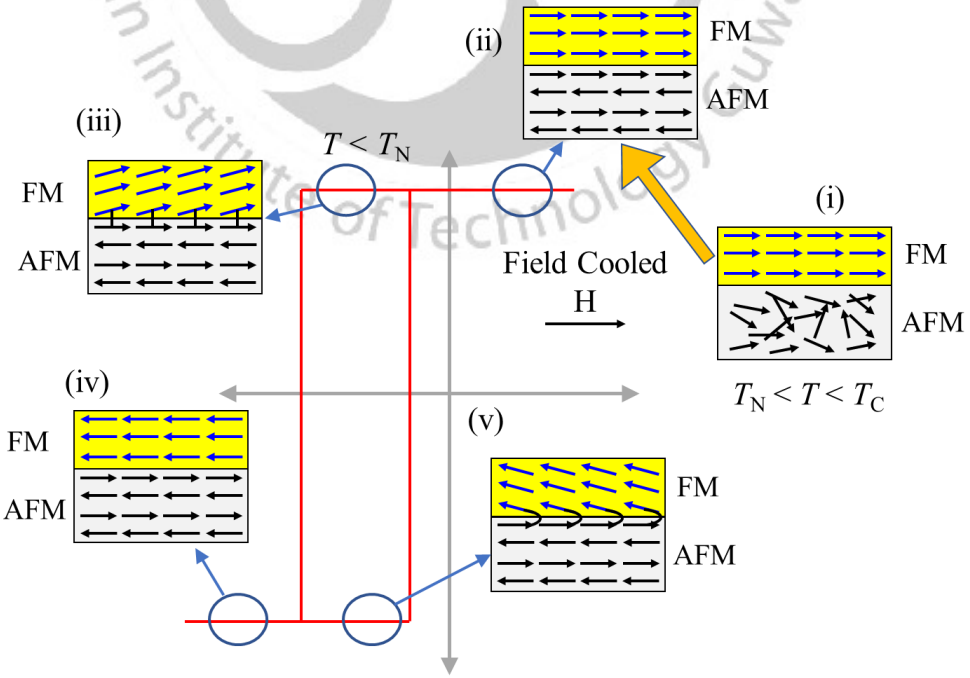

Fig. 1.13: Schematic of the spin orientation corresponding to the AFM-FM coupling at different stages of asymmetry M-H loop [71].

the AFM layer will now favour the magnetization reversal [Fig. 1.13(iv)]. In this situation the AFM ordering exerts a microscopic torque in the direction of applied magnetic field and less magnetic energy is required in the positive field direction. Therefore, along the positive and negative field directions, an unequal magnetic energy is required to rotate the spins in the FM layers, hence as a consequence the whole hysteresis loop shifts towards the negative field direction. The magnitude of exchange bias (H_{EB}) and coercive (H_C) field of a system can be calculated as: $H_{EB} = (H_+ + H_-)/2$ and $H_C = (H_+ - H_-)/2$, respectively. The EB phenomena is not only observed in bi-layer thin-film/superlattice systems but also observed in the bulk single-phase alloys and other nanostructures composed with a variety of magnetic phases coexisting such as ferromagnetic, antiferromagnetic, ferrimagnetic, spin-glass, cluster-glass, charge ordered and disordered magnetic states [69-76].

1.5 Spin Glass state:

Mathematically speaking, spin-glass phase is referred to as multiple ground states present in a crystalline system. For the last 30 years, the Spin (magnetic moment) - Glass (disorder) (SG) phenomena have drawn immense attention due their substantial physical and mathematical interest [76-81]. Usually, at low temperatures the magnetic disorderness arises due to the different competing FM and AFM exchange interactions between the randomly distributed localized magnetic moments. In a magnetic system, spin glass state is a combination of random and mixed interacting state (Fig. 1.14), where the competing FM/AFM increases the frustration and randomness. This leads to spin disorderness and it freezes randomly at a certain temperature T_F which is known as freezing temperature or spin-glass temperature. One important feature of SG state is that it exhibits a multiple number of ground states, therefore a SG system is not in thermal equilibrium and slowly relaxes to lower energy states. Generally, the alloys with dilute dispersion of magnetic atoms, show the SG behaviour. Metallic alloys such as $Cu_{1-x}Mn_x$, $Au_{1-x}Fe_x$ are the typical examples of SG system in which the site-randomness causes glassy behaviour [82,83].

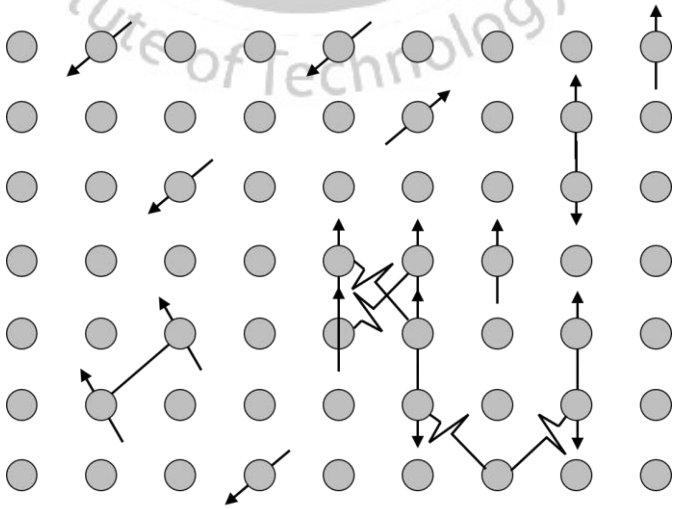

Figure 1.14: Schematic representation of randomly distributed spins in a square lattice with FM interaction between the nearest neighbours (nn) and AFM interaction between next-nearest neighbours (nnn). The zig-zag lines represent the possibility of the frustrated spin.

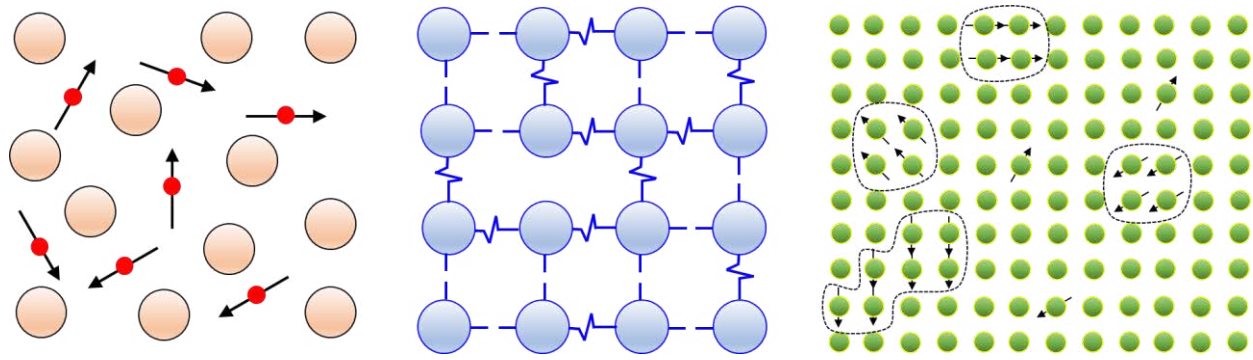

Figure 1.15: Illustration of (a) disordered lattice sites occupied by magnetic ions, (b) the random bond spin-glass and (c) the cluster spin-glass. In figure (b) the dashed lines represent FM coupling and the zig-zag sign signifies the AFM coupling.

The random-site occupancy of magnetic ions and random bondings are the main reasons for the presence of randomness in any compound, if such disorderness is combined with competing or mixed interactions which originates frustration inside the lattice. Also, site dilution of the magnetic ions with non-magnetic elements makes the system chemically disordered, while such disorderness disturbs the long-range interaction and causes short-range interactions like SG. The magnetic moments of the metal ions in $Cu_{1-x}Mn_x$, $Au_{1-x}Fe_x$ can couple with each other through the RKKY exchange interactions $J_{RKKY}(R)$ and the strength of $J_{RKKY}(R)$ (either FM or AFM) depends on the distance between two magnetic ions as shown in Fig. 1.14. This leads to competing magnetic interactions between the Mn spins which are randomly distributed and therefore, at low temperatures these magnetic interactions freeze in random direction (Fig. 1.15 (a)). In contrast, the $Rb_2Cu_{1-x}Co_xF_4$ and $Fe_{1-x}Mn_xTiO_3$ compounds are the standard examples of SG system which occur due to the randomness in bond formation (Fig. 1.15 (b)). Both the systems have perfect lattice structure, however, the competing magnetic exchange interactions (J) between the nearest neighbour spins results the randomness inside the system [78,84,85]. As, the temperature is lowered from T_F, the neighboring spins begin to interact over sufficiently longer range. For $T<<T_F$, the randomly distributed spins freely rotate and construct themselves into locally correlated units or clusters (Fig. 1.15 (c)). Such clusters can even be treated as local domains which rotate collectively. However, it is also possible that few spins act as independent entities which do not belonging to any cluster. These spins remain as they are and mediate the interaction between two clusters, thus enhancing the cluster sizes and relaxation times. Therefore, the system finds a ground-state (T = 0 K) configuration for the particular distribution of spins and exchange interactions. Such ground-state signifies the lock or freezing of the favourable set of randomly aligned spins generated by the local anisotropy. The temperature at which spin freezes randomly is called the 'freezing temperature' (T_F or T_{SG}) for a spin glass system [78]. Furthermore, with respect to the perfectly ordered FM or an AFM state, the SG state exhibits the non-zero value of the time average of spin ($\langle S_i S_j \rangle \neq 0$). Therefore, a spin glass state shows a sharp cusp in the ac-susceptibility measurement as shown in Fig. 1.16 for the $Cu_{1-x}Mn_x$ (0.94 at.%) alloy [75]. This figure shows the real component of ac-susceptibility (χ') measured at different driving frequencies (2.6, 10.4, 234 and 133 Hz) under zero-field-cooling condition. The peak temperature in χ' is

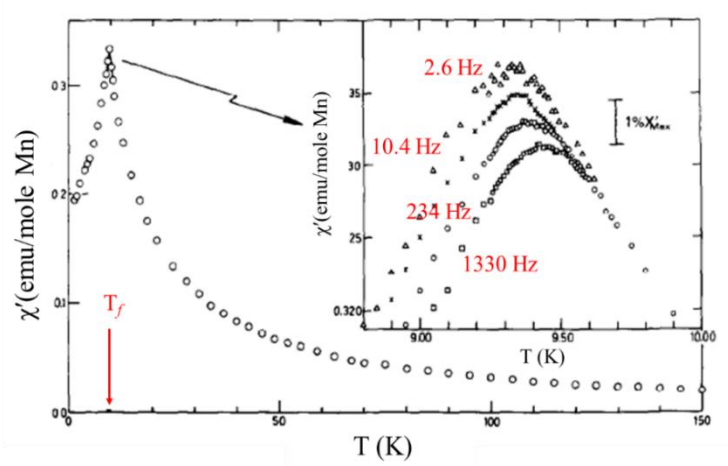

Figure 1.16: Temperature dependence of the zero-field real component of the ac-magnetic susceptibility $\chi'(T)$ for $Cu_{1-x}Mn_x$ magnetic alloy measure at different frequencies. The inset shows zoomed view of $\chi'(T)$ showing clear cusp at T_F and its shift to higher temperature side with increasing frequency [82].

called the spin-glass freezing temperature T_F. The graph clearly indicates the frequency dependence of χ' below the T_F, where T_F shifts to higher temperatures with increasing frequencies of the applied ac-magnetic field (h_{ac}) which is the most important property of a spin-glass state. Such behaviour indicates that the system possesses many metastable ground states which cover a wide range of characteristic excitation and relaxation time scales. The measurement history dependence of χ_{ac} measurements also unveils various other magnetic phenomena in SG systems such as revolution, aging, and memory effects [86]. In the present thesis (see Chapter 4) we discuss the above phenomena by means of dynamic ac-susceptibility in insulating spin glasses which exhibits SG behaviour of different time scales.

1.6 Crystal field theory and Jahn-Teller distortion:

It is a well-known fact that a strong crystal field (either tetragonal or octahedral crystal field) significantly influences the *3d* electron pairing configuration in the t_{2g} and e_g levels and decides whether the magnetic ions should be in a low spin state or a high-spin state [87,88]. For example, in case of the normal spinels such as Co_3O_4 and $ZnCo_2O_4$ where the magnetic moment of Co^{3+} ion is completely nullified due to very high crystal field in the octahedral symmetry attains low-spin state. Thus, the absence of a permanent moment on Co^{3+} ion is explained as a result of the splitting of the *3d* levels by the octahedral cubic field into upper doublet e_g, and lower triplet t_{2g} levels, these effects will be discussed in the investigated compounds in coming chapters. Keeping in view of above-mentioned important properties, below we present a brief discussion on the crystal field theory and its role on the magnetic behaviour of few transition metal oxides. The crystal field theory was first developed by physicists Hans Bethe and John Hasbrouck van Vleck in 1930. This concept deals with the effects of the coordination symmetry and it is quite useful in understanding the physical properties of a few transition metal oxides [29,89]. In the octahedral symmetry (O_h), the cations are surrounded by six oxygen anions and the electrostatic repulsion acting between them breaks the symmetry of degenerate *d* orbitals. Consequently, these *d*-orbitals are split in two groups: lower triplet t_{2g} (d_{xy}, d_{yz} and d_{zx}) and higher doublet e_g ($d_{x^2-y^2}$ and d_{z^2}) states (see Fig. 1.17).

Table 1.2: The strength of Jahn Teller distortion for different electronic configurations for d-orbitals electron for both high and low spin state. The weak and strong distortion is designated with 'W' and 'S' [90].

No. of electrons	Octahedral				Tetrahedral	
	High spin		Low spin		High spin	
	configuration	distortion	configuration	distortion	configuration	distortion
d^1	$(t_{2g})^1$	W	-	-	$(e_g)^1$	weak
d^2	$(t_{2g})^2$	W	-	-	$(e_g)^2$	0
d^3	$(t_{2g})^3$	0	-	-	$(e_g)^2(t_{2g})^1$	S $(c/a > 1)$
d^4	$(t_{2g})^3(e_g)^1$	S $(c/a > 1)$	$(t_{2g})^4$	W	$(e_g)^2(t_{2g})^2$	S $(c/a < 1)$
d^5	$(t_{2g})^3(e_g)^2$	0	$(t_{2g})^5$	W	$(e_g)^2(t_{2g})^3$	0
d^6	$(t_{2g})^4(e_g)^2$	W	$(t_{2g})^6$	0	$(e_g)^3(t_{2g})^3$	weak
d^7	$(t_{2g})^5(e_g)^2$	W	$(t_{2g})^6(e_g)^1$	S $(c/a > 1)$	$(e_g)^4(t_{2g})^3$	0
d^8	$(t_{2g})^6(e_g)^2$	0	-	-	$(e_g)^4(t_{2g})^4$	S $(c/a > 1)$
d^9	$(t_{2g})^6(e_g)^3$	S $(c/a > 1)$	-	-	$(e_g)^4(t_{2g})^5$	S $(c/a < 1)$
d^{10}	$(t_{2g})^6(e_g)^4$	0	-	-	$(e_g)^4(t_{2g})^6$	0

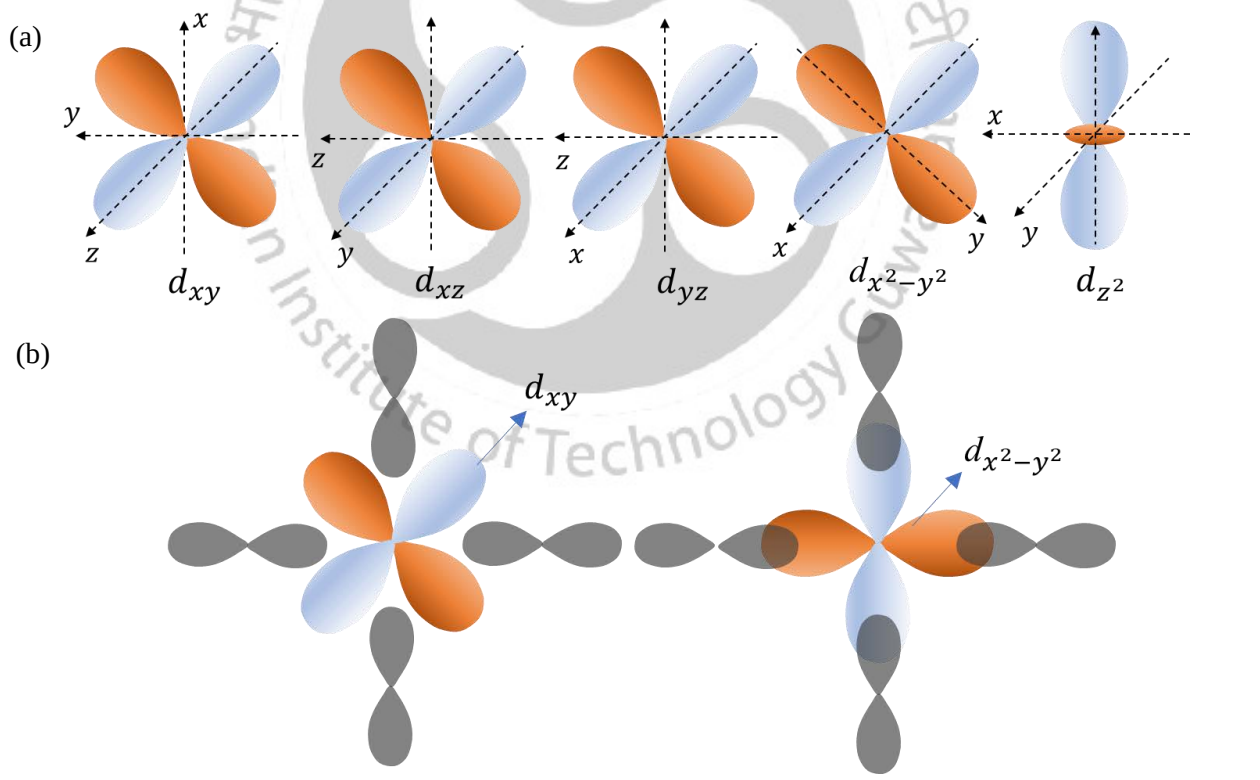

Fig. 1.17: Schematic representation of (a) five *d* orbitals (d_{xy}, d_{xz}, d_{yz}, $d_{x^2-y^2}$, d_{z^2}) and (b) higher t_{2g} and lower e_g energy level.

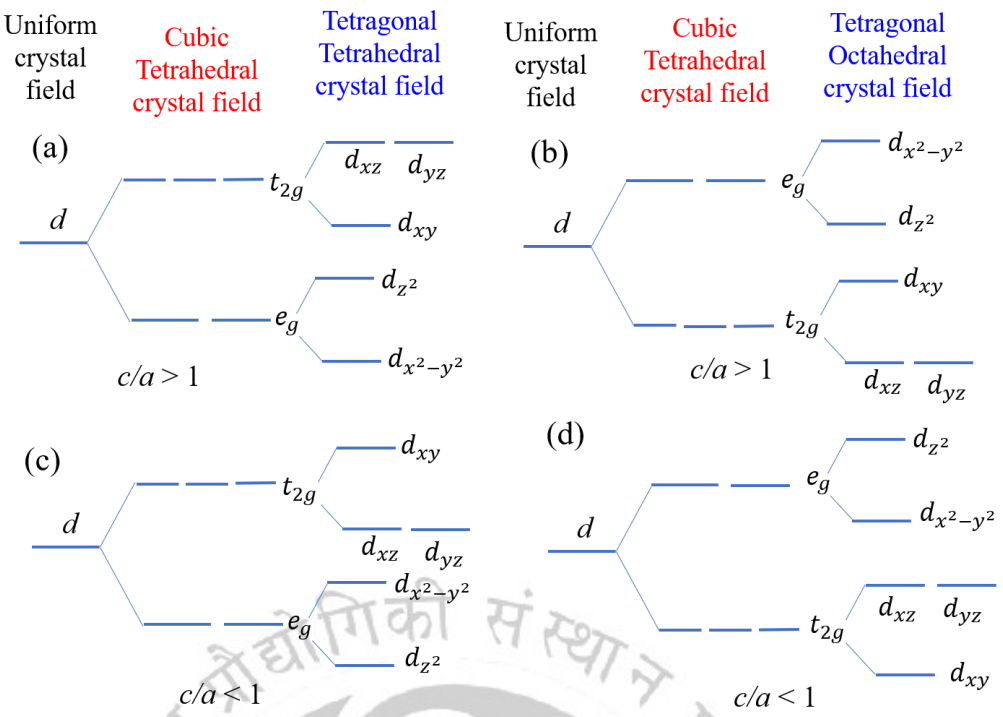

Fig. 1.18: Schematic of crystal field splitting of *d* orbitals for cubic and tetragonal structure for both (a and c) tetrahedral A- and (b and d) octahedral B sites.

For the O_h configuration the e_g orbitals lie along the same direction of the *p* orbitals of the oxygen anion and the energy of these states increase due to direct repulsion. On the other hand, the t_{2g} orbitals lie in between the *p* orbitals and hence the t_{2g} states attain lower energy than the e_g orbitals. Similarly, in the tetrahedral symmetry (T_h), the t_{2g} (e_g) levels lie along the *p* orbital and hence the t_{2g} orbital exhibits higher energy than e_g orbital. The energy difference between the two set of orbitals are denoted as Δ_{Oct} and Δ_{Tet} for octahedral and tetrahedral crystal fields, respectively and the crystal fields are related as: $\Delta_{Tet} = -\frac{4}{9}\Delta_{Oct}$ [90]. According to the above relation, the strength of the tetrahedral crystal field is always smaller than the octahedral crystal field. The crystal fields also depend on the cation and anion bond length which vary inversely with the bond length. In this regard it is important to mention about the 'Jahn-Teller (J-T) distortion' which arises due the electronic configuration of a non-linear molecule and undergoes a geometrical distortion to remove the orbital degeneracy. This phenomenon is mostly observed in transition metal complexes. Depending upon the different electronic configuration of the *d*-orbitals, the strength of the J-T effect is determined and in Table 1.2 we summarize this assertion [90]. In Fig. 1.18, we present a schematic energy level diagram for the *d*-orbitals under different crystal fields for the tetrahedral and octahedral sites for *c/a* ratio greater or less than 1. Therefore, the J-T effect is an important feature which is linked with the crystal and magnetic properties of different compounds. The crystal field splitting and J-T distortion is discussed in a more detailed manner in the corresponding chapters.

1.7 Description of the research problem:

Recent experimental studies reveal large negative magnetization along with reentered spin-glass state in diluted spinels such as Co_2TiO_4 and Co_2SnO_4 [22-24,42]. Such exotic behaviour strongly motivated us to investigate the role of dilution with elements such as Ru, Ge, Ti, Sn, Al, in Co_3O_4 bulk system. Although there exist reasonably large experimental reports on these diluted spinels but their electronic structure and other properties (such as density of states and energy band structure) were completely unknown in the literature when we undertook this research problem. Therefore, we planned to study these systems in detail with special emphasis on the electronic structure calculations based on density functional theory (DFT) and complement our calculations with experimental observations (Chapter 3). Among all the spinels, Co_2RuO_4 was less studied system and very little literature was available focusing on the magnetic structure of this system. Therefore, a detailed temperature dependence of ac-magnetic susceptibilities and dc-magnetization analysis is required to resolve the magnetic ground state of Co_2RuO_4 (Chapter 4). Also, the lack of experimental evidence on Co_2TiO_4 and Co_2SnO_4 single crystal samples, motivated us to perform the precise neutron diffraction studies below T_N and to pin down the spin configurations much accurately which helped us to understand the density functional theory calculations at absolute temperature (Chapter 5). Lastly, Co_2TiO_4 and $GeCo_2O_4$ both exhibits interesting magnetic properties along with different crystal structure. Nevertheless, while going from inverse spinel configuration of Co_2TiO_4 to normal spinel pyrochlore configuration $GeCo_2O_4$, very few literatures are available. Although there are few reports describing the magnetic features of $Co_2Ti_{1-x}Ge_xO_4$ sample up till some critical composition $x_c \leq 0.4$, but beyond this x_c there is no experimental evidence reported in the literature (Chapter 6). All these aspects motivated us to probe the structural, electronic and magnetic studies on $Co_2Ti_{1-x}Ge_xO_4$ ($0.0 \leq x \leq 1.0$) system in detail and fill the miscibility gap ($0.4 \leq x \leq 1.0$) in the composition dependent phase diagram. The concept of magnetic dilution and the magnetic compensation makes the diluted spinels very important systems both from fundamental and applications point of view hence, in the present doctoral thesis, we focus on both theoretical calculations and experimental studies with special emphasis on the structural, magnetic, electronic and optical properties of antiferro/ferri-magnetic Co-based diluted spinels.

Chapter 2
Numerical and experimental methodology

In this chapter we present the numerical and experimental techniques employed in the current thesis work. The chapter is mainly divided into two parts. The initial portion of the chapter covers the theoretical basis of many-body electron systems and the Density Functional Theory (DFT), which is implemented in the Vienna Ab initio Simulation Package (VASP) [91,92]. This is the primary tool that we employed in this work to achieve our research goals related to the calculated electronic structure of different spinels. We also discuss few important approximations that are being considered in DFT calculations. In the second part of this chapter we discuss the experimental methodology including the fabrication of the investigated system with a detailed description of characterization techniques along with their working principles. These techniques are mainly aimed to understand the electronic and crystal structure along with the magnetic properties of the selected compounds. In the following we discuss the different many body theories.

2.1 Theoretical background:

Many body electron problems are quite difficult to handle theoretically. To understand the physics of the material at the microscopic level it is essential to employ the *ab initio* electronic structure calculations. This implies that we have to solve the Schrödinger equation for many-body systems which can be obtained either using the Hartree-Fock method or the DFT techniques [93]. The Hartree-Fock method is almost an exact method as it deals with very few approximations. On the other hand, the main disadvantage of the Hartree-Fock method is that it required high computational power and is also time consumable. Due to this reason, DFT calculations are considered as appropriate while dealing with many-body electron systems. However, few approximations are required to solve the many-body electron problem which we discussed in the earlier sections. The DFT calculations replicate the many-body interacting system into a non-interacting single-particle system, which has made the required breakthrough to arrive at parameter-free, “First-principles” methods, and gained robust and accurate results of materials properties. Over the years, DFT is used to study the complex magnetic properties, electronic structure and other different physical properties. This DFT result compliments the experimental observations for different spinel systems and perovskites for both bulk and low-dimensional structures, which confirm the accuracy of these methods. Additionally, the advanced softwares such as Vienna *ab initio* simulation package (VASP), Quantum Espresso, Gaussian etc; based on the DFT based first-principles methods makes it easy to tackle the complex problems accurately within reasonable time scales. Besides, in the recent years, DFT is not only used to interpret the experimental results but also to predict the properties of new materials where there is lack of any experimental evidences. Therefore, in this doctoral research work, we have used the DFT based first-principles methods for a better understanding of the electronic and magnetic structure of the investigated systems which are complemented with the experimental observations. In the following sections we discuss the detailed experimental methodology that we implemented in this work.

2.1.1 The many-body problem in solids:

Generally, the electronic structure of a solid can be obtained by solving the nonrelativistic, time-independent Schrödinger Equation given below:

$$\hat{H}\,\boldsymbol{\Psi}\,(\mathbf{r}_1, \mathbf{r}_2, \ldots, \mathbf{r}_i, \mathbf{R}_1, \mathbf{R}_2, \ldots, \mathbf{R}_I, \ldots) = E\,\boldsymbol{\Psi}\,(\mathbf{r}_1, \mathbf{r}_2, \ldots, \mathbf{r}_i, \mathbf{R}_1, \mathbf{R}_2, \ldots, \mathbf{R}_I, \ldots) \tag{2.1}$$

In Eq. (2.1), $\boldsymbol{\Psi}$ is the many body wave function, $\hat{H}$ is the Hamiltonian and E is the total energy of the system. The wave function $\boldsymbol{\Psi}$ is dependent of both positions of the electrons (index as $\boldsymbol{r}_i$) and nuclei (index as $\mathbf{R}_I$). For a system composed of nuclei and electrons the Hamiltonian can be expressed as:

$$\hat{H} = -\frac{\hbar^2}{2}\sum_I \frac{\nabla_I^2}{M_I} - \frac{\hbar^2}{2}\sum_i \frac{\nabla_i^2}{m_i} + \frac{1}{2}\sum_{I\neq J} \frac{Z_I Z_J e^2}{|\boldsymbol{R}_I - \boldsymbol{R}_J|} + \frac{1}{2}\sum_{i\neq j} \frac{e^2}{|\boldsymbol{r}_i - \boldsymbol{r}_j|} - \sum_{i,I} \frac{Z_I e}{|\boldsymbol{r}_i - \boldsymbol{R}_I|} \tag{2.2}$$

In the above Eq. (2.2), M_I, R_I and m_i, r_i are the mass and electronic co-ordinates of nuclei and electrons, respectively, and Z is the atomic number [93]. The first and the second terms represent the kinetic energies of nuclei and electron, respectively. The third, fourth, and fifth terms correspond to the Coulombic interactions between nuclei-nuclei, electron-electron, and nuclei-electron, respectively. Although the Hamiltonian is modelled but practically it is quite impossible to solve it using the available computational resources due to the presence of large number of atoms (~10^{23}) present in the solids. Therefore, one needs few approximations to simplify Eq. (2.2). Here the mass of the electron is significantly less as compared to nuclei ($m_i << M_I$), consequently, in the presence of any external potential the electron reacts much quickly than the ions ($v_i >> V_I$) and the time scales linked with motions of electrons and nuclei are substantially different. It can be assumed that electrons move almost instantaneously (adiabatically) with respect to the motion of nuclei. In 1927, Born-Oppenheimer introduced this idea also known as Born-Oppenheimer approximation [94]. Following this, one can assume the position coordinates of nuclei (R_I) are fixed. Therefore, we can neglect the kinetic energy of nuclei ($K.E_{electon} >> K.E_{nuclei}$) and further can treat the coulomb interaction between nuclei and nuclei as constant. This suggests that the electronic motion is independent of the nuclear coordinates. Therefore, the total wavefunction can be represented as the product of electronic and ionic wavefunctions ($\boldsymbol{\Psi} = \boldsymbol{\Psi}_I(R)\boldsymbol{\Psi}_e(r,R)$) and the electronic Schrödinger Equation can be written as:

$$\hat{H}_e \Psi_e = E_e \Psi_e \tag{2.3}$$

and the Hamiltonian using the Born-Oppenheimer approximation becomes:

$$\hat{H}_e = -\frac{\hbar^2}{2}\sum_I \frac{\nabla_i^2}{m_i} + \frac{1}{2}\sum_{i\neq j} \frac{e^2}{|\boldsymbol{r}_i - \boldsymbol{r}_j|} - \sum_{i,I} \frac{Z_I e}{|\boldsymbol{r}_i - \boldsymbol{R}_I|} = \hat{T}_e + \hat{V}_{e-e} + V_{ext} \tag{2.4}$$

Here first term represents the kinetic energy of the electrons, second term the Coulombic potential acting between the electrons and the third term coulomb potential acting between the electron and nuclei. Nevertheless, the Born-Oppenheimer approximation suggests that the third term only depends on the electron coordinate as the nuclei coordinate is fixed. The last term in Eq. (2.4) is related to the external

potential acting on the electrons. We find that even after incorporating the Born-Oppenheimer approximation the electronic wave functions depend on the coordinates of nuclei (**R**) and electron (***r***).

Since the exact solution of Eq. (2.4) is not possible therefore few approximations are required to obtain the solutions of the Schrödinger equation. So, various theories are developed starting from Thomas-Fermi-Dirac model, Hartree-Fock method to now the modern density-functional theory to solve the many-body electron Hamiltonian [93]. The first two methods are built on the wavefunction and the latter one is based on the electron density. In 1928, Hartree proposed that each electron can be treated as independent entities where every electron is assumed to move in an effective potential composed of the external potential due to the nuclei and a contribution which describes the average electrostatic interaction between the electrons. Since the electrons are independent, the total energy can be represented as the sum of N numbers of one-electron energies and the wave function is simply approximated as the product of N numbers of one-electron wave functions. However, this method does not follow two fundamental principle of the quantum mechanics: the anti-symmetry principle and Pauli's exclusion principle. Additionally, it does not even consider the exchange and correlation energies which arise due to the electrons. In 1930, based on the one-electron and the mean-field approach by Hartree, Fock proposed a much better way to deal the many body electron problem which is known as Hartree-Fock (HF) method. In this method the electronic wavefunction is considered as linear combination of noninteracting single-particle orbitals $\varphi_i(\mathbf{r},s)$, i =1,…, *N*, such that the wave function is expressed in the form of a Slater determinant:

$$\Psi(x_1,\dots,x_N) = \frac{1}{\sqrt{N!}} det[\varphi(x_1),\dots,\varphi(x_N)]$$

$$\Psi(x_1,\dots,x_N) = \frac{1}{\sqrt{N!}} \begin{vmatrix} \varphi_1(x_1) & \varphi_1(x_2) & \cdots & \varphi_1(x_N) \\ \varphi_2(x_1) & \varphi_2(x_2) & \cdots & \varphi_2(x_N) \\ \vdots & \vdots & \ddots & \vdots \\ \varphi_N(x_1) & \varphi_N(x_2) & \cdots & \varphi_N(x_N) \end{vmatrix} \tag{2.5}$$

As a result, the electronic wave function is antisymmetric in nature and thus, total wave function in the HF method changes its sign when two electron indices are "exchanged," from which the terminology "exchange energy" is originated. It corrects the overestimation of the energy and makes the HF model closer to the actual system. These theories mostly rely on the variational principle for the energy. It tells us how to look for ground-state solutions by guessing them. For instance, the exact ground-state wave-function minimizes the expectation value of the Hamiltonian, H:

$$E_0 = \min_{\Psi} \frac{\langle \Psi | \hat{H} | \Psi \rangle}{\langle \Psi | \Psi \rangle} \tag{2.6}$$

A guess approximates normalized wave-function will always give an upper bound to the ground-state energy unless of course the guess is exact. A systematic derivation of the variational principle is as follows. Imagine we start with a trial wavefunction Ψ, which can be expanded in the complete basis of exact solutions for a chosen Hamiltonian as $\Psi = \sum_i c_i \varphi_i$, where $\hat{H}\varphi_i = E\varphi_i$. The basic requirement is that the trial wave-function should be normalized:

$$\langle \Psi | \Psi \rangle = \sum_i c_i^2 = 1 \tag{2.7}$$

So, the energy expectation value using the trial wave-function becomes,

$$E = \langle \Psi | \hat{H} | \Psi \rangle = \sum_i |c_i|^2 E_i \tag{2.8}$$

Therefore, upon applying the Born-Oppenheimer approximation it can be expressed as:

$$E = \langle \Psi_e | \hat{H} | \Psi_e \rangle = \langle \Psi_e | \hat{T}_e + \hat{V}_{e-e} + V_{ext} | \Psi_e \rangle = \langle \Psi_e | \hat{T}_e + \hat{V}_{e-e} | \Psi_e \rangle + \langle \Psi_e | V_{ext} | \Psi_e \rangle \tag{2.9}$$

Since E_0 is the lowest-energy eigenvalue of $\hat{H}$, so $E_i > E_0$, by construction. Since $|c_i|^2$ is nonnegative so the Eq. (2.8) proves the variation theorem (i.e. $E > E_0$ for any trial wavefunction). Two popular electronic structure methods, HF and density functional theory (which will be discussed later part of this section), rely on this principle.

Although the HF theory makes our life little easier to solve the many body problems but it has few disadvantages. Firstly, the same-spin electrons are kept away from each other by the antisymmetry requirement, and the HF treatment fully counts this quantum effect by the exchange energy. The electrons of different spins also tend to stay away from each other by the same charges they have, and this is called the correlation. This electron correlation is still missing in the HF method. Secondly, the scaling of the HF method is roughly order of N^4 and thus a doubling of system size will increase the computer-time about 16 times, which left us with the same numerical and computational challenge. In the following section we discuss the density functional theory.

2.1.2 Density functional theory (DFT):

The incorporation of Born Oppenheimer approximation simplifies the Hamiltonian, yet there are many challenges are involved to solve the many-body problem. On 1964, based on the theoretical concepts introduced by Hohenberg and Kohn [95] followed by Kohn-Sham Ansatz (1965) [96] DFT was introduced in the scientific community. The main idea of DFT is to map the many-body problems into one electron density instead of several electronic wavefunctions, as it reduces the dimension from 3N to 3. In late 1920s, Thomas [97] and Fermi [98] first proposed that the one electron density approach to solve the many body problem and obtain the ground state properties. However, this model neglected the exchange and correlation effects between the electrons which leads to bitterly incorrect results. In the below subsections we discuss few important theorems related to the DFT methodology.

2.1.2.1 Hohenberg-Kohn (HK) theorems:

Hohenberg-Kohn proposed two theorems based on the density of electron to solve the many body Hamiltonian.

First theorem states that for a system of interacting particles in an external potential V_{ext} (**r**), the potential V_{ext}(**r**) is determined uniquely, except for a constant, by the ground state particle density n_0(**r**) [95].

Second Theorem states that a universal functional for the energy E[n] in terms of $n(\mathbf{r})$ can be defined, which is valid for any external potential $V_{ext}(\mathbf{r})$. The exact ground state energy of the system is the global minimum value of this functional, and the density that minimizes the functional is the exact ground state density $n_0(\mathbf{r})$ [95].

However, Eq. (2.9) can also be written in terms of electron density n(r) as follow:

$$E[n] = F[n] + \int V_{ext}(\boldsymbol{r})n(\boldsymbol{r})d\boldsymbol{r} \tag{2.10}$$

In Eq. (2.10), the first term consists of kinetic and potential energy of the electrons which is universal functional of the electron density n(r). The second terms represent the interaction energy with the external potential. Nevertheless, the many-body problem becomes much simpler after the implementation of the HK theorem, but numerically determining $F[n]$ is still quite difficult due to $V_{e\text{-}e}$ term [93]. Later, Kohn and Sham proposed a way to bypass this problem by proposing an ansatz which convert the interacting system to sets of effective non-interacting systems. This is also considered as the modern formulation of DFT to solve the electronic structure of many-body related problems which we discuss in detail in the following section.

2.1.2.2 Kohn-Sham (KS) ansatz:

Following the work of Hohenberg-Kohn in 1965, Walter Kohn and Lu Jeu Sham came up with a way to solve the many-body electron problem by proposing an ansatz which states that the ground state density of non-interacting electrons is equal to the original interacting electrons in the presence of an external potential V_{ext}. The main advantage of considering the non-interacting electrons is that one can separate them and the wave function can be expressed as Eq. (2.5). The Kohn-Sham approach and the variational principle leads the following form of the Schrödinger Equation:

$$(H_{KS} - \varepsilon_i)\,\varphi_i(\boldsymbol{r}) = 0 \tag{2.11}$$

In the above expressions, H_{KS} and ε_i are the effective Kohn-Sham Hamiltonian and eigenvalues, respectively. The H_{KS} is given by

$$H_{KS} = -\frac{1}{2}\nabla^2 + V_{eff} \tag{2.12}$$

where,

$$V_{eff} = V_{ext}(\boldsymbol{r}) + V_{Hatree}(\boldsymbol{r}) + V_{xc}(\boldsymbol{r}) \tag{2.13}$$

The second term in above expression is known as Hatree potential which is the electrostatic/coulombic interaction acting between the electrons given as

$$V_{Hatree} = \frac{1}{2}\int \frac{n(\boldsymbol{r})n(\boldsymbol{r}')}{|\boldsymbol{r} - \boldsymbol{r}'|}d\boldsymbol{r}d\boldsymbol{r}' \tag{2.14}$$

and the last term is related to the exchange correlation potential which is defined as,

$$V_{xc} = \frac{\delta E_{xc}[n]}{\delta n(\boldsymbol{r})} \tag{2.15}$$

The exchange correlation energy term, E_{xc} contains all the corrections which will arise due to the mapping of the real interacting system into fictitious non-interacting system and the exchange energy term can be expressed as:

$$E_{XC}[n] = \Delta T[n] + \Delta V_{e-e}[n] \tag{2.16}$$

where, $\Delta T[n]$ $(= T[n] - T_{non\ int}[n])$ is the correction in kinetic energy and the second term ΔV_{e-e} represents all the corrections to the electron-electron repulsion energy [93,99,100]. Thus, accurate evaluation of E_{XC} is very much necessary to determine the ground state electron density. Nonetheless, the determination of exact E_{XC} is fairly a difficult task and one has to rely on few approximations [93,99,100].

The total number of electrons are fixed in the system and is obtained as

$$N = \int n(\boldsymbol{r}) d\boldsymbol{r} \tag{2.17}$$

and the density of electronic wavefunctions can be calculated from single electron orbitals:

$$n(\boldsymbol{r}) = \sum_{i=1}^{N} |\varphi_i(\boldsymbol{r})|^2 \tag{2.18}$$

In order to solve the KS equation, the V_{eff} and V_{Hatree} are required, which can be evaluated from the electron density expressions given in Eq. (2.13) and (2.14). However, from Eq. (2.18) it is clear that to determine $n(\boldsymbol{r})$ we should have the information about the single electron orbitals $\varphi_i(\boldsymbol{r})$ which can be obtained from the KS equation (Eq. (2.11)). Overall, we can say it is a self-consistent problem and can be solved using the

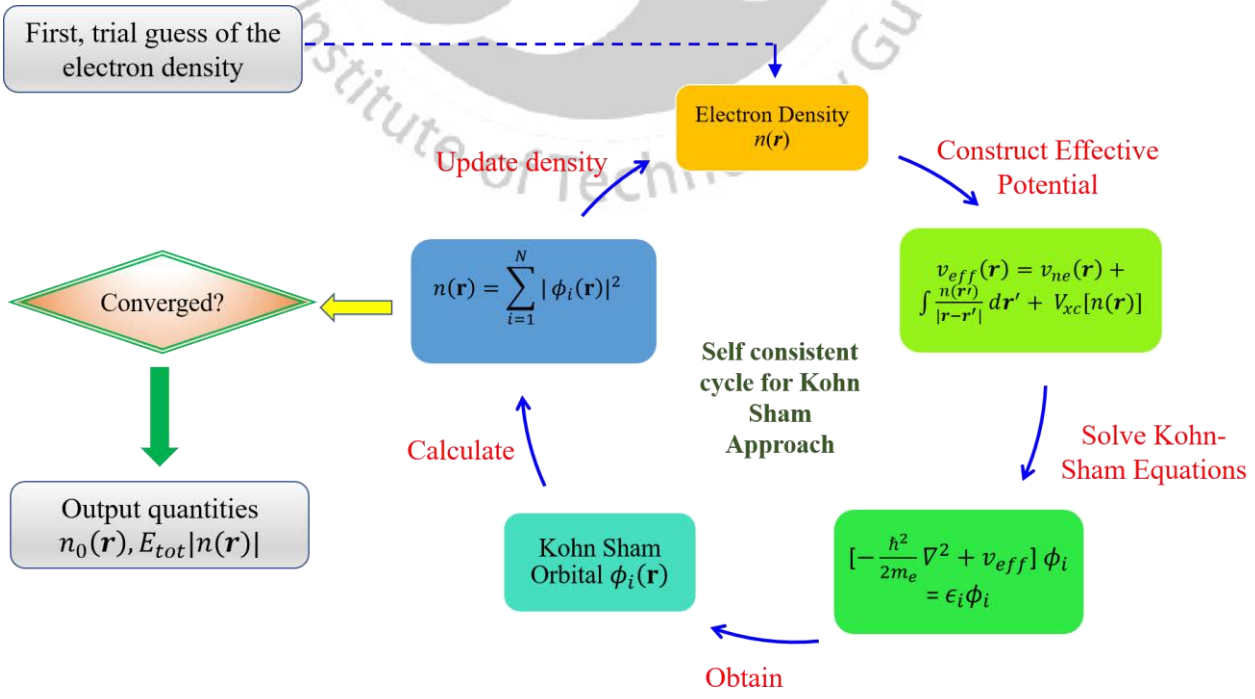

Fig. 2.1: Schematic of a typical DFT procedure by iterative self-consistent loop.

iteration process. To start the iteration process we first provide an initial guess of $n(\boldsymbol{r})$ and construct the effective potential. Later, one can incorporate the effective potential in the KS equations (Eqs. (2.11) and (2.12)) and calculate $\varphi_i(\boldsymbol{r})$, which eventually provide the information of final density $n(\boldsymbol{r})$. At this stage if the converge criteria is satisfied (difference between initial and final density $n(\boldsymbol{r})$) then the self-consistent calculation is terminated, otherwise using the new electron density ($n_{\mathrm{KS}}(\boldsymbol{r}) = n(\boldsymbol{r})$) the iteration process is continued until the convergence criteria is met. This procedure provides the true ground state density of the system. In Fig. 2.1 we provide a schematic flowchart for a better understanding of the self-consistent cycle which is a general approach used to solve the KS equations. Here we find that we need to model V_{xc} in order to get accurate ground state density. In the following we discuss the different scheme for V_{xc} approximation.

2.1.3 Approximations for exchange-correlation energy:

In general, the exchange correlation energy term (E_{xc}) consists of all the key information related to the kinetic energy difference between real interacting and fictitious non-interacting system together with ΔV_{e-e}. It consists of all the quantum corrections of mechanical exchange and electron-electron correlation effects occurring in real interacting systems, which is ignored in non-interacting systems. Here, the exchange energy between the electrons with the same spin is represented with E_x while, E_c denotes the correlation energy between electrons of different spins. In such case the exchange correlation energy can be represented as:

$$E_{xc} = \frac{1}{2}\iint \frac{n(\boldsymbol{r})n_{xc}(\boldsymbol{r},\boldsymbol{r}')}{\boldsymbol{r}-\boldsymbol{r}'}\,d\boldsymbol{r}d\boldsymbol{r}' \tag{2.19}$$

The average exchange-correlation density is represented by $n_{xc}(\boldsymbol{r},\boldsymbol{r}')$, which signifies that an electron at point $\boldsymbol{r}$ reduces the probability of finding another electron at $\boldsymbol{r}'$.

2.1.3.1 Local density approximation (LDA):

LDA is one of the first approximations which is widely used to provide the approximate model of V_{xc} [101-103]. The main idea of LDA is to consider the electronic density varying uniformly at each point in space which depends upon the local electron density instead of the overall density of the system. Therefore, it is easy to map a complex system into many uniform pieces of electron density with different magnitude.

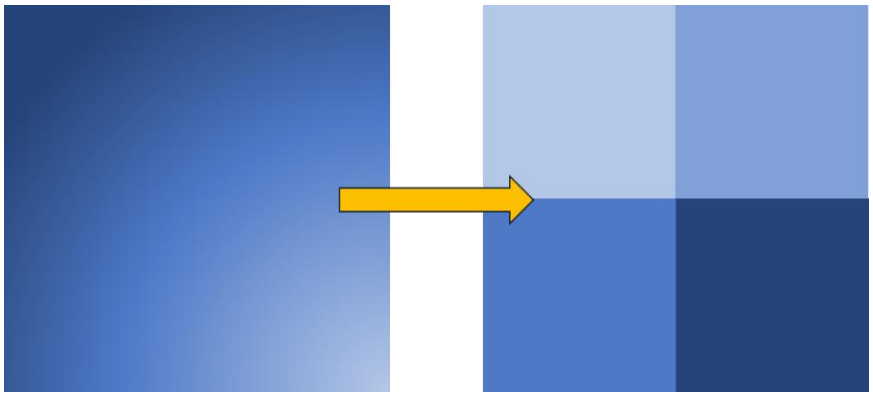

Fig. 2.2: Schematic of Local Density Approximations (LDA) in 2-D. The left panel shows the actual electron-density distribution and right panel shows the approximated four local elements of uniform electron densities.

In Fig. 2.2 we have presented a schematic depiction of LDA in 2-D for the actual density depicted in the left panel. Now to obtain the exchange correlation energy we need to sum up the E_{XC} of individual electrons with constant electron density at respective segments. So, we have

$$E_{xc}^{LDA} = \int n(\boldsymbol{r})\varepsilon_{XC}^{LDA}[n_0(\boldsymbol{r})]d\boldsymbol{r}, \tag{2.20}$$

where, $\varepsilon_{XC}^{LDA}[n_0(\boldsymbol{r})]$ is the exchange-correlation energy per particle in a homogeneous uniform system. This LDA works well for those system where the electronic density does not vary much with space. However, the LDA predicts higher bulk modulus, lower lattice parameter, and bond lengths for different systems.

2.1.3.2 Generalized gradient approximation (GGA):

To overcome the limitations of LDA, GGA was introduced where the information of both the local (the electron density) and semilocal (gradient of electron density) environment of the electrons was considered at a given point.

$$E_{xc}^{GGA} = \int n(\boldsymbol{r})\varepsilon_{XC}^{GGA}[n_0(\boldsymbol{r}), \nabla n(\boldsymbol{r})]d\boldsymbol{r} \tag{2.21}$$

The GGA predicts much better results as the real systems are inhomogeneous in nature with varying density landscape around electrons. There is no unique way to determine $\nabla n(\boldsymbol{r})$ as there are many non-empirical and empirical formulism already reported in the literature, among them Perdew, Burke and Ernzerhof (PBE) approximation is the most commonly used method for GGA functional [104]. The PBE-GGA predicts much better lattice parameter, bond-lengths and bulk modulus which are close to the experimental observations.

2.1.4 DFT+U formalism for strongly correlated system:

As discussed in the earlier sections 2.2 and 2.3, using DFT calculation one can able to solve the many body problems, however, the DFT have failures in treating the strongly correlated system. The formulism of DFT calculations is mainly based on the single electron orbitals representation and the electron-electron interaction. But for the strongly correlated system the electrons are localized in nature and the wavefunctions generally represents the many-body system. Hence, LDA and GGA fails to predict the correct ground state electronic density of the systems which exhibits *d* and *f* orbital electrons, and this leads to extremely incorrect lattice parameters, magnetic moments, vibrational spectrum, and all the other physical properties of the system. This problem is observed in both LDA and GGA exchange correlation functional which occurs due to the over-delocalize valence electrons and over stabilized metallic ground states of the electrons. To overcome such difficulty, the well-known Hubbard model is used where the physics of correlated materials is considered and the real-space second quantization formalism is suited to describe systems with electrons localized on atomic orbitals [105-110]. The Hamiltonian for the simple one band Hubbard model can be written as follows:

$$H_{Hub} = -t \sum_{<ij>,\sigma} \hat{c}_{i,\sigma}^{\dagger}\hat{c}_{j,\sigma} + U\sum_{i} \hat{n}_{i\uparrow}\hat{n}_{i\downarrow} \tag{2.22}$$

here $< ij >$ represents as the nearest-neighbour atomic sites, $\hat{c}_{i,\sigma}^{\dagger}$, $\hat{c}_{j,\sigma}$ and $\hat{n}_{i,\sigma}$ are respectively electronic creation, annihilation and number operators for electrons of spin σ on site *i*. The first term corresponds to the hopping process, where the motion of the electrons from one atomic site to its neighbouring sites can be described for strongly localized electrons. In this term *t* is the amplitude and it is proportional to the dispersion of the valance electron (bandwidth). In the second term of Eq. (2.22), U denotes the strength of the Coulomb repulsion between the electrons which occupies the same atomic site due to its strong localization. The competition between *t* and *U* decides the stable electronic ground state of the system. For *t* >> *U*, the single particle energy term dominates and DFT can easily describe the system, however, for *t* << *U*, the electrons do not possess enough kinetic energy to overcome the Coulomb repulsion between the neighbouring sites. Hence the hopping process in not possible and DFT fails miserably in such cases.

Incorporating the Hubbard model in the DFT functionals gives the correct ground state for the strongly correlated systems which is popularly known as DFT+U approach. The main idea behind this approach is that the Hubbard parameter U deals with the localized *d* or *f* orbital electrons and rest of the valance electrons will get the standard DFT treatment. Within this approximation, the energy functional for DFT+U can be expressed as:

$$E_{DFT+U} = E_{DFT} + E_{Hub} - E_{dc} \tag{2.23}$$

in the above expression E_{Hub} is the electron-electron interactions obtained from the Hubbard Hamiltonian, and is equivalent to

$$E_{Hub} = \frac{U}{2}\sum_{i\sigma} n_{i,\sigma} n_{i,-\sigma} \tag{2.24}$$

In Eq. (2.23), E_{dc} is known as the double counting term, to get rid of the extra term from E_{Hub} which is already considered in E_{DFT}. The E_{dc} is expressed as:

$$E_{dc} = \frac{U}{2}\sum_{\sigma} N_{\sigma}(N_{-\sigma} - 1) \tag{2.25}$$

where, N_{σ} is the eigenvalues of the number operators and it also signifies the number of localized electrons with a given projection of spin σ. In 1998, Duradev and co-workers [111] proposed a model which deals the total energy of DFT+*U* in a very simple way as given below.

$$E_{DFT+U} = E_{DFT}[n(\boldsymbol{r})] + \frac{(U-J)}{2}\sum_{l,j,\sigma} n_{jl}^{\sigma} n_{jl}^{\sigma}. \tag{2.26}$$

In the above equation n_{jl}^{σ} is the density matrix of localised electrons, *U* is the Columbic repulsion corresponding to the Hubbard model and *J* is the Hund's coupling parameter. We used this DFT+*U* formulism in our calculations which is implemented in the VASP package, in this present thesis as we will be dealing with transition metal oxides.

2.1.5 Pseudopotential method:

According to the Bloch's theorem, the Eigen states of electrons in the presence of periodic potential of the crystal are periodic modulations of the plane waves (PW) and the PW can be used as a natural basis set to

obtain the electronic states in the solids [112-115]. However, the wavefunctions corresponding to the core electrons close to the nucleus are rapidly oscillating in nature and the variation in the wavefunction is moderately slow for the valence electrons. Hence to represent the wavefunction, a large number of PW are required especially for the core electrons and this will increase the computational cost significantly. To get rid of this issue, in 1935, Hellman [116] and later in 1959, Phillips and Kleinman [117] came up with the idea of the pseudopotential method where the electronic states are divided into core states and valence states, and both the states are treated separately. In the case of core states, atomic orbitals provide all the relevant information of the wave functions and the PW can describe the valence states. Therefore, the coulombic potential is replaced with the pseudopotential which contains all the features of the nucleus and the core states within a certain cut-off radius ($\mathbf{r}_C$) and merged with the actual Coulombic potential beyond r_C. The main advantage of this pseudopotential method is that it removes the wiggles in the wave functions in the core region (below $\mathbf{r}_C$) and reduces the total number of electrons used in the DFT calculations. As a result, a relatively small number of the plane waves are required to determine the KS orbitals.

2.1.6 Projected augmented wave method:

In 1994, Blöchl proposed the idea of the Projected Augmented Wave (PAW) method to obtain better numerical results using DFT calculations [118]. The main idea is to retain all the information related to the wavefunctions of core electrons *via* mathematical linear transform approach. Another important aspect of PAW is that it contains all the information which is lost due to pseudopotential approximation and it controls

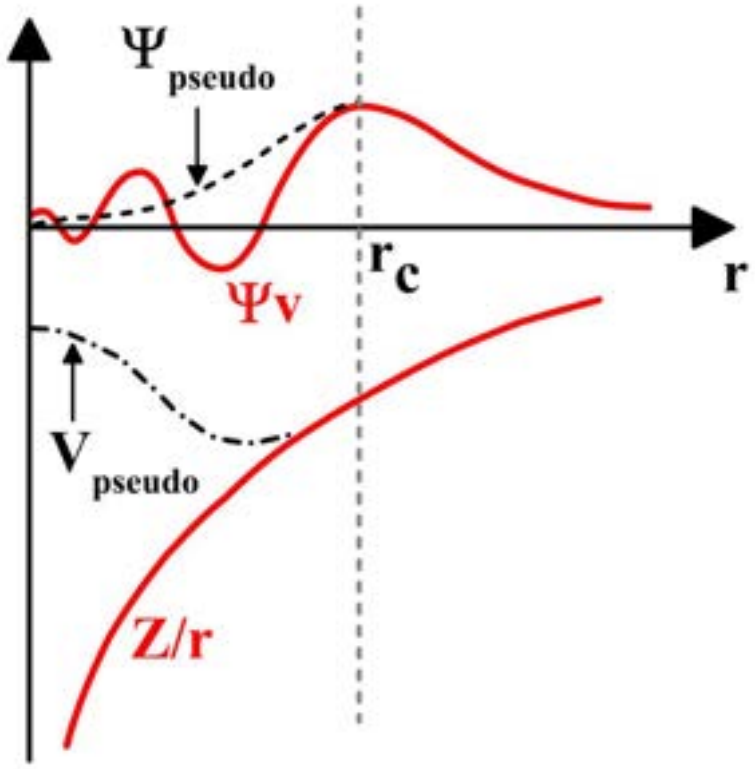

Fig. 2.3: Schematic representation of the pseudopotential and the pseudo wavefunction. Both the real and the pseudopotential matches beyond a given cutoff radius $\mathbf{r}_C$.

the properties linked to the nucleus, i.e. hyperfine parameters, and electric field gradients. In this method, the electronic wavefunctions is divided into two parts: a partial wave expansion within an atom centred sphere and an envelope function outside. In other words, PAW method combines the valence electrons wave functions with the pseudo wavefunctions. Figure 2.3 shows the schematic diagram of the real and pseudo electronic wavefunction, where both the wavefunctions are smoothed and matched very nicely at the edge of the sphere of radius $\mathbf{r}_C$. A brief discussion on the PAW method is illustrated below.

Firstly, by means of the linear transform operator $\hat{T}$ the auxiliary pseudo wavefunction $|\tilde{\psi}_n\rangle$ and the real electron wavefunction $|\psi_n\rangle$ can be mapped:

$$|\psi_n\rangle = \hat{T}|\tilde{\psi}_n\rangle \tag{2.27}$$

In Eq. (2.27), *n* represents the quantum level consisting of band, spin and $\vec{k}$-indices. Hence the wavefunction is matching quite nicely with the smooth wavefunction beyond certain distance from the nucleus, therefore $\hat{T}$ should modify the wavefunctions of the core electrons near the nucleus. This implies that beyond the augmentation cut-off the transformation must be unitary and the operator can be written as a sum of atom-centred contributions inside the wavefunction as:

$$\hat{T} = I + \sum_a \hat{T}^a \tag{2.28}$$

where $\hat{T}^a$ are transformation operator and linked with the atom centres a. The transformation is not effective beyond the cut-off radius $\boldsymbol{r}_C^a$. Hence, the cut-off radius $\boldsymbol{r}_C^a$ should be chosen in such a way that there is no overlap of the augmentation spheres. Within the augmented spheres the real and the auxiliary smooth functions can be represented in terms of partial waves as given below.

$$|\psi_n\rangle = \sum_i C_{ni}\,|\phi_i\rangle \tag{2.29}$$

$$|\tilde{\psi}_n\rangle = \sum_i C_{ni}\,|\tilde{\phi}_i\rangle \tag{2.30}$$

Here C_{ni} represents identical coefficient in Eqs. (2.29) and (2.30). Subtracting Eq. (2.30) from Eq. (2.29) and rearranging the terms one can write

$$|\psi_n\rangle = |\tilde{\psi}_n\rangle - \sum_i C_{ni}\,|\tilde{\phi}_i\rangle + \sum_i C_{ni}\,|\phi_i\rangle \tag{2.31}$$

Due to linear transformation operator $\hat{T}$, C_{ni} must be scalar product and can be represented as

$$C_{ni} = \langle \tilde{p}_i|\tilde{\psi}_n\rangle \tag{2.32}$$

where, $\langle \tilde{p}_i|$ is the smooth projector operator and it satisfies the completeness relation

$$\sum_i |\tilde{\phi}_i\rangle\langle \tilde{p}_i| = 1 \;\Rightarrow \langle \hat{p}_{i_1}|\hat{\phi}_{i_2}\rangle = \delta_{i_1,i_2} \tag{2.33}$$

and above relation indicates that within the range of augmented spheres, the smooth projector operator and the partial waves are mutually orthogonal. Hence, using Eqs. (2.31), (2.32) and (2.33), the transformation operator can be written as below

$$\hat{T} = I + \sum_i \left(|\phi_i\rangle - |\tilde{\phi}_i\rangle\right)\langle \tilde{p}_i| \tag{2.34}$$

Implying the transformation operator, the KS equations leads to the below result

$$H|\psi_n\rangle = H\hat{T}|\tilde{\psi}_n\rangle = \varepsilon_n \hat{T}|\tilde{\psi}_n\rangle \Rightarrow \hat{T}^{\dagger}H\hat{T}|\tilde{\psi}_n\rangle = \varepsilon_n \hat{T}^{\dagger}\hat{T}|\tilde{\psi}_n\rangle \tag{2.35}$$

Thus solving Eq. (2.35), we can obtain the smooth wavefunction $|\tilde{\psi}_n\rangle$ and subsequently solving Eq. (2.27) we can also determine the true electron wavefunctions $|\psi_n\rangle$.

In this thesis we have extensively used VASP to calculate the electronic and magnetic properties of complex spinel oxides which uses the same methodology discussed in this section. We will give more details of the parameters for different compounds in the corresponding chapters.

2.2 Experimental methods:

In this section we discuss the fabrication of the investigated system and a detailed description of characterization techniques. Initially, we provide a brief summary about the basic concept of each characterization method along with its working principle. These techniques are mainly aimed to understand the crystal structure, electronic and magnetic properties of the selected compounds.

2.2.1 Synthesis method:

2.2.1.1 Solid-state reaction technique:

In the present work all the samples were prepared by standard solid-state reaction method in the form of bulk polycrystals. This method involves mechanically mixing of the constituent binary transition metal oxides (BTMO) followed by intermediate grinding and sintering at high temperatures. The solid-state reaction method is thermodynamically stable process in which ions diffuses across the solid interface and this diffusion process occurs very slow. Typical reaction time in any solid-state reaction ranges from few days to few weeks and the heat-treatment involves very high temperatures (>1000°C) to overcome the diffusion barrier. In the present case, all the polycrystalline compounds: Co_3O_4, Co_2AlO_4, Co_2GeO_4, Co_2TiO_4, Co_2RuO_4, and Co_2SnO_4 were synthesized using the solid-state reaction using the stoichiometric amounts of commercially available BTMO (Al_2O_3, TiO_2, SnO_2, RuO_2, GeO_2 and Co_3O_4) from Alfa-Aesar GmbH. High purity BTMO have been selected as precursors. Firstly, appropriate amounts of precursors are grounded together using an agate mortar with pestle for six hours duration to ensure homogeneous mixing. These mixed powders were pressed into cylindrical pellets of size ~ 13 mm in diameter using a KBr die set and hydraulic press (40 kN/m^2). Further it was sintered at or above 1200°C for 12 hours in air with heating rate 5°C per minute and then cooled down to room temperature naturally. This sintering process leads to the chemical decomposition and resulting in the desired compounds with perfect homogeneity and high-density material. These pellets are crushed and sintered several times at slightly higher temperatures as compared to the initial sintering temperature under same conditions to yield single phase compounds. After this heat

treatment process, all the compounds are tested for the phase purity and for a detailed crystal structure by means of an x-ray diffraction method described below.

2.2.2 Characterization details:

In this section we present the details of various characterization techniques employed in the present work. Firstly, we discuss about the structural characterization of the samples performed using X-ray diffraction measurements, including the magnetization measurements.

2.2.2.1 Structural characterization:

We employed X-ray diffraction (XRD) technique to study the crystal structure of the investigated system. This is an important non-destructive technique primarily used for the identification of crystal structure and provides detailed information about the unit cell dimensions and interaxial angles of the investigated system. This technique also provides useful information about various structural properties of crystalline compounds such as micro-strain, grain-size, phase composition and defect structure. The XRD analysis is based on constructive interference of monochromatic X-rays after being reflected from the crystalline specimen. When an X-ray beam, generated by a cathode ray tube, is allowed to incident upon a crystal, the beam undergoes diffraction from the set of planes (Miller indices (hkl)), as the geometrical condition satisfies the Bragg's law [119]: $2d_{hkl}\sin\theta = n\lambda$. Here '$d_{hkl}$' is the inter-planer spacing between the set of (hkl) planes, θ is the Bragg's angle or Diffraction angle, 'n' is an integer and λ is the wavelength of X-ray radiation. Figure 2.4 shows the geometry of the Bragg's law for the X-ray diffraction from a set of crystallographic planes. The locus of the diffracted beams taken together from the different sets of planes is collectively known as the diffraction pattern of the crystal. In the present work we used a high-resolution X-ray diffractometer from Rigaku (Model: TTRAX-III) (18 kW rotating anode X-ray source) with Cu K_α source radiation with λ = 1.5406 Å. In order to extract the detailed crystallographic information from the obtained diffraction pattern we performed the Rietveld refinement using the open source programs FullProf-Suite and Powder-cell [120,121].

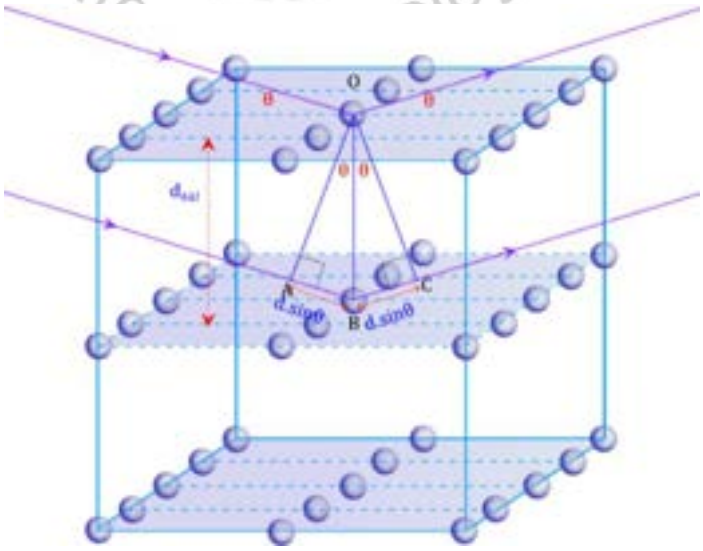

Fig. 2.4: Schematic diagram showing the diffraction of X-rays from lattice planes and the Bragg's law.

2.2.2.2 Magnetic characterization:

In this section we present a detailed description related to the magnetic characterization employed in the present work. The magnetic properties of most of the polycrystalline compounds in the current thesis investigated by both superconducting-quantum-interference-device (SQUID) based magnetometer (Magnetic property Measurement system, MPMS-XL5 from Quantum-Design) and physical property measurement system (PPMS) with vibrating-sample-magnetometer (VSM) accessory for high field (± 9 T) and low-temperature (1.95 K) measurements [122,123]. For selected compounds we used the neutron diffraction measurements. It is well known that the SQUID magnetometer is most effective and sensitive tool which can detect low magnetic moments with very high resolution ($> 10^{-7}$ emu) and very small magnetic field (10^{-18} T) using the Josephson junctions [124,125]. Usually, SQUID consists of two superconductors separated by thin insulating layer to form two parallel Josephson junctions as shown in Fig. 2.5(a). These Josephson junctions act as a magnetic flux-to-voltage transducer. The basic principle governing the operation of SQUID device is based on the flux-quantization in superconducting (SC) loops and the Josephson-effect [126]. In 1962, Josephson showed that the electrical current density through a weak electric contact between two superconductors depends on the phase difference $\Delta\varphi$ of the two SC wave functions [122,125]. Following subsections deals with the instrumentation, basic principles, units relevant to SQUID magnetometry, sensitivity and detection limits of the instrument.

2.2.2.2.1 DC-magnetization:

In this section we present the particulars of extraction of DC-magnetization and the working principle of a SQUID. Typically, in a SQUID when the current enters at the terminal 1, it gets divided into two parts, namely I_1 and I_2 which experience a phase shift while passing through the two Josephson junctions X and Y (see Fig. 2.5(a)). The two phase shifted currents (I_1' and I_2') interfere at the terminal 2 and the resultant current oscillates between a maximum and a minimum value. The magnetic flux (φ) inside any SC ring is quantized and defined as $\varphi = nhc/2e = n\varphi_0$, where n is an integer and φ_0 is magnetic flux quantum = $hc/2e = 2.07\times10^{-7}$ Gauss-cm^2. The maximum value of the current occurs when the magnetic flux inside reaches an integral number of flux quantum, whereas, the minimum corresponds to the half integral of the flux quantum. The voltage which also oscillates depending on the change in magnetic flux is measured across the two terminals 1 and 2. Thus SQUID acts as a transducer which converts magnetic flux into voltage. In the magnetometer, this SC loop is connected with the pickup coil which is also located inside the magnetic field. The pickup coil is made of SC wire with four windings (Fig. 2.5(b)). When a sample moves up and down inside the SC wires the magnetic moment of the sample induces an electric current in the coil which couples with magnetic flux through the coil with the SQUID sensor, as shown in Fig. 2.5(a). The SQUID sensor changes the magnetic flux to the output voltage which is proportional to the change in magnetic moment of the sample (Fig. 2.5(c)). The voltage is then magnified and read out by the magnetometer electronics. It is well known that SQUID can only detect magnetic flux φ ($= \int \boldsymbol{B} \cdot d\mathbf{A}$, magnetic flux density B times the area A of the SQUID loop and every SQUID magnetometer has to be calibrated with a sample of known magnetic moment such that one can obtain the fringing/stray field (since the actual area A of each SQUID is not precisely

known). However, commercially available SQUID magnetometers detect the change of magnetic flux created by mechanically moving the sample through a SC pick-up coil which is converted to a voltage V_{SQUID}. In a typical MPMS, the position is denoted as the *x*-direction which is parallel to the external magnetic field H_{ext} so that one obtains raw data, often called as "lastscan," where V_{SQUID} is plotted against x_{pos} (Fig. 2.5(b)). In order to suppress the influence of all kinds of external magnetic fields, the pick-up coil is made as second order gradiometer (surveying instrument used for measuring the gradient). The entire detection system is sketched in Fig. 2.5(b) with a clear depiction of single SQUID scan in the inset where the maximum of V_{SQUID} at x_{pos} = 2 cm corresponds to the sample directly positioned in-between the double coil of the pick-up gradiometer. After mounting the sample, this center-position has to be determined using a long scan to accurately adjust the sample position with respect to the pickup coils (this procedure is popularly known as centering). During the centering process one has to record relatively long scans so that not only the maximum but also two minima should be included in the scan. In this process the sample can be imagined like an ideal point dipole which is exactly pinned on the axis of the magnetometer. Usually, the software allows one to perform the fit in two ways: First, it either assumes a fixed sample position and only fits the amplitude of the V_{SQUID} (x_{pos})-curve with a single fitting parameter which is the magnetic moment of the assumed point dipole often called as the linear-regression-mode in the MPMS. In the second method the sample position is fitted together with the amplitude by iterative regression mode which is very convenient method for measuring the temperature dependent magnetization. The iterative regression mode easily compensates for the thermal expansion of the sample holder assembly. To minimize errors in the fit due to the point dipole approximation in either fitting routine, the specimen size should be limited to a maximum of 5 mm along the scan direction. Whereas, the lateral size of sample is naturally limited to 5-6 mm depending upon the design of the sample holder.

In the present case we mounted the sample at the centre of a transparent plastic straw. But, for highly sensitive measurements, the following parameters turned out to be a good compromise between accuracy and time: 4 cm of sample movement, average over 5 scans with 10 oscillations each at 1 Hz, and iterative regression mode for the fit routine. Concerning the units, magnetization (*M*) of a homogeneous sample of volume (V) is related to the magnetic moment (μ) with $M = \mu/V$. Typically, magnetometry measurements are different from susceptometry measurements where the magnetic susceptibility tensor χ_{ij} is given by $\chi_{ij} = \partial M_i/\partial H_j$. Here *H* represents the magnetic field intensity, which is not to be mistaken with *B* the magnetic flux density (or magnetic induction). In the cgs units, *B* is measured in Gauss (G) while *H* is measured in Oersted (Oe) and in vacuum, both quantities are same. In the SI units, *B* is measured in Tesla (T), whereas, *H* is measured in A/m and in vacuum, $B = \mu_0 H$; the conversion from cgs to SI is 10000 Oe = 1 T. The MPMS uses the cgs-unit emu for 'm', which can be easily converted into the SI-units. Usually, the measured magnetic moment from SQUID magnetometry is often given in emu/g which is easier to be measured and does not require the density of the material and this quantity can be easily representable in μ_B/atom (1 μ_B =9.274×10^{-21} emu). The sensitivity of commercial SQUID magnetometers is usually provided in emu; for the MPMS-XL5, it is < 10^{-8} emu below 250 mT and less than 2×10^{-7} emu up to full field conferring to the

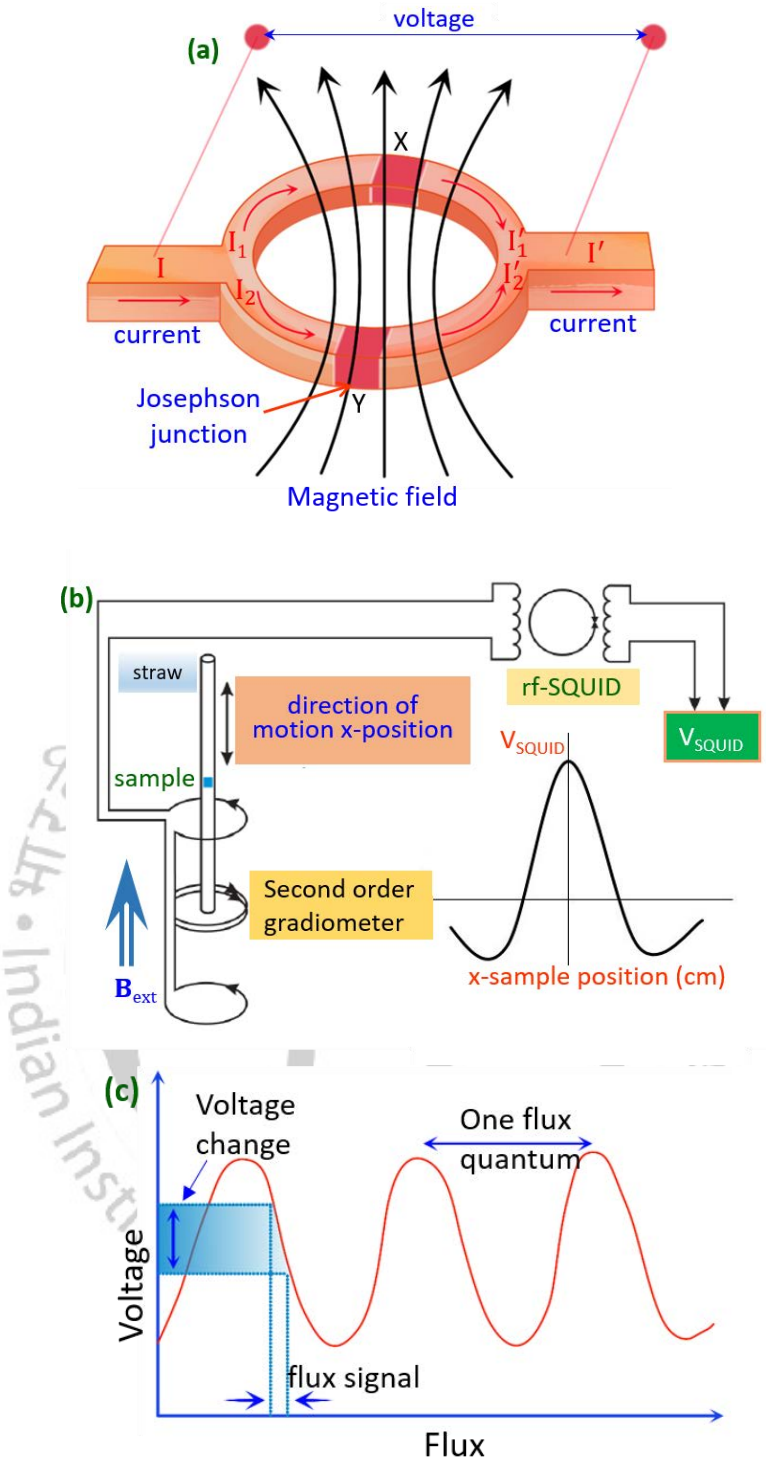

Fig. 2.5: (a) Schematic diagram of a SC ring consists with two Josephson junctions inside the DC SQUID magnetometer. (b) The SC pick-up coil with second order gradiometer (four circular rings). Inset shows the SQUID response V_{SQUID} versus sample position (*x*-pos.). (c) The output voltage plotted as a function of applied flux, here a small change in flux corresponds to the measurable voltage change across the SQUID.

manufacturers specifications which is ~ 2×10^{-7} emu corresponding to the magnetic moment of a single atomic layer of nickel.

In the present study, fully automated "standard sequences" were used for the temperature dependence of magnetization and magnetic hysteresis loops performed using a SQUID magnetometer. Throughout this work we used standard MPMS sequences for the *M-H* and *M-T* measurements under both zero-field-cooled

(ZFC) and field cooled (FC) conditions. For the *M-H* curve we used the following experimental protocol. First, a full *M-H* is measured at 300 K under five cycle hysteresis mode (0→+5T→0→–5T→0→+5T) using the "no overshoot" mode (field is approaching the desired magnetic field from one side and exactly stabilizes the magnetic field at the requested value; magnet is in persistent mode during the actual measurement). Then the sample is cooled down in the presence of field H_{dc} and no-field (H_{dc} = 0 Oe) to 2 K and then a full $M(H)$ curve is recorded. We performed the $M(H)$ curve at 2 K under field-cooled conditions to see whether the investigated system exhibits exchange-bias effects or not. This procedure also allows us to probe the field imprinted magnetic phenomena like the uncompensated antiferromagnets or ferrimagnets. On the other hand, temperature dependence (2 K to 300 K) of magnetization $M(T)$ was measured using the standard protocols, ZFC and FC by cooling the compound in the presence of field/no-field (≤100 Oe) and under settle mode with small temperature interval. However, few measurements were performed under sweep mode (no stabilization of the temperature). Before the beginning of sequence for low-field measurements, 1 kOe field is set using the "oscillation" mode and set to zero, such that one can minimize the residual/stray fields and ensure perfect virgin state. After this procedure, we performed the low-field $M(T)$ measurements in which field is applied with no-overshoot condition. The major components of the SQUID measurement system comprise the following major constituents: (i) Temperature control system: Precision control of the temperature in the range 2 K to 400 K, (ii) Magnet control system: Current from a power supply is set to provide magnetic fields from zero to ±7 T. (iii) Superconducting SQUID amplifier system: The DC−SQUID detector is the heart of the magnetic moment detection system. It provides reset circuitry, auto-ranging capability, a highly balanced second-derivative sample coil array. (iv) Sample handling system: The ability to step and rotate the sample through the detection coils without transmitting undue mechanical vibration to the SQUID is of primary importance. (v) Computer operating system: All operating features of the MPMS are automated and computer controlled. The user interface at the PC console provides the option of working under standard sequence control or diagnostic control which will invoke individual functions.

2.2.2.2.2 AC-magnetic susceptibility:

In this sub-section we discuss the theory and experimental methods related to dynamic magnetic susceptibility under time varying magnetic field together with the measurement technique. In the ac-susceptometer, the sample is mounted in the center within the pick-up coil and a small time varying sinusoidal magnetic field $h_{AC} = h_0 \sin(\omega t)$ is applied on the sample. Here ω (= $2\pi f$) is the angular frequency of the oscillating magnetic field.

The frequency (f) is typically varied between 0.1 kHz and 10 kHz. The response of the magnetization is recorded, $M_{AC} = \frac{dM}{dH} h_0 \sin(\omega t)$; where the AC-susceptibility is defined by the expression: $\chi_{AC} = M_{AC}/h_{AC}$. Usually, the frequency of the oscillating magnetic field is comparable to the timescale of the magnetic dipole relaxation of the system. It is possible that there may be some phase lag (consequently, dissipation takes place) when the perturbation is slightly faster or slower than the natural frequency of the system. Thus, the response is reported in two parts. The in-phase (χ'_{AC}) and out-of-phase (χ''_{AC}) (or real and imaginary components). Here, the imaginary component (χ''_{AC}) relates to dissipation/loss in the system. Thus, the ac-

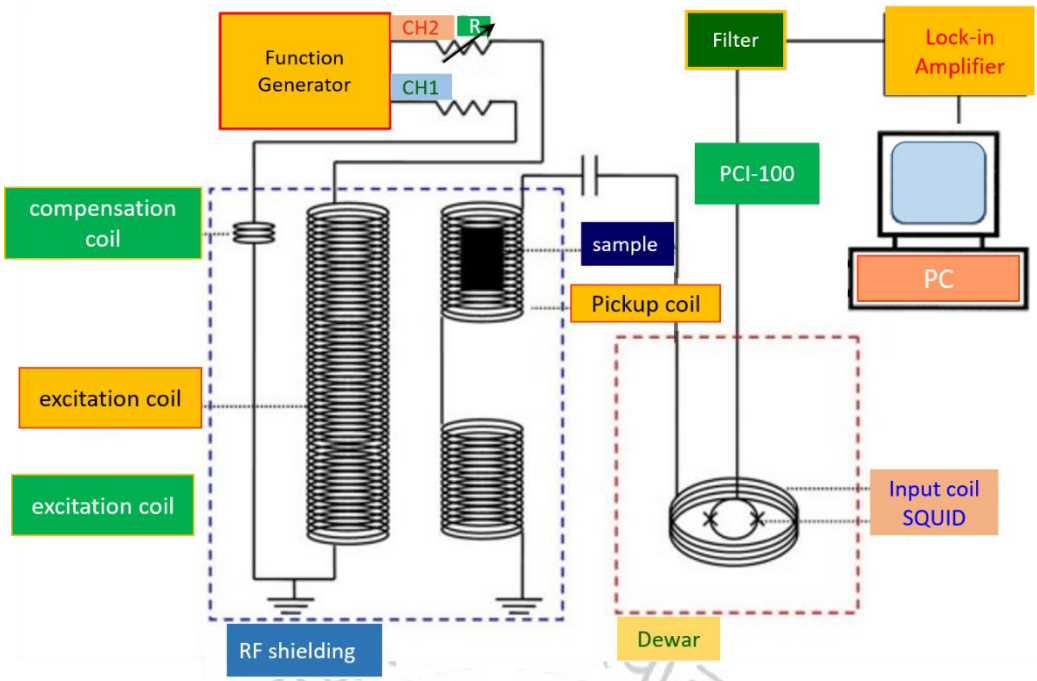

Fig. 2.6: Schematic setup of a SQUID-based ac-susceptometer [127].

susceptibility may be written as a complex quantity: $\chi_{AC} = \chi'_{AC} + i\chi''_{AC}$.

Here,

$$\chi' = Re[\chi_{AC}] = \chi_0 cos\varphi = \frac{\chi_0}{1 + (\omega\tau_{eff})^2} \tag{2.36}$$

$$\chi'' = Im[\chi_{AC}] = \chi_0 sin\varphi = \frac{\chi_0}{1 + (\omega\tau_{eff})^2}\ \omega\tau_{eff} \tag{2.37}$$

and $\chi'/\chi'' = \tan\varphi = \omega\tau_{\text{eff}}\ (t)$. In the above expressions, φ represents the phase delay of the time-varying magnetization ($M(t)$) relative to the applied ac magnetic field ($h_{ac}(t)$) and τ_{eff} is the effective relaxation rate which characterizes the ability to retain magnetization after the dc-field is removed. As compared with the dc-magnetic susceptibility, the temperature dependence of ac-susceptibility $\chi_{AC}(T)$ gives sharp transitions and the ac-data clearly separates out the order - disorder transitions from the local short-range magnetic orderings [78]. In this work we employed the same SQUID magnetometer as discussed above for the temperature and frequency dependence of ac-susceptibility data. However, ac-measurements are performed using a PPMS (Quantum Design) along with the ac-measurement system (ACMS) accessory. In general, any home-made ac-magnetic system contains sensing coils including excitation coil, pick-up coil and compensation coil. First, the excitation coil was excited with a certain frequency of ac signals where the pickup coil is used in gradient configuration and the compensation coil is used to recover the balance of the pickup coil. By means of a lock-in amplifier the real ($Re[\chi_{AC}]$) and imaginary components ($Im[\chi_{AC}]$) of ac-susceptibility can be detected. Figure 2.6 shows a schematic of the detection process of ac-susceptibility.

2.2.2.3 Specific heat:

For selected compounds we performed the temperature dependence of specific heat ($C_p(T)$) using the PPMS (from Quantum Design) with heat capacity accessory in which heat added and removed from a sample by monitoring the resulting change in temperature [128]. It is well known that heat capacity C is defined as the amount of heat, Q required to effect a corresponding change in temperature T at a constant volume; $C = dQ/dT$. At low temperatures, the heat capacity of material may be written as the sum of electron and phonon contribution: $C = \gamma T + AT^3$, where γ and A are the constants and characteristic of the material under investigation. The contribution from electronic part is linear with T and is dominant at very low temperature. In each measurement cycle, a known amount of heat is supplied to the sample at constant power for a fixed time, then this heating period is followed by a cooling period of the same duration. After each cycle, the software option fits the temperature response of the sample stage to an appropriate mathematical model. It is possible that weak thermal contact between the sample and sample-platform causes thermal relaxation. Hence, the model considers the thermal relaxation of the sample stage to the thermal bath and also the relaxation between the sample-platform and the sample itself which offers the accurate value of C_p of the sample [129]. Figure 2.7 illustrates the schematic of thermal connections to the sample and sample platform in PPMS Heat Capacity accessory. A heater and a thermometer are attached at the bottom of the sample stage. The sample is attached on the stage by thin layer of Apiezon N Grease which helps to make thermal contact between sample and the sample-platform. Highly sensitive wiring system is connected with the heater and thermometer to provide electrical and thermal connections. Usually, the additional measurements are performed before the $C_p(T)$ measurement of the sample, which consists of measuring the C_p of the sample holder. In the additional run, a thin layer of Apiezon N Grease is placed on the sample stage and the measurement is taken. After the completion of additional run, the sample is carefully attached with the grease without disturbing it. The measurement is performed once more and the correct value of the C_p of the sample is determined by subtracting the C_p of the sample holder from the total magnitude. Next section we discuss the methodology of Neutron diffraction technique, we have used to investigate the structure and magnetic behaviour of some of our complex spinel oxides (i.e. Co_2TiO_4 and Co_2SnO_4).

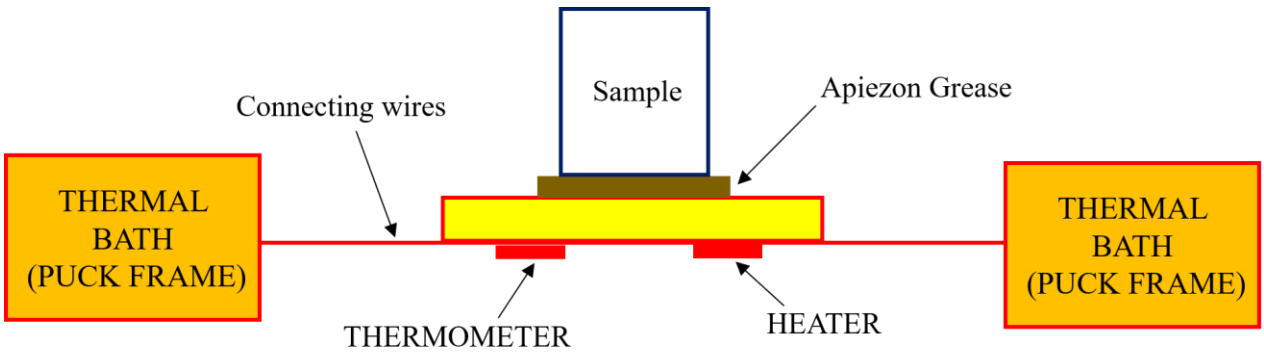

Fig. 2.7: Schematic of the specific heat measurement assembly and connections adopted from Quantum Design PPMS.

2.2.2.4 Neutron diffraction measurements:

For few specific systems we performed low-temperature neutron diffraction experiments at Helmholtz Zentrum Berlin (HZB), Germany**.** These measurements are aimed to probe the site dependent magnetic moment, magnetic ground state and detailed crystal structure at various temperatures below the T_C/T_N. In principles the neutron powder diffraction uses similar method as that of XRD where x-rays interact with the electron cloud, but neutron scattering occurs at the atom nuclei since the neutrons carry magnetic moment. This principle makes neutrons as excellent candidates to probe the magnetic properties of materials. Using this method one can accurately determine the magnitude of the magnetic moment. Below we discuss some of the basic understanding of neutron scattering. It is well known that the neutrons are uncharged particles, hence, it experiences very weak or no Coulombic barrier and penetrate deeply into materials and interact directly with the atomic nucleus. On the other hand, Neutron consist quarks and gluons and possesses spin-1/2 with magnetic moment $\mu_n = -1.913\ \mu_N$, where $\mu_N = \frac{e\hbar}{2m_p}$ is the nuclear magnetic moment. Thus, the neutron's magnetic moment interacts with the unpaired electron spins of magnetic atoms with a comparable strength and gives the magnetic structure of the compounds. Furthermore, due to large mass (1.675×10^{-27} kg) neutron leads to a thermal-neutron de-Broglie wavelength [$\lambda = \frac{h}{mv}$] of about 1.8 Å, which is of the order of the interatomic distances, generating possible interference patterns which gives the structural information about the system. Consequently, neutron diffraction technique is a powerful tool to probe the crystal and magnetic structure of crystalline samples under elastic and inelastic scattering conditions [129-131]. For the scattering measurements the neutron beam is typically produced using two mechanisms: The first one is 'fission process' in which a steady flux of neutrons is produced inside a nuclear reactor and the second mechanism is 'spallation source' where neutrons are produced by bombarding heavy metal atoms with energetic protons from accelerators [132]. The neutrons generated from the two sources usually possess very high energy, thus their energy can be categorized in different ranges; cold neutrons and thermal/hot neutrons depending on the temperature/energy range. In the present case we performed the neutron diffraction measurements at HZB using the BER II reactor as source along with a fine resolution powder diffractometer (E9). We also used the focusing powder diffractometer (E6) with a 2D detector, and a flat-Cone diffractometer (E2). A detailed description about all these three diffractometers can be found in [132]. A brief theory of neutron scattering and working principle of neutron diffractometer is outlined below.

2.2.2.4.1 Theoretical and experimental background:

A collimated beam of neutrons are thermally accelerated from the source with initial momentum, $\hbar k_i$ and energy, E_i and then they get diffracted from the crystal at an angle θ with final wave vector k_f and energy E_f. During the scattering process, the transferred momentum ($\hbar Q$) and energy (E_T) to the sample is defined as (according to the conservation of total energy and momentum):

$$\hbar Q = \hbar k_f - \hbar k_i \tag{2.38}$$

where, $Q^2 = k_f^2 + k_i^2 - 2k_i k_f cos\,(2\theta)$ and $E_T = E_f - E_i = \frac{\hbar^2}{2m_n}\,(k_f^2 - k_i^2)$

Figure 2.8 shows the schematic demonstration of the scattering process. For elastic scattering, no energy is transferred from the neutron to the sample, therefore $E_T = 0$, $|k_i| = |k_f|$ and the transferred wave vector is $Q = 2|k|^2 \sin\theta$. Whereas, in an inelastic scattering process both energy and momentum are transferred from the neutron to the sample, hence $E_T \neq 0$ and $|k_i| \neq |k_f|$. Consequently, the change in energy is measured during the experiment which gives the detailed information about dynamics of the material. Therefore, the number of neutrons scattered into solid angle $d\Omega$ per second around $\Omega(\theta, \phi)$ with the final energy between E_f to $E_f + \Delta E_f$ is called double differential scattering cross section $\left(\frac{d^2\sigma}{d\Omega dE_f}\right)$, where σ represents the flux of scattered neutrons. It is the basic quantity measured during a neutron scattering experiment and depends strongly on the interaction strength between the neutron and the samples. Hence, the partial differential cross section of neutrons scattered by the specimen's internal potential V is given by the below expression [130]:

$$\frac{d^2\sigma}{d\Omega dE_{k_i \to k_f}} = \frac{k_f}{k_i}\left(\frac{m}{2\pi\hbar^2}\right)^2 \sum_{\lambda_i, s_i} p_{\lambda_i} p_{s_i} \sum_{\lambda_f, s_f} |\langle \boldsymbol{k}_f s_f \lambda_f | \hat{V} | \boldsymbol{k}_i s_i \lambda_i \rangle|^2 \, \delta\left(E_{\lambda_i} - E_{\lambda_f} + E_i - E_f\right) \qquad (2.39)$$

Here s_i and s_f represents the incident and scattered neutron spin states. After the scattering sample state changes from λ_i to λ_f. p_λ, p_s are statistical weight factors (assuming Boltzmann distribution) for the initial states $|s_i \lambda_i\rangle$ and $\hat{V}$ is the operator corresponding to the scattering potential V. Moreover, E_i and E_f represents the corresponding energy of the individual states, respectively. During the neutron scattering experiment an incident neutron interacts with the i^{th} atomic nuclei positioned at r_i through an interaction potential which can be described by a Fermi pseudo potential function as below [130]:

$$V_N(r) = \frac{2\pi\hbar^2}{m_n} \sum_i b_i \delta(r - r_i) \qquad (2.40)$$

In the above equation, b_i represents the scattering lengths of each atomic nucleus. The nuclear force is strong within the short-range limit and spherically symmetric and the potential is defined by the delta function. Summing over all the nuclei and using the above potential function the total scattering cross section can be calculated [133]. When an un-polarized neutron source falls on the materials the partial differential cross-section can be written as a sum of coherent and incoherent term:

$$\frac{d^2\sigma}{d\Omega dE_f} = \frac{d^2\sigma_{coh}}{d\Omega dE_f} + \frac{d^2\sigma_{incoh}}{d\Omega dE_f} = \frac{k_f}{k_i}(S_{coh}(\boldsymbol{Q}, \omega) + S_{incoh}(\boldsymbol{Q}, \omega)) \qquad (2.41)$$

where $S_{coh}(\boldsymbol{Q}, \omega)$ and $S_{inc}(\boldsymbol{Q}, \omega)$ are the dynamic correlation functions and are represented as:

$$S_{coh}(\boldsymbol{Q}, \omega) = \frac{1}{2\pi\hbar \mathrm{N}} \sum_{ll'} b_l b_{l'} \int_{\bar{\infty}}^{\infty} \langle e^{-i\boldsymbol{Q}.\boldsymbol{r}_{l'}(0)} \, e^{i\boldsymbol{Q}.\boldsymbol{r}_l(t)} \rangle e^{-i\omega t} \, dt \qquad (2.42)$$

$$S_{inc}(\boldsymbol{Q}, \omega) = \frac{1}{2\pi\hbar \mathrm{N}} \sum_{l} b_l \int_{-\infty}^{\infty} \langle e^{-i\boldsymbol{Q}.\boldsymbol{r}_l(0)} \, e^{i\boldsymbol{Q}.\boldsymbol{r}_l(t)} \rangle e^{-i\omega t} \, dt \qquad (2.43)$$

Here, $\langle e^{-i\boldsymbol{Q}.\boldsymbol{r}_{l'}(0)} \, e^{i\boldsymbol{Q}.\boldsymbol{r}_l(t)} \rangle$ term signifies the correlation between the position of one nucleus at time t = 0 with another nucleus at a later time t.

Thus, $S(\boldsymbol{Q},\omega)$ provides the microscopic properties of sample by measuring the strength of the correlations collectively. The $S_{coh}(\boldsymbol{Q},\omega)$ arises from the coherent interference between the same nucleus at different times along with the interference from different nuclei at different times. Consequently, the coherent scattering provides information about the crystal structure and lattice excitations. On the other hand, incoherent scattering arises only from interference effects of the same nucleus at different times. It is proportional to the variance in the neutron scattering lengths and causes an isotropic background in the intensity of scattered neutron. For a crystalline sample the major contribution comes from coherent nuclear scattering due to the elastic scattering from the periodic atomic planes which produces peaks in the scattered pattern. These peaks satisfy the Bragg condition and known as Bragg peaks. The scattering cross-section for nuclear elastic scattering is [134]:

$$\left(\frac{d^2\sigma}{d\Omega dE_f}\right)_{nuc.\ elast.} = \delta(\hbar\omega)\frac{d\sigma_N}{d\Omega}(Q) = \frac{N(2\pi)^3}{V_0}\,|F_N(\boldsymbol{Q})|^2\delta(Q-\tau)\delta(\hbar\omega) \tag{2.44}$$

where $F_N(\boldsymbol{Q})$ is called the nuclear scattering factor which gives the results for all nuclei present within one-unit cell. In Eq. (2.44), τ is the crystal reciprocal lattice vector and $\delta(Q-\tau)$ reflects the periodicity of the crystal lattice and N is the number of unit cells included in the volume V_0. On the other hand, magnetic scattering arises from the interaction of the magnetic moment of the neutron with magnetic fields of the spin and orbital momentum of the unpaired electrons. The neutron magnetic moment $\mu_n = -\gamma S\mu_N$, where γ is the gyromagnetic ratio, S is the Pauli spin operator and μ_N is the nuclear magneton. Due to the unpaired electrons of the magnetic ions the local magnetic flux density (B) can be created which is related to the interaction potential (V_M) for magnetic scattering as: $V_M(\mathrm{r}) = -\mu_n.\mathrm{B}(\mathrm{r})$. Using Maxwell's equations, the Fourier transformed interaction potential can be expressed as: $V_M(\boldsymbol{Q}) = -\mu_n.\mu_0 M_\perp(\boldsymbol{Q})$. Where, $M_\perp(\boldsymbol{Q})$ is the component of the magnetization perpendicular to the scattering vector Q. Like the nuclear Bragg peaks, magnetic Bragg peaks originates from the scattering of neutrons from the magnetic lattice when the scattering vector $\boldsymbol{Q}$ coincides with the reciprocal magnetic lattice vector. Consequently, the magnetic scattering differential cross-section for the compound can be obtained by plugging the magnetic interaction potential $V_M(\boldsymbol{Q})$ into the equation and the final expression can be written as below [131]:

$$\left(\frac{d^2\sigma}{d\Omega dE_f}\right)_{\text{nuc. elast}} = \delta(\hbar\omega)\frac{d\sigma_M}{d\Omega}(\boldsymbol{Q}) \tag{2.45}$$

$$= \frac{N_m(2\pi)^3}{V_{0m}}\left(\frac{\gamma r_0}{2}\right)^2\sum_{\alpha\beta}\langle(\delta_{\alpha,\beta}-\widehat{\boldsymbol{Q}}_\alpha\widehat{\boldsymbol{Q}}_\beta)F^\alpha(\boldsymbol{Q})F^{\beta*}(\boldsymbol{Q})\rangle\times\delta(Q-\tau_m)\delta(\hbar\omega)$$

In the above expression the parameter b_m is the reciprocal magnetic lattice vector and the sum over α,β = x; y; z. $\langle\ldots\ldots\rangle$ represents the average value for all the magnetic domains in the lattice, and F^α is called the magnetic structure factor which is expressed as:

$$F^\alpha(Q=\tau_m) = \sum_i \mu_i^\alpha f_i(\boldsymbol{Q})\exp(i\boldsymbol{Q}.r_i)\exp\big(W_i(\boldsymbol{Q},T)\big) \tag{2.46}$$

Here μ_i^{α} is the α^{th} component of the magnetic moment of the i^{th} ion, r_i is the corresponding position within the magnetic unit-cell. The exponential term $\exp\big(W_i(\boldsymbol{Q},T)\big)$ represents the Debye-Waller factor and $f_i(\boldsymbol{Q}) = \int s_a(r)e^{i\boldsymbol{Q}.r}dr$ is the magnetic form factor. The parameter s_a is the normalized density of the unpaired electrons of ion a. The form factor originates due to the finite spatial extent of the unpaired electron cloud which cannot be expressed by a δ-function contrary to the case of nuclear scattering. Since the magnitude of $f(\boldsymbol{Q})$ decreases rapidly with $\boldsymbol{Q}$, the range of magnetic scattering is limited and it can be observed in the low-$\boldsymbol{Q}$ region only.

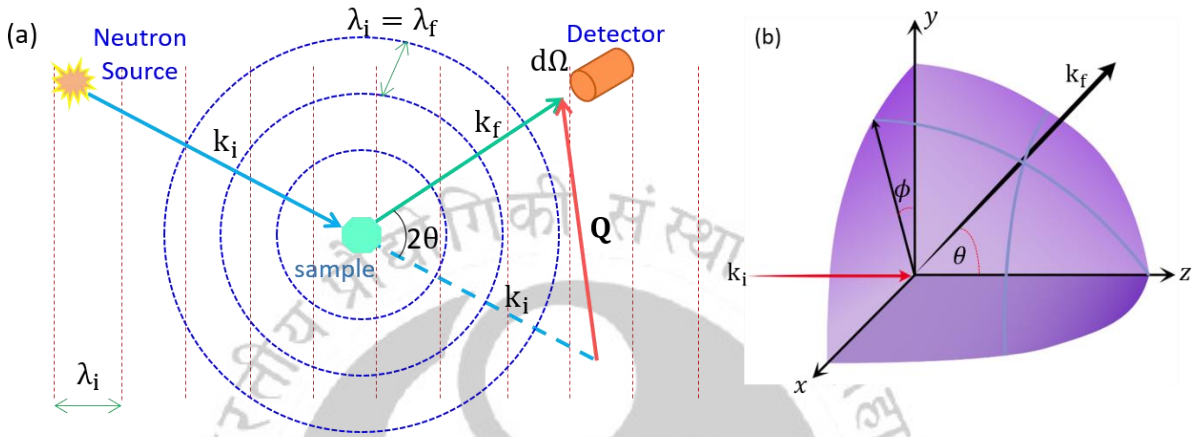

Figure 2.8: Illustration of neutron scattering wave fronts from an atom: (a) k_i (k_f) and λ_i (λ_f) represents the initial (final) wave-vector and wavelength describing a neutron scattering from a single nucleus with positive scattering length. (b) The geometry of a scattering experiment where the incident neutrons with k_i are scattered in the direction θ and ϕ with final wave-vector k_f.

Chapter 3
Electronic structure and magnetic ordering in diluted cobaltites

This chapter deals with a comprehensive study on the electronic and magnetic structure obtained from the first-principles DFT+U calculations along with the experimental results on few spinel cobaltites. Here we focused our studies mainly on the role of site-specific dilution on the structural, magnetic, electronic, and optical properties of antiferromagnetic Co_3O_4. A systematic correlation between the theoretical and experimental results has been established. First, we provide a brief introduction to the systems under investigation and outline the details of theoretical and experimental methods in line with the previous chapter. Next, we provide a detailed description on the analysis of the results followed by the summary of important findings.

3.1 Outline and background:

The main objective of the research work presented in this chapter is to study the role of magnetic dilution on the AFM ordering of spinel Co_3O_4 (= $(Co^{2+})_A[Co^{3+}]_BO_4$). According to the theory proposed by Néel, the dominant magnetic exchange interaction (J_{AB}) between ions in the A (tetrahedral) and B (octahedral) sites in any AFM/FiM spinel system is negative [88,135-142]. As compared to the J_{AB} the other interactions such as A-A and B-B are weak but negative following the general trend $J_{AA} < J_{BB} < J_{AB}$. However, the J_{AA} interaction in Co_3O_4 is surprisingly large in which the spins of divalent Co orders antiferromagnetically ($(\downarrow\mu(Co^{2+})_A+\uparrow\mu(Co^{2+})_A)$) with spins on A sites are bounded by four nearest neighbors with opposite spins below 30 K (Néel temperature T_N) [140,143-145]. Interestingly, such long-range ordering can be systematically tailored by site specific substitution of any non-magnetic/magnetic elements (Ge, Al, Ti, Ru, or Sn) in Co_3O_4 matrix. As a consequence of substitution, significant imbalance in the moments on A and B sites result in ferrimagnetic or reentrant spin-glass behavior along with substantial change in cationic distribution resulting to slight tetragonal distortion with inverted spinel configuration (e.g. cobalt orthotitanate/stannate (Co_2Ti/SnO_4)) [21,23,146-148].

Our main focus here is to probe the low-temperature magnetic ordering in the such diluted spinels (Co_2TiO_4, Co_2SnO_4, Co_2RuO_4, Co_2AlO_4, and Co_2GeO_4). Although there are several experimental studies focused on this aspect, a detailed theoretical study dedicated to the role of dilution was lacking in the literature when we initiated our study. In particular, coexistence of different spin-arrangements along the longitudinal (FiM) and transverse (spin-glass) directions leading to some exotic properties such as bipolar exchange-bias (H_{EB} ~ -20 KOe at 10 K) and spin-liquid state (< 20K) are the motivating aspects of the current study [21,43]. Significant developments in the characterization techniques and availability of rich experimental conditions led to reinvestigate the magnetic structure of these compounds with high precession in last ten years [21-24,43,143,144,149]. Especially, the competing local inter-sublattice interactions yield FiM state with T_N ~ 41 K, 47.8 K and 16 K and spin-glass freezing temperature T_F ~ 39 K, 32 K and 16 K for Co_2SnO_4, Co_2TiO_4 and Co_2RuO_4, respectively [21-24,43]. At a first glance both the systems Co_2SnO_4 and Co_2TiO_4 look undistinguishable (lattice parameter

$a_{Co_2SnO_4}$ = 8.66 Å, > $a_{Co_2TiO_4}$= 8.45 Å), but their magnetic structure is markedly different due to the different temperature dependence of magnetic ions and the imbalance in the Co^{2+} spins at tetrahedral (μ(A) = $3.87\mu_{B-Co_2SnO_4}$ and $3.87\mu_{B-Co_2TiO_4}$) and octahedral sites (μ(B) = $4.16\mu_{B-Co_2SnO_4}$ and $5.19\mu_{B-Co_2TiO_4}$). Interestingly, the inverted spinel Co_2TiO_4 exhibits distinct FiM magnetic ordering and electronic structure below T_N as compared to the Co_2SnO_4 which results: (*a*) compensation effect at T_{COMP} (~32 K) where the bulk-magnetization of two sub-lattices balance each other, (*b*) dissimilar electronic structure $(Co^{2+})[Co^{3+}Ti^{3+}]O_4$ as compared to the $(Co^{2+})[Co^{2+}Sn^{4+}]O_4$, (*c*) dominance of negative magnetization at low-temperatures [22,24,43]. On the other hand, a detailed first principles based *ab initio* study on these spinels is very much needed to understand the electronic and magnetic structure. Previous studies by Walsh *et al.* reported a direct gap of Co_3O_4 of 1.67 eV and 1.23 eV at Γ and X high symmetry points of Brillouin zone, respectively using the DFT + U calculations [145]. However, considering U = 4.4 eV for Co^{2+} ions and 6.7 eV for Co^{3+} ions, Chen *et al.* showed a minimum energy band gap of 1.96 eV at X point with an AFM configuration of spins at A-sites for PBE and FM configuration for PBE+U [150]. Using hybrid functionals, Lima reported energy band gap (E_G) values between 0.35 eV and 2.58 eV at the X high symmetry point of the Brillioun zone [151]. In another work, Lima demonstrated that the AFM configuration is energetically more favorable than the FM configuration of Co_3O_4 and reported the E_G ~ 1.60 eV and 2.04 eV for U = 3.0 and 4.4, respectively [152]. Selcuk *et al.* calculated the E_G of Co_3O_4 at 0.24 eV, 1.13 eV, and 1.80 eV for U = 0.0, 3.0 and 5.9, respectively [153]. By means of PBE+U (with U = 2.0), Xu *et al.* reported the locations of the electronic transitions within the band gap of Co_3O_4 at (*i*) 2.2 eV due to O(2p) → $Co^{2+}(t_{2g})$, (*ii*) 2.9 eV due to O(2p) → $Co^{3+}(e_g)$, and (iii) 3.3 eV due to $Co^{3+}(t_{2g})$ → $Co^{2+}(t_{2g})$ [154]. A comprehensive theoretical study based on DFT+U as summarized above in the investigated system is missing in the literature, hence the present work fills the gap in the literature. Therefore, we report the electronic and magnetic structure of Co_3O_4 for different value of U with a special emphasis on the magnetic dilution with elements such as Ge, Ti, Ru, and Sn at the Co tetra/octahedral sites along with the experimental results.

The arrangement of the subsections are as follows, first we compare the structural properties predicted from *ab initio* calculations with the experimental investigations and provide the details of electronic structure analysis followed by the magnetic and optical properties of both pristine and diluted systems. In the final section we present the salient findings of the results.

3.2 Computational methods and experimental details:

We have employed the density functional theory (DFT) based calculations to probe the electronic structure and magnetic properties of the spinel cobaltites using VASP as discussed in Chapter 2. The simulations were performed on 8×8×8 k-grid points. Periodic boundary conditions are employed in all directions. A plane wave basis set with an upper threshold value 500 eV was employed to perform the integration in Brillouin zone. Periodic boundary conditions are employed in all directions. The Kohn-Sham equations are solved self-consistently using the projector augmented wave (PAW) basis set (see section 2.1.6 for details). A plane-wave

basis set with an upper threshold value of 500 eV is employed. The exchange correlation part of the Hamiltonian is treated with the Perdew-Burke-Ernzerhof (PBE) GGA functional (see section 2.1.3.2). The details of this are given in Chapter 2. To begin the calculations, we first took two formula units of the spinel primitive cell and optimized the structure by relaxing the internal positions, followed by relaxation of volume and shape using self-consistent DFT approach. Subsequently the relaxed configuration is used to obtain the required density of states (DOS) and electronic band structure. In this study we considered strong on-site coulomb interactions and are treated using DFT+U formulism within the Dudarev's approach (see section 2.1.4). The coupling is represented through an effective parameter U_{eff} = U - J, where U is the strength of the Coulomb interaction and J is the Hund's coupling constant. For all the calculations, J is considered to be 0 eV. The coulomb parameter U is considered in the range 2 - 6 for both octahedral and tetrahedral sites of Co. The electronic self-consistency is continued until the energy convergence is of the order of 10^{-7} eV. Structural relaxations are performed until residual forces on each atom converge to less than 10^{-4} eV/Å.

On the other hand, the experimental details consist of both synthesis and characterization details which are elucidated in Chapter 2. Nevertheless, here we provide some more details in brief. In case of Co_2SnO_4 system we used slightly higher heat treatment conditions (sintered at 1350ºC for 12 h in air) to avoid the formation of SnO_2. The phase purity and crystal structure information were examined by Rigaku (TTRAX III) X-ray diffractometer with Cu-K_α source radiation of wavelength λ = 1.5406 Å. Diffraction patterns of all the systems are refined with the Fullprof-Rietveld-Refinement suite [155]. Magnetic measurements at various temperatures between 2 K and 330 K were performed using a superconducting quantum interference device (SQUID) based magnetometer MPMS XL from Quantum design. In the below section we present both the theoretical and experimental results on various spinal oxides.

3.3 Results and discussion:

As stated in the above section, to study the effect of strong on-site coulomb interaction on the crystal structure, electronic, and magnetic properties, we vary U for the Co-ion from U = 2 - 6, while keeping the U fixed for the dopants. The interaction between crystal-field and the valence electron of the ions plays important role in deciding the magnetic, electronic and optical behavior of these spinels. In Fig. 3.1 we show a schematic diagram of energy levels splitting in the presence of crystal-field. The occupations of the valence *d* orbital electrons of Co and Ru for both tetrahedral and octahedral sites are also shown explicitly. In Co_3O_4, Co^{2+} ion occupies the tetrahedral site, having high spin state, whereas, Co^{3+} occupies the octahedral site with a low spin state. However, the inverse spinels Co_2TiO_4 and Co_2SnO_4 display different electronic configuration: Co^{2+} ions occupy both the tetrahedral and octahedral sites and remaining half of the octahedral site are filled by the non-magnetic ions, whereas, in case of Co_2RuO_4, the tetrahedral sites are occupied by the divalent Co and the octahedral sites are equally shared by Co^{3+} and Ru^{3+}. Interestingly, when Co_3O_4 is diluted with Ge the system retains the normal spinel structure where Ge^{4+} occupies the tetrahedral site and both the Co^{2+} are favorable to the octahedral sites.

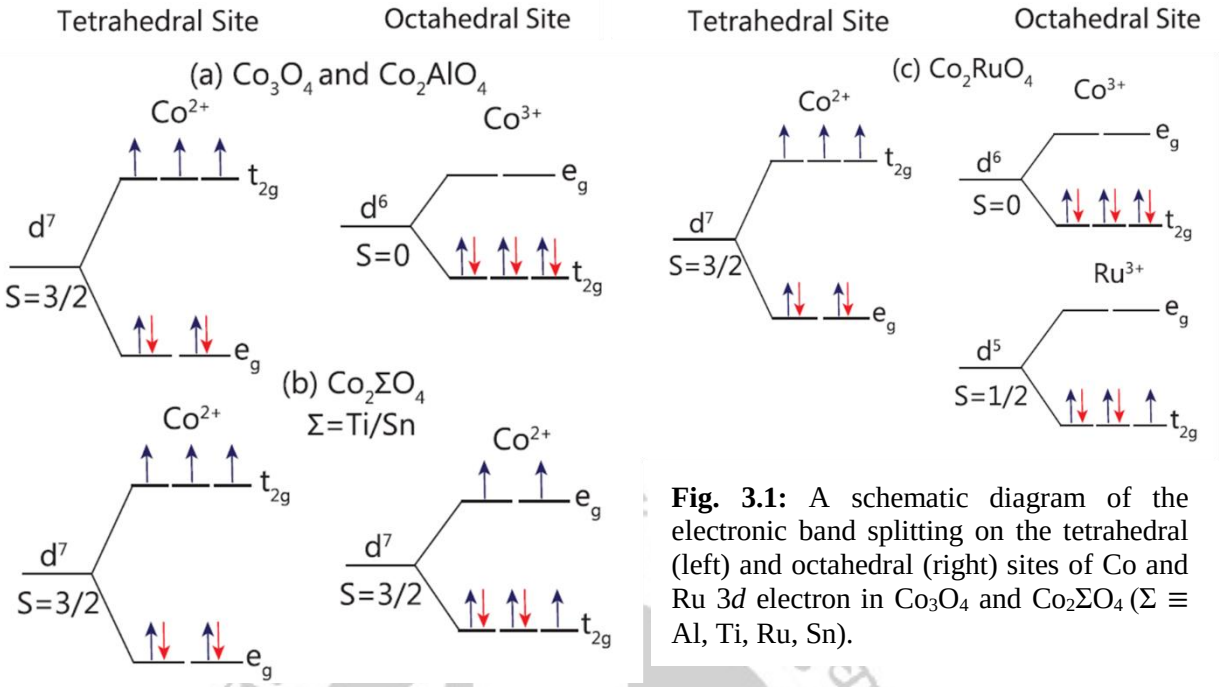

Fig. 3.1: A schematic diagram of the electronic band splitting on the tetrahedral (left) and octahedral (right) sites of Co and Ru 3*d* electron in Co_3O_4 and $Co_2\Sigma O_4$ ($\Sigma \equiv$ Al, Ti, Ru, Sn).

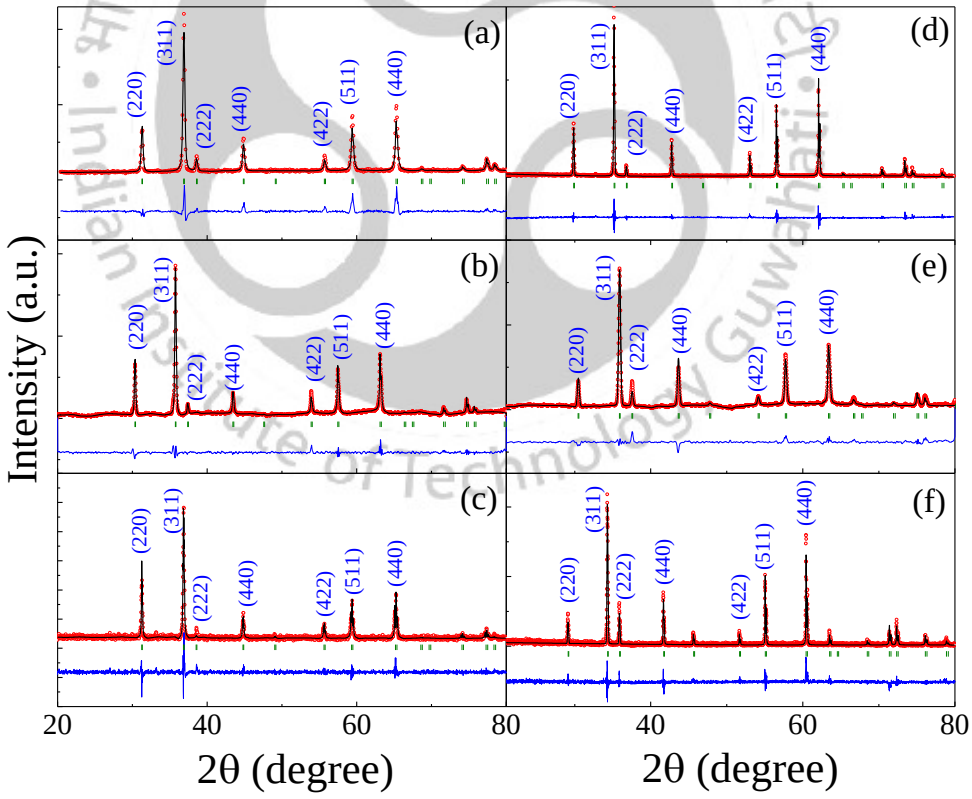

Fig. 3.2: XRD pattern together with the Rietveld refinement data of various Co-spinels: (a) Co_3O_4, (b) Co_2GeO_4, (c) Co_2AlO_4, (d) Co_2TiO_4, (e) Co_2RuO_4, and (f) Co_2SnO_4. The red hollow symbols represent the experimental data and black solid continuous line is for the data obtained using Rietveld refinement. The blue lines at the bottom represent difference pattern observed from experiment and refinement data.

3.3.1 Structural properties:

We first discuss the results obtained from the X-ray powder diffraction (XRD) method which is used to probe the information on crystal structure. Figure 3.2 shows the XRD pattern together with the Miller Indices of planes of different compounds along with the Rietveld refinement data performed using Fullprof-Rietveld-Refinement-Suite. This analysis reveals that except the pristine compound Co_3O_4 and Co_2GeO_4 (which belongs to normal spinel) all the remaining compounds belongs to the family of inverse spinel crystal structure with space group *Fd-3m* (227). In order to probe the minute changes occurring in the crystal structure due to the dilution of different non-magnetic elements in Co_3O_4 we have evaluated the average bond-angle ($\Theta_{A\text{-}O\text{-}B}$) and bond-lengths ($l_{B\text{-}O}$). For Co_3O_4, the lattice parameters obtained from the X-ray diffraction is of the order a = 8.08 ± 0.02 Å, however, for all the inverse spinels Co_2AlO_4, Co_2TiO_4, Co_2RuO_4, and Co_2SnO_4 we obtained a = 8.09 ± 0.03 Å, 8.45 ± 0.01 Å, 8.29 ± 0.01 Å, and 8.66 ± 0.02 Å, respectively. These diffraction patterns confirm the mono-phase nature of the samples prepared from the solid-state reaction method.

In Table 3.1 we list the DFT+U calculated lattice parameters and the oxygen parameters for the parent spinel Co_3O_4 as well as the diluted spinels after incorporating the non-magnetic elements at the octahedral sites. For all the compounds we observe that the lattice parameter (a) gradually increases with increase of U_{Co} (for the pristine compound Co_3O_4, a change from 8.11 Å to 8.14 Å when U_{Co} increases from 2 to 6). These values are in good agreement with the previously reported experimentally observed data [143-145]. For the case of Co_2SnO_4 we observed the larger unit-cell volume (V_{UC} ~ 679.1 Å^3 for U_{Co} =2 and 683.8 Å^3 for U_{Co} = 6) owing to the fact that Sn^{4+} has bigger ionic radius (0.69 Å). However, for Co_2RuO_4 (with Ru^{+3} ionic radius 0.68 Å) a large increase in V_{UC} ($\Delta V_{UC}/V_{UC}$ ~ 9.6%) was noticed as U_{Co} increases from 2 to 6. Whereas, no significant change in V_{UC} was observed for the Co_2TiO_4 (with Ti^{4+} (0.61 Å)), Co_2AlO_4 (with Al^{3+} (0.54 Å)) and Co_2GeO_4 (with Ge^{4+} (0.39 Å)). Our results are in good agreement with the numerical work carried out by Walsh *et al.* [145]. These authors reported the lattice constants 8.11 Å and 8.16 Å respectively, for normal Co_3O_4 and inverse Co_2AlO_4 spinel. These observations are consistent with our results ($a_{Co_3O_4}$ = 8.11Å and $a_{Co_2AlO_4}$ = 8.13Å). On the other hand,

Table 3.1: Calculated lattice constants (Å) and oxygen parameters [*uuu*] of cobalt oxides (Co_3O_4) and cobalt based spinels [$Co_2\Sigma O_4$ ($\Sigma \equiv$ Al, Ti, Ru, Sn, Ge)] for different values of U for cobalt and U = 2 for Ti and Ru. U = 0 was considered for Al, Sn, and Ge.

Composition	Lattice parameter (Å)						Oxygen Parameter		
	Coulomb interaction U (eV)					Expt.	U = 2.0 eV		
	2.0	3.0	4.0	5.0	6.0		u_x	u_y	u_z
Co_3O_4	8.11	8.12	8.14	8.14	8.14	8.08	0.2634	0.2634	0.2634
Co_2GeO_4	8.42	8.42	8.42	8.43	8.43	8.33	0.2514	0.2514	0.2481
Co_2AlO_4	8.13	8.14	8.15	8.16	8.17	8.09	0.2654	0.2654	0.2602
Co_2TiO_4	8.53	8.55	8.56	8.57	8.57	8.45	0.2692	0.2692	0.2692
Co_2RuO_4	8.30	8.33	8.35	8.35	8.56	8.29	0.2558	0.2558	0.2749
Co_2SnO_4	8.79	8.80	8.80	8.81	8.81	8.66	0.2639	0.2639	0.2538

Table 3.2: The equilibrium bond lengths and bond angles for Co_3O_4 and $Co_2\Sigma O_4$ (Σ = Ge, Al, Ti, Ru, Sn) obtained from DFT+U calculations using U = 2 eV are presented. Experimental values obtained from the x-ray diffraction measurements are given in square brackets. In the diluted $Co_2\Sigma O_4$ spinels, we noticed a Jahn-Teller type distortion at the octahedral sites. Bond lengths ($l_{B\text{-}O}$) and bond angles ($\Theta_{O\text{-}B\text{-}O}$) at B site are given for each asymmetric octahedral configuration. All lengths are in Å units and angles are in degrees.

Composition	$l_{A\text{-}O}$ (Å)	$l_{B\text{-}O}$ (Å)	$l_{A\text{-}B}$ (Å)	$l_{B\text{-}B}$ (Å)	$\Theta_{O\text{-}A\text{-}O}$ (°)	$\Theta_{O\text{-}B\text{-}O}$ (°)	$\Theta_{A\text{-}O\text{-}B}$ (°)
Co_3O_4	1.95	1.93	3.36	2.87	109.5	83.3	120.7
$(Co^{2+})[Co^{3+}Co^{3+}]O_4$	[1.94]	[1.92]			[109.5]	[83.3]	[120.6]
Co_2GeO_4	1.83	2.08, 2.11 (Co-O)	3.51 (Ge-Co)	2.98	109.2	89.5, 90.5 (Co-O-Co)	125.2 (Ge-O-Co)
$(Ge^{4+})[Co^{2+}Co^{2+}]O_4$	[1.98]	[1.99]					[121.1]
Co_2AlO_4	1.95	1.93	3.37 (Co-Al)	2.88	109.4	84.0, 95.8 (O-Al-O)	119.9 (Co-O-Co)
			3.37 (Co-Co)	2.88		82.5, 97.5 (O-Co-O)	121.4 (Co-O-Al)
$(Co^{2+})[Al^{3+}Co^{3+}]O_4$	[1.93]	[1.93]			[109.5]	[84.8]	[118.3]
Co_2TiO_4	1.97	1.99, 2.02 (Ti-O)	3.53 (Co-Ti)	3.01	109.8	88.5, 91.5 (O-Ti-O)	122.1 (Co-O-Ti)
		2.07, 2.16 (Co-O)	3.50 (Co-Co)		108.5	82.7, 97.3 (O-Co-O)	121.1 (Co-O-Co)
$(Co^{2+})[Ti^{4+}Co^{2+}]O_4$	[1.98]	[2.03]					[121.7]
Co_2RuO_4	1.98	2.04, 2.06 (Ru-O)	3.46 (Co-Ru)	2.95	111.3	86.5, 93.5 (O-Co-O)	121.8 (Co-O-Co)
		1.95, 1.97 (Co-O)	3.42 (Co-Co)			82.4, 97.6 (O-Ru-O)	118.7 (Co-O-Ru)
$(Co^{2+})[Ru^{3+}Co^{3+}]O_4$	[1.98]	[1.98]			[114.3]	[85.2]	[123.9]
Co_2SnO_4	2.03	2.10, 2.18 (Co-O)	3.62 (Co-Sn)	3.09	109.6	85.1, 94.9 (O-Co-O)	123.4 (Co-O-Co)
		2.11, 2.08 (Sn-O)	3.62 (Co-Co)			92.9, 87.1 (O-Sn-O)	121.4 (Co-O-Sn)
$(Co^{2+})[Sn^{4+}Co^{2+}]O_4$	[1.88]	[2.16]			[114.3]	[85.2]	[125.0]

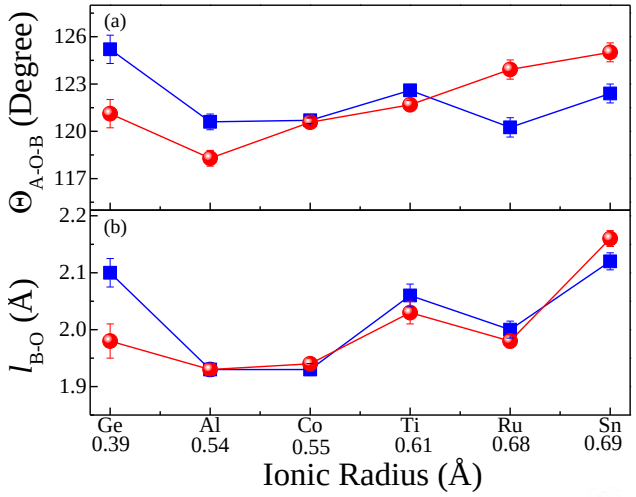

Fig. 3.3: Variations of (a) Bond angle ($\Theta_{A\text{-}O\text{-}B}$) and (b) Bond length ($l_{B\text{-}O}$) with the ionic radius of the dilutants. Red solid spheres represent the experimental data whereas the blue squares represent the theoretical predictions for U = 2.

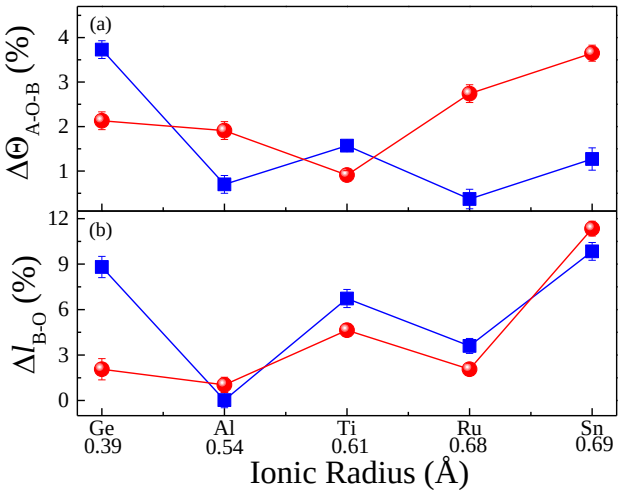

Fig. 3.4: Deviation of (a) Bond angle ($\Delta\Theta_{A\text{-}O\text{-}B}$) and (b) Bond length ($\Delta l_{B\text{-}O}$) of different compound $Co_2\Sigma O_4$ ($\Sigma \equiv$ Ge, Al, Ti, Ru, Sn) compared to pristine compound Co_3O_4. Red solid spheres represent the experimental data whereas the blue squares represent the theoretical predictions for U = 2.

we have evaluated the equilibrium bond-lengths as: (*i*) Co_{tet}-O = 1.95Å and (*ii*) Co_{oct}-O =1.93Å for Co_3O_4, and Co_{tet}-O = 2.03 Å and Co_{oct}-O_{AVG} =2.14 Å for inverse spinel Co_2SnO_4. Table 3.2 summarizes all the structural parameters including the bond-lengths and bond-angles for different normal and inverse spinels. These values are in good agreement with the previously reported numerical and experimental observations [21-24,43,145]. Note that the bond angle ($\theta_{O\text{-}A\text{-}O}$) exhibits some deviation from the ideal value (109.5°) although the compound retains the global symmetry. This may be attributed to the local distortion arising from the imbalanced electronic configuration of dopant [141, 156]. Figure 3.3 shows the variation of $\Theta_{A\text{-}O\text{-}B}$ and $l_{B\text{-}O}$ as a function of ionic radius (r) of different elements. The red colored solid spheres represent the experimental data whereas the square symbols represent numerically calculated values. $\Theta_{A\text{-}O\text{-}B}$ values increase progressively with increasing r. Up to r = 0.61 Å the experimental data of $\Theta_{A\text{-}O\text{-}B}$ agrees quite well with DFT results, but for $r \geq 0.68$ Å a systematic deviation was observed ($(\Theta_{A\text{-}O\text{-}B})_{AVG} \sim 120.3°$ for r_{Ru} = 0.68 Å and $(\Theta_{A\text{-}O\text{-}B})_{AVG} \sim 122.4°$ for r_{Sn} = 0.69 Å). However, this variation is within 3%, which can be ascribed to the limitations of the generalized gradient PBE approximations. The variation of average bond-lengths $l_{B\text{-}O}$ increases with increasing r ($l_{B\text{-}O}$ =2.06 Å for r_{Ti} = 0.61 Å and $l_{B\text{-}O}$ =2.12 Å for r_{Sn} = 0.69 Å). Figure 3.4 shows the deviation in bond-angle, $\Delta\Theta = (\Theta_{A-O-B_{Co_2\Sigma O_4}} - \Theta_{A-O-B_{Co_3O_4}}) / \Theta_{A-O-B_{Co_3O_4}}$ and bond-length, $\Delta l = (l_{B-O_{Co_2\Sigma O_4}} - l_{B-O_{Co_3O_4}}) / l_{B-O_{Co_3O_4}}$ of $Co_2\Sigma O_4$ (Σ = Ge, Al, Ti, Ru, and Sn) from the pristine compound Co_3O_4. For Co_2TiO_4, the experimental data are in good agreement with the theoretical results ($\Delta\Theta \sim 1.16$). However, with the increasing size of dopants ($r \geq$ 0.68 Å) significant variation was noticed in the experimental ($\Delta\Theta_{A\text{-}O\text{-}B}$ = 2.74 for r_{Ru} = 0.68 Å and $\Theta_{A\text{-}O\text{-}B}$ = 3.65 for r_{Sn} = 0.69 Å) and theoretical ($\Delta\Theta_{A\text{-}O\text{-}B}$ = 0.37 for r_{Ru} = 0.68 Å and $\Theta_{A\text{-}O\text{-}B}$ = 1.27 for r_{Sn} = 0.69 Å) results. On

the other hand, deviations in Δl match quite well for all the compounds except for the inverse spinel Co_2TiO_4 in which a small deviation is observed between the theoretical and experimental values. Such tiny deviations in the structure leads to minor tetragonality at low temperatures in the single crystals of Co_2TiO_4 will be discussed using neutron diffraction data Chapter 5 in detail. We expect that such deviation plays a significant role on the magnetic exchange interactions and electronic properties of the material. In the following section we present the electronic structure obtained from our DFT+U calculations.

3.3.2 Electronic density of states:

In Fig. 3.5 we show the density of states for Co_3O_4, Co_2GeO_4, Co_2AlO_4, Co_2TiO_4, Co_2RuO_4, and Co_2SnO_4 for the AFM configuration with U = 2. For tetrahedral Co in Co_3O_4, a splitting in the minority spins of t_{2g} and e_g states is observed at E = 2 eV and -1.3 eV, respectively (Fig. 3.5(a)). The $e_g^{\downarrow}$ (down-spin) states (minority spins) appear to be localized around the valence band (E = -0.8 eV), while the $t_{2g}^{\downarrow}$ states are situated far away from the Fermi level in the conduction band at E ~ 2.5 eV. The up-spin states majority spins of $t_{2g}^{\uparrow}$ and $e_g^{\uparrow}$ remain isolated and appear distinctly at the energies E = -2.5 eV (Fig. 3.5(a)). However, for octahedrally coordinated Co, we obtain a low spin state (S = 0), which is quite evident from the equal contributions of the majority and minority spin states near Fermi-level. For Co_2GeO_4, we find that the $e_g^{\uparrow}$ and $e_g^{\downarrow}$ states of the tetrahedral Co exhibit peaks around -1.39 eV and -2.62 eV, respectively. On one hand, $t_{2g}^{\uparrow}$ states are localized around top of the valence band maximum (~ -0.88 eV) and the conduction band minimum (~ 1.02 eV). Interestingly, both octahedral Co ions compensate each other's contribution and exhibit stable AFM configuration in Co_2GeO_4. The contribution from Ge is quite negligible in the total density of states near the Fermi-level. The electronic states of Co_2AlO_4 appear same as those of Co_3O_4 (See Fig. 3.5(c)). The $t_{2g}^{\downarrow\uparrow}$ states of tetrahedral Co occupy the energy state of -2.4 eV and 2 eV, whereas the octahedrally coordinated Co are localized at the top of the valence band (E ~ -0.4 eV).

As we look at these details meticulously regarding the role of dilution on the density of electronic states on Co_3O_4, several interesting observations emerge. For example, in the inverse spinel Co_2TiO_4, the energy gap appears at 0.57 eV. The $t_{2g}^{\uparrow}$ states are localized away from the Fermi level around energy ~ -2.1 eV, whereas the $t_{2g}^{\downarrow}$ states are located around 1.8 eV. For the octahedrally coordinated Co, $e_g^{\uparrow}$ and $e_g^{\downarrow}$ states are localized with the energies E ~ 2.66 eV and -1.90 eV respectively, with negligible contribution and for $t_{2g}^{\downarrow\uparrow}$ states, these are centered at ~-0.9 eV ($t_{2g}^{\uparrow}$) and –2.3 eV ($t_{2g}^{\downarrow}$). Here our results indicate that t_{2g} states (~ 1.73 eV) of octahedrally coordinated Ti contribute quite significantly to the conduction band. While the e_g states appear to delocalize between -2 eV and -6 eV. Interestingly, Ru and Sn dilution result in the localization energy at -2.9 eV and -2.1 eV, respectively as compared to -2.1 eV observed in Co_2TiO_4. Thus, the energy gap decreases to 0.46 eV for Co_2RuO_4 as compared to the pristine compound and is minimum among all the spinels. This may be the reason why Co_2RuO_4 exhibits drastic reduction in long-range magnetic ordering (~16 K) as compared to 47.8 K for

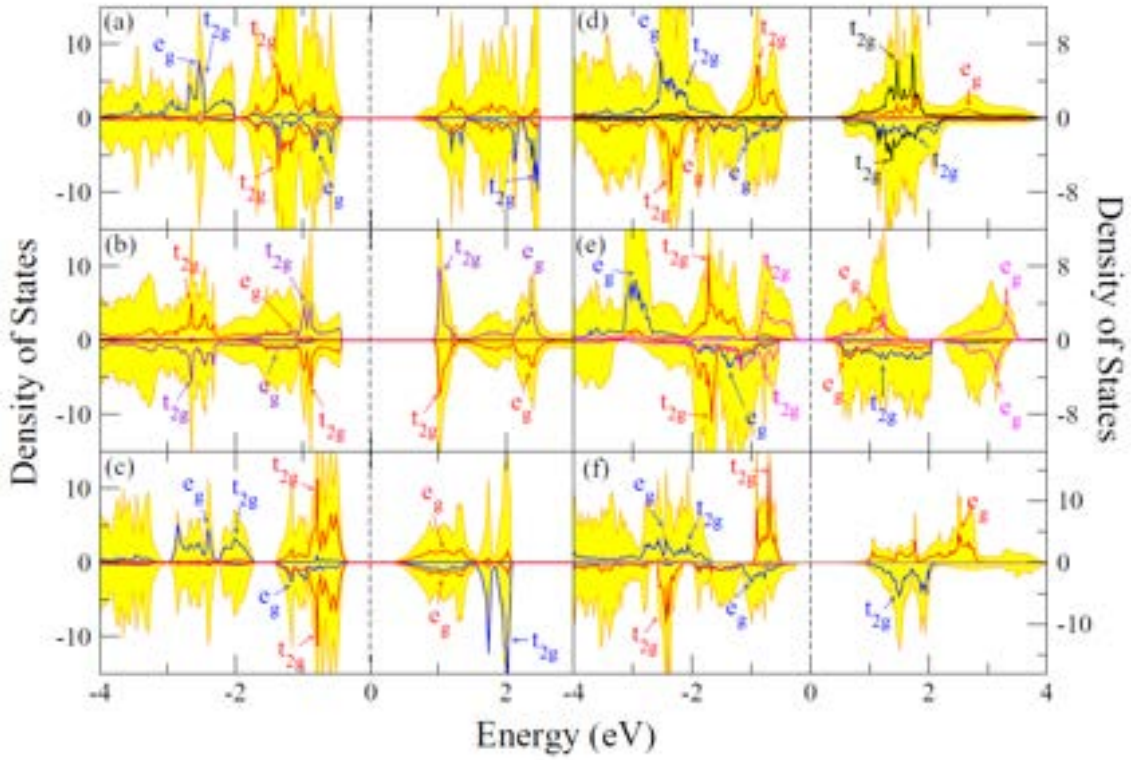

Fig. 3.5: Total and atom-projected electronic density of states calculated using U=2: (a) Co_3O_4, (b) Co_2GeO_4, (c) Co_2AlO_4, (d) Co_2TiO_4, (e) Co_2RuO_4, and (f) Co_2SnO_4. The total density of states is represented using the yellow shade. The blue and red lines represent respectively the density of states related to the Co present in the tetrahedral and octahedral sites. The color codes represent: solid black lines (Ti), magenta (Ru), brown (Sn). The solid violet line in (b) represents contribution from the other octahedral Co of Co_2GeO_4. Dotted vertical line at E = 0 depicts the Fermi-level. The partial density of states of Sn and Ge are not visible due to their small magnitude intensity.

Co_2TiO_4 and 30 K for Co_3O_4 [21,22,43,143,144]. We will discuss the magnetic properties of Co_2RuO_4 precisely in the next chapter using both ac- and dc-magnetic susceptibility. As we see the detailed electronic structure we found that $t_{2g}^{\uparrow}$ and $e_g^{\uparrow}$ states of tetrahedrally coordinated Co are localized around -2.9 eV, whereas, the down-spin states of $t_{2g}^{\downarrow}$ appear to be completely delocalized from the minimum of the conduction band (exhibiting a peak around the energy 1.3 eV as shown in Fig. 3.5(e)). For the octahedrally coordinated Co, the majority and minority spins of t_{2g} states are more symmetric as compared to the e_g states which lead to the low spin state. On the other hand, the t_{2g} states of the octahedrally coordinated Ru appear to localize at the vicinity of the valence band maximum (~ -0.8 eV), and the corresponding e_g states are located quite far-away from the Fermi level (~ 3.2 eV).

Fig. 3.5(f) shows the contribution of electronics states across the Fermi level for Co_2SnO_4 indicating the narrow down of the overall energy gap (≥ 0.7 eV) as compared to the pristine compound Co_3O_4. As far as the electronic state contributions are concerned at the octahedral and tetrahedral sites we found that in $t_{2g}^{\downarrow}$ and $e_g^{\uparrow}$ states split around 1.7 eV and -2.5 eV, respectively for Co atoms located at the tetrahedral sites. A detailed

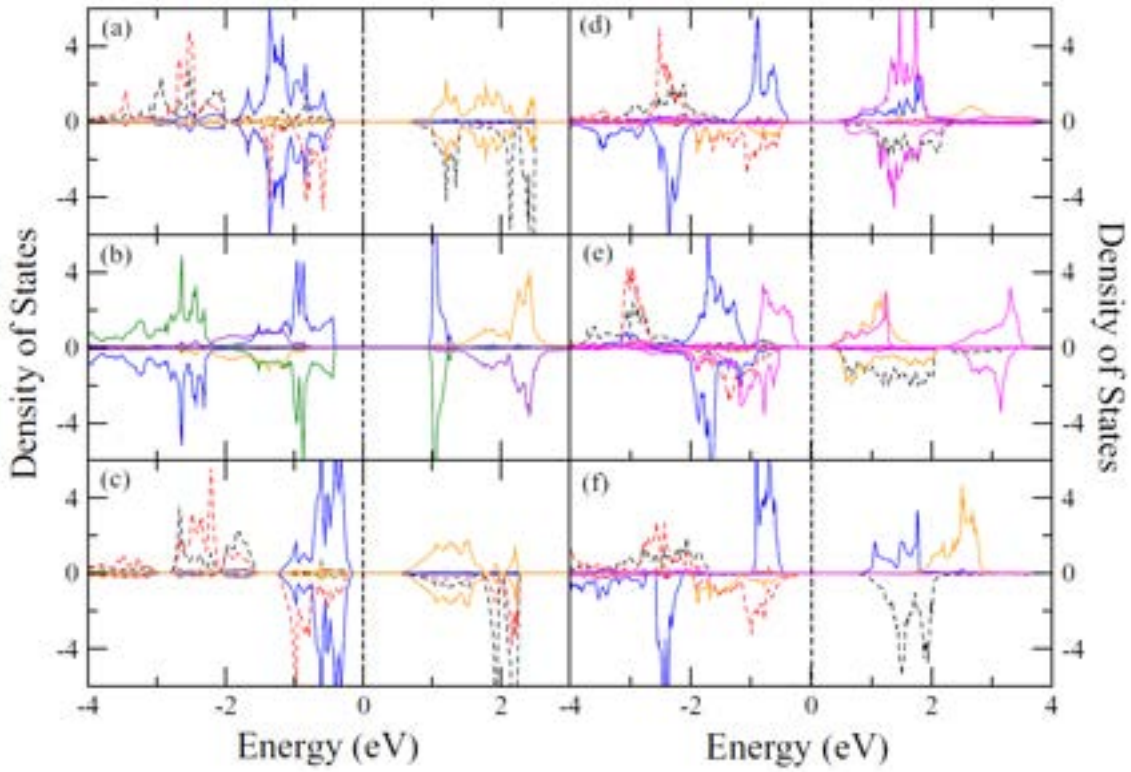

Fig. 3.6: Atom-projected electronic density of states calculated using U=2: (a) Co_3O_4, (b) Co_2GeO_4, (c) Co_2AlO_4, (d) Co_2TiO_4, (e) Co_2RuO_4, and (f) Co_2SnO_4. For tetrahedral Co, the black and red dotted lines represent the density of t_{2g} and e_g states, respectively. For octahedral Co, the blue and orange solid lines represent the density of t_{2g} and e_g states, respectively. In case of Co_2GeO_4, the density of t_{2g} and e_g states of second octahedral Co is denoted by solid green and violet line, respectively. The solid magenta line represents the density of states of dilutants $\Sigma \equiv$ Ge, Ti, Ru and Sn. Dotted vertical line at E = 0 depicts the Fermi-level. The partial density of states of Sn and Ge are not visible due to their lower intensity.

Table 3.3: Exchange splitting (Δ_{EX}) and crystal field splitting (Δ_{CF}) for Co_3O_4 and $Co_2\Sigma O_4$ (Σ=Ge, Al, Ti, Ru, Sn) for U =2 in eV units.

System	Ion	Tetrahedral site (in eV units)				Ion	Octahedral site (in eV units)			
		$\Delta_{EX}^{e_g}$	$\Delta_{EX}^{t_{2g}}$	$\Delta_{CF}^{\downarrow}$	$\Delta_{CF}^{\uparrow}$		$\Delta_{EX}^{e_g}$	$\Delta_{EX}^{t_{2g}}$	$\Delta_{CF}^{\downarrow}$	$\Delta_{CF}^{\uparrow}$
Co_3O_4	Co^{2+}	1.8	5.2	3.3	0.1	Co^{3+}	0.0	0.0	2.5	2.5
Co_2GeO_4	Ge^{4+}	-	-	-	-	Co^{2+}	3.8	1.7	1.2	3.3
						Co^{2+}	3.6	1.8	1.5	3.8
Co_2AlO_4	Co^{2+}	1.3	4.9	3.2	0.4	Co^{3+}	0.0	0.0	1.8	1.8
Co_2TiO_4	Co^{2+}	1.5	3.9	2.8	0.4	Co^{2+}	4.6	1.5	0.5	3.6
						Ti^{4+}	0.9	0.1	6.4	7.3
Co_2RuO_4	Co^{2+}	1.7	4.2	2.6	0.1	Co^{3+}	0.5	0.1	2.3	2.9
						Ru^{3+}	0.2	0.0	3.9	4.1
Co_2SnO_4	Co^{2+}	1.6	3.6	2.5	0.5	Co^{2+}	4.4	1.7	0.6	3.2

interpretation of this result provides the evidence that the $t_{2g}^{\uparrow}$ states are localized at -2.1 eV, whereas the $e_g^{\uparrow}$ and $e_g^{\downarrow}$ states are localized at -2.5 eV and -1.0 eV, respectively. Nevertheless, the octahedral coordinated Co-ion does

not show any signature of splitting of the bands (as shown in Fig. 3.5(f)). Here the $e_g^{\uparrow}$ states are more delocalized as compared to the $e_g^{\downarrow}$ states (-1.8 eV). For octahedrally coordinated Sn, the t_{2g} states hardly contribute to the total density of states near the Fermi-level. Note that partial density of states for Ge and Sn are not visible due to their lower intensity (±0.05 states/eV for Ge and ±0.3 states/eV for Sn) compared to the other cations.

Overall, we find that the doping has important consequences on the electronic structure of the cobalt spinels. It is quite evident from our study that Co_3O_4 exhibits strong hybridization between the majority spins in $t_{2g}^{\uparrow}$ and $e_g^{\uparrow}$ states (see Fig. 3.6) [157]. This hybridization becomes weaker for diluted compounds except for Co_2RuO_4 which exhibits identical hybridization strength as that of undoped Co_3O_4. Another important feature we noticed was the overlapping of the minority spins at t_{2g} and e_g in the vicinity of valence band of Co_3O_4 which become quite feeble for Co_2RuO_4 and Co_2AlO_4, due to the reduction of a Co atom at the octahedral sites. It is interesting to note that this hybridization is not at all present in Co_2TiO_4 and Co_2SnO_4, as the octahedrally coordinated Co possesses different electronic states (see Fig. 3.1). The hybridization of $t_{2g}^{\uparrow}$ and $e_g^{\uparrow}$ states at the octahedral Co site is also observed in Co_3O_4 which remains absent for the diluted systems Co_2AlO_4 and Co_2RuO_4. Nevertheless, in Co_2TiO_4 and Co_2SnO_4 we observe a weaker hybridization of down spins of Co e_g states occupying the tetrahedral and octahedral sites. At this stage we wish to compare the effect of dilution on the exchange and crystal field splitting of all the inverse spinels. We have calculated the exchange splitting (Δ_{EX}) and crystal field splitting (Δ_{CF}) from the density of states of the materials as: (*a*) $\Delta_{EX}^{e_g} = e_{g\uparrow} - e_{g\downarrow}$, (*b*) $\Delta_{EX}^{t_{2g}} = t_{2g\uparrow} - t_{2g\downarrow}$, (*c*)$\Delta_{CF}^{\uparrow} = e_{g\uparrow} - t_{2g\uparrow}$, and (*d*) $\Delta_{CF}^{\downarrow} = e_{g\downarrow} - t_{2g\downarrow}$. Accordingly, Table 3.3 summarizes the exchange splitting (Δ_{EX}) and crystal field splitting (Δ_{CF}) parameters for the pristine and diluted spinels (for U = 2) in which Co^{2+} ions occupy the tetrahedral site only for all the compounds, except Co_2GeO_4 where Ge^{4+} occupies the tetrahedral sites. The magnitude of $\Delta_{EX}^{e_g}$ remains nearly constant for all the compounds and $\Delta_{EX}^{t_{2g}}$ gradually decreases upon increasing the lattice parameter varying up to 3.6 eV for Co_2SnO_4 (a = 8.79 Å), except Co_2GeO_4 (r_{Ge} = 0.39 Å). In the present case for the normal spinel Co_3O_4 the calculated values of $\Delta_{EX}^{e_g}$ and $\Delta_{EX}^{t_{2g}}$ are 1.8 eV and 5.2 eV, respectively. The crystal field splitting (Δ_{CF}) changes drastically with increasing the size (r) of the diluting ions: the crystal field splitting for the down-spins ($\Delta_{CF}^{\downarrow}$) decreases from 3.34 eV (for r_{Co} = 0.55 Å) to 2.5 eV (r_{Sn} = 0.69 Å). The magnitude of up-spin crystal field ($\Delta_{CF}^{\uparrow}$) does not display a clear trend. For Co_3O_4 and Co_2RuO_4 the splitting values are relatively small (~ 0.1 eV) compared to the other compounds, Co_2TiO_4 ($\Delta_{CF}^{\uparrow} = 0.4$ eV) and Co_2SnO_4 ($\Delta_{CF}^{\uparrow}$ =0.5 eV). The Co^{3+} ions located in the octahedral crystal field do not exhibit any exchange splitting owing to its low-spin configuration. On the other hand, for octahedral Co^{3+} we observed $\Delta_{EX}^{e_g}$ = 0.5 eV and $\Delta_{EX}^{t_{2g}}$ = 0.1 eV in the Co_2RuO_4. This implies that the crystal field splitting does not change significantly by the substituting of Co^{3+} by Ru^{3+} at octahedral sites. For Co_2TiO_4, Co_2SnO_4 and Co_2GeO_4 the magnitudes of $\Delta_{CF}^{\uparrow}$ and $\Delta_{CF}^{\downarrow}$ are nearly identical (see Table 3.3).

3.3.3 Magnetic structure:

In this section we will analyze the magnetic properties of all the investigated systems using both experimental methods as well as theoretical calculations in consonance with the electronic structure and density of states as discussed above. In Table 3.4 we have enlisted the magnetic moment of cations in the tetrahedral (μ_{tet}), octahedral (μ_{oct}) sites together with the total moment (μ_{Total}) for different values of U. The unequal and opposite moment of Co in both A- and B-sites, signifies the ferrimagnetic configuration. The magnetic moments corresponding to tetrahedral and octahedral sites increase with the increasing value of U. For all the six compounds, Co^{2+} occupies tetrahedral site with a high-spin configuration ($e_g^4 t_{2g}^3$). As a result of these three unpaired electrons contribute to the total magnetic moment at the tetrahedral sites yielding magnetic moment of the order of $3\mu_B$. Our calculations yield the moment μ_{tet} between 2.53 μ_B and 2.8 μ_B for U = 2 and 6, respectively and these results are in good agreement with previous numerical studies by Walsh *et al*. [145].

As we discussed in the previous section the total density of states shows nearly equal contribution from up and down-spin states near Fermi-level which implies zero net magnetic moment. The only exception is the inverse spinel with Ru dilution. This anomaly can be attributed to the presence of trivalent electronic state of Ru ions at the octahedral sites of the spinel lattice. For Ru^{3+} the magnetic moment is $0.77\mu_B$ at the octahedral site while the total magnetic moment is 1.92 μ_B (a detailed H-T phase diagram will be discussed later in next Chapter 4). The corresponding magnetic moments for different values of U are listed in Table 3.4. Notably, recent experimental observations suggest the formation of trivalent electronic state of Ti instead of tetravalent oxidation state usually expected at the octahedral sites of inverse spinel Co_2TiO_4. Nevertheless, in our *ab intio* simulations the cubic structure is more stable for the tetravalent electronic state of Ti. The experimental observations are mainly based on the X-ray photoelectron spectroscopy measurements performed at 300 K (which is much higher than the long-range magnetic ordering considered at the DFT level) under high vacuum conditions [149].

In the case of cobalt orthostannate, Co and Sn remain in divalent and tetravalent electronic configurations in the octahedral site, respectively. These results are consistent with the recent experimental studies where the divalent and tetravalent electronic configuration of Co and Sn are supported from the X-ray photoelectron spectroscopic observations [23,24,140,149]. However, the computed magnetic moment (2.6 μ_B) which is lower by ~37.55% owing to the fact that DFT simulations are carried out at 0 K while the experimental studies are performed at finite temperatures above T_N [21-24,43,149]. Usually, the trivalent Co exhibits a low spin configuration state for Ru diluted spinel, obtaining a magnetic moment of $0.1\mu_B$. It is interesting to note that as we increase the Coulomb parameter to U = 6 for Co_2RuO_4, the magnetic moment of octahedral Co^{3+} increases and turns out to be $0.89\mu_B$. Likewise, cobalt orthogermanate, Co_2GeO_4 both the divalent Co in the octahedral sites exhibits an opposite magnetic moment of $2.60\mu_B$, whereas, Ge obtains a non-magnetic tetravalent configuration.

Table 3.4: The magnetic moment of tetrahedral (μ_{tet}) and octahedral (μ_{oct}) cations and the total moment (μ_{Total}). All the magnetic moments are calculated in Bohr magneton unit. Experimental values obtained from the previously reported neutron diffraction studies are given in square brackets.

U (eV)	System	Tetrahedral A-site	μ_{tet}	Octahedral B-site	μ_{oct}	μ_{Total}
2.0	Co_3O_4	Co^{2+}	2.53	Co^{3+}	0.0	0.0
	Co_2GeO_4	Ge^{4+}	0.0	Co^{2+}/Co^{2+}	-2.64/2.64	0.0
	Co_2AlO_4	Co^{2+}	2.60	Co^{3+}	0.0	0.0
	Co_2TiO_4	Co^{2+}	2.58	Co^{2+}/Ti^{4+}	-2.61/0.05	-0.035
	Co_2RuO_4	Co^{2+}	2.54	Co^{3+}/Ru^{3+}	0.1/-0.84	1.91
	Co_2SnO_4	Co^{2+}	2.61	Co^{2+}/Sn^{4+}	-2.62/0.03	-0.032
3.0	Co_3O_4	Co^{2+}	2.61	Co^{3+}	0.0	0.0
	Co_2GeO_4	Ge^{4+}	0.0	Co^{2+}/Co^{2+}	-2.69/2.69	0.0
	Co_2AlO_4	Co^{2+}	2.66	Co^{3+}	0.0	0.0
	Co_2TiO_4	Co^{2+}	2.65	Co^{2+}/Ti^{4+}	-2.66/0.05	-0.035
	Co_2RuO_4	Co^{2+}	2.61	Co^{3+}/Ru^{3+}	0.12/-0.87	1.92
	Co_2SnO_4	Co^{2+}	2.67	Co^{2+}/Sn^{4+}	-2.68/0.03	-0.032
4.0	Co_3O_4	Co^{2+}	2.68	Co^{3+}	0.0	0.0
	Co_2GeO_4	Ge^{4+}	0.0	Co^{2+}/Co^{2+}	-2.74/2.74	0.0
	Co_2AlO_4	Co^{2+}	2.71	Co^{3+}	0.0	0.0
	Co_2TiO_4	Co^{2+}	2.70	Co^{2+}/Ti^{4+}	-2.71/0.04	-0.030
	Co_2RuO_4	Co^{2+}	2.67	Co^{3+}/Ru^{3+}	0.14/-0.89	1.94
	Co_2SnO_4	Co^{2+}	2.72	Co^{2+}/Sn^{4+}	-2.73/0.02	-0.028
5.0	Co_3O_4	Co^{2+}	2.73	Co^{3+}	0.0	0.0
	Co_2GeO_4	Ge^{4+}	0.0	Co^{2+}/Co^{2+}	-2.78/2.78	0.0
	Co_2AlO_4	Co^{2+}	2.75	Co^{3+}	0.0	0.0
	Co_2TiO_4	Co^{2+}	2.75	Co^{2+}/Ti^{4+}	-2.75/0.04	-0.028
	Co_2RuO_4	Co^{2+}	2.72	Co^{3+}/Ru^{3+}	0.2/-0.92	1.94
	Co_2SnO_4	Co^{2+}	2.76	Co^{2+}/Sn^{4+}	-2.77/0.02	-0.027
6.0	Co_3O_4	Co^{2+}	2.78	Co^{3+}	0.0	0.0
	Co_2GeO_4	Ge^{4+}	0.0	Co^{2+}/Co^{2+}	-2.74/2.74 [3.02]	0.0
	Co_2AlO_4	Co^{2+}	2.78	Co^{3+}	0.0	0.0
	Co_2TiO_4	Co^{2+}	2.76 [2.11]	Co^{2+}/Ti^{4+}	-2.71/0.04 [2.89/0.72]	-0.030
	Co_2RuO_4	Co^{2+}	2.67	Co^{3+}/Ru^{3+}	0.14/-0.89 [-/1.73]	1.94
	Co_2SnO_4	Co^{2+}	2.72 [2.04]	Co^{2+}/Sn^{4+}	-2.73/0.02 [2.57/-]	-0.028

We performed the magnetization measurements at different temperatures in order to probe the effect of dilution on the magnetic ordering temperature of Co_3O_4. In what follows we present a systematic analysis of these experimental observation. Figure 3.7(a-f) show the temperature dependence of magnetization M(T) recorded under both zero-field-cooled (ZFC) and field-cooled (FC) conditions. The data have been recorded while heating with an external dc-magnetic field H_{DC} of 500 Oe. In the case of undoped Co_3O_4, both the magnetization curves $M_{ZFC}(T)$ and $M_{FC}(T)$ exhibit peak at 38 K (Fig. 3.7(a)) indicating the AFM ordering below this temperature and paramagnetic behavior above. It is well known that the magnetic moment in Co_3O_4 arises due to the divalent Co

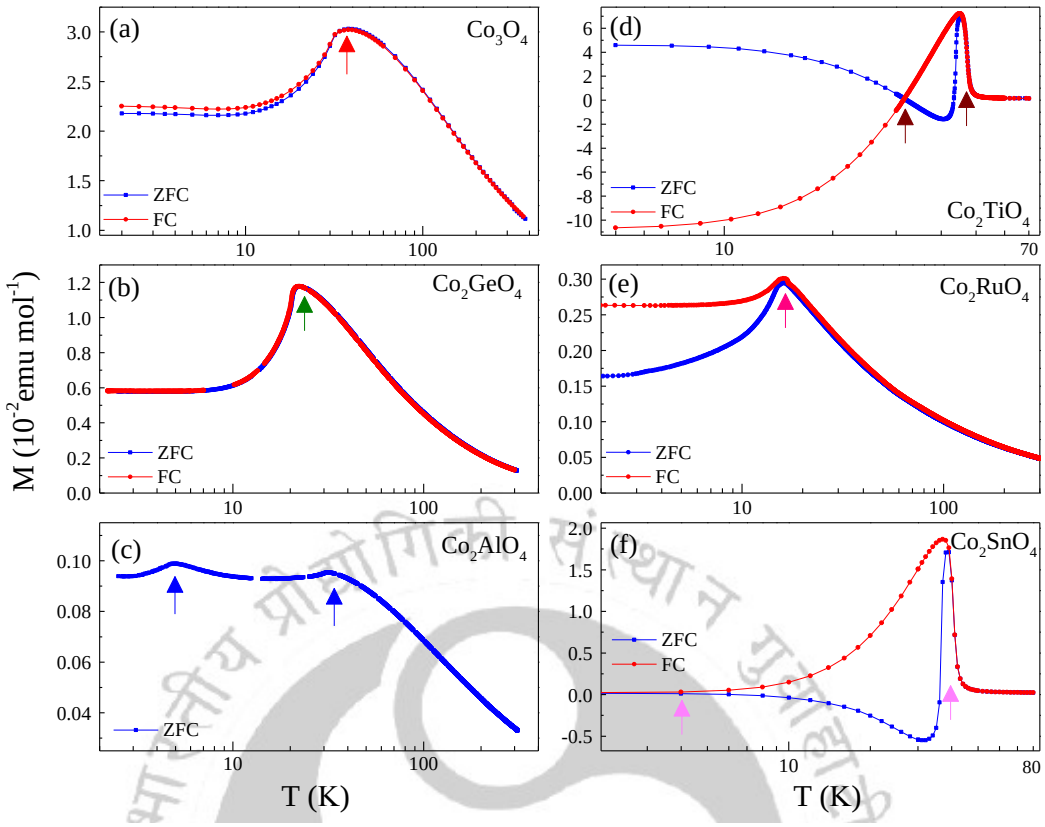

Fig. 3.7: The temperature dependence of magnetization measured zero-field-cooled (ZFC) and field- cooled (FC) (H_{dc} = 500 Oe) conditions for (a) Co_3O_4, (b) Co_2GeO_4, (c) Co_2AlO_4, (d) Co_2TiO_4, (e) Co_2RuO_4, and (f) Co_2SnO_4.

ions ($e_g^4 t_{2g}^3$), and negligible contribution from the spin-orbit coupling [87,143,144]. Whereas, trivalent Co ions do not possess any permanent magnetic moment owing to the splitting of 3*d* levels by the octahedral crystal field and complete filling of t_{2g} levels. For this case the AFM Néel temperature T_N (= 30 K) is estimated form the differential susceptibility curve $\partial(\chi T)/\partial T$ ($\chi = M_{ZFC}/H$) which is in good agreement with the previous experimental observations [143,158]. Almost similar features have been observed in the case of Ge diluted system (Co_2GeO_4) except the T_N = 20.4 K (Fig. 3.7(b)) which is in good agreement with the results of Hubsch and Gavoille who reported T_N = 20.25 K [148]. On the other hand, dilution of Co_3O_4 with Al shifts T_N significantly towards the lower temperatures ~ 4.8 K. It is interesting to notice that Co_2TiO_4 exhibits completely different behavior with giant bifurcation between M_{ZFC} and M_{FC} below the FiM ordering temperature 47.8 K, as shown by the arrow in Fig. 3.7(d). Such FiM ordering is arising due to unequal magnetic moments of divalent Co ions at the tetrahedral A sites and octahedral B sites. Below this T_{FN} magnetization curves display compensation behavior (T_{COMP} ~ 31.6 K) where the two sub-lattices balance with each other. However, such compensation effect is very feeble which occurs at very low temperatures (~ 4 K) in case of Co_2SnO_4 (Fig. 3.7(f)). This system also shows FiM ordering at 41 K which is in-line with the recent experimental reports [23,24]. However, a completely distinct magnetic behavior was noticed in the case of Co_2RuO_4 where the long-range ordering was collapsed and glassy signatures were evident below 16 K consistent with the previous reports [21]. A detailed analysis of the magnetic

behavior of Co_2RuO_4 along with the H-T phase diagram will be discussed in the next chapter.

In the coming sections we focus on the pairwise magnetic exchange interactions in all the investigated systems. For this we first compute the magnetic exchange parameters by mapping DFT+U total energies onto a Heisenberg Hamiltonian [150,159]. The contribution of the magnetic moment in Co_3O_4 is due to high spin state of tetrahedral Co^{2+}. We calculated the exchange coupling parameter (J_{ij}) using the Heisenberg spin Hamiltonian (see Eq. 1.19): $H = -\sum_{ij} J_{ij} \boldsymbol{S}_i \cdot \boldsymbol{S}_j$, where i and j denote the nearest neighbor sites. The results are given in Table 3.5. We find that the three exchange parameters ($J_{A\text{-}A}$, $J_{B\text{-}B}$, $J_{A\text{-}B}$) are all AFM with only one exception of Co_2SnO_4. With the dilution of Ti (r = 0.61 Å) we observe a decrease in the strength (~ −0.842 meV) of A-A interactions. Interestingly, we observe a huge increase in the coupling strength as one goes from Co_3O_4 to Co_2RuO_4 ($J_{A\text{-}A}$ = −14.211 meV). However, diluting with tetravalent Sn in the pristine compound results dominant ferromagnetic A-A interactions with a strength of 6.4 meV.

The coupling strength $J_{B\text{-}B}$ for Co_2SnO_4 and Co_2TiO_4 is −2.13 meV and −2.57 meV, respectively. In case of Co_2RuO_4, the coupling strength increases to −7.11 meV due to the trivalent Ru ions of magnetic moment ~ $0.9\mu_B$. Such increase of magnetic moment can be attributed to the availability of unfilled spins in t_{2g} states. The exchange coupling $J_{A\text{-}B}$ increases with increasing the size of dilutants (e.g. $J_{A\text{-}B}$ = −1.50 meV for Co_2TiO_4 and $J_{A\text{-}B}$ = −2.66 meV for Co_2RuO_4). For Co_2SnO_4, $J_{A\text{-}B}$ displays the weakest coupling strength of 0.17 meV with ferrimagnetic A-B coupling. Among all the dilutants, Co_2RuO_4 possesses strong AFM couplings between A-A (−14.21 meV), B-B (−7.11 meV) and A-B (−2.66 meV) sites. Such large interactions between the spins occur due to the larger crystal field splitting of Ru^{3+} than Co^{2+} (see Table 3.3) further resulting very high anisotropy which is quite evident from the experimental data (Fig. 3.7). Moreover, from the electronic configuration we noticed that trivalent Ru exhibits half-filled d states on B sites (d^5), whereas divalent Co exhibits unfilled d states on A site (d^7). As a result of this, the A-B coupling strength becomes prominent in Co_2RuO_4. The exchange interaction $J_{A\text{-}B}$ also exhibits increasing trend for Co_2TiO_4 to Co_2RuO_4. This feature can be understood from the point of view of the reduction of the bond-length between the A and B cations from 3.50 Å to 3.42 Å for Co_2TiO_4 and Co_2RuO_4, respectively. As we compare our calculated results with the neutron diffraction results reported earlier we find a good consistency. Whereas, the Ge system exhibits $\mu_{\mathrm{Co-oct}} \sim 3.02\mu_B$ (1.6 K) close to the

Table 3.5: Calculated magnetic exchange parameters (J_{ij} in meV) of Co_3O_4 and $Co_2\Sigma O_4$ ($\Sigma \equiv$ Ge, Al, Ti, Ru, Sn) for U = 2.0 eV. In the parentheses corresponding experimental values are mentioned.

System	$J_{A\text{-}A}$	$J_{B\text{-}B}$	$J_{A\text{-}B}$
Co_3O_4	-1.73 (0.65)	0.0 (0.0)	0.0 (0.0)
Co_2GeO_4	0.0	-22.31	0.0
Co_2AlO_4	-1.33	0.0	0.0
Co_2TiO_4	-0.84 (-0.53)	-2.57 (-0.39)	-1.50 (-0.44)
Co_2RuO_4	-14.21	-7.11	-2.66
Co_2SnO_4	6.4 (0.34)	-2.13 (0.45)	0.17 (0.36)

calculated value 2.81μ_B [160]. On the other hand, the Ru diluted system exhibits magnetic moment ~ 1.73μ_B at 4 K for Ru^{3+}, which is close to the calculated values (~1.53μ_B) [21]. The exchange interaction between the cations located at tetrahedral sites $J_{A\text{-}A}$ exhibits strong coupling that corroborates the current numerical results (Table 3.5) [21].

3.3.4 Electronic band-gap:

In this section we focus our studies on the energy band structure of all the spinels which will be interpreted based on our experimental data related to the optical absorption performed using the diffusive reflectance spectroscopy. First, we discuss our computational results obtained for different U. Figure 3.8 shows the electronic band structure calculated along different high symmetry directions in the reciprocal space for U = 2 for different spinels. In Co_3O_4 the octahedral Co 3*d* states are mainly contributing to the conduction band, whereas the valence band maxima are supported by both tetrahedral Co 3*d* and O 2*p* states. Since Γ and X are high symmetry points, they contribute to the valence and conduction band. Here we restrict our discussion to the energy band-gap displayed at high symmetry points Γ and X. The direct Γ-Γ and X-X, and the indirect Γ-X energy band gaps are enlisted in the Table 3.6 for the compounds for different values of U.

In case of the normal spinel Co_3O_4 (for U = 2) the energy gap at Γ-Γ and X-X turns out to be 2.33 eV and 1.02 eV, respectively, whereas the indirect band gap at Γ-X is 1.57 eV. These values increase with increasing U. For instance, the gap at Γ-Γ increases to 3.76 eV and 2.70 eV at X-X for U = 6. These band gaps calculated for the symmetry point X-X at U = 2 and 3, agree quite well with the previously reported results (E_g = 1.5-2.5 eV) [150-154,161]. It should be noted that for U values between 4 and 6 the gap appears with a higher magnitude than those previously reported theoretical values [145,150-154]. For U = 2 the direct Γ-Γ band gap exhibits

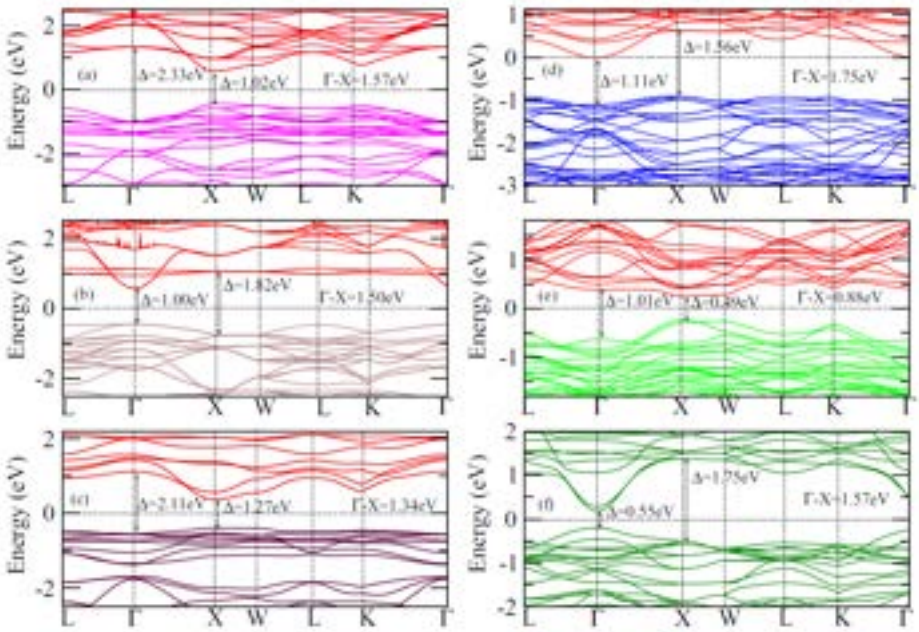

Fig. 3.8: Band structure is calculated using U=2: (a) Co_3O_4, (b) Co_2GeO_4, (c) Co_2AlO_4, (d) Co_2TiO_4, (e) Co_2RuO_4, and (f) Co_2SnO_4 and plotted with the symmetry points in the reciprocal lattice.

decreasing trend (e.g. Γ-$\Gamma_{Co_2TiO_4}$= 1.11 eV, Γ-$\Gamma_{Co_2RuO_4}$= 1.02eV and Γ-$\Gamma_{Co_2SnO_4}$= 0.55 eV) with the increasing size of the dilutants. For example, E_g X-X = 1.56 eV and 1.75 eV for Co_2TiO_4 and Co_2SnO_4, respectively. However, for Co_2GeO_4 we find the direct Γ-Γ and X-X band gaps of 1.0 eV and 1.82 eV, respectively, for U = 2, despite Ge has the lowest ionic radius among the dopants (i.e., r ~ 0. 39 Å). The observed band gaps for Co_2GeO_4 appear to be closer to Co_2SnO_4 which may occur due to identical valence electronic structure of *d* orbitals in Ge^{4+} ($3d^{10}$) and Sn^{4+} ($4d^{10}$). Interestingly, with the incorporation of Ru (r ~ 0.68 Å) the gap at symmetry points (X-X) happens to be lowest as compared to the remaining inverse spinels (0.48 eV). For Co_2RuO_4 the band gap at Γ-Γ symmetry points remains nearly equal upon increasing U (Γ-Γ = 1.02 eV and 1.15 eV for U=2.0 eV and 6.0 eV, respectively) except for U ≥ 6.0 an anomalous trend was noticed (Tables 3.6, 3.7). In order to probe the role of the *d*-orbital electrons and their correlations in Ru diluted compound on the band gap at the symmetry points Γ-Γ, X-X and Γ-X transitions we varied the magnitude of U for Ru from 2 to 6

Table 3.6: The calculated direct Γ-Γ and X-X, and indirect Γ-X transitions of different Co based spinel for different value of U.

U (eV)		2.0	3.0	4.0	5.0	6.0
Co_3O_4	Γ-Γ	2.33	2.92	3.39	3.62	3.76
	X-X	1.02	1.46	1.89	2.33	2.70
	Γ-X	1.57	2.09	2.52	2.73	2.85
Co_2GeO_4	Γ-Γ	1.00	1.39	1.74	1.95	2.09
	X-X	1.82	2.60	3.28	3.74	4.13
	Γ-X	1.50	2.28	2.98	3.53	3.91
Co_2AlO_4	Γ-Γ	2.11	2.59	3.03	3.23	3.41
	X-X	1.27	1.75	2.21	2.53	2.83
	Γ-X	1.34	1.81	2.23	2.44	2.64
Co_2TiO_4	Γ-Γ	1.11	1.45	1.71	1.92	2.06
	X-X	1.56	1.94	2.25	2.50	2.68
	Γ-X	1.34	2.11	2.42	2.68	2.85
Co_2RuO_4	Γ-Γ	1.01	1.07	1.11	1.15	0.89
	X-X	0.49	0.50	0.49	0.44	0.97
	Γ-X	0.88	0.92	0.95	094	1.30
Co_2SnO_4	Γ-Γ	0.55	0.59	0.79	1.05	1.17
	X-X	1.75	2.39	2.91	3.41	3.89
	Γ-X	1.57	2.00	2.48	3.07	3.46

Table 3.7: The calculated direct Γ-Γ and X-X, and indirect Γ-X transitions of Co_2RuO_4 for different value of U.

U (eV)		2.0	3.0	4.0	5.0	6.0
U fixed for Ru	Γ-Γ	1.01	1.07	1.11	1.15	0.89
	X-X	0.49	0.50	0.49	0.44	0.97
	Γ-X	0.88	0.92	0.95	0.94	1.30
U fixed for Co	Γ-Γ	1.01	1.48	1.68	1.65	1.74
	X-X	0.49	0.82	1.08	1.23	1.43
	Γ-X	0.88	1.34	1.58	1.60	1.66

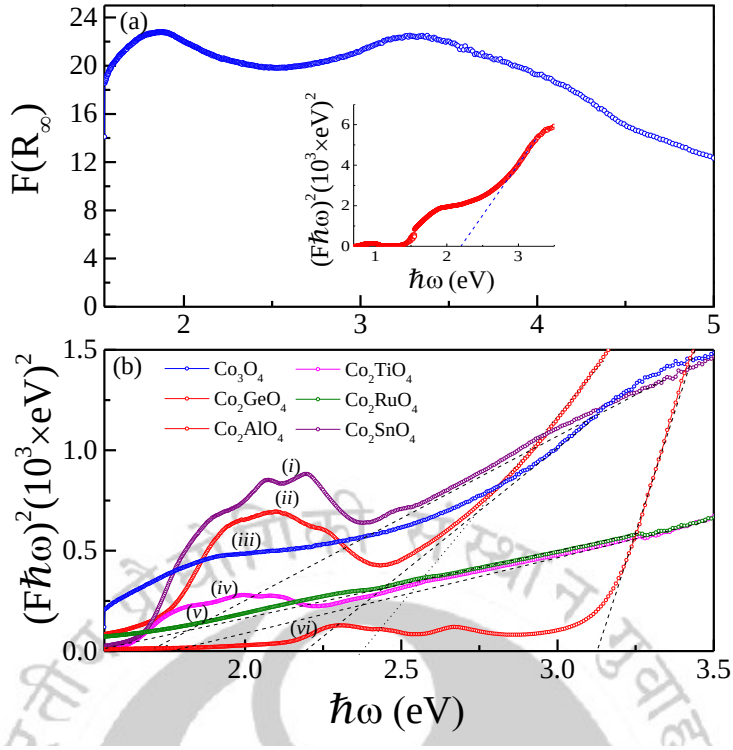

Fig. 3.9: (a) Experimental F(R_∞) vs photon energy $\hbar\omega$ for Co_3O_4. The inset shows the plot of $[F(R_\infty)\hbar\omega]^2$ aganist the photon energy $\hbar\omega$. (b) $[F(R_\infty)\hbar\omega]^2$ is plotted as a function of $\hbar\omega$ for Co_3O_4 and $Co_2\Sigma O_4$ ($\Sigma \equiv$ Ge, Al, Ti, Ru, Sn). The solid lines are the extrapolation of the linear region to determine the optical band-gap E_g.

while keeping fixed value of U of Co at 2. These computed data are listed in Table 3.7. Accordingly, we noticed a systematic increasing trend of Γ-Γ and X-X band gap (Γ-$\Gamma_{U=3.0}$=1.48 eV and Γ-$\Gamma_{U=6.0}$=1.74 eV; X-$X_{U=3.0}$=0.82 eV and X-$X_{U=6.0}$=1.43 eV) with increasing the magnitude of U of Ru. This interesting observation reveals that the vital role of strong electronic correlations in *d*-orbital of Ru in determining the overall band-gap characteristics. Unlike other compounds where we varied only the U values of Co ions while keeping fixed values of U for dilutants Ge, Al, Ti, and Sn. The U values in Co_2RuO_4 needed to be varied for both Co as well as Ru.

We performed the room temperature optical absorbance measurements using the diffuse reflectance spectroscopy (DRS) in UV visible and near IR range. For a precise determination of optical band-gap E_g we used the experimentally obtained reflectance data and employed the Kubelka-Munk (K-M) analysis [162]. It is well known that for a parabolic shaped band structure, the K-M equation can be expressed in terms of energy of a single photon $\hbar\omega$, the band-gap of the system E_g (eV) and remission function or K-M function $F(R_\infty)$ as:

$$[F(R_\infty)\hbar\omega]^2 = \alpha(\hbar\omega - E_g) \quad (3.1)$$

In the above equation α is a constant (absorption coefficient). Figure 3.9(a) shows the variation of $F(R_\infty)$ as a function of photon energy ($\hbar\omega$) (eV) for the undiluted Co_3O_4 normal-spinel. The inset of Fig. 3.9(a) represents its corresponding modulation function $[F(R_\infty)\hbar\omega]^2$ plotted as a function of $\hbar\omega$. Extrapolation of the band tail

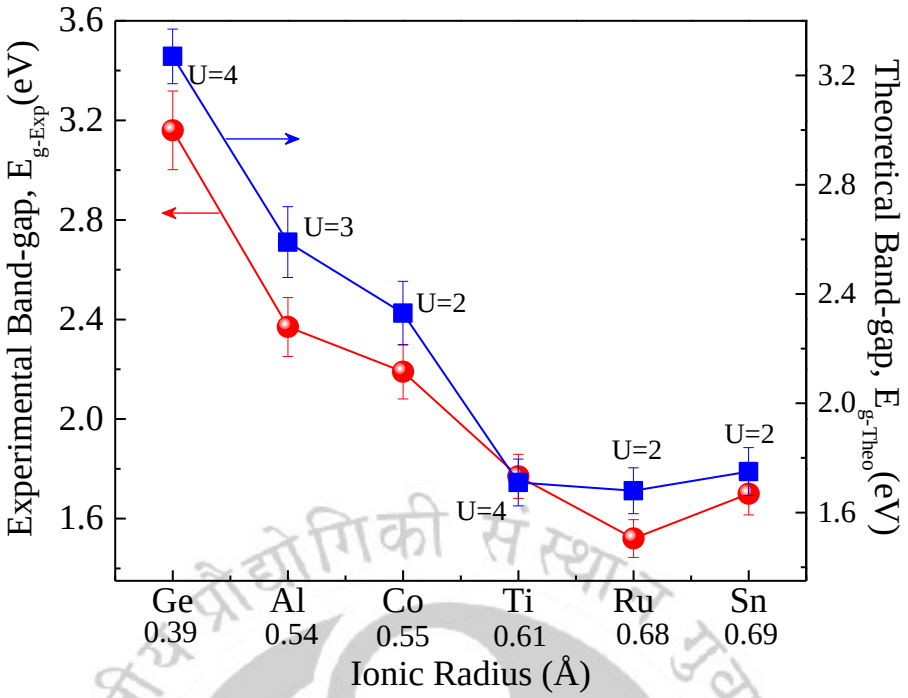

Fig. 3.10: The band gaps (Eg) as a function of ionic radius of the dilutants. The right panel shows the experimental band-gap ($E_{g\text{-}Exp}$) and the left panel indicates the theoretical band-gap ($E_{g\text{-}Theo}$) Values of U_{Co} (as indicated in the figure) are chosen to obtain the theoretical result closure to the experimental observation.

(as shown by the dotted lines) intercepts the *x*-axis at $\hbar\omega$ = 2.19 eV which corresponds to the direct band gap of the system which is consistent with the previously reported values for the bulk Co_3O_4 system [140,161]. Similar analysis has been performed to determine the E_g of diluted systems (Fig. 3.9(b)). The left-hand-side scale of Fig. 3.10 shows the corresponding E_g values obtained for different diluting elements and is plotted as a function of their ionic radius (0.39 Å(Ge) ≤ r ≤ 0.69 Å(Sn)). We compared the experimentally obtained bandgap $E_{g\text{-}Exp}$ with E_g values obtained from the DFT calculations ($E_{g\text{-}Theo}$) which was plotted on the right-hand-side scale of Fig. 3.10. Both the experimental and calculated results are consistent with each other till r ≤ 0.68Å (Co_2RuO_4). An overall decreasing trend has been observed in the E_g values with increasing the size of diluting element. For pristine compound Co_3O_4, experimentally obtained band-gap is 2.19 eV which is quite near to the calculated value 2.33 eV. The theoretical and experimentally obtained band gaps for Co_2GeO_4 are respectively 3.28 eV and 3.16 eV, whereas, for Co_2AlO_4 those are 2.37 eV and 2.59 eV, respectively (indicating high E_g as compared to the normal spinel Co_3O_4). However, for Co_2TiO_4, Co_2RuO_4 and Co_2SnO_4, the band-gap varies between 1.77 eV (for Co_2TiO_4) and 1.52 eV (for Co_2RuO_4). Table 3.6 summarizes the $E_{g\text{-}Theo}$ values obtained from DFT+U calculations for different dilutants and different U values. Moreover, we noticed the signatures of internal *d-d* transitions ($t_{2g}(Co^{3+}) \rightarrow t_{2g}(Co^{2+})$) from the experimental $F(R_\infty)$ versus $\hbar\omega$ plots. These transitions are much prominent for the Co_3O_4 case than the diluted spinels.

3.4 Conclusions:

In this chapter the role of magnetic dilution on the electronic structure and antiferromagnetic ordering of Co_3O_4 (T_N = 30K) has been extensively studied using both DFT+U calculations and experiments such as SQUID magnetometry, UV-Vis-NIR spectroscopy and X-ray diffraction. The numerically computed crystal structure parameters, which include bond angle, bond length, lattice constants etc. are in good agreement with those obtained in the experiment using the Rietveld analysis of XRD data. These results demonstrate that the dilution leads to a stable inverse spinel crystal structure for all these compounds (except for Co_2GeO_4, which exhibits normal spinel configuration) unlike the pristine compound Co_3O_4 in which the size of unit cell increases on replacing the octahedrally coordinated Co^{3+} ions with the dilutant element. The DFT+U calculations suggest that in Co_3O_4 the crystal field splitting ($\Delta_{CF}^{\downarrow}$) changes significantly (3.3-2.5 eV) with increasing the unit-cell volume (527.51 $Å^3$- 649.46 $Å^3$) except for Co_2GeO_4, whereas, the exchange splitting $\Delta_{EX}^{e_g}$ does not exhibit any significant change with increasing the size of the dopant for U=2. On the contrary, $\Delta_{EX}^{t_{2g}}$ shows decreasing trend (5.2 eV - 3.6 eV) with increase of the lattice parameter (8.08 Å - 8.66 Å). Numerical calculations reveal an AFM configuration for Co_2AlO_4, Co_2GeO_4 and Co_3O_4, in contrast to other inverse spinels (Co_2TiO_4, Co_2RuO_4 and Co_2SnO_4) which we found to have the tendency to form FiM structure. These results are consistent with our magnetization measurements which yield the order parameters for antiferromagnetic Co_2AlO_4, Co_2GeO_4 and Co_3O_4 with Néel temperatures T_N = 4.8 K, 20.4 K and 30 K, respectively. Whereas, for the inverse spinels, we obtained the Néel temperature at 16 K, 47.8 K and 41 K for Co_2RuO_4, Co_2TiO_4, and Co_2SnO_4, respectively. For all these systems, at absolute temperature, the computed intrinsic magnetic moments are nearly zero, except Co_2RuO_4 which exhibits non-zero magnetic moment ($1.91\mu_B$) suggesting the restoring of magnetic moment while substituting the Co^{3+} with Ru^{3+}. This observation is consistent with the experimentally obtained temperature dependence of magnetization data whereas we noticed a significant shift of the magnetic-ordering temperature towards the lower value (16 K) as Co is substituted with Ru.

The Kulbelka-Munk analysis of the optical absorption spectra obtained from diffusive reflectance spectroscopy reveal that the optical band gap energy (E_g) of the spinels are in good agreement with the theoretically calculated E_g (for Co_3O_4, 2.33 eV($E_{g\text{-}Thy\text{-}U=2}$) and 2.19 eV($E_{g\text{-}Exp}$)). It was found that the E_g decreases (1.52 eV) on increasing the ionic radius (r_{Ru}=0.68Å) of the dilutant. For Co_2GeO_4 and Co_2SnO_4 the experimental band-gaps (3.16 eV and 1.75 eV) are consistent with X-X direct band gap, whereas for the remaining compound, they agree well with the Γ-Γ direct band-gap obtained theoretically.

Chapter 4
Coexistence of glassy antiferromagnetism in Co_2RuO_4

In this chapter we mainly focus our study on the low-temperature spin-glass state just below the antiferromagnetic ordering of the Co_2RuO_4 (CRO) spinel. Particularly, a detailed experimental study on the frequency dependence of dynamical magnetic susceptibility and H-T phase diagram of CRO are discussed. A lot of emphasis has been given to the elucidate the novel phenomena, such as magnetic exchange interactions, magnetic entropy changes, and exchange bias in bulk polycrystalline CRO system. In the previous chapter, we discussed the crystal and optical properties, however, the detailed magnetic properties with special attention on the relaxation dynamics, exchange interactions, exact ground state, and H-T phase diagram were scarce in literature which is the main reason for choosing this system. The first section of this chapter summarizes the important magnetic properties of this compound and subsequent sections deals with the experimental results and analysis followed by summary of important findings.

4.1 Introduction and motivation:

For the strongly correlated spinel oxides, several ground states have been observed due to the interaction between the spins, lattices, and orbital degree of freedom [163,164]. In case of the transition metal oxide and their composites, competition between the different exchange interactions increases the possibility of geometrical and orbital frustration which leads to some interesting properties, like, ferroelectric ordering of domains, giant sign reversible exchange bias, and reentrant spin-glass phenomena [41,163-165]. As demonstrated in previous chapter CRO crystallizes in the inverse spinel structure (space group *Fd-3m* (227)) with the electronic configuration $(Co^{2+})_A[Co^{3+}Ru^{3+}]_BO_4$. In this compound, Co^{2+} ions occupy the tetrahedral A-sites and exhibit a high spin (S = 3/2) state, whereas, the octahedral B-sites are occupied by the low spin configuration of Co^{3+} (S=0) and Ru^{3+} (S = 1/2) [21,146,166,167]. First scientific article on the synthesis of CRO was reported by Dulac using the solid-state reaction method [166]. Later, Krutzsch and Kemmler synthesized $Co_{3-x}Ru_xO_4$ ($0.4 \leq x \leq 1.0$) solid solutions using metallic powders of Co and Ru then oxidized these samples between 1123 K and 1473 K, and studied the vibrational modes of $Co_{3-x}Ru_xO_4$ [168]. Kawano *et al.* reported semiconducting behavior with a positive Seebeck coefficient in the solid-solutions of $Co_{3-x}Ru_xO_y$ ($0.50 \leq x \leq 0.70$, y = 3.8-3.9) [169]. On the other hand, while substituting 50% of Ru by Mn in CRO, a mixed ground state of long-range FiM and short-range order was reported. For 70% substitution of Ru it was observed that the disorder completely vanishes [170]. However, for $Mn_{0.5}Ru_{0.5}Co_2O_4$, Bhowmik *et al.* reported that a magnetic transition occurs from ferrimagnet to paramagnet across 100K. However, the authors were unable to observe any short-range magnetic interactions below 100K [171]. While incorporating Fe in the Ru site of CRO, the magnetic ordering temperature has been reported to vary from 120 K (x = 0.2) to 560 K (x = 0.8) and the variation of conductivity indicated that the incorporation of Fe decreases the concentration of free electrons [172]. There

is only single report available on the magnetic properties of undoped CRO by Mandrus *et al.* who studied the AFM behavior using the temperature dependence of ac- and dc-magnetic susceptibility along with the neutron powder diffraction experiments. Accordingly, these authors reported a spin-glass state below the freezing temperature T_F~16 K with overall AFM exchange coupling inferred from the Curie Weiss fit of the paramagnetic susceptibility [21]. Additional support for the lack of long-range AFM order below T_F was inferred from the absence of any new lines in the neutron powder diffraction pattern measured at 4 K compared to that measured at 25 K [21]. Mandrus *et al.* also investigated the temperature dependence of magnetic susceptibility of $ZnCoRuO_4$ in which non-magnetic Zn^{2+} is substituted for magnetic Co^{2+} at the tetrahedral sites; this material showed Curie-like paramagnetic behavior down to 2 K, signifying that the Ru^{3+}-Ru^{3+} exchange coupling at the B-sites is practically negligible [21]. This is important since Co^{3+} ions occupying the B-sites in CRO are in the low-spin S = 0 state. So, the only significant exchange couplings in CRO are expected to be the A-A type just as in Co_3O_4 (which is an antiferromagnet with T_N ~ 30 K [87,143]) modified perhaps somewhat by the much weaker A-B coupling between Co^{2+} and Ru^{3+}, the later randomly occupying only half the B-sites. The electronic structure of Co_3O_4 = $[Co^{2+}]_A[2Co^{3+}]_BO_4$ differs slightly from that of CRO in that all the B-sites in Co_3O_4 are occupied by non-magnetic Co^{3+} ions so that A-B and B-B exchange interactions are absent in Co_3O_4 [143]. Nevertheless, there is no detailed experimental study on the frequency dependence of relaxation dynamics of CRO is available in the literature which motivated us to undertake this work which lead to the discovery of few novel physical properties as discussed below.

4.2 Experimental details:

Polycrystalline sample of CRO was prepared using the solid-state reaction method as detailed in Chapter 2. We used slightly lower heat-treatment (1100ºC in air for 24 h in air) while preparing the pellets of CRO. To verify the structural purity of the prepared sample, X-ray diffraction (XRD) experiment was performed using a Rigaku, TTRAX III diffractometer with Cu-Kα radiation of wavelength λ = 1.5406 Å as source. This was followed by the Rietveld refinement of the diffraction pattern using the FullProf program as shown in Fig. 4.1. These results reveal that within the accuracy of the XRD technique, the only phase present in the sample is CRO since impurity lines from any other phase are not detected. The Rietveld refinement analysis yields the following structural parameters for CRO: lattice constant a = 0.829 nm, bond lengths A-O = 0.186 nm and B-O = 0.202 nm, and bond angles A-O-A= 109.4º and A-O-B =124.0º. On the other hand, same magnetic characterization procedure is employed as described in Chapter 2 except here we performed a very detailed frequency variation (from 0.17 Hz to 1202 Hz) of ac-magnetic measurements from 5 K to 400 K for dc-fields between 0 Oe ≤ H_{DC} ≤ 500 Oe with amplitude of the ac magnetic field H_{ac} = 4 Oe.

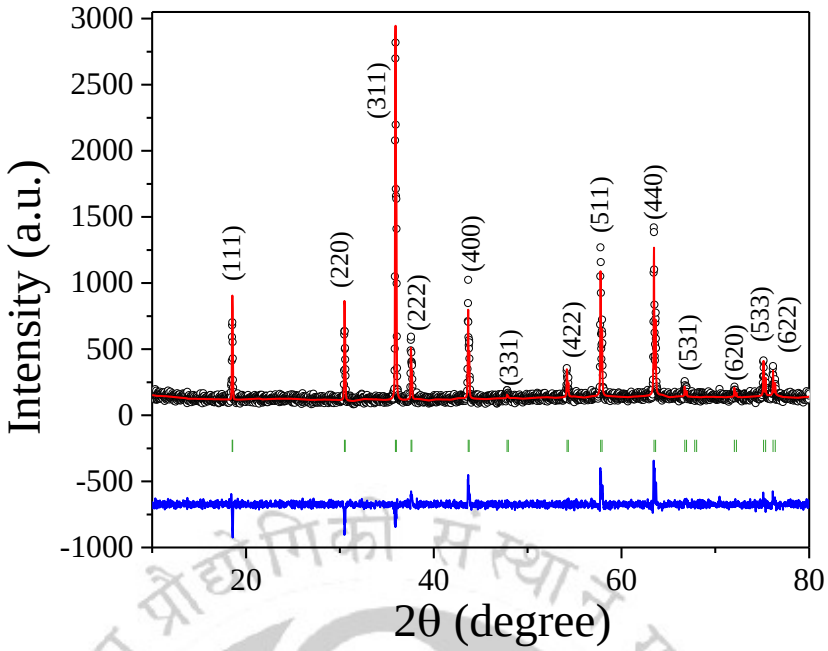

Fig. 4.1: Room temperature XRD patterns together with the Rietveld refined data of CRO. The blue lines at the bottom represent difference between the measured and simulated patterns.

4.3 Results, analysis and discussion:

4.3.1 Temperature dependence of dc-magnetic susceptibilities:

In this subsection, first we discuss a detailed temperature and field dependence of the dc-magnetization data and then proceed for the ac-susceptibility studied. Figure 4.2 shows the temperature dependent dc-magnetic susceptibilities χ(T) (=M/H) measured with H = 600 Oe under ZFC and FC conditions. Note that χ is given in molar units which is obtained by multiplying the measured units (M = emu/g) with the molecular weight of CRO (M.W.=282.94 mol/g). The data show a peak in χ near 16 K. In the inset of the figure we also plot the temperature dependence of [χ_{FC} - χ_{ZFC}] for T < 23 K showing a peak at 15.6 K and a broad minimum near 11.6 K. We later show that for this system, the Néel temperature T_N = 15.2 K representing PM to AFM transition whereas T_{SG} ~ 14.2 K represents transition to spin-glass state. It is noteworthy that Mandrus *et al.* [21] also noted that χ_{FC} bifurcates from χ_{ZFC} near 12 K. The bifurcation between the ZFC and FC curves below T_N suggests that the phase transition is not a classical Néel AFM, rather fraction of the spins are decoupled in some way i.e. there is presence of some weak ferromagnetic moments or uncompensated spins. As for an example, it has been reported that Sr_4FeRuO_8 and Sr_3FeRuO_7 exhibit similar type of temperature dependence of magnetization with T_N across 11 K and 23 K, respectively [173]. Koteswararao *et al.* reported the presence of weak ferromagnetic moments in the antiferromagnetic state of $Pb_6Ni_9(TeO_6)_5$ which led to clear bifurcation between the ZFC and FC curves [174]. As noticed in section 4.1, weakly coupled spins in CRO are likely due to Ru^{3+} ions with spin S =1/2 because of the weaker and random A-B coupling which we argue later is also the source of the SG state.

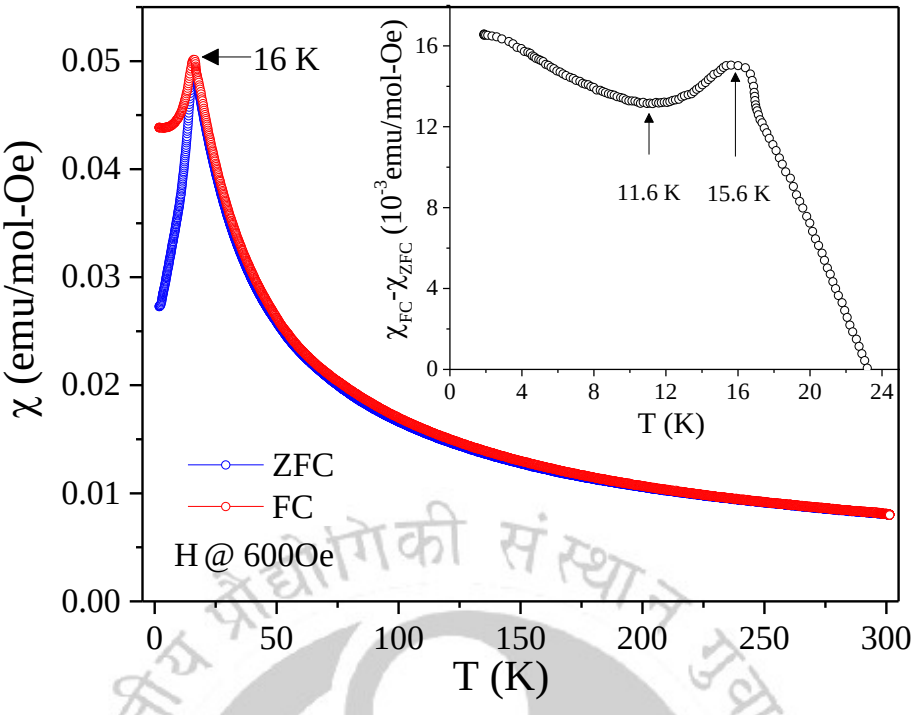

Fig. 4.2: Temperature dependence of the dc magnetic susceptibility (χ) of CRO in the range of 2 K to 300 K measured under the ZFC and FC conditions with applied H = 600 Oe. The inset shows the temperature variation of difference susceptibility (χ_{FC} - χ_{ZFC}) for the lower temperatures.

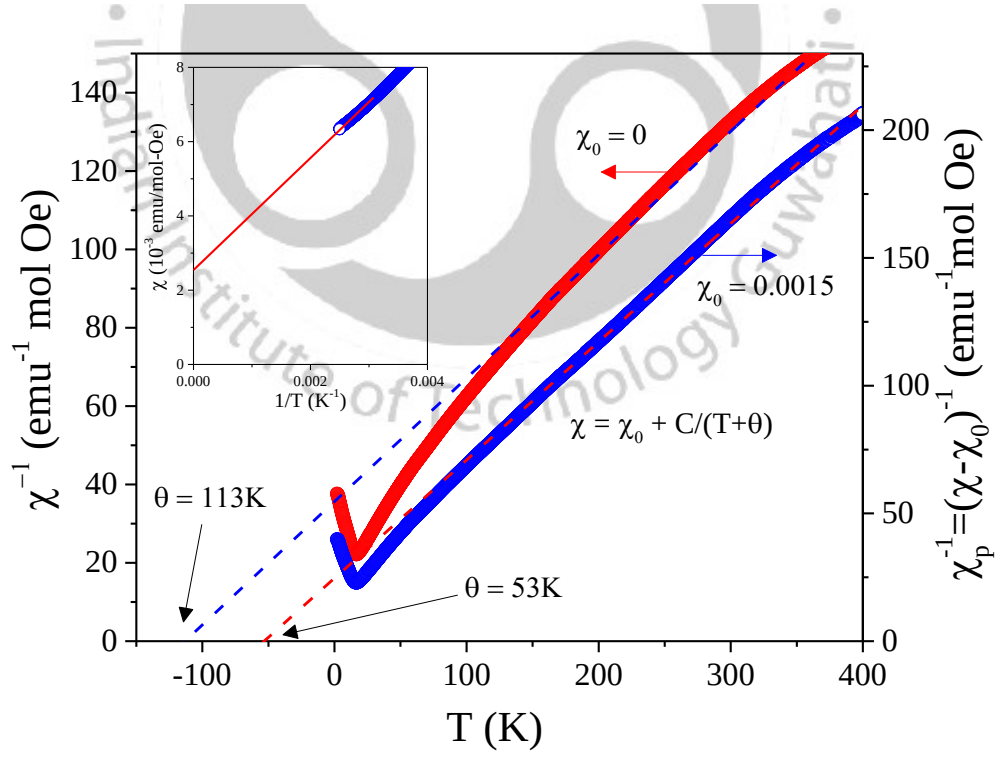

Fig. 4.3: Temperature variations of $\chi^{-1}_p = (\chi - \chi_0)^{-1}$ with χ_0 =0.0015 emu/mol-Oe (blue colour and right hand scale) and χ^{-1}(T) and with χ_0 = 0 (red colour and left hand scale) with the dotted lines fits to the Curie-Weiss law. Inset shows the plot of magnetic susceptibility χ of CRO vs. inverse temperature.

The temperature dependence of magnetic susceptibility χ of CRO for $T > T_N$ appears to fit well to the modified Curie-Weiss (CW) law given by:

$$\chi = \chi_0 + C/(T + \theta) \quad (4.1)$$

In the above Eq. (4.1), the χ_0 term is added to the conventional CW law to account for the (positive) Van Vleck susceptibility and (negative) diamagnetic susceptibility both of which are usually temperature independent, C ($=N_A\mu_{eff}^2/3k_B$) is the Curie constant and θ is the Curie-Weiss temperature. In the convention used in Eq. (4.1), θ is positive (negative) for antiferromagnetic (ferromagnetic) interaction. As shown in the analysis of the data in Co_3O_4 [143], including the proper magnitude of χ_0 is very important to accurately determined C (and hence magnetic moment μ_{eff}) and θ as we show here also. To determine χ_0 experimentally, χ versus 1/T is usually plotted with a focus on high-T data yielding $\chi = \chi_0$ by linear extrapolation to the limit $1/T \rightarrow 0$ where contribution of the paramagnetic term in Eq. (4.1) goes to zero. Using our data up to 400 K, such a plot is shown in the inset of Fig. 4.3 yielding χ_0 = 0.0025 emu/mol-Oe. However, we have used χ_0 = 0.0015 emu/mol-Oe in our analysis since as shown for Co_3O_4, using data up to 1000 K would have provided lower magnitude of χ_0 [143]. Using χ_0 = 0.0015 emu/mol-Oe in Eq. (4.1), we have plotted χ^{-1} vs. T (left hand scale) and $\chi_p^{-1}(= (\chi - \chi_0)^{-1})$ vs. T (right hand scale) in Fig. 4.3, with the slopes of the linear fits yielding C and intercept θ, in which differences for the two cases demonstrating the effects of χ_0. The obtained magnitudes of C (θ) are 3.25 emu/mol K (113 K) and 2.16 C (53 K) for χ_0 = 0 and χ_0 = 0.0015 emu/mol-Oe, respectively. Mandrus *et al.* reported a good fit for their data up to 300 K using χ_0 = 0.004 emu/mol-Oe and yielding C = 1.44 emu/mol K and θ = 4 K [21]. Using $C = N_A\mu_{eff}^2/3k_B$, the calculated effective magnetic moment for different magnitudes of C noted above are: μ_{eff} = 5.10, 4.16 and 3.39 μ_B per formula unit (f.u.) of CRO for C = 3.25, 2.16, and 1.44 emu/mol K, respectively. The expected magnitudes of μ_{eff} for CRO = $(Co^{2+})_A[Co^{3+}Ru^{3+}]_BO_4$ using spin S = 0 for Co^{3+}, S = 3/2 (μ = 3.87 μ_B) for Co^{2+}, and S=1/2 (μ = 1.73 μ_B) for Ru^{3+} is $\mu = \sqrt{(3.87)^2 + (1.73)^2}$ = 4.24 μ_B per f.u. This is in good agreement with μ = 4.16 μ_B /f.u. obtained from our analysis using C = 2.16 emu/mol K with χ_0 = 0.0015 emu/mol-Oe. Since fit to the modified CW law is possible for different magnitudes of χ_0 as discussed above, our choice of χ_0 = 0.0015 emu/mol-Oe for CRO based on the comparison with isostructural Co_3O_4 as noted above and yielding the theoretically expected magnitude of the magnetic moment is justified.

4.3.2 Evaluation of the exchange interactions:

The magnitudes of θ = 53 K and T_N =15.2 K determined above being significantly different from each other suggests the presence of at least two significant exchange interactions in CRO. Following the discussion in Co_3O_4 [143], the exchange constant J_1 (J_2) between the Co^{2+} ions on the A-site involves the path A-O-A (A-O-B-O-A) with z_1 = 4 (z_2 = 12) as the interacting neighbors. The molecular field theory then yields the following expressions for θ and T_N [143]:

$$3k_BT_N = S(S+1)\,[J_1z_1 - J_2z_2] \quad (4.2)$$

$$3k_B\theta = S(S+1)\,[J_1z_1+J_2z_2] \quad (4.3)$$

Using T_N = 15.2 K, θ = 53 K and S = 3/2 in Eqs (4.2) and (4.3) yield J_1/k_B = 6.8K and J_2/k_B = 1.26K for CRO. The effects of the weaker exchange coupling between Co^{2+} and Ru^{3+}, ignored in the above analysis, is considered later in the chapter. These magnitudes of J_1 and J_2 in CRO are about half the magnitudes for Co_3O_4 for which θ = 112 K and T_N = 30 K were reported [143]. An alternative approach to determine the dominant exchange constant J_1 is the use of high temperature series expansion (HTSE) for S = 3/2 using the Heisenberg Hamiltonian [175]. Such a series is given by [175]:

$$\chi_p = \frac{C}{T}\sum_{n=0}^{6} C_n \left(\frac{J_1}{K_B T}\right)^n \quad (4.4)$$

with coefficients C_0 = 1, C_1 = -7.5, C_2 = 45, C_3 = -234.56, C_4 = 1145.97, C_5 = -5581.67 and C_6 = 27674.74 for S =3/2 [175]. Since the values of C_n alternative in sign, we use only even number of terms up to n = 6 although terms up to n =7 are available [175]. Also, C = 2.16 emu/mol K and $\chi_p = \chi - \chi_0$ are used in this calculation which are determined from the analysis based on the modified CW law (Eq. (4.1)). The fit of the data to the CW law and the HTSE are compared in Fig. 4.4. Whereas the CW law begins to deviate from the data below about 100 K, the fit to the HTSE is shown to fit well below 40 K using C =2.16 emu/mol K and J_1/k_B = 5.8 K. The ratio test shows that the convergence of the series is valid for $J_1/k_BT < 0.2$ which for J_1/k_B = 5.8 K means T > 30 K, in line with the results shown in Fig. 4.4. The fit can be extended down to about 30 K using C =1.9 emu/mol K and J_1/k_B = 5.4 K but with slight deviation of the fit at higher temperatures. These magnitudes of J_1/k_B are in good agreement with those determined above using Eqs. (4.2) and (4.3) although HTSE is only available for a single exchange constant. Such determination of exchange constants for CRO have not been reported before.

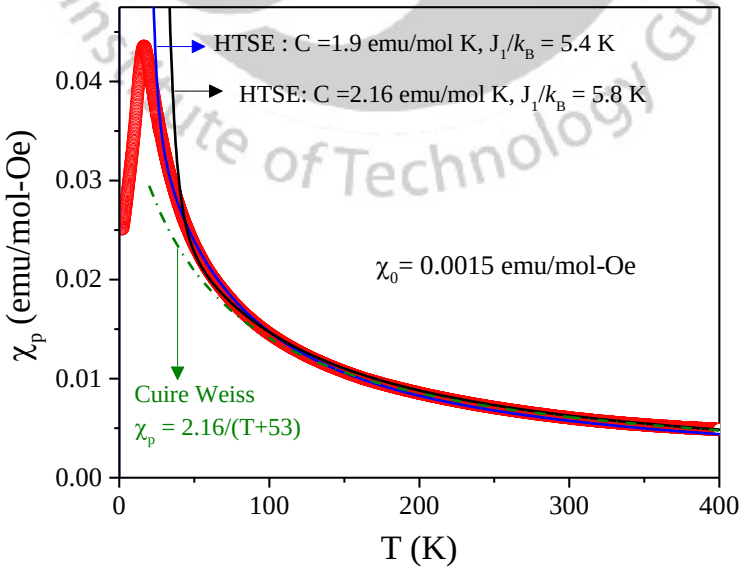

Fig. 4.4: Temperature variation of the PM susceptibility $\chi_p = (\chi - \chi_0)$ is fit to HTSE, the high temperature series expansion (black and blue lines) and the Curie-Weiss law (olive line) with the magnitudes of the fitted parameters listed.

4.3.3 Néel temperature, spin-glass transition and H-T phase diagram:

Both theoretically [176] and experimentally [143,177,178], it is known that the peak in χ vs. T in antiferromagnets usually occurs at temperature $T > T_N$ and instead T_N is accurately defined by the peak in $\partial(\chi T)/\partial T$. In Fig. 4.5(b), the plot of $\partial(\chi T)/\partial T$ vs. T in H = 100 Oe (the lowest H used in our χ vs. T measurements) shows a peak at 14.9 K. In Fig. 4.5(a), we also show the data of ac susceptibility χ'' vs. T at the lowest frequency f = 0.17 Hz and H = 0 which shows a peak at 15.2 K. We suggest T_N = 15.2 K to be the accurate value of T_N for CRO in H = 0 since the applied H lowers T_N as discussed below. Temperature dependence of χ_{ZFC} from 2 K to 300 K was measured under applied static magnetic fields H = 0.1, 0.4, 0.6, 1, 5, 6, 7, 8, 9, 10, 20, 30, 40, 50, and 70 kOe. The data for χ vs. T for H = 0.1 kOe was shown in Fig. 4.6(b) and the similar plots for representative values of H = 5, 8, 10, 20 and 30 kOe are shown in Fig. 4.7, along with the computed $\partial(\chi T)/\partial T$ vs. T curves. It is evident that with increase in H, the peak in χ vs. T becomes broader and there is clear evidence of the presence of two peaks in the computed $\partial(\chi T)/\partial T$. The H-dependence of the two peaks was measured carefully and from the analysis of this dependence, the lower temperature peak is interpreted to be due to spin-glass transition T_{SG}. This H-dependence of T_N (high temperature peak) and T_{SG} is shown in the H-T phase diagram of Fig. 4.7. Additional support for the designation of T_{SG} is presented later from the analysis of the data on ac susceptibilities

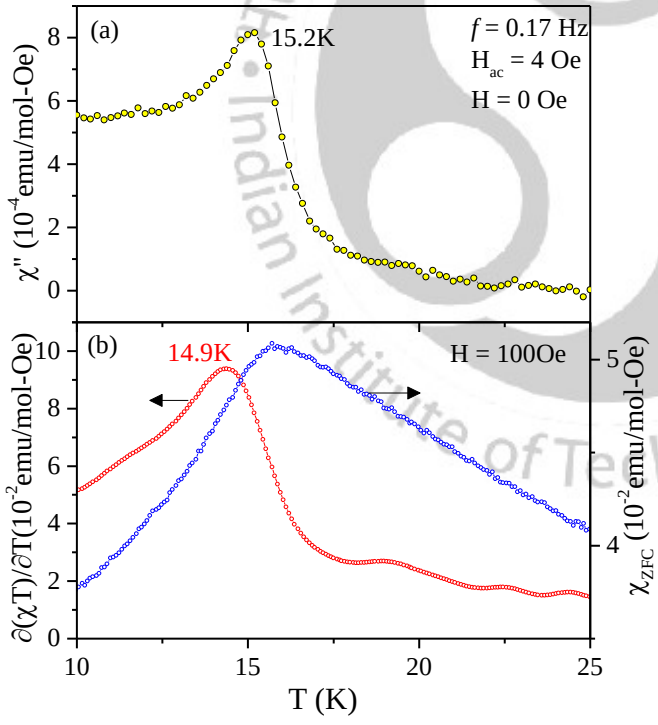

Fig. 4.5: (a) Temperature variation of the ac susceptibility χ'' at the lowest frequency f = 0.17 Hz and H = 0 Oe; (b) Temperature variation of dc susceptibility χ (blue symbols and right-hand scale) and corresponding $\partial(\chi T)/\partial T$ (red symbols and left-hand scale) for H = 100 Oe.

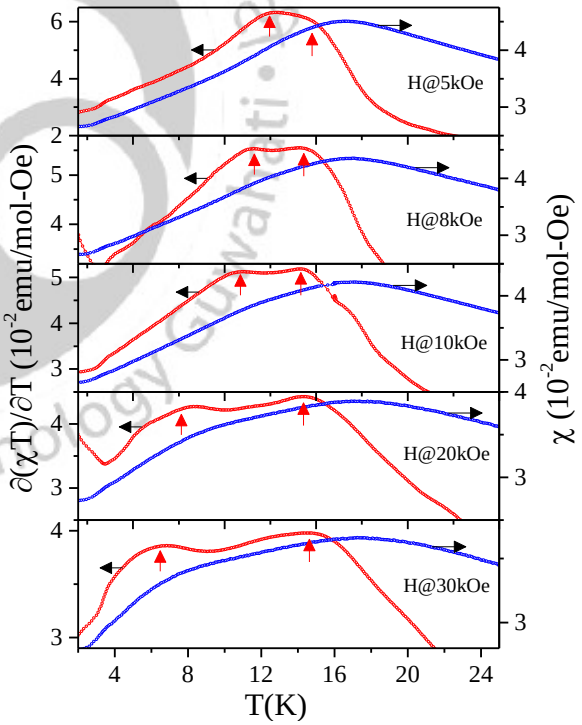

Fig. 4.6: Temperature variation of dc magnetic susceptibility χ = M/H (blue symbols and right-hand scale) measured under the ZFC conditions for H = 5, 8, 10, 20 and 30 kOe and that of $\partial(\chi T)/\partial T$ (red symbols and left-hand scale). The lower and higher temperature peaks marked by vertical arrows respectively correspond to T_{SG} and T_N of CRO.

(χ' and χ''), time dependence of the magnetization M(t), and temperature dependence of the hysteresis loop parameters. Based on molecular-field theory, the H-dependence of T_N in conventional antiferromagnets such as MnF_2 and Er_2O_3 has been shown to fit well with the relation: $T_N(H) = T_N(0) - D_1H^2$ with D_1 =7.3×10^{-9} K/Oe^2 for Er_2O_3 [178] and D_1= 1.6×10^{-10} K/Oe^2 for (MnF_2 [179]). For CRO, T_N does decrease with increase in H initially, although the peaks in T_N and T_{SG} are difficult to resolve for H < 5 kOe. For H = 50 kOe, T_N (H) = 14.4K compared to T_N (0) = 15.2K; these values yield D_1= 3×10^{-10} K/Oe^2, similar to the reported values for MnF_2 and Er_2O_3 noted above.

The H-dependence of T_{SG} for H > 7 kOe shows T_{SG} = 13.1K for H =7 kOe to T_{SG} = 3.4 K for H = 70 kOe. The observed data of the H-dependence of T_{SG} fit well with the relation, also known as non-mean field Almeida-Thouless (AT) line [180-184]:

$$T_{SG}(H) = T_{SG}(0)(1\text{-}AH^{2/\phi}), \quad (4.5)$$

where $T_{SG}(0)$ is the value of SG temperature in the absence of the magnetic field, A is the amplitude and ϕ is the crossover exponent. For the mean-field Almeida-Thouless (AT) line, the magnitude of ϕ = 3 [185-191]. The fit of the data to Eq. (4.5) in Fig. 4.8 yields $T_{SG}(0)$ = 14.2 K, ϕ = 3.2 and A = 7.4 × 10^{-4} Oe$^{-0.625}$. This supports our identification of T_{SG} as the spin-glass transition with T_{SG} (0) ≈ 14.2 K, which is somewhat lower than T_N (0) = 15.2 K. This suggests that in CRO, AFM ordering precedes the spin glass ordering as the temperature is lowered from above. The non-mean model has been used for different SG systems and thus ϕ varies significantly depending upon the SG system [180-184]. The magnitude of ϕ is mainly determined by the strength of the anisotropy relative to the magnetic field. The obtained ϕ = 3.2 for CRO resembles the random-anisotropy SG system such as α-DyNi system [180].

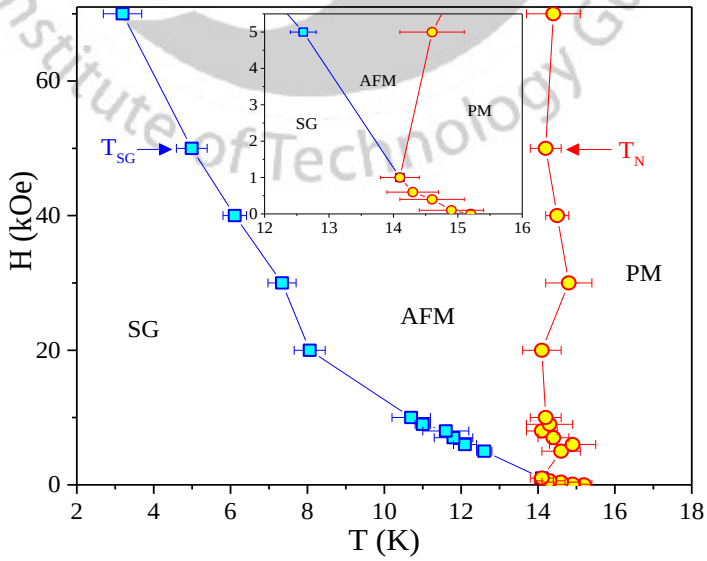

Fig. 4.7: Variation of T_N (solid yellow circles) and T_{SG} (solid blue squares) with applied magnetic field H obtained from magnetization data to yield the H-T phase diagram separating the PM, AFM, and SG regions. The inset shows the low H zoomed view between T = 12K and 16K.

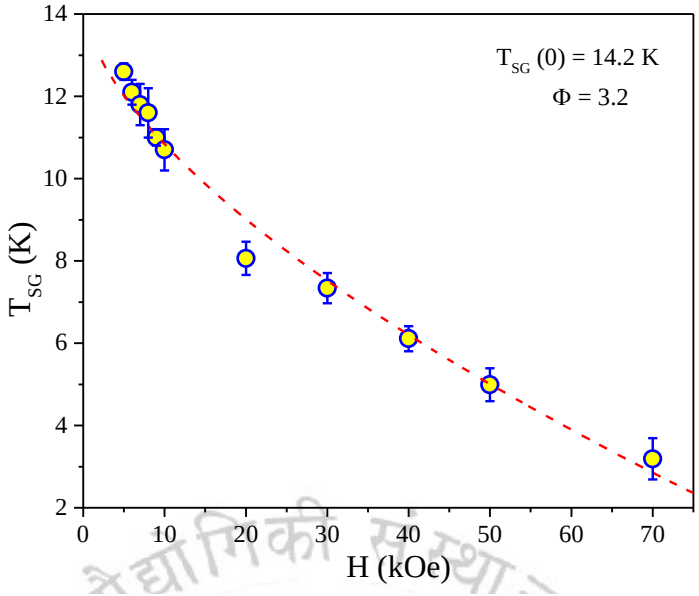

Fig. 4.8: Variation of T_{SG} (obtained from χ vs T data) against H, with the dotted line being the best fit to Eq. (4.5) with the parameters listed in the figure.

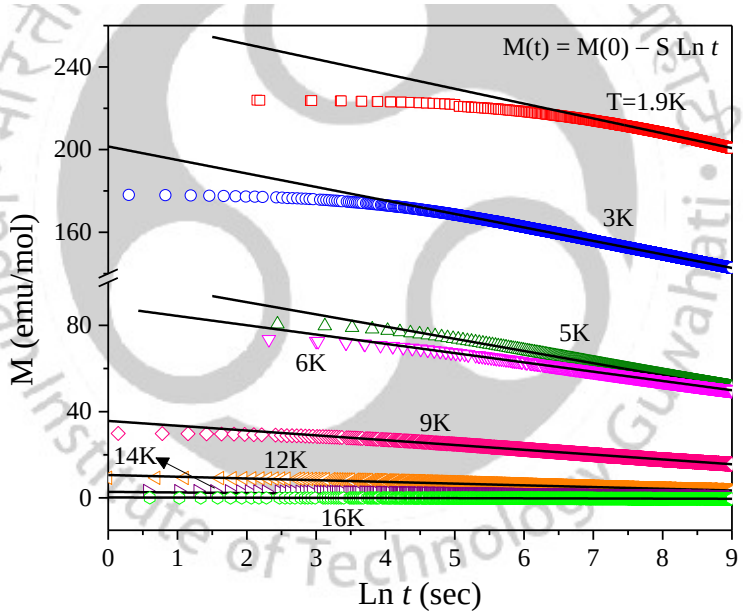

Fig. 4.9: Time dependence of thermoremanent magnetization (TRM) M(*t*) of Co_2RuO_4 measured at different temperatures after switching off the cooling magnetic field of 90 kOe. The solid curves are fits to the relations M(t) = M(0) – *S* Ln *t* for larger times.

4.3.4. Time dependence of magnetization and magnetic viscosity:

A characteristic feature of the SG state is time (*t*) dependence of its magnetization below T_{SG} leading to magnetic viscosity *S*. This time dependence of M(*t*), usually given by [185,189,191]:

$$M(t) = M(0) - S \text{ Ln } t \qquad (4.6)$$

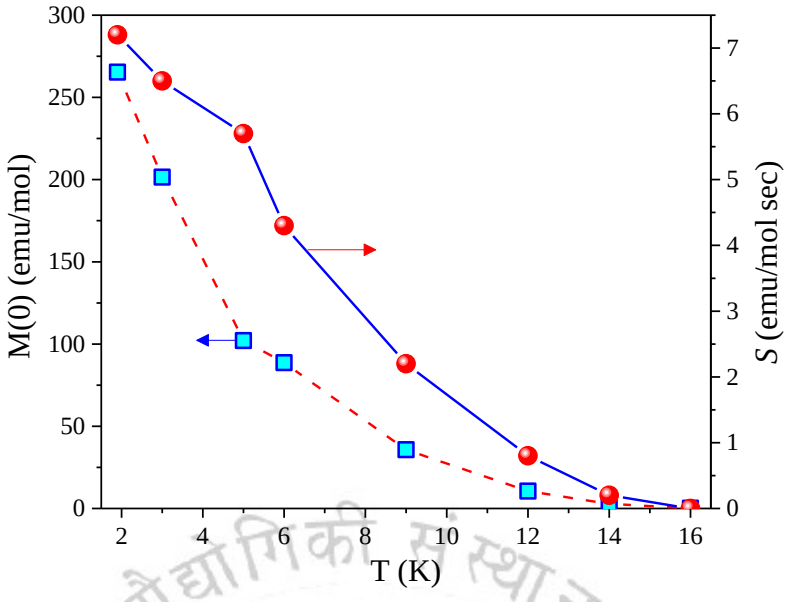

Fig. 4.10: Temperature variations of the initial magnetization M(0) (solid blue squares and left hand scale) and magnetic viscosity *S* (solid red circles and right hand scale) with the lines connecting the data points as visual guides.

Indicate the lack of a unique ground state for a spin-glass. For the measurements of *S* in CRO, the sample was cooled from room temperature to the measuring temperature in H = + 90 kOe. After the temperature became stable, H was switched to zero and magnetization M(t) was measured as a function of time (t) for t up to 2.5 h. To acquire the data for the next temperature, the sample was brought at room temperature, cooled back to the temperature in 90 kOe and the process was repeated. Plots of M(t) vs. *Ln* t for different temperatures are shown in Fig. 4.9 and further temperature dependence of magnetic viscosity *S* was determined from the slope and M(0) as shown in Fig. 4.10. Both *S* and M(0) decreases monotonically with increase in temperature approaching zero near 15K. The large value of M(0) at lower temperatures indicates the presence of ferromagnetic clusters or uncompensated spins, similar to the observations in the spin-glass $PrRhSn_3$ [191].

4.3.5 Relaxation dynamics and interdomain interactions:

In order to better understand the nature of magnetic ordering in CRO, temperature and frequency dependence of ac magnetic susceptibilities (χ' and χ'') were measured covering the frequency range f = 0.71 *Hz* to 1202 *Hz* (Fig. 4.12). The applied fields were H_{ac} = 4 Oe and H = 0 Oe. With increase in f, the peaks shift to higher T for both $\chi'$and χ'' although the peak amplitudes decrease for χ' but increase for χ'', a behavior often observed for spin glasses [23,24,141,186]. To quantify the shift in the peak temperature T_p of χ'' with change in frequency from f_1 to f_2, the quantity Ω (Mydosh parameter) defined by [82,141,186,192]:

$$\Omega = (T_{p2}-T_{p1})/T_{p1}(\log f_2 - \log f_1) \quad (4.7)$$

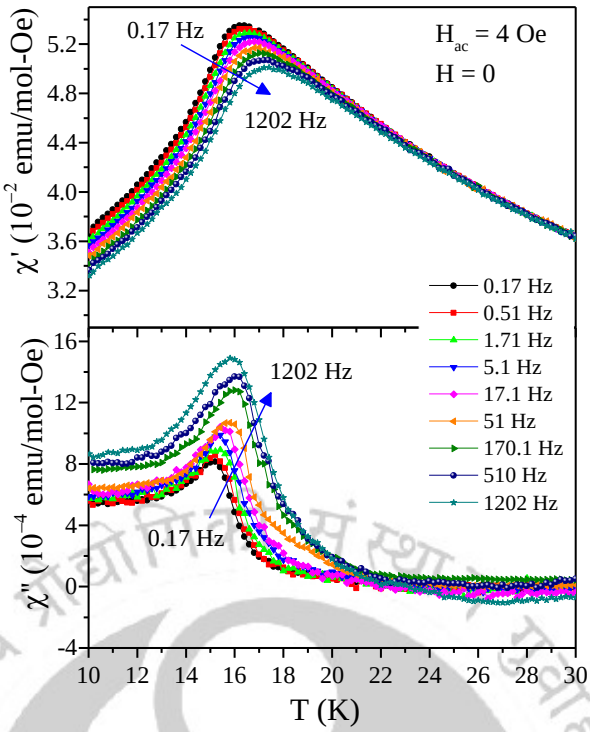

Fig. 4.11: Temperature dependence of ac magnetic susceptibilities $\chi'(T)$ and $\chi''(T)$ of CRO measured at various frequencies between 0.17 and 1202 Hz under warming conditions using H_{ac} = 4 Oe and H = 0 Oe.

is often calculated. From Fig. 4.11, T_p = 15.2K (15.8K) for f_0 = 0.17 Hz (1202 Hz) yielding Ω = 0.010, a magnitude typical of spin glasses [193]. Although similar frequency and temperature dependence of χ'' is also observed in interacting magnetic nanoparticles, the magnitude of Ω = 0.05 to 0.13 for magnetic nanoparticles is considerably larger in such cases, Ω increasing with decrease in inter-particle interaction [73,193-197]. For normal magnetic transitions, the magnitude of Ω is an order of magnitude smaller than Ω = 0.010 [73,193-197]. In case of canonical SG systems, the magnitude of Ω is generally one order less (e.g. for AuMn and CuMn, Ω is 0.0045 [82] and 0.005 [78], respectively), whereas for non-interacting ideal super-paramagnet it is one order higher (e.g. for α-[$Ho_2O_3(B_2O_3)$], Ω ≈ 0.28 [78]) from the value obtained for CRO. The obtained Ω value is comparable with those in cluster SG systems like $Cr_{0.5}Fe_{0.5}Ga$ (Ω = 0.017) [180], $PrRhSn_3$ (Ω = 0.086) [191], and $La_{1.85}Sr_{0.15}Cu_{1-x}Ni_xO_4$ (Ω ≈ 0.012) [198]. To further establish the spin-glass behavior in CRO, the frequency dependence of χ'' is analysed using two empirical scaling laws: (i) The Vogel-Fulcher law defined by the relaxation time $\tau = \tau_0 \exp [E_a/k_B(T-T_0)]$ [24,141,180,191,198] and (ii) the power law $\tau = \tau_0[(T-T_{SG})/T_{SG}]^{-z\upsilon}$ [24,141,180,191,198]. Here, $\tau = 1/2\pi f$ is relaxation time with τ_0 being related to the relaxation of individual cluster magnetic moment, T_0 represents strength of inter-cluster interaction, E_a is the activation energy and zυ is a critical exponent with magnitude between 4 and 12 for spin glasses [78,180]. The fit of the data using the peak position of χ'' to the Vogel-Fulcher law is shown in Fig. 4.12(a) yielding T_0 = 14.3K and $\tau_0 = 1.14\times10^{-9}$ s. Similarly, the fit to the power law, shown in Fig. 4.12(b), yields T_{SG} = 14.97 K, $\tau_0 = 1.16\times10^{-10}$ s and zυ = 5.2.

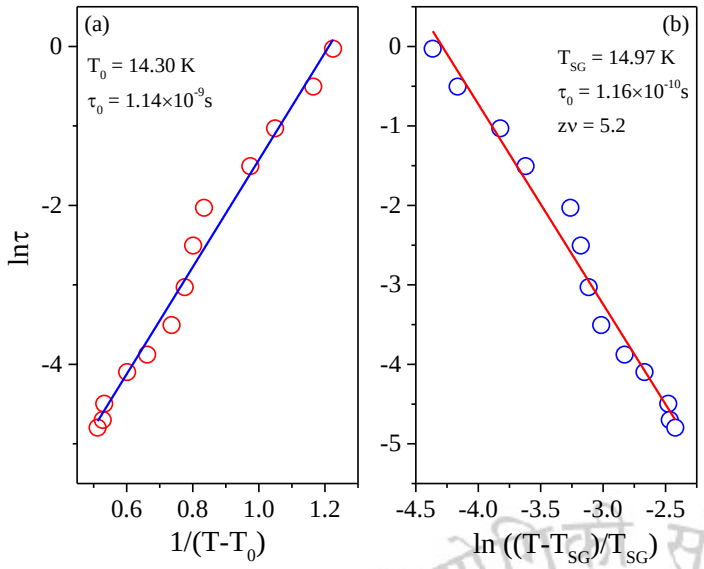

Fig. 4.12: (a) The best fit of the relaxation times determined for CRO to the Vogel-Fulcher law. (b) The best fit to the Power law, with the magnitudes of the fitted parameters listed in the figures.

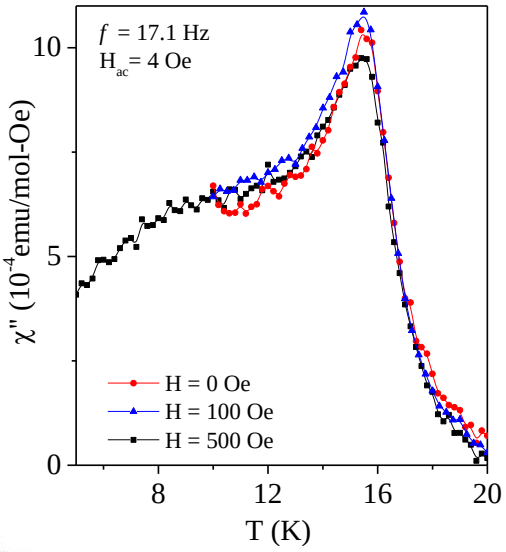

Fig. 4.13: Temperature variation of the ac magnetic susceptibility $\chi''(T)$ for CRO measured at 17.1 Hz in H_{ac} = 4 Oe with superposed dc bias fields H = 0, 100 and 500 Oe.

These magnitudes of the fitted parameters are supportive of the SG state in CRO for $T < T_{SG}$. For traditional spin glasses, the magnitude of τ_0 lies between 10^{-10} and 10^{-13} s, whereas, in case of canonical and cluster SG systems τ_0 varies in the range 10^{-12} - 10^{-13} s [180,198-202] and 10^{-7} -10^{-10} s, respectively [78,180,191,198,203]. The τ_0 value obtained from Vogel-Fulcher and Power law, both lies in the range valid for cluster SG system which is in line with the analysis of relative shift in the Mydosh parameter Ω. The comparatively high magnitude of τ_0 indicates the slow spin dynamics in CRO which is quite likely due to the presence of strongly interacting clusters rather than individual spins. On the other hand, the value of τ_0 obtained from Power law is one order higher than the Vogel-Fulcher law and this behavior has been observed for cluster SG system while using two different dynamical scaling laws [180,198,204]. Generally, the weak coupling between the interacting entities are defined when the strength of inter-cluster interaction is negligible compared to the activation energy ($T_0 \ll E_a/k_B$) and the opposite ($T_0 \gg E_a/k_B$) is true for the strong coupling. However, for CRO, T_0 is nearly 0.85 E_a/k_B and the value fall in the intermediate region which demonstrate the presence of finite interaction between the magnetic entities and the similar behavior has been reported for other cluster spin glass systems [180,198]. In our measurements of χ vs. T under different static magnetic fields H, T_{SG} is difficult to distinguish from T_N unless a large enough H is applied to shift the T_{SG} to lower temperatures. To see this effect in the ac susceptibilities, the data of χ'' vs. T taken with H_{ac} = 4 Oe and H = 0, 100 Oe and 500 Oe is shown in Fig. 4.13. As expected, the position of the peak representing T_N is not affected noticeably with increase in H. However, a broad hump in χ'' appears below about 12 K in the data taken with H = 500 Oe. It is suggested that this hump

is a signature of the spin-glass phase as for example reported in the case of α-$Ni(OH)_2$ [205]. A larger H is likely needed to obtain a distinct peak for T_{SG} as shown in the H-T phase diagram in Fig. 4.7.

The results and their analyze presented above show that CRO orders antiferromagnetically at $T_N \approx 15.2$K and with further lowering of temperature, spin-glass like ordering develops below $T_{SG} \approx 14.2$ K. It is known that the existence of SG state requires randomness and/or competing interactions. In CRO, half of the octahedral B-sites are occupied by non-magnetic Co^{3+} ions and the other half of the B-sites are occupied by Ru^{3+} ions with spin S=1/2. Since the occupancy of the B-sites by Co^{3+} and Ru^{3+} is random, any A-B exchange coupling between the Co^{2+} ions on the A-site and Ru^{3+} ions on the B-sites has a random character. Also, magnetic studies in $ZnCoRuO_4$ by Mandrus *et al.* [21] showed that any Ru^{3+}- Ru^{3+} (B-B) exchange interaction is quite negligible. Therefore, any magnetic ordering of the Ru^{3+} ions through A-B exchange interaction has spin-glass-like features even though Co^{2+} ions on the A-sites are ordered antiferromagnetically at T_N, just as in Co_3O_4 [143]. So overall, all the magnetic moments in CRO do not possess a long-range magnetic order below T_N, explaining the absence of any magnetic lines in the neutron diffraction studies of Mandrus *et al.* at 5K [21]. It is worthwhile to compare the results on CRO presented here with those reported for somewhat similar spinel Co_2SnO_4 = $[Co^{2+}]_A[Co^{2+}Sn^{4+}]_BO_4$ with Sn^{4+} ions on the B-sites being non-magnetic [23,24,167] similar to Co^{3+} ions in CRO. In Co_2SnO_4, T_N = 41K was reported due to ordering of the longitudinal components of the Co^{2+} spins followed by T_{SG} = 39.1K due to freezing of transverse spin components. These observations in Co_2SnO_4 were interpreted in terms of the magnetic dilution produced by the non-magnetic Sn^{4+} ions on the B-site, somewhat like the situation in CRO. In contrast Co_2TiO_4 = $[Co^{2+}]_A[Co^{3+}Ti^{3+}]_BO_4$, where all the cations have magnetic moment with $\mu(Co^{2+}) = 3.87\mu_B$, $\mu(Co^{3+}) = 4.89\mu_B$ and $\mu(Ti^{3+}) = 1.73\mu_B$, absence of a spin-glass phase was reported [22]. Thus, it can be inferred that magnetic dilution of the B-site leads to spin-glass phase. It is also known that the absence of the magnetic ions on the A-site such as present in $ZnFe_2O_4$ = $[Zn^{2+}][2Fe^{3+}]O_4$ [206] and the defect spinel $MgMnO_3$ with the structure $4MgMnO_3$ = $3[Mg^{2+}][Mg^{2+}_{1/3}Mn^{4+}_{4/3}\ V_{1/3}]O_4$ (V= vacancy), leads to magnetic frustration and lack of long-range magnetic order [206,208].

4.3.6 Asymmetry in hysteresis loops and exchange bias:

Temperature dependence of hysteresis loop parameters like the coercivity H_C, remanence M_R, and loop-shift or exchange bias H_{EB} for the ZFC and FC samples, provides a useful way to determine the nature of magnetic phases present in any magnetic compound. Particularly noteworthy is the result that H_{EB} is expected only if an AFM phase combined with another phase (ferromagnetic, ferrimagnetic, spin-glass or uncompensated spins) are present [209-213]. For these measurements of the hysteresis loops and the associated loop parameters, the sample was cooled from the PM phase to the measuring temperature in H = 0 for the ZFC or H = 90 kOe for the FC case. After completing the measurements, the sample was warmed to the PM region and cooled back again to the next measuring temperature and the process was repeated. Typical measured hysteresis loops for the ZFC and FC cases are shown in the Figs. 4.14 and 4.15.

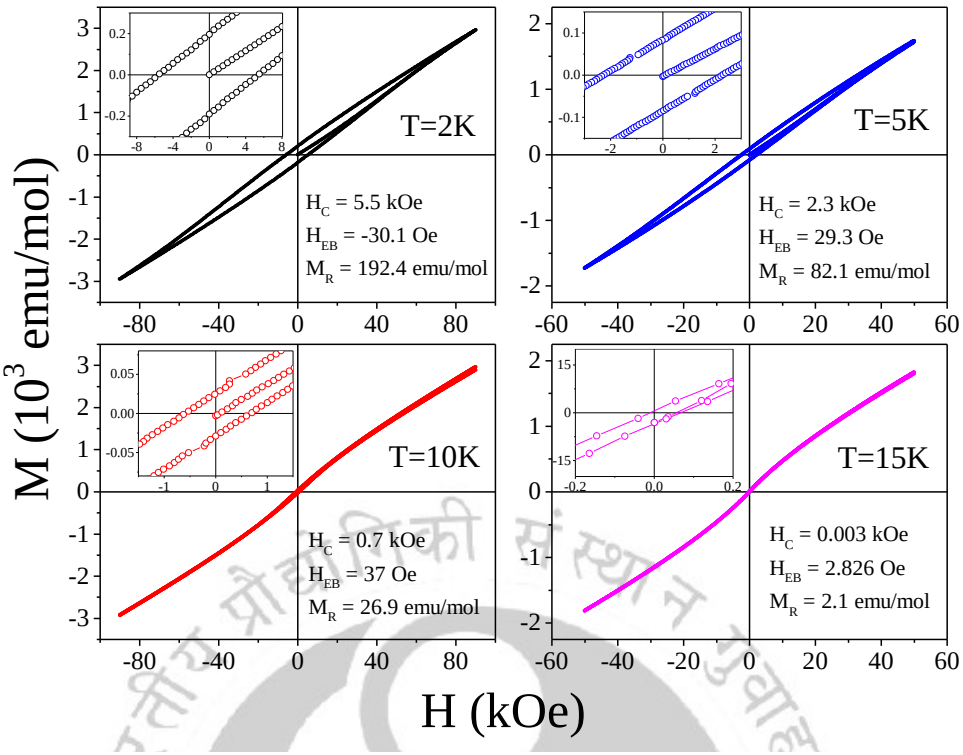

Fig. 4.14: Magnetization (M) versus magnetic field (H) hysteresis loops recorded at four different temperatures under zero-field conditions for CRO. The insets show the zoomed-view of M–H loops near the coercive region. Measured magnitudes of the loop parameters are also listed.

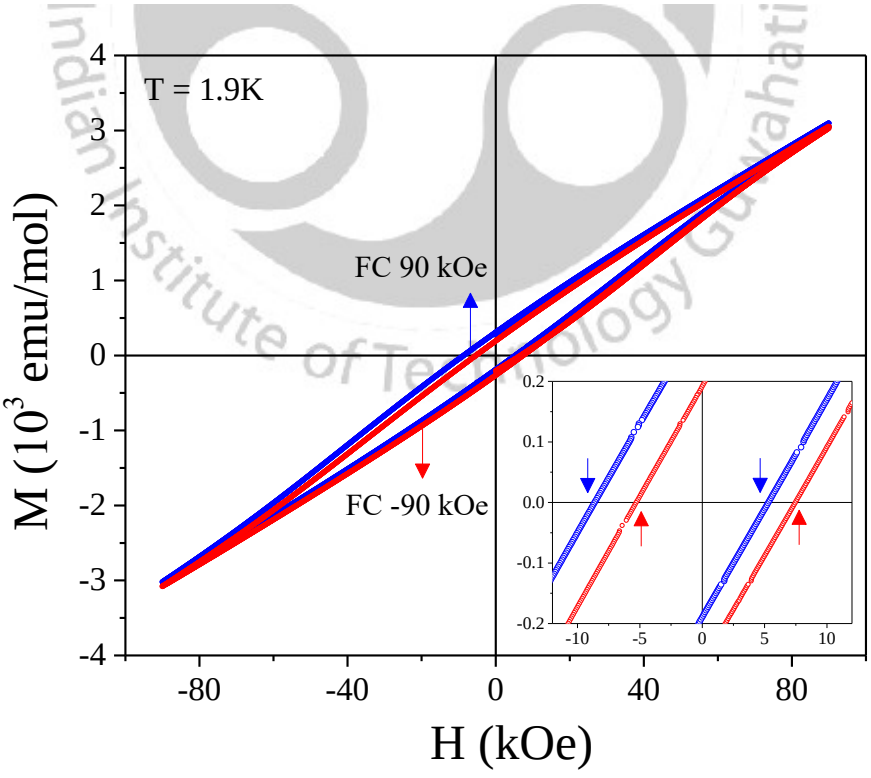

Fig. 4.15: Magnetization (M) versus magnetic field (H) hysteresis loops recorded at 1.9 K under field cooled conditions for CRO. The inset shows the zoomed-view of M–H loops near the coercive region.

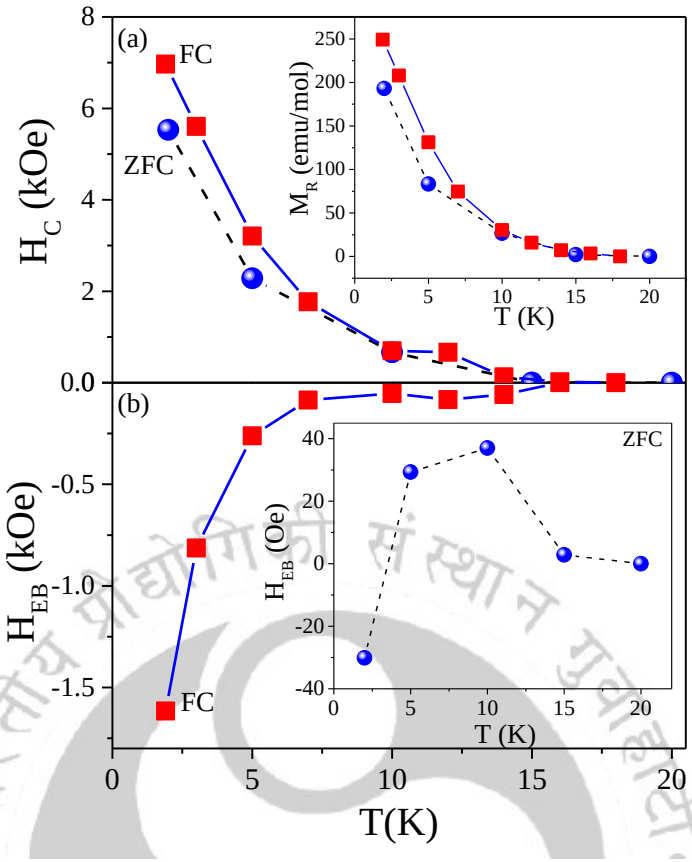

Fig. 4.16: (a)Temperature dependence of coercivity H_C and remanence M_R for the ZFC (solid blue circles) and FC (solid red squares) conditions; (b) Temperature dependence of exchange bias H_{EB} under similar conditions. The lines connecting the data points are drawn for visual guides.

The temperature dependence of the loop parameters for the ZFC and FC cases are displayed in Fig. 4.16. For the ZFC case, H_{EB} is practically zero since the measured value of approximately 20 Oe is within the experimental errors of measuring H. However, for FC in H = 90 kOe, H_{EB} becomes noticeable below 14 K, rising sharply below ≃ 8 K. Similarly, distinct differences between H_C (FC) and H_C (ZFC), and M_R (FC) and M_R (ZFC) begin to appear below ≃ 12K. These observations are consistent with the conclusions described in previous sections that CRO is a mixed phase system containing AFM and SG phases. As noted above, presence of significant H_{EB} for a FC sample is indicative of the presence of AFM phase combined with a phase containing a ferromagnetic component, such as the SG phase for CRO. Note that Mandrus *et al.* reported that in CRO at low temperatures, elongation of A-O bond-lengths and shrinking of B-O bond-lengths occur [21]. This may cause alteration of the spin arrangement and hence influence the AFM and SG couplings thereby resulting in the loop asymmetry or exchange bias in CRO.

4.3.7 Peculiarities in magnetic entropy change:

In this subsection, we present the peculiar changes occurring in the magnetic entropy change (ΔS_M) at temperatures below the long-range-ordering temperatures using the isothermal magnetization data. It is well

known that the magnetocaloric effect (MCE) is the change in the ΔS_M of a material under an applied field H resulting in associated change in its temperature T. For this, ΔS_M is written using the Maxwell equation given by [214-221]:

$$\Delta S_M = \int_0^H \left(\frac{\partial M}{\partial T}\right)_{H'} dH' \tag{4.8}$$

Experimentally, it is easier to measure the isotherms M vs. H at fixed T and determine the area under the isotherm given by $\int M_H dH$. In this case, Eq. (4.8) is replaced by

$$\Delta S_M = \frac{\partial}{\partial T}\int_0^H M\, dH'. \tag{4.9}$$

All the isotherms in CRO were measured under the ZFC condition to access the virgin magnetic state. The temperature difference ΔT between the isotherms were kept small for $T < T_N$ to determine the nature of magnetic ordering in detail. In Fig. 4.17(a), we show selected isotherms for $T > T_N$ and in Fig. 4.17(b), some selected isotherms for $T < T_N$ are shown. Areas under these curves were calculated from H = 0 to 90 kOe. Then the plot of the area (A) vs. T was made and $(\partial A/\partial T)$ vs. T was computed from this plot yielding ΔS_M vs. T according to Eq. (4.9). This plot of $(-\Delta S_M)$ vs. T for CRO is shown in Fig. 4.18(a). Clearly, $(-\Delta S_M)$ is positive for $T > T_P \simeq$ 17K and negative for $T < T_P$. In Fig. 4.18(b), we show the plot of M vs. T and computed $(\partial M/\partial T)$ vs. T covering the temperature range from 2 K to 100 K using the data taken with H = 70 kOe. According to Eq. (4.9), the variation of ΔS_M vs. T should mirror that of $(\partial M/\partial T)_H$ vs. T and this is indeed what is observed in Fig. 4.18. With decrease in T, M increases, reaching a peak at $T_P \simeq 17$ K and then M decreases with decrease in T, showing weak anomalies at T_N and T_{SG} as discussed previously in Fig. 4.6 where plots of χ = M/H and $\partial(\chi T)/\partial T$ are shown. The important points are that for $T > T_P$, $(\partial M/\partial T)$ is negative and so $(-\Delta S_M)$ is positive according to Eq. (4.8). At $T=T_P$, $(\partial M/\partial T)$ is zero making $(-\Delta S_M)$ also zero. For $T< T_P$, $(\partial M/\partial T)$ is positive and $(-\Delta S_M)$ is negative. This agrees with the plot of $(-\Delta S_M)$ vs. T in Fig 4.18(a) in which we have also marked the positions of T_P, T_N and T_{SG} for H ~ 0 where notable anomalies are observed.

The above argument can also be used to compare MCE in different magnetic systems. In paramagnets, and ferromagnets, M vs. T yield negative $(\partial M/\partial T)$, perhaps with an anomaly near T_C in ferromagnets. So, in these systems $(-\Delta S_M)$ is positive. In antiferromagnets and spin glasses, $(\partial M/\partial T)$ is negative (positive) above (below) the transition temperature and so a sign change in $(-\Delta S_M)$ vs. T from positive to negative is expected at T_P as observed in CRO above. The negative $(-\Delta S_M)$ i.e. positive (ΔS_M) implies that entropy and hence magnetic disorder increases when magnetic field is applied. As shown earlier, this is valid for CRO since both T_N and T_{SG} decrease with increase in H although at different rates.

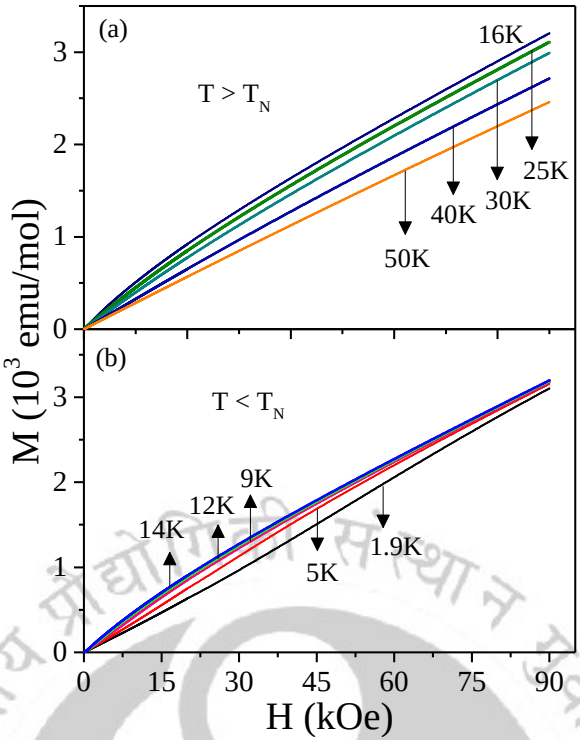

Fig. 4.17: Magnetic field dependence of the isothermal magnetization for selected temperatures are shown for $T > T_N$ in (a) and $T < T_N$ in (b).

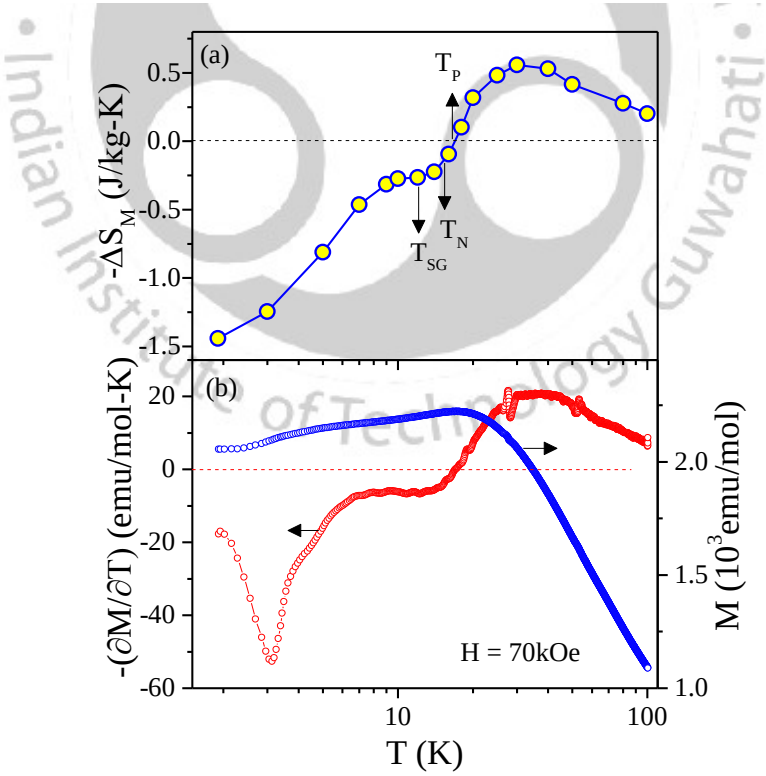

Fig. 4.18: (a) Temperature dependence of magnetic entropy change ($-\Delta S_M$) computed from M-H isotherms using Maxwell equations for a field change $\Delta H = 90$ kOe with the positions of T_N, T_{SG} and T_p marked for H ~ 0. (b) Plots of M vs. T measured under ZFC conditions at H = 70 kOe for CRO (right-hand scale) and computed $-(\partial M/\partial T)$ (left-hand scale).

This argument using the sign of $(\partial M/\partial T)_H$ vs. T can also be used to explain the observed sign change in ($-\Delta S_M$) vs. *T* reported in several other systems (Table 4.1). Most of the systems listed in Table 4.1 are antiferromagnets but some ferromagnets and ferrimagnets are also included in which there is a change in the sign of $(\partial M/\partial T)$ with change in temperature which correlates very well with the reported change in the sign of ($-\Delta S_M$) vs. *T*. These results, whose details can be accessed from the references cited in Table 4.1, provide strong support for the argument presented above and in Fig. 4.18 regarding the correlation of the sign of ($-\Delta S_M$) vs. T with that of $(\partial M/\partial T)$ vs. T in a system. This interpretation of the sign change in the temperature dependence of MCE in some magnetic systems is an important contribution of our work.

Table 4.1: Parameters related to the magnetic entropy change ($-\Delta S_M$) for different oxides.

System	ΔH (kOe)	T_C/T_N (K)	$-\Delta S_M$ (J/kg-K)(T)	Reference
Co_3O_4 (NP)	50	34 (T_N)	0.78 (at 44 K) −0.8 (at 30 K)	[222]
$ZnCr_2O_4$	90	13 (T_N)	0.05 (at 8K) −0.15 (at 15K)	[223]
$NiCr_{1.7}Mn_{0.3}O_4$	0.15	103 (T_C)	0.3 (at 110 K) −0.8 (at 85K)	[224]
$La_{0.125}Ca_{0.875}MnO_3$	70	125 (T_N)	1 (at 140K) −4 (at 115K)	[225]
$Sm_{0.6}Sr_{0.4}MnO_3$	50	118 (T_C)	4 (at 150K) −0.3 (at 10K)	[226]
$Co_2Ti_{0.9}Cr_{0.1}O_4$	1	58.5 (T_C)	0.0065 (at 59K) −0.0055 (at 35K)	[227]
$NdBaMn_2O_6$	90	290 (T_C) 210 (T_N)	4 (at 300K) 2.5 (at 250K) −2 (at 190K)	[228]
$PrBaMn_2O_6$	11	240 (T_N)	−0.1 (at 230K) 0.3 (at 320K)	[229]
Co_2TiO_4	50 kOe	45 (T_N) 31.7 (T_{Comp})	0.6 (at 40K) −0.8 (at 20K)	[43]
$La_{0.7}Sr_{0.3}MnO_3/SrRuO_3$ superlattice	22 kOe	105 (T_N)	0.65 mJ cm^{-3} K^{-1} (at 150K) −0.6 mJ cm^{-3} K^{-1} (at 100K)	[47]
Mn_3O_4	20	42.8 (T_N)	2 (at 40K)	[230]
$MnCr_2O_4$	90	41 (T_C)	1.8 (at 30K)	[223]
Co_2RuO_4	90	15.2 (T_N) 14.2 (T_{SG})	0.55 (at 30K) −1.44 (at 1.9K)	our work

4.4 Conclusions:

A summary of the major conclusions from the results presented in this chapter on CRO is as follows: (i) CRO orders antiferromagnetically with T_N = 15.2 K, followed by cluster spin-glass ordering at $T_{SG} \approx$ 14.2 K. These observations are confirmed by the expected H-dependence of T_N and T_{SG}. (ii) The H-dependence of T_N and T_{SG} is used to construct H-T phase diagram. (iii) The presence of cluster SG phase is further confirmed by the analysis of ac susceptibilities in terms of the Vogel-Fulcher and Power laws, temperature dependence of magnetic viscosity S, and the temperature dependence of coercivity and exchange-bias for a field-cooled sample vis-à-vis zero-field-cooled sample. (iv) The temperature dependence of the paramagnetic susceptibility χ_p (including the effect of χ_0 in Eq. (4.1)) is fit to the Curie-Weiss law yielding magnetic moment $\mu = 4.16\mu_B$ for CRO in good agreement with the expected $\mu = 4.24\mu_B$. and (v) Using molecular field theory, the dominant exchange constant $J_1/k_B \approx 6$K between the Co^{2+} ions on the A-site is determined which is further confirmed by fit of χ_p to high temperature series. (vi) The observed negative MCE below T_N is also related to the AFM and SG states and the correlation between the temperature dependence of $(\partial M/\partial T)$ and (ΔS_M) observed here in CRO is used to explain the observed change in sign of MCE in other oxide systems. And (vii) It is argued that T_N is determined by super-exchange coupling between Co^{2+} ions on the A-site, whereas, T_{SG} is due to the random nature of the weaker A-B interaction between Co^{2+} ions on the A-site and randomly distributed Ru^{3+} ions on the B-site of the spinel structure of CRO.

Chapter 5

Magnetic structure of Co_2TiO_4 and Co_2SnO_4 using neutron diffraction

For a clear and vivid picture of the magnetic structure and better understanding of the ground state spin configuration together with the site dependent magnetic moments, detailed 'Neutron diffraction' studies are very important. Also, to probe a weak tetragonal distortion and cationic distribution, neutron diffraction data are very useful, thus, keeping in view of these aspects we performed detailed low-temperature neutron diffraction measurements on the single-crystalline cobalt orthotitanate, Co_2TiO_4 (CTO) and cobalt orthostannate Co_2SnO_4 (CSO) using the E2, E6, and E9 instruments available at the BER II reactor of the Helmholtz-Zentrum Berlin. Thus, this chapter deals with a systematic comparative study of the neutron diffraction results of CTO and CSO along with the standard magnetization data.

5.1 Brief literature review:

As discussed in previous chapters, substitution of non-magnetic elements (dilution) within the spinel oxides at tetrahedral (A) or octahedral (B) sites often induces disorder or lattice distortions. Such issues may generate new pathways of magnetic interactions leading to some complex ferrimagnetic ordering with altered ground state [141,231-238] and brings about some interesting magnetic phenomena like reentrant spin-glass characteristics, magnetic frustration and bipolar exchange bias [21-24,42,230,239-242]. Among various classes of spinel compounds that exhibit above properties, CTO, cobalt-zinc titanates ($Co_{2-y}Zn_yTiO_4$), cobalt-germanium titanates ($Co_2Ge_xTi_{1-x}O_4$) and CSO are some of the best known FiM systems which shows glassy behavior just below T_N [43,147,243-251]. The magnetic ordering in these compounds have already been studied by several authors in polycrystalline form [22-24,43,147,242,245-249]. In this work we focus on the neutron diffraction studies of CTO together with the magnetic characterization of a single-crystalline sample and compared the results systematically with the polycrystalline CSO. The nature of magnetism in polycrystalline CTO was first investigated by Sakamoto and Yamaguchi in 1962 using temperature dependent remanence and torque measurements [252]. These authors report FiM behavior in CTO with Néel temperature T_N ~ 53 K together with displaced hysteresis loops along the magnetization axis at 4.2 K [252]. Further, Ogawa and Waki report the temperature dependence of specific heat C_P(T) in CTO synthesized by cobalt ammonium sulfate and TiO_2 as precursors [253]. These authors observed a weak anomaly across 49 K in the C_P(T) which is associated to the magnetic transition and reported the Debye temperature Θ_D ~ 560 K with $T^{3/2}$ dependence for T < 30 K [253]. Later studies by Hubsch and Gavoille reported a semi spin-glass transition T_{SG} ~ 46 K (< T_N) in CTO [147]. According to this report CTO undergoes a compensation temperature across 30 K where the two-sublattice magnetizations balance with each other [147]. In 1991, Gavoille *et al*. reported that the random anisotropy plays a major role on the global magnetic behavior of CTO system [245]. Such random anisotropy originates mainly in unsystematic lattice distortions which screen the local charge fluctuations due to large charge difference between the electronic configurations of Co^{2+} and Ti^{4+} [245].

The ac-magnetic susceptibility $\chi_{ac}(T)$ studies by Srivastava *et al*. reveals few multiple transitions in CTO below 20 K which are related to the 'Gaby and Toulouse' type mixed phases T_{M1} and T_{M2} [246,247]. The $\chi_{ac}(T)$ measurements performed in the presence of low dc-bias field dependence ($0 \leq H_{DC} \leq 150$ Oe) for frequency f = 21 Hz show the first transition at 16.5 K due to a transition from PM to SG state, which disappears as the dc-bias field approaches to 150 Oe [246]. In 1975, Sherrington and Kirkpatrick (SK) first established the theoretical study for such reentrant spin-glass behavior in spinels using mean-field approach [254-256]. Later, Gabay and Toulouse extended the SK Ising model calculations to the vector spin-glasses and showed that it is possible to have multiple phase transitions such as: magnetically ordered state $\overset{T_C \text{ or } T_N}{\longleftrightarrow}$ paramagnetic state $\overset{T_{M1}}{\longleftrightarrow}$ mixed phase-1 $\overset{T_{M2}}{\longleftrightarrow}$ mixed phase-2 [257-259]. Preciously our research group reported the electronic state of Ti in CTO should be Ti^{3+} instead of Ti^{4+}, unlike the case of CSO system where Sn^{4+} occupies the octahedral B-sites [22]. Using heat capacity, dc-magnetization and $\chi_{ac}(T)$ studies these authors reported that polycrystalline CTO exhibits a quasi-long-range ferrimagnetic state below $T_N \sim 47.8$ K and a compensation temperature $T_{comp} \sim 32$ K together with giant sign reversible exchange bias at low temperatures [22,42,43]. Although a significant frequency dispersion was observed in $\chi_{ac}(T)$ of CTO, the mathematical analysis based on the Power-law of critical slowing down $\tau = \tau_o [(T-T_{SG})/T_{SG}]^{-z\nu}$ yields a higher value of critical exponent $z\nu = 16$ as compared to $z\nu = 6.4$ for CSO [22,246]. Usually, for a typical SG system the magnitude of $z\nu$ should lie between 4 and 12 [79,260]. Therefore, the $\chi_{ac}(T)$ studies reported in Refs. [22,43] reveal a lack of perfect SG transition below T_N in CTO as compared to CSO (T_{SG} = 39 K < T_N = 41 K) even though the ac-susceptibility data follows the A-T line behavior ($H^{2/3}$ vs T_P) [43].

The coexistence of two magnetic phase transitions (FiM and SG states) in CSO is consistent with the semi spin-glass behavior predicted by Villain [261] and the experimental observations of Srivastava *et al.* [246,247]. Theoretical studies by Villain reveal that the long-range interactions between the canted local spins are responsible for the collective freezing of the transverse spin component at the spin-glass transition [261,262]. In all these studies, the samples are of polycrystalline in nature and no single-crystal study has been reported so far. Therefore, there is a need to pin down the spin configuration of single-crystals of CTO and its sister compound CSO precisely using neutron diffraction measurements below T_N.

5.2 Synthesis and characterization details:

The single-crystalline samples of CTO and CSO were prepared by the floating zone method. For this, the ceramic feed rod of CTO sample was first prepared using the binary transition-metal oxide precursors; cobalt (II, III) oxide (Co_3O_4) and titanium dioxide (TiO_2) of 4N purity powders were taken in appropriate amounts and mixed in ethanol. These mixtures were calcined at 500°C for 12 h in air and finally packed in a rubber tube of cylindrical geometry of 7 mm diameter and 100 mm length. These cylindrical samples were hydrostatically pressed at 2.5 kbars and sintered at 1350°C for 30 h in air (with 200°C/h heating and cooling rates) to obtain high density feed and seed rods for the floating zone growth. Small portions were cut-off from a feed rod and

used for powder X-ray diffraction and magnetization measurements. The CTO crystals have been grown by crucible-free floating zone method in air flow (500 ccm) using the four-mirror type image furnace (CSC, Japan) equipped with 1 kW halogen lamps. The pulling rate was maintained at 1.5-2.0 mm/h. The upper and lower shafts were counter rotated at 15 rpm in order to suppress temperature fluctuations in the molten zone. The as-grown ingot was about 55-60 mm in length and about 6.5 mm in diameter with a metallic luster. The powder samples of CSO have been prepared by standard solid-state-reaction method similar to the method given in section 2.2.1.1. Neutron powder diffraction experiments were carried out on a crushed CTO single crystal using the instruments E2, E6, and E9 available at the BER II reactor of the Helmholtz-Zentrum Berlin. The instrument E9 uses a Ge-monochromator with neutron wavelength λ = 1.309 Å, while the instruments E2 and E6 use a pyrolytic graphite (PG) monochromator of neutron wavelengths λ = 2.38 Å and λ = 2.42 Å, respectively. On these instruments powder patterns were recorded between different ranges of diffraction angles: (a) 19.2 and 95.3° (E2), (b) 5.5 and 136.4° (E6), and (c) 5 and 141.8° (E9). On the instrument E2, neutron powder diffraction patterns of single-crystal CTO and polycrystalline CSO were collected at 1.6 (magnetically ordered regime) and 80 K (paramagnetic region) with very good counting statistics (24 hrs/pattern). In order to improve the instrumental resolution during the experiments we have used a 15 min collimator. The temperature dependence of magnetic ordering of both CTO and CSO has been investigated on the instrument E6.

The crystal and magnetic structures of cylindrical form of CTO single-crystal of dimension d = 6.3 mm and h = 6.5 mm have been investigated using the four-circle diffractometer E5. The data were collected with a two-dimensional position sensitive ^{3}He-detector, 90 × 90 mm (32 × 32 pixels). The instrument E5 uses a Cu and PG monochromator selecting the neutron wavelengths λ = 0.896 and 2.39 Å, respectively. The shorter neutron wavelength has been used to collect a full data set to examine the crystal structure of CTO in detail. For the investigation of the magnetic structure we have used the plane grating (PG) monochromator. To study the crystal structure at low temperature, a powder sample (crushed crystal) of CTO was used. Neutron powder patterns were collected on the instrument E9 at 2 K and 60 K. Furthermore, we have followed the thermal variation of the intensity of prominent nuclear and magnetic Bragg reflections. The refinements of the crystal and magnetic structure were carried out with the *FullProf* suite [263]. In addition to this we have used the program *Xtal* 3.4 (Ref. [264]) for the refinements using the single-crystal data of CTO collected at room temperature. For the absorption correction (Gaussian integration) we used the absorption coefficient μ = 0.75 cm^{-1}. Secondary extinction has been corrected using the formalism of Zachariasen (type I) and the following nuclear scattering lengths were used [265]: b(O) = 5.805 fm, b(Ti) = 3.30 fm, b(Co) = 2.50 fm, and b(Sn) = 6.228 fm [266]. The magnetic form factors of Ti^{3+}, Co^{2+} and Co^{3+} ions were taken from Ref. [266]. The ac-magnetic susceptibility (χ_{ac}) and dc-magnetization measurements (M) were performed using a superconducting quantum interference device (SQUID) based magnetometer from Quantum-design with temperature ability to reach 2 K from 320 K and magnetic field (H) up to ±70 kOe. The low temperature heat capacity data were recorded by means of a physical property measurement system (PPMS) from Quantum Design.

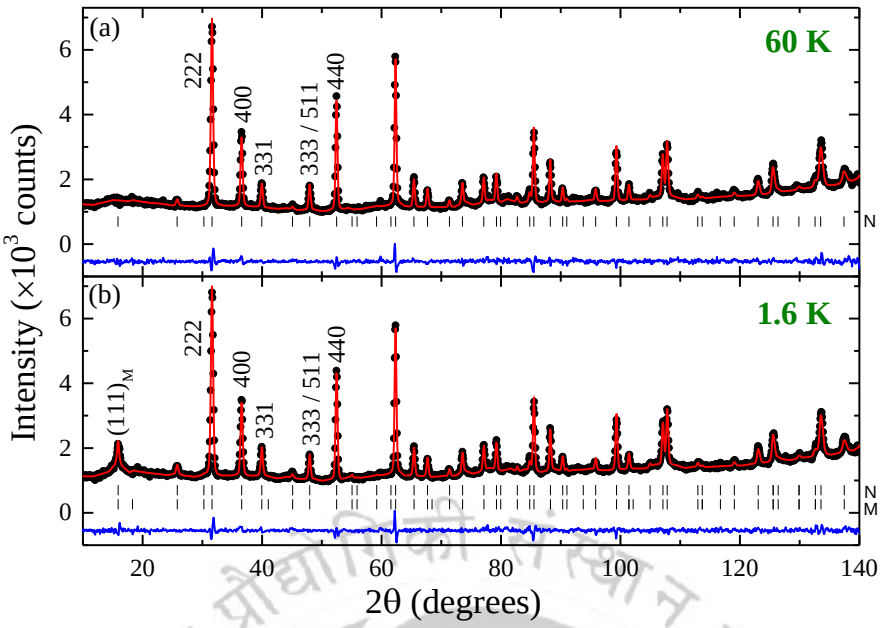

Fig. 5.1: Rietveld refinements of the neutron powder diffraction data of CTO collected at 1.6 K and 60 K. The crystal structure was refined in the cubic space group *Fd-3m*. The calculated patterns (red) are compared with the observed one (black circles). In the lower part of each diagram the difference pattern (blue) as well as the positions of the nuclear reflections of CTO are shown. In the powder pattern collected at 1.6 K magnetic intensity appears at the position of the reflections (111).

5.3 Results and discussion:

5.3.1 Crystal and electronic structure:

Figure 5.1 shows the neutron powder diffraction pattern of CTO collected at temperatures between 1.6 K and 60 K together with their Rietveld refinement data. The calculated patterns (shown in red color) are compared with the experimentally observed data (shown in black circles). In the lower part of each diagram the difference pattern (shown in blue color) as well as the positions of the nuclear reflections of CTO is shown. In the powder pattern collected at 1.6 K magnetic intensity appears at the position of the reflections $(111)_M$. In order to check the correctness of the chemical composition we have investigated the detailed crystal structure of CTO. At room temperature no additional reflections could be detected, which clearly indicated that the *F* centering and the *d*-glide planes are not lost. For the refinements a total of 1680 (94 unique) reflections were collected in the 2θ range from 5.3 to 48.6°. Due to the vastly different scattering lengths of the titanium and cobalt atoms we were able to determine the occupancies of these atoms with good accuracy. For the A site and B site the metal atoms are located at the Wyckoff positions 8*b*(⅜,⅜,⅜) and 16*c*(0,0,0), while the O atoms are located at the position 16*e*(*x*,*x*,*x*). During the refinement we allowed to vary the following parameters: (i) the overall scale and extinction factor *g*, (ii) the positional parameter *x* of the O atom, and (iii) the isotropic thermal parameters of the Ti and Co atoms as well as the anisotropic thermal parameters Y_{11} (= Y_{22} = Y_{33}) and Y_{12} (= Y_{13} = Y_{23}) of the O atom. For the A and B sites we have used the constraint *occ*(Ti) + *occ*(Co) = 1. Further we have used the

constraint for the isotropic thermal parameters Y of the atoms of the A and B sites. This is due to the fact that the scattering power of the B site is strongly reduced by a partial compensation of the positive and negative scattering lengths of the Co and Ti atoms. However, the refinements resulted in a satisfactory residuals R_F = 0.043 defined as $R_F = \sum(||F_o^2| - |F_c^2||) / \sum|F_o^2|$. For the A site we have obtained the occupancies occ(Ti) = -0.031(16) and occ(Co) = +1.031(16). This clearly shows that the A site is fully occupied with Co^{2+} ions. On the other hand, the occupancies of the B site were found to be occ(Ti) = 0.513(8) and occ(Co) = 0.487(8). These are very close to the expected values of 0.5. Thus, our investigation does confirm the highly unusual oxidation state of Ti ions (+3) in the crystal structure of CTO phase when prepared in air. For the extinction parameter g, which is related to the mosaic distribution, we obtained the value g = 929(113) rad^{-1}. The results of the refinements are summarised in Table 5.1.

In order to investigate the structural properties at low temperature we have collected neutron powder diffraction data on E9 at 1.6 and 60 K (Fig. 5.1), in the magnetically ordered regime as well as in the paramagnetic region. In Fig. 5.1 it can be seen that additional intensity occurs at the position of the reflection (111) due to a ferrimagnetic ordering at 1.6 K, which will be discussed in detail in the following section. Furthermore, in the low-temperature powder pattern we could not found any peak splitting or broadening. Therefore, within the instrumental resolution we cannot find a transition to a lower symmetric structure. For example, the normal spinel $NiCr_2O_4$ shows a transition from the cubic space group *Fd-3m* to tetragonal one with the space group $I4_1/amd$ followed by another transition into an orthorhombic structure with the space group *Fddd* [267]. A refinement in the next lower symmetric space group $I4_1/amd$ resulted in lattice parameters $a_{orth} = a_{tet}\sqrt{2}$ = 8.4402(14) Å, and $c_{orth} = c_{tet}\sqrt{2}$ = 8.4416(29) Å. Further, in Table 5.1 it can be seen that the changes of the refined parameters are negligible from 297 K down to 1.6 K. Interestingly, our single-crystal data showed that the thermal variation results in a strong change of the intensity of strong nuclear reflections (Fig. 5.2).

Table 5.1: Results of the refinements of the single-crystal (sc) neutron diffraction study of CTO collected on E5 at 297 K. The refinement of the crystal structure was carried out in the cubic space group *Fd-3m* (cell choice 2). The thermal parameters Y_{ij} (given in 100 $Å^2$) are in the form $\exp[-2\pi^2(Y_{11}\,h^2a^{*2} + \ldots 2Y_{13}\,hla^*c^*)]$. For symmetry reasons one finds for the O atom $x = y = z$, $Y_{11} = Y_{22} = Y_{33}$, and $Y_{12} = Y_{13} = Y_{23}$. In the lower part of the Table the positional and isotropic thermal parameter of the O atoms are given as obtained from the neutron powder diffraction study (pc) on E9 at 1.6 and 60 K, respectively.

E5, sc	*Fd-3m*	*x*	*y*	*z*	Y_{11}	Y_{12}
$Co2^{2+}$	8*b*	3/8	3/8	3/8	0.51(7)	-
$Ti^{3+}/Co1^{3+}$	16*c*	0	0	0	0.51	-
O	32*e*	0.24002(11)	0.24002	0.24002	1.06(5)	−0.23(2)
Lattice parameter: a = 8.4440(4) Å at 297 K, R_F = 0.043						
E9, pc	*Fd-3m*	*x*	*y*	*z*	Y_s	
$Co2^{2+}$	8*b*	3/8	3/8	3/8	0.80(2)	
$Ti^{3+}/Co1^{3+}$	16*c*	0	0	0	0.80	
O (at 60 K)	32*e*	0.23937(6)	0.23937	0.23937	1.07(2)	
Lattice parameter: a = 8.4413(2) Å at 1.6 K, R_F = 0.047; a = 8.4421(2) Å (60 K), R_F = 0.062						

The strong increase of the (400) reflection of about 65% (from 60 K down to 8 K) cannot be purely ascribed to an increase of magnetic intensity. From our powder data collected on E2 the increase is only 16%. In this case the increase in the intensity of the neutron powder diffraction peak (400) can be purely ascribed to an onset of the magnetic ordering, because of the absence of secondary extinction. On the contrary, for the single crystal one can clearly confirm the presence of extinction effects from the crystal structure refinements as discussed above. Such effect can be ascribed to a change of the orientation of mosaic blocks in the single crystal caused by strain effects and results in an increased broadening of Bragg reflections with decreased extinction. Since the extinction coefficients '*y*' refer to the reductions in F^2 ($y \sim F_{obs}^2/F_{cal}^2$), the intensities of the strongest reflections are significantly affected. Moreover, for the reflection (222), which is at 60 K even stronger than the (400), this effect is much less pronounced. Here we found an increase of only 7% and 14% from the powder (E2) and the single-crystal diffraction (E5) experiments, respectively. This indicates that the change of mosaicity (or extinction) is anisotropic at low temperature. This effect was also observed by a high-resolution synchrotron powder diffraction study of $Ni_{0.85}Cu_{0.15}Cr_2O_4$, where a strong peak broadening was observed for (400), whereas

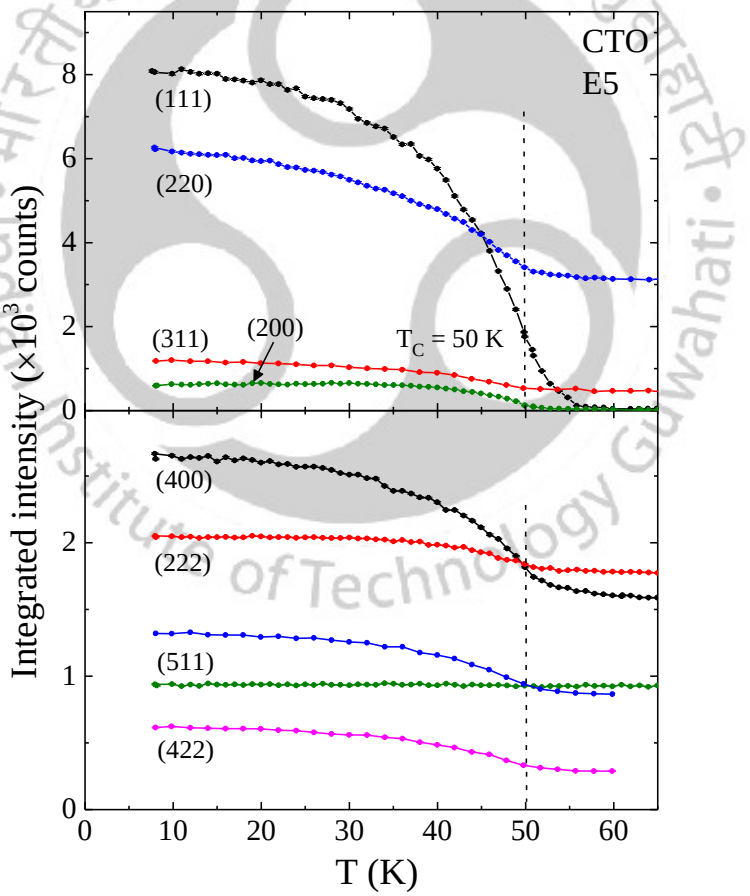

Fig. 5.2: Temperature dependence of nuclear and magnetic Bragg reflections of CTO single crystal. The strongest magnetic intensity shows the reflections 111, which is increasing well above Curie temperature T_C = 50 K. The presence of the magnetic reflection 200 can be ascribed to an additional weak antiferromagnetic ordering. The strong increase of the 400 indicates the existence of anisotropic change of the mosaicity in the crystal.

the reflection (222) remains unchanged [267]. Thus, the strong anisotropic strain broadening is essentially based on competing Jahn-Teller effects acting along different crystallographic axes. For the Co^{2+} ions at the A site, which have the $3d^7$ configuration, cooperative distortions of the CoO_4 tetrahedra through the Jahn-Teller effect should be absent. Nevertheless, electronic energy could be gained for the Ti^{3+} and Co^{3+} ions having the $3d^1$ and $3d^6$ configurations, respectively. For both ions the t_{2g} levels are expected to split into a lower d_{xy} level and a higher twofold generate d_{xz}/d_{yz} level. Thus, one would expect for both ions tetragonal distortions with a c/a ratio smaller than 1. From the refined tetragonal lattice parameters of CTO in the space group $I4_1/amd$ as given above we obtained a c/a ratio of 1.0002(7), which is practically equal to 1. On the other hand, it has to be mentioned that the reflection (400) measured at 1.6 K was found to be slightly broader than that measured at 60 K (FWHM from 0.414° to 0.429°). A similar trend shows the reflection (222) (FWHM from 0.423 to 0.440°). However, the observed FWHM values practically represent the instrumental resolution. Therefore, the FWHM of the reflection (222) is slightly larger than that of the (400). This confirms that a tetragonal splitting is hard to detect from our powder data, since a significant peak broadening should only expect for the reflection (400) (into (400)/(040) and (004)). For comparison the reflection (400), measured in our single-crystal experiment, was found to be even broader (FWHM = 0.73°) considering the instrumental resolution ($\mathrm{FWHM}_{sam} = \sqrt{\mathrm{FWHM}_{obs}^2 - \mathrm{FWHM}_{instr}^2}$). As discussed above the intrinsic peak broadening can be ascribed to a rougher orientation of mosaic blocks in the single crystal. Due the worse resolution of the PG monochromator and the intrinsic peak broadening no change of the peak width is observable between 8 and 80 K. Furthermore, it is important to note that CTO does not show a spontaneous structural phase transition, which agrees with our neutron powder data. In Fig. 5.2 it can be seen that such a transition is smeared out due to the structural disorder in this material. However, extinction effects can give us additional information about the increase of anisotropic strain effects, which are locally induced by the Jahn-Teller effect in the CTO single crystal.

In order to determine the electronic state of all the ions present in the single crystal CTO systems, we performed the X-ray photoelectron spectroscopy (XPS) measurements with Al-K_α X-rays as source. Figure 5.3 shows the photoelectron intensity of the sample versus binding energy (eV) of the core level spectra of (a) Co-2*p* (b) Ti-2*p* and (c) O-1*s*, and (d) Co-2*p* (e) Sn-3*d* and (f) O-1*s* for CTO single crystal and CSO polycrystal, respectively. We noticed two major peaks at 780.58 eV and 795.68 eV associated with the spin-orbit splitting ($^2p_{3/2}$ and $^2p_{1/2}$ levels) which are further deconvoluted into four peaks at 780.35 eV(P_1), 782.26 eV(P_2), 795.85 eV(P_3) and 797.26 eV(P_4) signifying the presence of Co^{3+} state [Doublet: P_2–P_4] in addition to the Co^{2+} [Doublet: P_1–P_3]. In addition, three weak broad satellite peaks were noticed at 773.46 eV (S_1), 785.84 eV (S_2) and 802.45 eV (S_3). Usually, the energy splitting (ΔE) between the two levels due to spin-orbit coupling should be different for the divalent and trivalent Co ions with ΔE = 15.7 eV and 15.0 eV for Co^{2+} and Co^{3+}, respectively [268-270]. In the present case for CTO single crystal the separations between the doublet peaks found to be $\Delta E_{P1\text{-}P3}$ = 15.5 eV and $\Delta E_{P2\text{-}P4}$ = 15 eV corresponding to the Co^{2+} and Co^{3+} respectively. On the other hand, the highest intensity

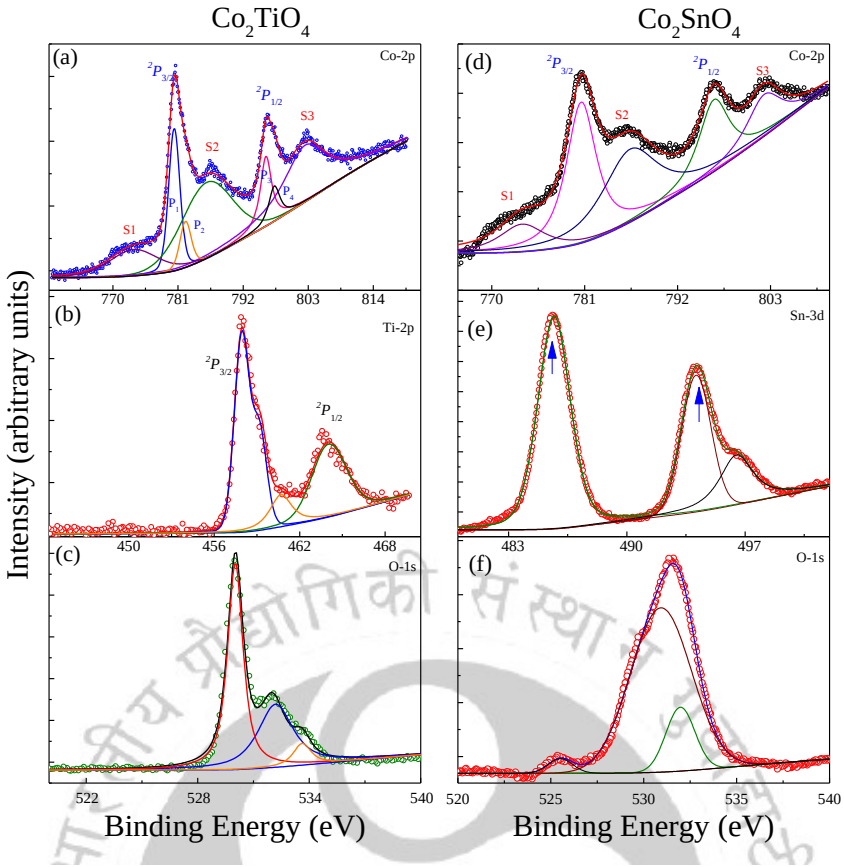

Fig. 5.3: The X-ray photoelectron spectra (XPS) of (a) Co-2p, (b) Ti-2p and (c) O-1s peaks of single crystal CTO and (d) Co-2p, (e) Sn-3d and (f) O-1s peaks of polycrystalline CSO.

peak for Ti-$^2p_{3/2}$ centered at 457.93 eV, together with this peak we noticed a second peak across 463.75 eV corresponding to Ti-$^2p_{1/2}$ (Fig. 5.3(b)). Usually, Ti ions exhibit tetravalent oxidation state in most of the oxides; for example in TiO_2 the binding energy separation for doublets of Ti $\Delta[^2p_{3/2}\text{-}^2p_{3/2}]$ = 5.7 eV, however, in the present case the $\Delta[^2p_{3/2}\text{-}^2p_{3/2}]$ = 5.82 eV signifying the presence of Ti^{3+}. The observed position of the peak at 457.93 eV agrees with the previously reported data of Ti^{3+} surface defects in TiO_2 system [271]. Moreover, our observations rule out the presence of any metallic 'Ti' ions in CTO matrix which usually show their signatures in XPS spectra at 454 eV [272]. Fig. 5.3(c) shows the core level spectra of O-1*s* which requires a minimum of three Gaussian-Lorentzian peaks to reproduce the experimentally observed XPS spectra. These deconvoluted peaks are centered at 530.03 eV, 532.20 eV and 533.63 eV signifying the presence of surface oxygen, metal-ligand bonding and excess oxygen present in the system [268-270,138,273,274]. On the contrary, the Co-2*p* XPS spectrum (Fig. 5.3(d)) for CSO deconvoluted only into two major peaks at 780.6 eV and 796.3 eV, with satellite peaks at 786.15 eV and 802.4 eV. The binding energy seperation ΔE between the two major peaks ($^2p_{3/2}$ and $^2p_{1/2}$) is 15.7eV, which confirms the presence of divalent oxidation state of Co *i.e.* Co^{2+}, and no additional signatures for the Co^{3+} state are observed in CSO. Fig. 5.3(e) shows the Sn-3*d* core level XPS spectrum for CSO which exhibits sharp peaks at 485.65 eV and 494.8 eV and a weak shoulder at 496.75 eV signifying the presence of the Sn^{4+} state. The O-1*s* XPS spectra (Fig. 5.3(f)) show the characteristics of Co–O lattice oxygen and surface oxygen. As compared to the single crystal O-1*s* core level spectra there is a significant asymmetric peak

broadening was noticed which may be associated with the presence of increase in surface oxygen vacancies [275]. Usually polycrystalline samples contain many grain boundaties and dislocations as compared to the single crystalline sample. Moreover, in polycrystalline cobalt orthotitanate the peak positions are shifted towards higher binding energy (and an additional peak at 527.8 eV) due to the significant role of electronegativity (since the oxygen ions are linked with different electronic states of cobalt and titanium ions) [276]. On the contrary, in cobalt orthostannate the oxygen ion is bonded with only divalent cobalt ions at both tetrahedral-A and octahedral-B sites along with the tetravalent stannus ions, therefore electronegativity play a small role [276]. From this analysis we observed that CTO single crystal exhibits electronic structure (give as $[Co^{2+}][Co^{3+}Ti^{3+}]O_4$) similar to that of the polycrystalline samples reported recently [22].

5.3.2 Microscopic magnetic moments and magnetic structure:

For a detailed understanding of the magnetic order in CTO we have collected the powder patterns on the instruments E2 and E6. It has already been mentioned above that Co^{2+} occupies the A site, and the magnetic ions Ti^{3+} and Co^{3+} statistically occupies the B site. Complementary to this study we also have investigated the magnetic ordering of CSO to separate out the individual contributions of the Co^{2+} and Co^{3+} ions. In this compound the B site is occupied with magnetic Co^{2+} and diamagnetic Sn^{4+} ions. Neutron powder diffraction patterns of CTO and CSO were collected at 1.6 and 80 K on the instrument E2. In Fig. 5.4 it can be seen that the intensities of the nuclear Bragg reflections are significantly different for CTO as compared to CSO. This can be attributed to the strongly different scattering lengths of the Ti and Sn atoms. The refinements of structural parameters at 80 K resulted in satisfactory residuals of R_F = 0.031 (CTO) and R_F = 0.014 (CSO). In contrast, the difference patterns of both compounds (Fig. 5.4) look very similar indicating that their magnetic structures are practically the same. Here all magnetic intensities were found to be on the positions of allowed nuclear Bragg reflections, which indicate a FiM ordering between the atoms located at the tetrahedral and octahedral sites. Figure 5.4 shows that both the strongest magnetic intensities can be observed at the position of the reflection (111). The only difference arises through the presence of the magnetic reflection $(200)_M$ in the powder pattern of CTO, which is forbidden for the cubic space group *Fd-3m*. Thus, the presence of this reflection suggests a loss of at least one of the *d*-glide planes resulting in an additional antiferromagnetic ordering with a moment direction perpendicular to the ferrimagnetic ones. Magnetic intensity of the $(200)_M$ can be generated, if the moments of the Co1(Ti) atoms at the positions (1) 0,0,0; (2) ¾,¼,½; (3) ¼,½,¾; (4) ½,¾,¼ show the spin sequences $+--+$, $+-+-$ and $++--$. Due to the fact, that the reflection $(200)_M$ could only be observed for CTO the existence of an additional AFM ordering in CSO can be excluded.

A similar type of ordering was found for the Cu-rich chromites in the system $Ni_{1-x}Cu_xCr_2O_4$ [277]. In both spinel types one finds strong exchange interactions between the atoms located at the tetrahedral and octahedral sites resulting in a ferrimagnetic spin alignment. For the chromites, where orthorhombic distortions (space group *Fddd*) are strongly pronounced, the ferri- and antiferromagnetic components were found to parallel to the *a* and

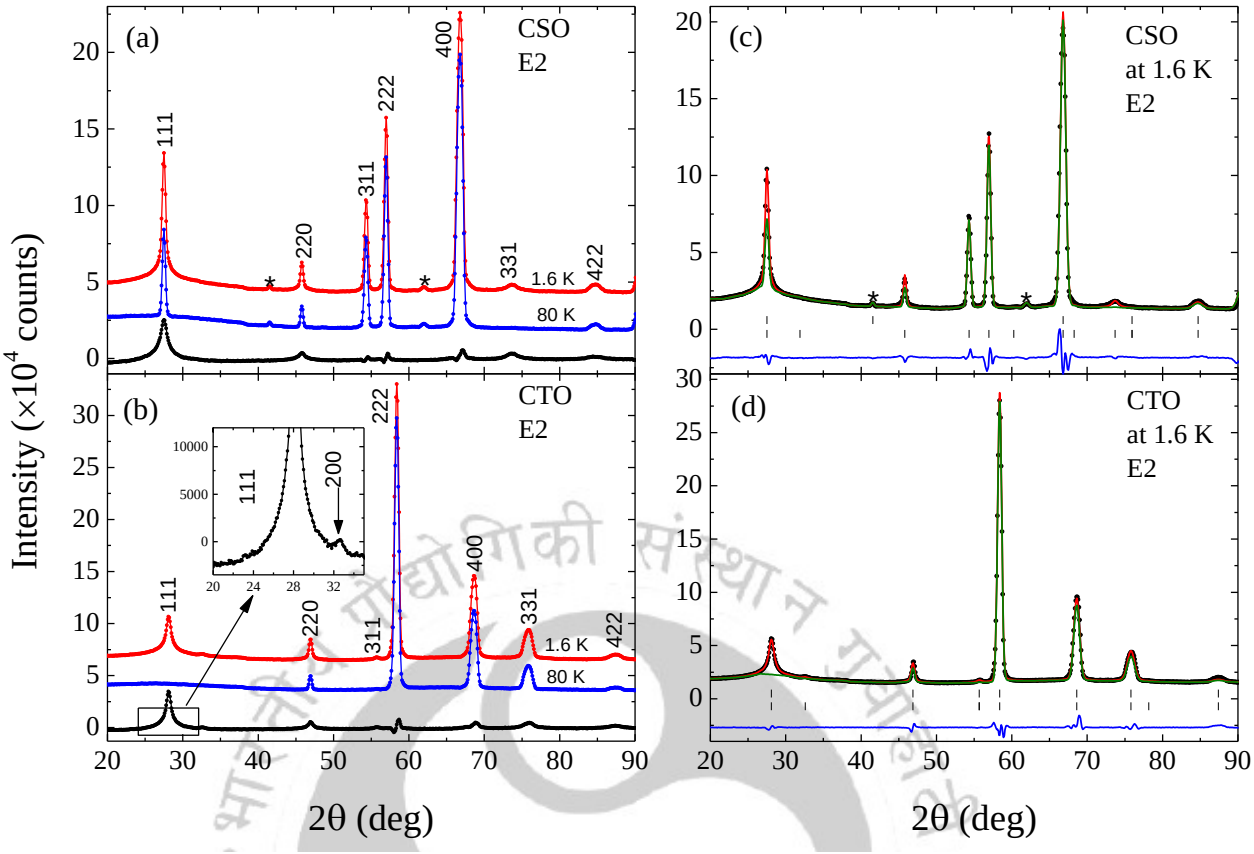

Fig. 5.4: Neutron powder patterns of (a) CSO and (b) CTO at 1.6 (blue) and 80 K (red) collected on the instrument E2. Due to the vastly different scattering lengths of the Ti and Sn atoms the intensities of the nuclear reflections of CTO and CSO strongly differ. In contrast, the difference patterns (black) of both compounds are very similar indicating that the magnetic ordering is practically the same. The only difference arises through the presence of the magnetic reflection $(200)_M$ in the powder pattern of CTO. The observed and calculated powder patterns of (c) CSO and (d) CTO as obtained from Rietveld refinements are compared in the right part of the figure. The calculated patterns (red) are compared with the observed one (black circles). In the lower part of each diagram the difference pattern (blue) as well as the positions of the nuclear reflections of CTO are shown. For comparison the calculated of the pure nuclear part (green) is also shown. The sample of CSO contains a small impurity of SnO_2. The positions of the strongest reflections are marked with stars.

c axis, respectively. Further it has to be mentioned that in $NiCr_2O_4$ the ferrimagnetic and the antiferromagnetic transition sets in at two different magnetic transition temperatures, where the magnetic ordering can be described with two different propagation vectors [277].

In contrast to the system $Ni_{1-x}Cu_xCr_2O_4$, we could not distinguish the difference between the three cubic axes of CTO and CSO. For the Co^{2+} ions (in our case Co_2) at the A site, which have the $3d^7$ configuration ($e_g^4t_{2g}^3$), cooperative distortions of the CoO_4 tetrahedra through the Jahn-Teller effect should be absent. Assuming a high-spin state three unpaired electrons in the t_{2g} level give a magnetic moment $\mu_{eff} = g \cdot S = 3.0\ \mu_B$. On the other hand, electronic energy could be gained for the Ti^{3+} and Co^{3+} ions (in our case Co_1) having the $3d^1$ ($t_{2g}^1e_g^0$) and $3d^6$ ($t_{2g}^4e_g^2$) configurations, respectively. For both ions the t_{2g} levels are expected to split into a lower d_{xy} level and a higher twofold generate d_{xz}/d_{yz} level. Here Ti^{3+} have one and Co^{3+} have four unpaired electrons and

accordingly one expects magnetic moments μ_{eff} = 1.0 μ_B and μ_{eff} = 4.0 μ_B, respectively. Therefore, we have used in the refinements, as described in detail below, of CTO a constraint $\mu(Co^{3+}) = 4\ \mu(Ti^{3+})$.

Interestingly, in Fig. 5.4 it can be seen that the magnetic peak $(111)_M$ of both CTO and CSO is much broader than the nuclear one (111) observed for CSO. The Rietveld refinements of the powder patterns of both CTO and CSO (collected on E2) resulted in the best fit for the nuclear reflections, where a pure Gaussian profile was used. In contrast, for the magnetic reflections, a pure Lorentzian resulted in the best fit. Usually, the diffraction profiles of both the nuclear and magnetic reflections are expected to be the same. The origin of the peak broadening of the magnetic $(111)_M$ reflection in the powder pattern may be related to the disorder of the Ti and Co cations at the B site, which form perfect-crystal microdomains (called magnetic mosaic blocks) leading to a Lorentzian distribution. On the other hand, the absence of secondary extinction in the powder diffraction data signifies the fact that the magnetic moments are not perfectly ordered. Usually in the case of a perfect 3-dimensional magnetic order, one would expect the similar peak profiles as observed in the case of nuclear ones. The cause of this effect might be the statistical distribution of Co and Ti/Sn atoms at the B site. Therefore, one can assume that a part of the moments shows a partial disorder in a so-called spin-glass state (the ac-magnetization dynamics discussed later provides further evidence to the existence of spin-glass state in the CTO single crystals). In order to estimate the degree of 3-dimensional magnetic ordering we have deduced the correlation lengths (defined as ξ = 1/*HWHM*) from the strongly broadened magnetic reflection $(111)_M$. For CTO, where the magnetic reflection $(111)_M$ is much stronger pronounced that the nuclear one (111), we could obtain from the neutron powder data

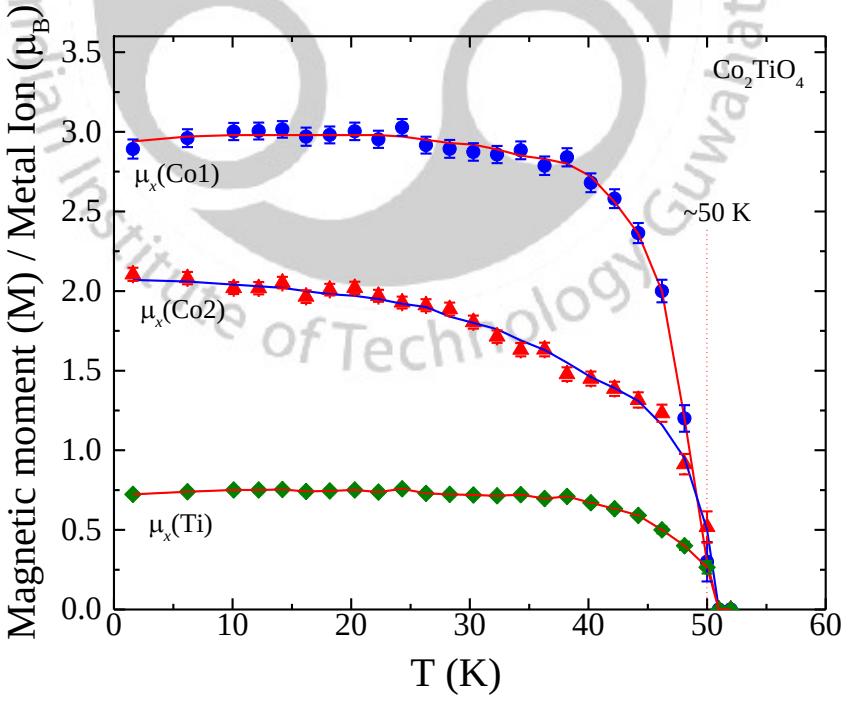

Fig. 5.5: Temperature dependence of magnetic moments of the cobalt and titanium atoms in CTO. Below the Curie temperature T_C = 50 K the magnetic moments of Co1 and Ti atoms located at the B site are coupled antiparallel to the moments of the Co2 atoms located at the A site. During the refinement we have used a moment ratio $\mu(Co^{3+})/\mu(Ti^{3+}) = 4$. As well as the moment direction parallel to the *a* axis.

Table 5.2: Magnetic moments (in μ_B) of the Co and Ti atoms in CTO and CSO at 1.6 K as obtained from the refinements using the neutron diffraction data collected on the instruments E2 and E6. In the space group $Fd\bar{3}m$ (cell choice 2) the magnetic Co1(Ti) atoms are located at the positions (1) 0,0,0; (2) ¾,¼,½; (3) ¼.½,¾; (4) ½,¾,¼; while the Co2 atoms are located at (1) ⅜,⅜,⅜; (2) ⅛,⅝,⅛, respectively. The ferrimagnetically (FI) and antiferromagnetically (AF) coupled moments are lying orthogonal to each other.

Moment	CTO, E2	CTO, E6	CSO, E2	CSO, E6
μ(Co1), FI	3.04(6)	2.89(6)	2.57(11)	2.18(11)
μ(Ti), FI	0.76(2)	0.72(2)	-	-
μ(Co1), FI	0.89(9)	0.55(17)	-	-
μ(Ti), AF	0.22(2)	0.14(4)	-	-
μ_{tot}(Co1)	3.17(5)	2.94(6)	2.57(11)	2.18(11)
μ_{tot}(Ti)	0.79(2)	0.74(2)	-	-
μ(Co2), FI	1.62(4)	2.11(4)	2.04(7)	1.97(6)
R_M	0.058	0.083	0.060	0.124

the correlation length ξ ~ 15 Å. For comparison, the obtained correlation length ξ ~ 20 Å, obtained from the single-crystal data, was found to be somewhat larger. However, in the present study we have used the integrated magnetic intensities of both CTO and CSO to estimate the magnitude of the magnetic moments (μ). The results of the refinements are summarized in Figs. 5.4, 5.5 and in Table 5.2. For the Co^{2+} and Co^{3+} ions one finds three and four unpaired electrons, respectively. Assuming a spin-only system the expected theoretical magnetic moments ($\mu_{eff} = g\,S\,\mu_B$) are $\mu_{eff} = 3.0\ \mu_B$ (Co^{2+}) and $\mu_{eff} = 4.0\ \mu_B$ (Co^{3+}). Assuming Co^{2+} on the A site and Co^{3+} on the B site it can be seen that the experimental moments are somewhat reduced, where one finds for Co1 atoms on the B site $\mu_{tot}(Co1) = 3.17(5)\mu_B$ (E2) and $\mu_{tot}(Co1) = 2.94(6)\mu_B$ (E6), and for the Ti atoms $\mu_{tot}(Ti) = 0.79(2)\mu_B$ (E2) and $\mu_{tot}(Ti) = 0.74(2)\mu_B$ (E6). For Co2 on the A site the moments are $\mu_{tot}(Co1) = 1.62(4)\mu_B$ (E2) and $\mu_{tot}(Co1) = 2.11(4)\mu_B$ (E6). Due to the much better counting statistics on E2 we were able to determine the *z* component of Co1/Ti with better accuracy. Here we found the values $\mu_x(Co1) = 0.89(9)\mu_B$ and $\mu_x(Ti) = 0.22(2)\mu_B$. For CSO the strongest magnetic intensity was also found at the position of the reflection (111). In Fig. 5.4, it can be seen that the nuclear intensity of the (111) of CSO is rather strong, whereas in the case of CTO it was negligible. Therefore, the magnetic moments could not be determined with same accuracy as those of CTO. Interestingly for CSO no intensity could be observed on the position of the reflection 200 (as shown in Fig. 5.4), suggesting the absence of an additional AFM component. Due to this reason we were not able to determine the temperature dependence of magnetic moments of CSO precisely from our E6 experimental data. Therefore, in Fig. 5.5 we only present the temperature dependence of the magnetic moments of the cobalt and titanium atoms in CTO. Below the ferrimagnetic Néel temperature T_N ~ 48.6 K (estimated from $\partial(\chi_{DC}T)/\partial T$ vs. T as shown in Fig. 5.6) the magnetic moments of Co1 and Ti atoms located at the B sites are coupled antiparallel to the moments of the Co2 atoms located at the A site. During the refinement we have used a moment ratio

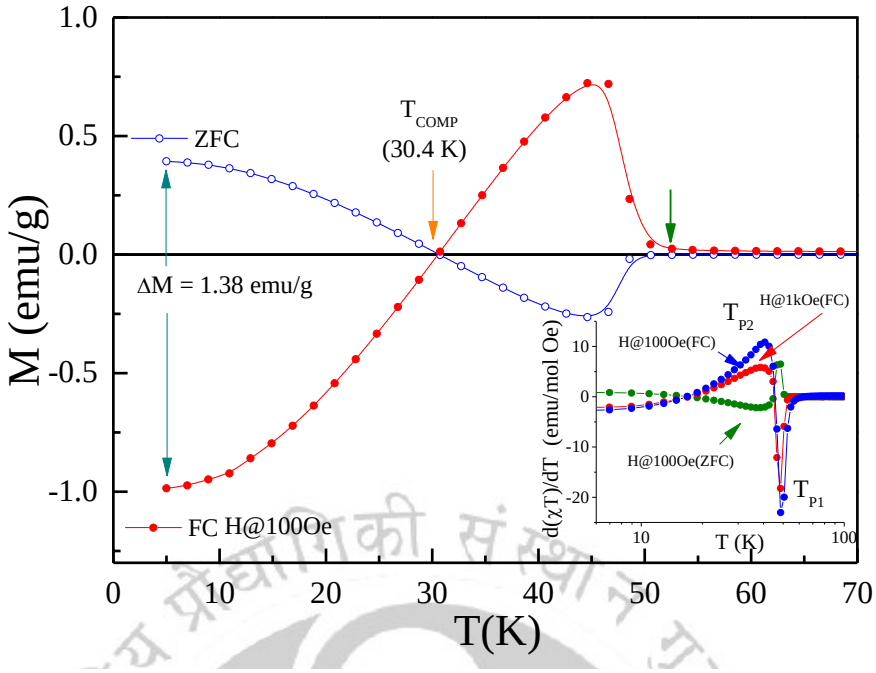

Fig. 5.6: The temperature variation of the magnetization M(T) recorded under zero-field-cooled (ZFC) and field-cooled (FC) conditions with H = 100 Oe for CTO single-crystal. The inset shows the plots of d(χT)/dT versus T of CTO single-crystal at various external fields H_{dc} = 100 Oe (ZFC and FC), and 1000 Oe (ZFC). The two-sublattice magnetizations balanced each other at the compensation temperature T_{COMP} ~ 30.4 K (vertical orange color arrow) below the Néel temperature (indicated by the vertical olive color arrow). At low-temperature (<10 K) the difference (ΔM) between the magnetization values M_{ZFC} and M_{FC} is approximately 1.38 emu/g.

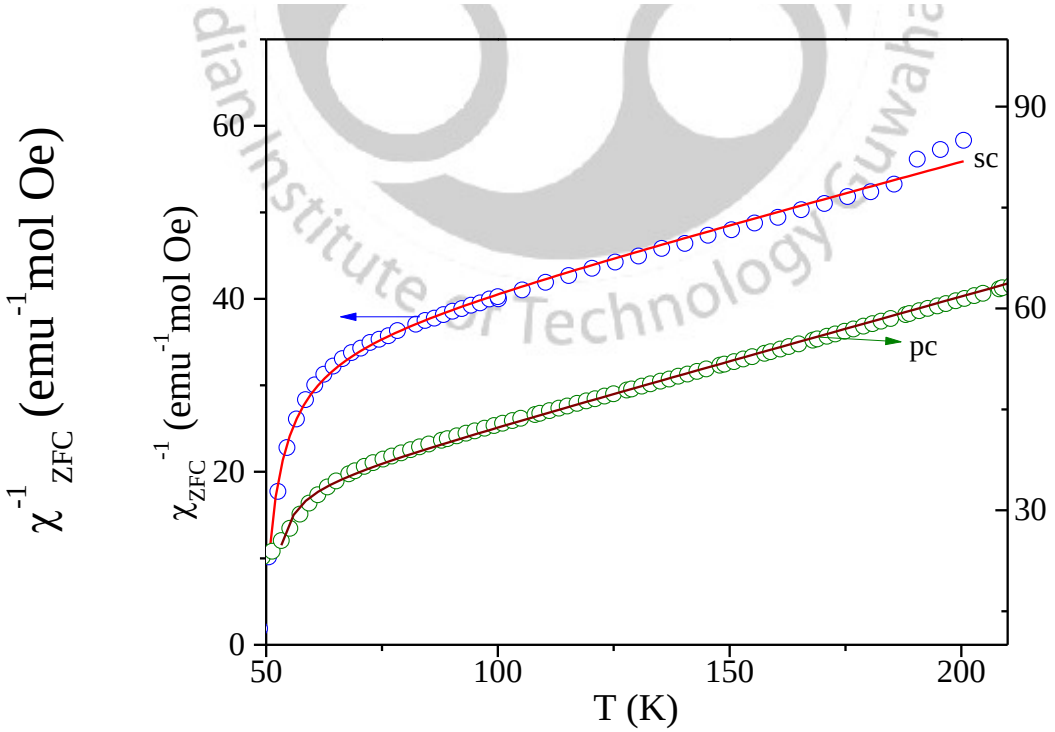

Fig. 5.7: Temperature variation of the inverse paramagnetic susceptibility $\chi^{-1}(T)$ of CTO single crystal (sc) and polycrystal (pc) samples. The solid lines are best fits to the Nèel's expression for ferrimagnets.

Table 5.3: The list of various parameters obtained from the Néel fits of χ_{ZFC}^{-1} versus *T* curve recorded under zero-field-cooled condition for both single-crystal and polycrystalline CTO.

Systems	C (emu K mol^{-1} Oe^{-1})	χ_o (emu mol^{-1} Oe^{-1})	σ_o (emu^{-1}Oe mol K)	θ (K)	μ_{eff} (μ_B)	μ (A) (μ_B)	μ (B) (μ_B)
CTO (Single-crystal)	7.087	0.035 **N_{AA}** 63.453	99.812 **N_{BB}** 41.372	46.736 **N_{AB}** 84.385	7.526 **J_{AA}** 11.98 k_B	3.87 **J_{BB}** 12.32 k_B	6.46 **J_{AB}** 14.66 k_B
CTO (Poly-crystal)	5.245	0.0419 **N_{AA}** 17.319	31.55 **N_{BB}** 12.720	49.85 **N_{AB}** 35.700	6.5 **J_{AA}** 3.25 k_B	3.87 **J_{BB}** 4.47 k_B	5.19 **J_{AB}** 3.18 k_B

$\mu(Co^{3+})/\mu(Ti^{3+}) = 4$. As well as the moment direction parallel to the '*a*' axis. Moreover, in order to obtain the effective magnetic moment μ_{eff}, the temperature dependence of inverse paramagnetic susceptibility curves $\chi_{ZFC}^{-1}(T)$ ($\chi_{ZFC} = M_{ZFC}/H$) (Fig. 5.7) for CTO single-crystal and poly-crystal are fitted to the experimental data with the Néel's expression for ferrimagnets viz. $1/\chi = (T/C) + (1/\chi_0) - [\sigma_0/(T-\theta)]$ [186]. A systematic comparison of all the fitting parameters including the molecular field constants (N_{AA}, N_{AB} and N_{BB}) and exchange constants (J_{AA}, J_{AB} and J_{BB}) obtained from the above analysis for CTO single and polycrystalline samples are listed in Table 5.3. The effective magnetic moment μ_{eff} = 7.526 μ_B/f.u. of CTO is determined by using the relation $C = N\mu_{eff}^2/3k_B$. Since the tetrahedral co-ordination does not allow orbital contribution, the magnetic moment at A-site of Co^{2+} ions is fixed as μ(A) = 3.87 μ_B with spin $S = 3/2$ and $g = 2$ and μ(B) = 6.46 μ_B is determined using the formula $\mu_{eff}^2 = [\mu(A)]^2 + [\mu(B)]^2$ for CTO single crystal which yields ferrimagnetism below 'T_N' with net small moment of 2.59 μ_B/f.u. and these values are greater (1.32 μ_B) than their polycrystals. The experimentally obtained value μ_{eff} = 7.526 μ_B for CTO single crystal is slightly larger (~1.04 μ_B per formula unit) than the theoretically predicted value 6.48 μ_B ($= \sqrt{[(3.87\mu_B)^2]_{A=Co^{2+}} + [(1.73\mu_B)^2]_{B=Ti^{3+}} + [(4.9\mu_B)^2]_{B=Co^{3+}}}$). This is due to the significant role of orbital contribution of the cations occupying the octahedral sites. Note that in the present case the trivalent titanium ions Ti^{3+} with its $3d^1$ electronic configuration has magnetic moment μ = 1.73 μ_B. Considering the magnetic moment of Ti^{3+}, μ_{eff} = 7.526 μ_B and μ(A) = 3.87 μ_B our calculation yields the total moment of $\mu(Co^{3+})$ ~ 6.218 μ_B, which is greater than its spin-only moment 4.9 μ_B signifying the orbital contribution (1.318 μ_B) in the octahedral sites. On the contrary, no such orbital contribution was noticed for the polycrystalline CTO which exhibits μ_{eff} = 6.5 μ_B/f.u. and is less than the μ_{eff} obtained for single-crystal but higher than the isostructural compound CSO. The important difference between the CTO and CSO is that the B sites are occupied by trivalent Co and Ti in CTO both of which exhibits non-zero magnetic moment, however, non-magnetic tetravalent Sn and divalent Co fills the octahedral B sites in CSO. Consequently, the effect of magnetic dilution is expected to be very less in CTO as compared to its sister compound Co_2SnO_4. The strength of the antiferromagnetic exchange coupling between the two Co^{2+} spins on the tetrahedral "A" and octahedral "B" sites is often termed as

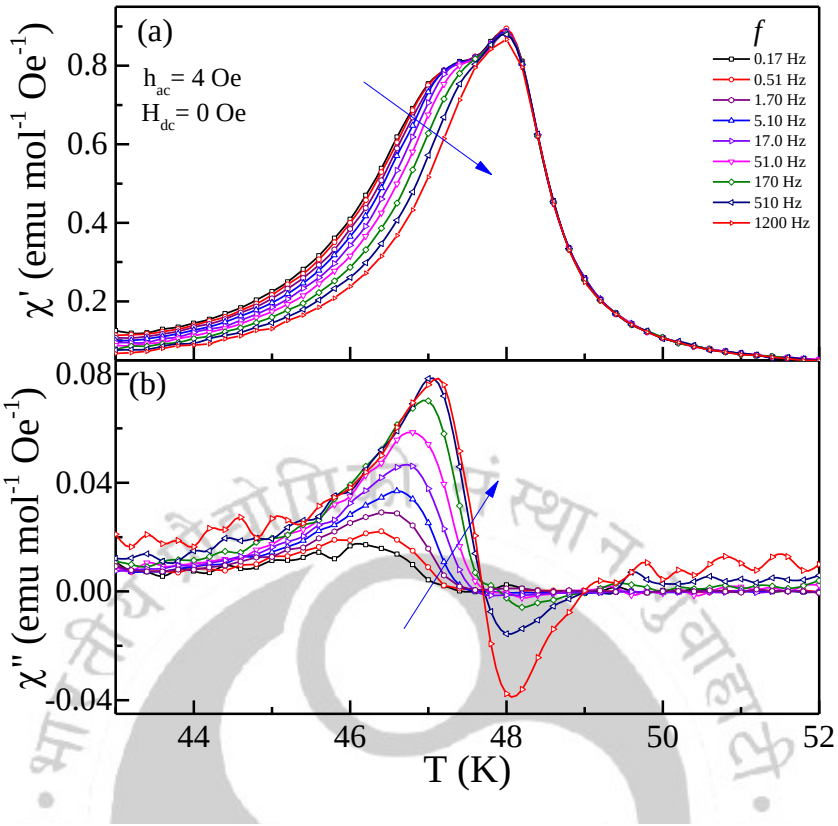

Fig. 5.8: Temperature dependence of ac-magnetic susceptibility of CTO single crystal (a) real component $\chi'(T)$, and (b) imaginary $\chi''(T)$ components measured at various frequencies between 0.17 Hz and 1200 Hz under warming condition using ac-peak-to-peak amplitude H_{ac}= 3 Oe without any external dc-magnetic field.

asymptotic Curie temperature $T_a = C/\chi_0$. The corresponding value of T_a are 202.48 K and 125.18 K for single crystal and polycrystalline CTO, respectively. Another key feature of CTO is the observation of compensation effect at T_{COMP} ~ 30.4 K below the FiM ordering temperature. In order to confirm the spin-glass behavior a detailed frequency dependence (0.17 Hz $\leq f \leq$ 1200 Hz) of ac-magnetic susceptibility studies were performed. Figure 5.8 shows the temperature dependence of real- and imaginary-components of $\chi_{ac}(T)$ (= $\chi'(T)$ + i $\chi''(T)$) for different values of '*f*'. For these measurements the peak-to-peak amplitude of ac-magnetic field h_{ac} is set to ~ 4 Oe with negligible H_{DC}. It is clearly evident that the peak maximum (T_P) in $\chi'(T)$ shifts towards higher temperature side with increasing the frequency which is a typical characteristic of spin-glass system. To examine such behavior, the variation of T_P with-respect-to *f* has been analyzed using the dynamic scaling-laws both V-F and P-L which is discussed in Chapter 4. The scattered points shown in Fig. 5.9(a) show the logarithmic variation of T_P as a function of 'τ' and the straight lines represent the least square fits (ln [τ] against ln[$(T - T_{SG})/T_{SG}$]) to the T_P data obtained from $\chi_{ac}(T)$. This fitting analysis yields the following parameters for the single crystal of CTO: $f_o = 3.746\times10^{25}$ Hz, T_{SG} = 46.85 K and 'zv' = 12.04 ± 0.05 for $T_P(\chi')$ and $f_o = 3.746\times10^{16}$ Hz, T_{SG} = 41.59K and 'zv' = 2.17 ± 0.05 for T_P (χ''). The magnitudes of 'f_o' and 'zv' are consistent with the glassy characteristics

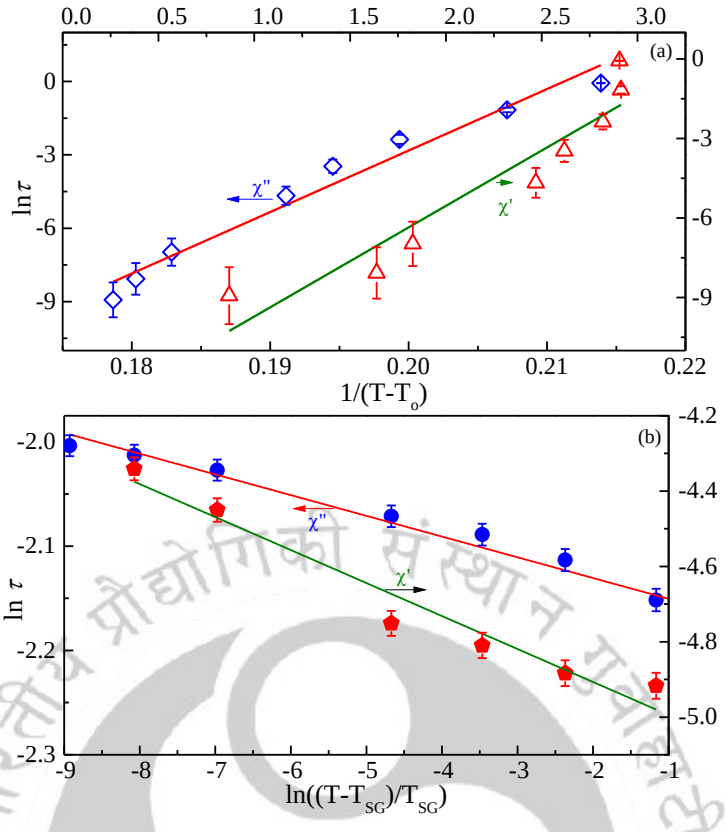

Fig. 5.9: (a) Plots associated with the Vogel-Fulcher law ln [τ] versus [$1/(T - T_o)$] using the peak positions in $\chi'(T)$ and $\chi''(T)$ and the solid lines shows the best-fit to experimental data. (b) The logarithmic variation of the peak-temperature obtained from $\chi'(T)$ and $\chi''(T)$ (i.e. Power law analysis ln [τ] versus ln($[T - T_{SG}]/T_{SG}$)) the solid line represents the best fit to the experimental data.

of prototype spin-glasses reported in literature [278-281]. On the contrary, our earlier report dealing with the polycrystalline CTO samples shows $z\nu > 16$ indicating the departure from a proper spin-glass nature [234]. In particular, the magnitude of $f_0 \simeq 10^{16}$ Hz corresponds to spin-flip frequency of magnetic moments of ions or atoms [186,278,282,283]. The solid-lines in Fig. 5.9(b) represents the best fits corresponding to the above discussed Vogel-Fulcher law to the experimental data points obtained from $\chi_{ac}(T)$. This exercise yields T_0 = 46.86 K (41.52 K) and $f_0 = 1.081 \times 10^{15}$ Hz (1.07×10^{15} Hz) for $\chi'(\chi'')$. Usually, the large values of f_0 have been seen in other spin-glass systems as well, for example AgMn, CuMn, and AuFe which indicates the presence of interacting magnetic spin clusters of significant sizes in the investigated system [186,278,279,282,283]. The competition between ferrimagnetism and magnetic frustration in the system is the main source of existence of spin clusters which leads to a short-range order occurring just below T_N. Earlier investigations on the magnetic properties of $Y_{0.7}Ca_{0.3}MnO_3$ and $La_{0.96-y}Nd_yK_{0.04}MnO_3$ ($0 \leq y \leq 0.4$) reported the formation of such spin-clusters with short-range order [280,281]. Another important gauge to understand the nature of the spin-glass freezing processes is that the determination of relative shift (Φ) of the peak temperature per decade frequency using the expression $\Phi = \Delta T_p/(T_p\, \Delta \log f)$, where ΔT_P is the change in T_P with change in $\Delta \log f$ which is already discussed in Chapter 4. Accordingly, we have calculated the values of Φ = 0.0044 and 0.0052 using χ' versus T and χ''

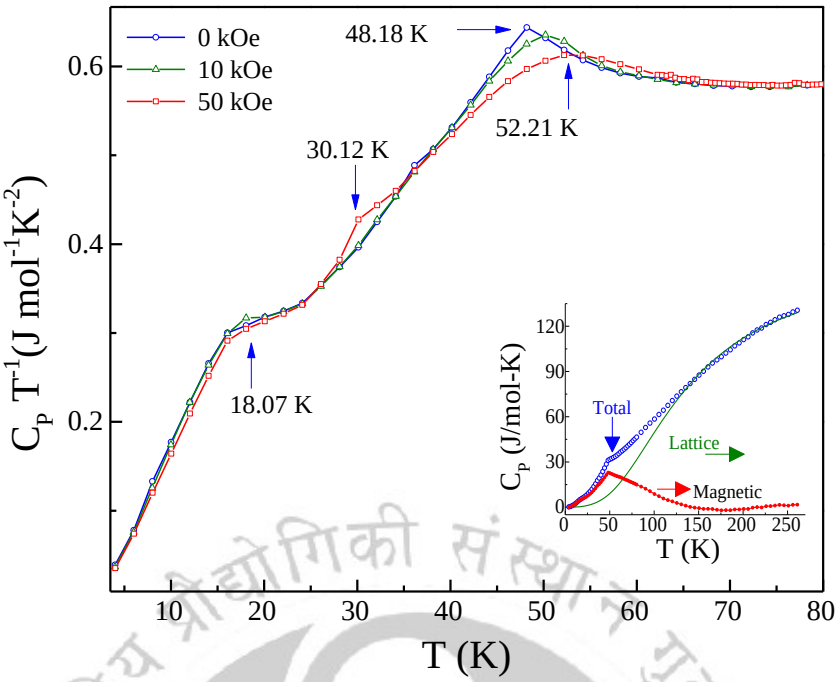

Fig. 5.10: The temperature dependence of specific-heat $C_P T^{-1}(T)$ measured at different magnetic fields (0, 1 and 2 T) of CTO single-crystal. The inset shows temperature dependence of heat-capacity data $C_P(T)$ with individual contributions of lattice specific-heat ($C_L(T)$ olive-color solid line), magnetic ($C_M(T)$ red-color solid circles) and total specific-heat (blue circles).

versus T, respectively. Usually, Φ parameter should lie between 0.005 and 0.05 for typical spin-glasses [78]. Thus, the values of Φ estimated from both real- and imaginary components of $\chi_{ac}(T)$ are consistent with the literature data on spin-glass ordering and is supporting the scaling analysis discussed above. Further evidence to the spin-glass behavior in CTO single crystals was noticed from the temperature dependence of heat-capacity $C_P(T)$ (Fig. 5.10). The fact that peak in 'C_P' at 'T_N' in H = 0 is quite weak compared to peaks observed in typical second order transitions in 3D systems is due to unconventional ordering in CTO (lack of proper long-range order and the presence of spin-glass-like features). Therefore, the absence of sharp peak in the $C_P(T)$ is a well-known characteristic feature of the existence of disordered spin configuration and proof to the existence of spin-glass nature [284].

The temperature variation of C_P/T (Fig. 5.10) for T < 100 K for H_{dc} = 0, 10 and 50 kOe suggests the entropy loss due to spin-glass-like ordering starting near to T_{P2} (Figs. 5.6 and 5.10). The zero-field $C_P T^{-1}$ data shows a weak hump across the T_N (=T_{P2}) and without any signatures across the compensation point T_{COMP}. However, after applying the field a sharp transition across T_{COMP} emerged with complete suppression of the hump observed across T_{P2}. There is a one-to-one concurrence between the location of these anomalies and the sharp transitions noticed in $\chi_{dc}(T)$ data at 48.18 K and 30.4 K. Nevertheless, no significant measurable difference was observed in the C_P values measured at H = 0 and 50 kOe except the emergence of T_{COMP} and disappearance of weak anomaly across T_N. Nonetheless, a rapid decrease in $C_P T^{-1}$ with decreasing T beginning near 25 K (a

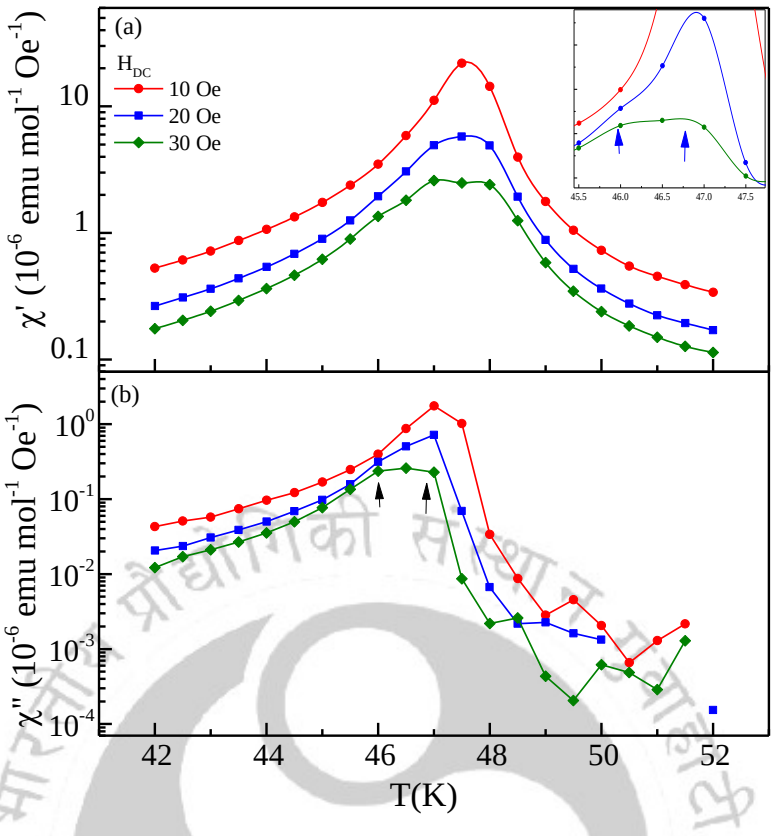

Fig. 5.11: Temperature dependence of ac-magnetic susceptibility (a) real part $\chi'(T)$, and (b) imaginary $\chi''(T)$ components of single crystalline CTO system measured at three different bias fields H_{dc} (10, 20 and 30 Oe) at a constant frequency of 2 Hz and ac-magnetic field peak-to-peak amplitude of 4 Oe. The inset shows peak splitting in $\chi'(T)$ which is significant at higher values of H_{dc}.

hump across 18 K), indicating further changes in the magnetic ordering of the system. These anomalies are clearly evident in the computed plots of differential magnetic entropy $\partial S_M/\partial T$ versus T curves. It is well known that in magnetic materials the total specific heat $C_P(T)$ consists of two main components: the first one is due to lattice specific heat (C_L) and the second contribution is from magnetic counterpart (C_M). The lattice contribution consists of the electronic part C_e and the phonon part $C_{Phonon} = Nf_D(\Theta_D/T) = 9NR(T/\Theta_D)^3\int_0^{\frac{\theta_D}{T}}\frac{x^4e^x}{(e^x-1)^2}dx$, where $f_D(\Theta_D/T) = 9R\,(T/\Theta_D)^3\int_0^{\frac{\theta_D}{T}}\frac{x^4e^x}{(e^x-1)^2}dx$ is the single Debye function, N is the number of atoms per formula unit, R is the universal gas constant (8.314 J/mol K), and Θ_D is the Debye temperature [253]. Usually, the electronic contribution is significant only at very low temperatures, the phonon contribution has been extracted from the total specific heat. For this we fitted the experimentally obtained heat capacity data using Debye function [$f_D(\Theta_D/T)$] at temperatures much higher than the T_N where the magnetic contribution vanishes [285]. For the single crystalline CTO the extrapolated data are shown in the inset of Fig. 5.10. The solid continuous line depicts the contribution of the phonon and the solid-circles represents the magnetic-specific heat component individual derived from the above relation. Consequently, we obtained Θ_D = 554.16 K which is higher than the Θ_D = 525

K pure Co_3O_4 reported by Roth [87] but consistent with the polycrystal data and are in close agreement with Θ_D = 560 K reported by Ogawa and Waki for CTO [253]. Furthermore, the temperature variation of the $\partial S_M/\partial T$ (= C_{MP}/T) exhibit a hump across 18 K and a sharp peak across the T_{COMP} of CTO at high fields (≥ 1 T) typical for a first-order-like transitions, however, this field-dependent anomaly is not sharp at low fields. Previous studies from Ogawa and Waki reveal that the $C_P(T)$ data of CTO follow the simple $T^{3/2}$ dependence in a narrow range of temperatures, whereas, the modified $T^{3/2}$ dependence (according to the equation $C_M = (k_B/8)(k_BT/\pi\hbar a)^{3/2} F(x)$) was noticed over a wide range of temperature (5-30 K). The effective anisotropy constant K_a (~1.2×10^5 erg/cc) estimated by them is less than $K_a = 9.3\times10^5$ erg/cc obtained from the present case (at T = 10 K).

Extensive ac-magnetization studies on polycrystalline CTO and CSO reported by Srivastava *et al.* observed four different transitions in the $\chi_{ac}(T)$ data recorded in the presence of small probing external dc-magnetic field in the range 285 - 460 Oe with f = 21 *Hz* and V_{p-p} ~ 0.5 Oe [246,247]. The first two transitions and their field dependence given in these reports are in-line with the two transitions observed in the $\chi_{ac}(T)$ data (Fig. 5.11) of CTO single crystals measured in the same temperature window as that of frequency dependence studies discussed above, however, with a superimposition of a small fixed dc-bias field H_{dc} =10, 20 and 30 Oe similar to that reported in [22]. Figure 5.11 shows the $\chi'(T)$ and $\chi''(T)$ measured at various H_{dc} with fixed f = 2 Hz with H_{ac} = 4 Oe. The amplitude of both $\chi'(T)$ and $\chi''(T)$ decreases significantly (~88%) with increasing the H_{dc} by 0.2 %, nevertheless, two peaks are clearly evident in $\chi'(T)$ curves (inset of Fig. 5.11) with the extent of splitting increases with increase of H_{dc}. This behavior is consistent with the two-peak scenario of differential dc-magnetic susceptibility shown in the inset of Fig. 5.6. Since the out-of-phase component of the $\chi_{ac}(T)$ is related with the transverse spin component, the current observations support the co-occurrence of FiM in the longitudinal spin component at T_N and spin-glass ordering of the transverse spin component at a slightly lower temperature across T_{SG}. Such phenomenon of semi-spin-glass state was predicted by Gabay and Toulouse and Villain in insulators with non-magnetic impurities [257,261,262].

5.4 Conclusions:

Here we summarize the salient features of the experimental results obtained from the neutron scattering studies on the single crystal compounds CTO and CSO along with the heat-capacity, dc-magnetization and ac-susceptibility results. Both compounds exhibit strongest magnetic intensity for the $(111)_M$ reflection due to ferrimagnetic ordering. Also, a low intensity magnetic reflection $(200)_M$ was noticed in CTO due to additional weak antiferromagnetic ordering. A significant broadening of the $(111)_M$ reflection has been observed due to the disordered character of the Ti and Co atoms on the B sites. The neutron diffraction study of CTO single-crystals showed that some nuclear reflections exhibit a strong increase in their peak intensity below the ordering temperature of about 50 K which is associated to a change of the mosaicity of the crystal. The cause of anisotropic local strain effects in the crystal appears due to the competing Jahn-Teller effects acting along different crystallographic axes in which the t_{2g} levels of both the trivalent cations Ti^{3+} and Co^{3+} split into a lower

d_{xy} level resulting to a higher twofold degenerate d_{xz}/d_{yz} level. As a consequence, one can expect a tetragonal distortion in CTO with a c/a ratio less than 1. Nevertheless, our powder diffraction data could not show any evidence of peak splitting, which could indicate a transition into a tetragonal structure. Based on the dynamic scaling analysis of ac-susceptibility and the heat-capacity measurements, we find that CTO first goes through a ferrimagnetic ordering across 48.6 ± 1 K, and then subsequently goes through a reentrant spin-glass transition across 46.8 K with critical exponent 'zv' = 12.04 ± 0.05 as determined from the frequency dependence of real-component of ac-magnetic susceptibility $\chi'(T)$. From the temperature dependence of heat-capacity $C_P(T)$ data we estimated the Debye temperature Θ_D = 554.16 K for the single crystalline CTO which is significantly higher than the Θ_D = 525 K for polycrystalline Co_3O_4 reported by Roth [87]. A weak hump across 18 K was noticed from the C_PT^{-1} vs. T data indicating further change in the magnetic ordering which is independent of the external applied magnetic field.

Chapter 6
Tunable magnetic properties of Ge substituted Cobalt orthotitanate

In extension with the content of previous chapters, here we provide a detailed electronic and magnetic structure of Ge substituted Co_2TiO_4 using the DFT+U calculations. Several important conclusions are drawn from this piece of work such as tunable electronic and magnetic structure with respect to the site occupancy of Ge atom (cation disorderness), weak tetragonal distortion and large exchange splitting. This chapter is organized as follows: first we will provide a brief introduction to the system under investigation, exposing the gaps in the literature, theoretical methodology and the discussion of results. Subsequently we summarize the key results obtained from these computational study.

6.1 Introduction:

In this section we provide a brief introduction to the end compound $GeCo_2O_4$ ($=(Ge^{4+})_A[2Co^{2+}]_BO_4$) which has been extensively studied due to its unique magnetic behaviour like: long-range AFM ordering below 22 K, Jahn-Teller distortion (~16 K), orbital frustration, and exclusive field-induced magnetic transitions [4,20,148,160,177,286-291]. The neutron diffraction studies revealed the pyrochlore lattice of Co^{2+} ion and a complex crystal structure comprising of alternative planes of Kagomé (KGM) and triangular (TRI) spins develop in the system [20,160,148,286]. The different types of exchange interaction in the Kagomé and triangular lattice planes generate the magnetic frustration in $GeCo_2O_4$ (GCO) [20,160,148,286]. The temperature dependent magnetization and the specific heat analysis on this system reveal the presence of short-range 2D ferromagnetic order near 100 K which is consistent with the specific studies performed by Lashley *et al.* [290]. Using the high temperature magnetic susceptibility data, Pramanik *et al.* calculated the magnitude of the dominant ferromagnetic exchange constant (J_1/k_B ~14.7 K) [177]. The authors also determined the optical band-gap of the system which is nearly 3.2 eV using diffusive reflectance spectroscopy and supported the optical data with DFT calculations as discussed in Chapter 3. Interestingly, the field dependence analysis provides the evidence of magnetic field induced transitions at 11 kOe, 44 kOe and 97 kOe, which is evident from the recent studies of Pramanik *et al.* who proposed a H-T phase diagram which gives a clear idea about the spin orientation of the magnetic ions in three different regions [177]. Besides the basic interesting physics, GCO can be used as electrodes in the storage devices like Li-ion batteries which makes it an important compound to explore [177,292,293].

There are several studies which suggest some interesting feature shown by Co_2TiO_4 when Ti is substituted with Ge [243,294,295]. For the compositions $x \geq 0.5$ generally polycrystalline samples of $Co_2Ti_{1-x}G_xO_4$ (CTGO) were unstable due to the presence of a small amount of GCO [243,295]. Strooper *et al.* performed detailed magnetization studies on Ge doped Co_2TiO_4 (CTGO) and was able to synthesize upto $x = 0.4$ [243]. These authors determined the first nearest neighbour exchange interaction between the A and B sites using both paramagnetic susceptibility data and the difference of two Brillouin functions on the spontaneous magnetization curves [243]. For the undoped case, they obtained the magnitudes of Curie

constant as C = 5.4601 K cm^3/mol, and exchange constants as $J_{AB} \sim -6.3$ K, $J_{AA} \sim -4.6$ K, and $J_{BB} \sim -5.5$ K. Motivated by these studies, in this chapter we present detailed DFT based numerical investigations aiming to probe the electronic and magnetic structure of CTGO solid solutions. To the best of our knowledge such theoretical study is completely new and has not been reported till now in the literature. Our results fill up the miscibility-gap ($0.4 \leq x \leq 1$) in the composition dependent phase diagram of CTGO which is essential to understand the electronic, crystal, magnetic structure of these solid solutions.

The organization of this chapter is as follows: in the next section we present the computational details followed by result and discussion where we present the numerical result related to our DFT calculation. Here first crystal structure of Ge substituted Co_2TiO_4 is presented which is followed by the electronic structure and magnetic properties of the investigated compound and final section deals with the conclusion.

6.2 Computational details:

To probe the structural, electronic and magnetic properties of the CTGO we employed the DFT studies as implemented in VASP whose details are given in Chapter 2. The crystal and electronic structure were optimized using the projector augmented wave (PAW) basis-set. We used the Perdew-Burke-Ernzerhof implementation of generalized gradient approximation (GGA) for exchange-correlation function as given in Section 2.1.3.2 of Chapter 2. The valence electronic configurations used in PAW pseudopotentials are: Co ($3d^8 4s^1$), Ti ($3d^3 4s^1$), Ge ($4s^2 4p^2$), and O ($2s^2 2p^4$). The self-consistent calculations 2×2×2 Gamma *k*-grid points with 24 irreducible **k** vectors and the energy cut off 650 eV have been considered to perform the integration in Brillouin zone. Due to the presence of strongly correlated *d* electrons we adopted the Dudarev's approach (see Section 2.1.4). Accordingly, the effective parameter is represented as $U_{eff} = U - J$, where, U characterizes the on-site Coulomb correlation and J represents the Hund's coupling. In the present case all the calculations were performed by considering U = 4 eV for both Co atoms, U = 2 eV for Ti atoms and U = 0 eV for Ge atoms (see Chapter 3), whereas, J is assumed to be 0 eV. The convergence criteria for the total energies and the forces on individual atoms were set to be 10^{-6} eV and 0.01 eV/Å, respectively.

As we are interested to probe the electronic and structural properties of Ge substituted Co_2TiO_4 system (CTGO) for a wide range of compositions x = 0-1, a careful procedure is required to prepare the sample. Generally quasi-random methods [296,297] and substitutional disorder techniques [298,299] are used for such purposes. For our studies we have adopted the substitutional disorder technique for replacing the Ti with the Ge in the supercells. In brief we begin with a particular configuration of the parent compound and replace the Ti with Ge atoms at randomly chosen sites. Further we prepare several mental copies of the structure following the same procedure and compute the total energy of the system. We find that all the structures have same energy with negligible variation ($\sim 10^{-4}$) which indicate the formation of good samples. As, we move from inverse spinel to normal spinel we introduced a parameter *y* which is known as cationic disorder. In the present study, we considered three different magnitudes of *y* namely (*i*) Complete octahedral occupancy of Ge (y = 0), (*ii*) Half way occupancy of Ge atoms at both tetrahedral and octahedral sites (y =0.5), and (*iii*) Ge atoms entirely occupying the tetrahedral sites (y = 1.0). To perform the simulations, we

Table 6.1: Compositions of A and B sub-lattices in CTGO for different values of *x* and *y*. In all the calculations, we used a cell size of 112 atoms.

Compositions (*x*)	*y*	Composition at A site	Composition at B site
0.125	0	Co_{16}	$Co_{16}Ti_{14}Ge_2$
	0.5	$Co_{15}Ge_1$	$Co_{17}Ti_{14}Ge_1$
	1.0	$Co_{14}Ge_2$	$Co_{18}Ti_{14}$
0.25	0	Co_{16}	$Co_{16}Ti_{12}Ge_4$
	0.5	$Co_{14}Ge_2$	$Co_{18}Ti_{14}Ge_2$
	1.0	$Co_{12}Ge_4$	$Co_{20}Ti_{14}$
0.5	0	Co_{16}	$Co_{16}Ti_8Ge_8$
	0.5	$Co_{12}Ge_4$	$Co_{20}Ti_8Ge_4$
	1.0	Co_8Ge_8	$Co_{24}Ti_8$
0.75	0	Co_{16}	$Co_{16}Ti_4Ge_{12}$
	0.5	$Co_{10}Ge_6$	$Co_{22}Ti_4Ge_6$
	1.0	Co_4Ge_{12}	$Co_{28}Ti_4$
1.0	0	Co_{16}	$Co_{16}Ge_{16}$
	0.5	Co_8Ge_8	$Co_{24}Ge_8$
	1.0	Ge_8	Co_{32}

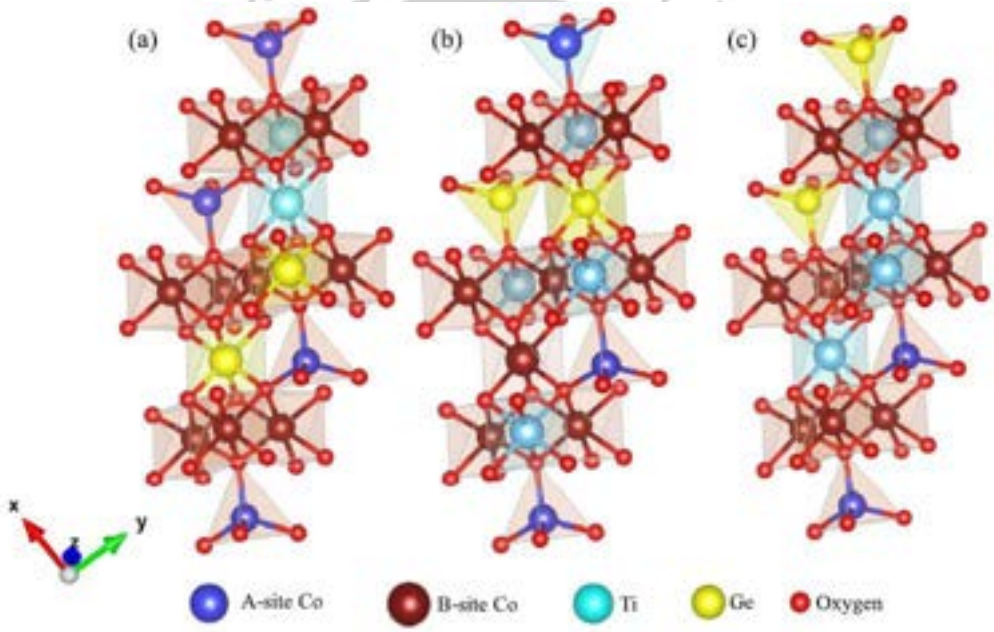

Fig. 6.1: (a) Schematic of the crystal structure of CTGO for different cationic disorder (a) *y* = 0, (b) *y* = 0.5, and (c) *y* = 1.0.

construct a supercell of Co_2TiO_4, which consists of 112 atoms (16 Co_A, 16 Co_B, 16Ti_B, 64 O atoms) and for different value of *x* we substituted the Ti with the Ge atoms (see Fig. 6.1). In the present study, we considered different compositions of CTGO which can be expressed as: $(A_{1-xy}C_{xy})_{tetra}[B_{1-x}A_{1+xy}C_{x-xy}]_{octa}$. In the Table 6.1, we list the cationic configurations at A and B sites for different magnitudes of cationic disorder (*y*) and composition (*x*). In the following section we present our numerical results for electronic structure and magnetic properties of Ge substituted Co_2TiO_4 using DFT calculations.

6.3 Results and discussions:

6.3.1 Cationic disorderness, free energy and crystal structure:

This section deals with the compositional and cationic disorder driven changes in the free energy of CTGO because it is very much necessary to determine the stable and energetically favourable ground state of the system for different compositions. Since both the end compounds CTO (x = 0) and GCO (x = 1) exhibit a slight tetragonal distortion at low temperatures [149,291], it is worth to study the role of tetragonal distortion as well as degree of disorder on the physical properties of the pristine compound for different levels of Ge substitution. To find out the favourable structure we calculated the total energy as a function of *c/a* for eight different compositions and three different values of '*y*'. Figure 6.2(a-d) shows the total energy per formula unit (*E/f.u.*) as a function of *c/a* ratio. For y = 0.0, all the compositions show the lowest energy except for the GCO system (x = 1.0) which exhibits the lowest energy for y = 1.0 and is in-line with the recent experimental observations [177]. It is quite interesting to see that for all the compositions Ge are favourable to occupy the octahedral B-sites, but at the vicinity of the phase boundary (x = 1.0) they prefer the tetrahedral A-sites. As the structure changes from inverse to normal spinel the *E/f.u.* gradually decreases independent of any y value for x = 0.125 (y = 0) the value of *E/f.u.* = - 48.10 eV and for x = 0.875 (y = 0) the value of *E/f.u.* = - 44.15 eV. The corresponding energy difference between the two configurations is ~ 0.11 eV (e = $(E/f.u.)_{y=1}$-$(E/f.u.)_{y=0}$) considering no tetragonal distortion (*c/a* = 1). This energy difference, e, gradually increases and attains maximum of e = 0.5 eV and 1.48 eV for x = 0.75 and x = 0.875, respectively. Such changes become quite significant as system composition approaches close to the pyrochlore stable region of GCO in which competing exchange interactions play a significant role which as a result for y = 1.0 shows higher energy with respect to the other values of y. The experimental results based on temperature dependence of specific heat measurements on similar type of systems reported that the low-temperature disorder in the ground state is essentially induced by magnetic frustration [290,300].

To probe the tetragonal distortion present in the system we calculated the energy difference between the cubic structure (*c/a* = 1) and tetragonally distorted unit cell ($c/a \neq 1$) ($\Delta E = E_{(c/a=1)} - E_{(c/a\neq1)}$) and plotted as a function of *c/a* ratio, as shown in Fig. 6.2(e-h). Here the pristine compound (x = 0) with only one configuration, that is Ti^{4+} ions at octahedral B-sites exhibit the lowest energy configuration under tetragonal configuration than the cubic structure (with $c/a > 1$) which is discussed in the previous chapter. For y = 0.0 (complete B-site disorder), for dilute dispersion of Ge (x = 0.125) in the spinel lattice, the system crystallizes in perfect cubic structure without any tetragonal distortion. However, with increasing Ge content the system exhibits slight distortion, for y = 0.5 (partial B-site disorder situation), the system energetically favours cubic structure up to some moderate compositions $x \leq 0.25$. Nevertheless, the system remains tetragonal distorted with $c/a > 1$ up till x = 0.75, but beyond x = 0.75, system exhibits *c/a* = 0.99, a slight shrinkage in the tetragonal unit cell due to the different ionic radius of the cations Ge and Ti. For y = 1.0 (complete A-site disorder), depending upon the composition the overall system oscillates its energetically favourable situation between the tetragonal structure and cubic. For example, the combination of y = 1.0 and x = 1.0, causes the system to stable with $c/a < 1.0$, which is in contrast with the earlier experimental observations where the

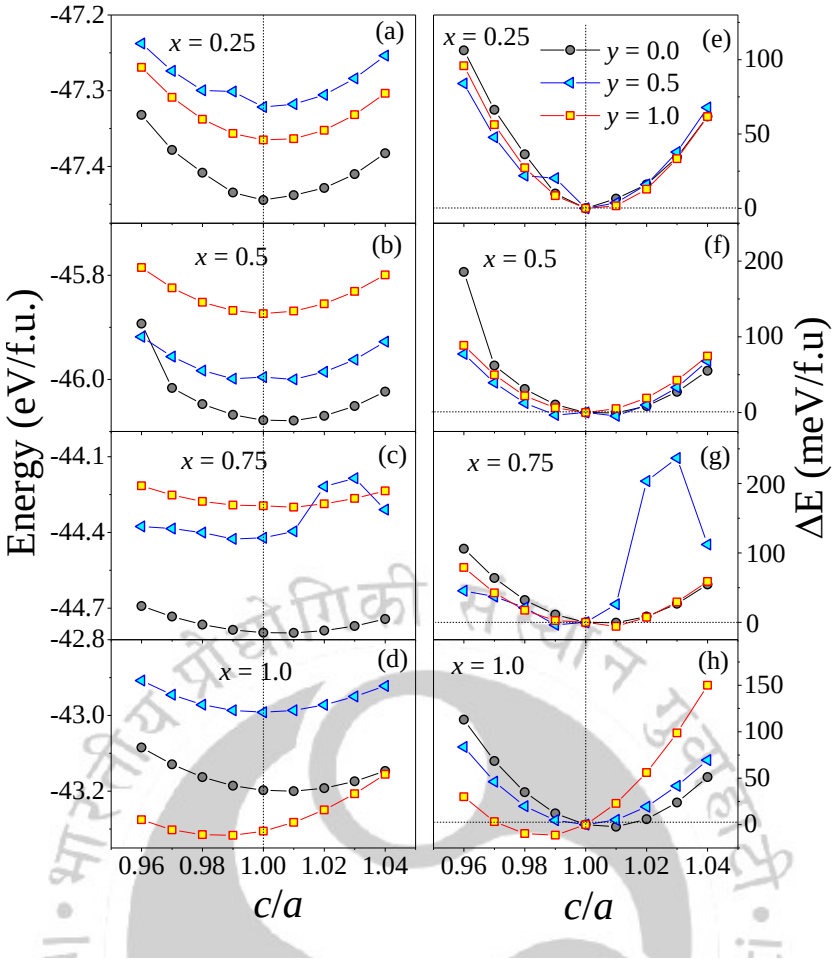

Fig. 6.2: The variation of total free energy/f.u. [(a), (c), (e), and (g)] and ΔE (=$E_{(c/a=1)}$− $E_{(c/a\neq1)}$) (meV/f.u.) [(b), (d), (f), and (h)] as a function of tetragonal distortion (*c/a*) ratio for different compositions of CTGO.

authors noticed a giant tetragonal distortion with *c/a* ~ 1.4 [291]. As a special case our calculations with the experimental lattice parameters yield very high magnitude of *E/f.u.* signifying the fact that the experimentally obtained parameters are not effective at low-temperatures, especially at absolute temperature where the calculated results are valid. Regardless of any composition of *y* and *x* values the *c/a* of this interesting spinel system oscillates between 0.99 and 1.01 signifying a mild tetragonal distortion persists in the system (Fig. 6.2(h)). For *x* = 1, that is pyrochlore GCO case where Ge atoms disperse from *y* = 0.0 (B-site) to *y* =1.0 (A-site), we noticed a systematic change in *c/a* ratio. In the following sections, we discuss this scenario more clearly in terms of partial density of states of octahedrally coordinated Co ions.

In order to confirm the most stable ground state configuration we calculated the formation energy of the system for three different values of *y* (see inset of Fig. 6.3(a)). Generally, the ground state formation energy was determined from the energy difference between the alloy and the sum of the total energies of elements in its actual solid form of weighted over concentration as follows:

$$E_{form} = E_{Co_2Ti_{1-x}Ge_xO_4} - 2E_{Co} - (1-x)E_{Ti} - xE_{Ge} - 4E_{Oxy} \quad (6.1)$$

In the above Eq. (6.1), the first term is the total energy in formula unit of the supercell, whereas the last four terms are the individual energies corresponding to the elements Co, Ti, Ge and O atoms, respectively. These results are in good agreement with previous analysis discussed above pertaining to the energy minimization

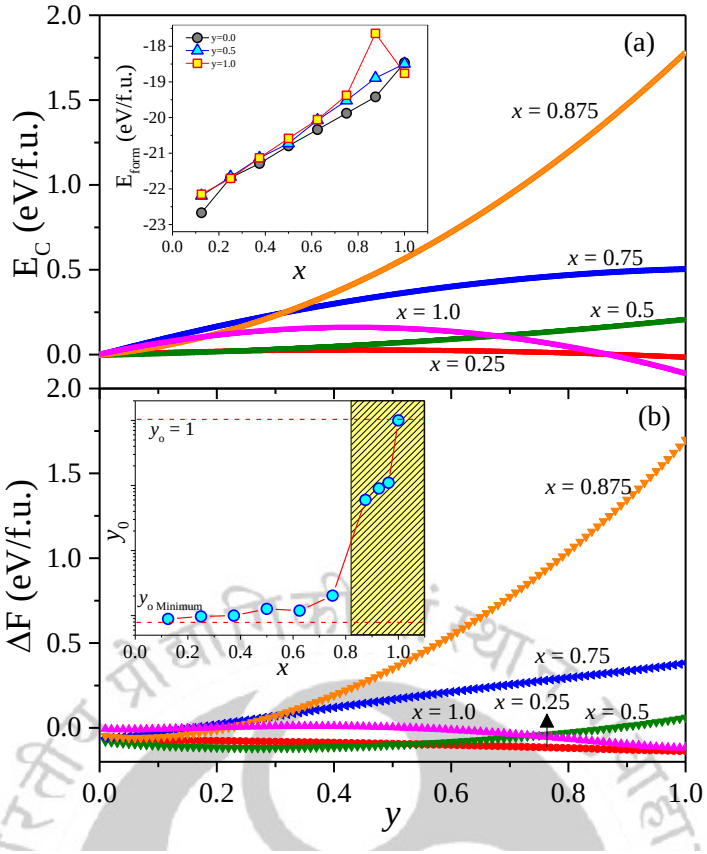

Fig. 6.3: Variations of the (a) cation disorder energy (E_C) and (b) configurational free energy (ΔF) with respect to the cation disorder parameter (y) of CTGO, for different compositions 'x' at T~1250 K, the sintering temperature of the sample. Inset of figure (a) shows the calculated formation energy (E_{form}) of CTGO, whereas, (b) shows the variations of the equilibrium cationic disorder (y_0) for different compositions of CTGO.

calculation. For x = 0.125 with perfect inversion the formation energy exhibits minimum value of the order of −22.67 eV and the formation energy gradually decrease to −19.42 eV upon increasing the Ge substitution for all the values of y. For x = 1.0 without any inversion (y = 1.0) the system possesses lowest energy of ~ −18.75 eV. In order to examine the site occupancy of Ge atoms in CTGO system, we propose two distinct ways. The first possibility is that the 'Ge' atoms occupy the tetrahedral site only for x = 1 or they start occupying the tetrahedral sites over a range of compositions before it attains the perfect pyrochlore structure, such small zone of compositions (δx) is referred to as Morphotropic phase boundary.

Generally, the degree of cationic disorder 'y' at any finite temperature can be calculated from the thermodynamic consideration of cation distributions by treating it as a simple chemical equilibrium configuration [301]. According to Navrotsky and Kleppa, the configurational free energy of cation disorder per formula unit (ΔF) is given as: $\Delta F = E_C - T\Delta S_C$, where the E_C is cation disorder energy per formula unit, T is the sintering temperature, $\Delta S_C = -k_B \sum_{i,b} p_i^b \ln p_i^b$ is the configurational entropy, and p_i^b is the concentration of the cations b at the i^{th} sub-lattice [301]. In the present case the cation disorder energy, E_C is the energy difference between the inverted state and the other disordered states. In order to obtain the dependence of E_C on the entire range of y we fitted E_C with a quadratic relation $E_C = \alpha y + \beta y^2$, where α and β are the constants. Following the Kriessmen and Harrison method of quadratic dependence of the cation

disorder energy we determined the E_C for y = 0, 0.5 and 1 for different values of x [302]. As a second step these energies are fitted with the quadratic equation given above and obtained the variation of E_C for the entire range of y. At the equilibrium the degree of cation disorder parameter (y_0) for any temperature can be obtained by minimizing the configurational free energy, ΔF, with respect to y and further the y_0 can be evaluated for different compositions. Figures 6.3(a) and 6.3(b) show the variation of E_C, and ΔF with y for different Ge concentration x at sintering temperature T = 1250 K [243]. The variation of E_C as a function of y shows nearly identical trend for all the x values below 0.75. However, for higher compositions close to the morphotropic phase boundary $E_C(y)$ displays parabolic variation, specifically, for x = 0.875 such trend is more prominent, as the difference between the cation disorder energy is significantly high ($E_C \geq$ 1.8 eV/f.u). This result indicates that the disorderness play an important role on the formation energy. In the present case E_C varies between 0 and 0.4 eV/f.u for lower compositions, whereas, E_C reaches more than 1.8 eV/f.u for higher compositions. For these cases except x = 1.0, E_C attains a minimum at y = 0.0 which is quite consistent with our previous analysis. Similarly, the $\Delta S_C(y)$ plots reveal gradually increase of entropy with y and for most of the compositions the maximum value of change in entropy lies between y = 0.5 and 0.8. However, by considering the configurational entropy of the system, we obtained a slightly different result in case of $\Delta F(y)$ (Fig. 6.3(b)) as compared to $E_C(y)$. Summing-up all this variation, in the inset of Fig. 6.3(b) we show the compositional dependence of equilibrium cation disorder ($y_0(x)$) which infers that the Ge atoms are more favourable to B-site occupancy rather than A-site for low (x < 0.3) and intermediate compositions ($0.3 \leq x \leq$ 0.75) with an anomaly between x = 0.45 and 0.55, whereas for x > 0.875, Ge atoms start occupying the A-sites. Nonetheless, a sharp increase in y_0 is clear as x approaches the morphotropic phase boundary shown by the yellow highlighted region before reaching the final stable pyrochlore structure with 100% Ge atoms at tetrahedral A-sites.

After determining the ground state configuration of the system CTGO, we turn our focus on the crystal structure, bond-lengths and the variation of lattice parameter as a function of x and y. In Table 6.2 we list the lattice parameters a, c and cation-anion bond lengths for different values of x and y. Accordingly, the lattice parameters a and c obtained from DFT+U calculations are 8.54 Å (8.62 Å) and 8.50 Å (8.42 Å) for x = 0 and 1, respectively. These values are slightly higher than those reported earlier using x-ray diffraction measurements which could be due to the choice of GGA while considering the exchange correlation part in the Hamiltonian (see Chapter 3). For y = 0, we obtained a ~ 8.54 Å for x = 0.0 which decreases to 8.48 Å for x = 1.0 due to the fact that the ionic radius of Ge^{4+} (~ 0.53Å) is smaller as compared to Ti^{4+} (~0.61Å). However, for the case of y = 0.5 and 1, a non-linear trend was observed in which a varies between 8.4 Å and 8.6 Å due to unstable structure driven by the cation disorder. But under the limit of dilute dispersion ($x \leq$ 0.125) of Ge, system retains almost cubic structure for all the values of y without any distortion, but exhibits departure from cubic structure as the Ge substitution increases in Co_2TiO_4 with slight tetragonality. Interestingly, for certain combinations of x and y we observed that the lattice parameter c is much smaller than the a. Ascribed to the lower co-ordination number of A-site Ge^{4+} and shrinkage of ionic radius to 0.39Å as a consequence one may notice minor changes in the lattice parameters a and c (Table 6.2). For the case of x = 1.0, the contraction of $[Co]_{oct}$–O bond length is significant along the z-axis hence one may expect

Table 6.2: The list of parameters viz: Bond distance (cation-anion) and lattice constants in the spinel lattice of CTGO for various combinations of '*x*' and '*y*' in Å units.

x	*y*	*a* (Å)	*c* (Å)	A-site		B-site		
				Co-O (Å)	Ge-O (Å)	Co-O (Å)	Ti-O (Å)	Ge-O (Å)
0	0.0	8.54	8.62	1.99	-	2.11	2.01	-
0.125	0.0	8.53	8.53	1.99	-	2.11	2.00	1.96
	0.5	8.53	8.53	2.00	1.83	2.10	2.02	1.96
	1.0	8.53	8.53	1.99	1.83	2.11	2.02	-
0.25	0.0	8.52	8.60	2.01	-	2.11	2.01	1.96
	0.5	8.54	8.54	1.99	1.83	2.10	2.02	1.97
	1.0	8.52	8.60	2.00	1.84	2.12	2.01	-
0.5	0.0	8.50	8.58	2.01	-	2.10	2.02	1.96
	0.5	8.51	8.60	2.00	1.85	2.11	2.03	1.97
	1.0	8.49	8.49	1.96	1.84	2.11	2.03	-
0.75	0.0	8.48	8.56	2.00	-	2.10	2.01	1.96
	0.5	8.49	8.41	2.01	1.85	2.11	2.02	1.98
	1.0	8.47	8.55	1.98	1.84	2.12	2.03	-
1.0	0.0	8.48	8.56	2.02	-	2.10	-	1.97
	0.5	8.46	8.46	1.97	1.86	2.10	-	1.99
	1.0	8.50	8.42	-	1.83	2.12	-	-

decrease of '*c*', however, the $[Co]_{oct}$−O bond length expands in the *xy*-plane giving rise to unequal lattice constants leading to *c/a* ratio deviating from unity. For $x = 0$ (Co_2TiO_4) we obtained the bond-lengths $[Co]_A$−O (1.99 Å) that are less than $[Co]_B$−O (2.11 Å) which are in line with the results given in Chapter 3. These results are quite obvious as the effective ionic radius of high-spin Co^{2+} state is 0.58 Å and 0.75 Å at A and B-sites, respectively. However, the bond lengths do not change significantly with the variation of *x* and *y*. For the $[Co]_A$−O case the average bond length varies between 1.96 Å and 2.00 Å, whereas, for the octahedral site the average bond length between Co and O varies between 2.10 Å and 2.12 Å associated with the weak Jahn-Teller like distortion. The low spin Ge at the tetrahedral A and octahedral B-sites (with tetravalent electronic state) exhibits large difference in the effective ionic radius of 0.39 Å and 0.53 Å, respectively. As a result, the average bond length of $[Ge]_A$−O (~1.83 Å) is significantly lower than $[Ge]_B$−O (~1.97 Å). Therefore, the average bond lengths of the cation and anions at octahedral sites display systematic decreasing trend ($[Co]_B$−O > $[Ti]_B$−O > $[Ge]_B$−O) with the shannon ionic radius of the atoms (Co^{2+} ~ 0.75 Å > Ti^{4+} ~ 0.61 Å > Ge^{4+} ~ 0.53 Å).

To understand the origin of slight tetragonal distortion present in the CTGO system we interpret the data based on the crystal field theory reported by Dunitz and Orgel as discussed in Section 1.6 (Chapter 1). Accordingly, the tetragonal distortion and cubic symmetry mainly depends on the electronic configurations of the cations occupying the tetrahedral and octahedral sites. In the present case, the A-site Co^{2+} have the electronic configuration $(e_g)^4(t_{2g})^3$ while B-site Co^{2+} configuration is $(t_{2g})^5(e_g)^2$. Since, the Ge^{4+} and Ti^{4+} do not have any *d* electron so their atoms do not contribute in the tetragonal distortion. From the crystal field theory, it is quite clear that the weak tetragonal distortion is plausible due to the presence of Co^{2+} atom in B-site, whereas, the Co^{2+} atom in A-site does not have any contribution. Now, as we increase the cation disorder

y, the presence of tetragonal distortion increases progressively due to the increasing occupancy of Co atoms at the B sites. As a result, the degeneracies associated with the e_g orbitals increase significantly ($c/a \neq 1$), indicating the presence of tetragonal distortion for all the compositions with $y = 0.5$ and 1 (Fig. 6.2).

6.3.2 Electronic structure and magnetic behavior:

In this section we discuss about the variation of electronic density of states (DOS) and magnetic properties by focusing the compositional variation and the dependency of cation disorder. Figures 6.4, 6.5 and 6.6 show the DOS of CTGO for various Ge composition with different cation disorder y = 0.0, 0.5 and 1.0, respectively. The density of states corresponding to Co and Ti play a significant role as compared to the Ge states which is quite negligible. For pure Co_2TiO_4 ($x = 0$), the top of the valence band mainly consists of t_{2g} majority band of the tetrahedral Co. The majority spin configurations of t_{2g} and e_g of tetrahedral and octahedral Co, respectively lie deep inside the valence band (~ 6 eV). Due to this reason, a large exchange splitting (Δ_{EX} ~ 8 eV) has been observed for the Co atoms occupying both A and B sites. Furthermore, the feature of DOS plots confirms that the t_{2g} states of A-site Co are half filled and the e_g states are completely filled. Whereas, in case of B-site Co ions, the e_g states are half filled and t_{2g} states are more than half filled which is left with only one unpaired electron. On the other hand, the conduction band maxima (~1.5 eV) dominated by the up and down spin of t_{2g} states of Ti along with the A-site Co states. It is interesting to note

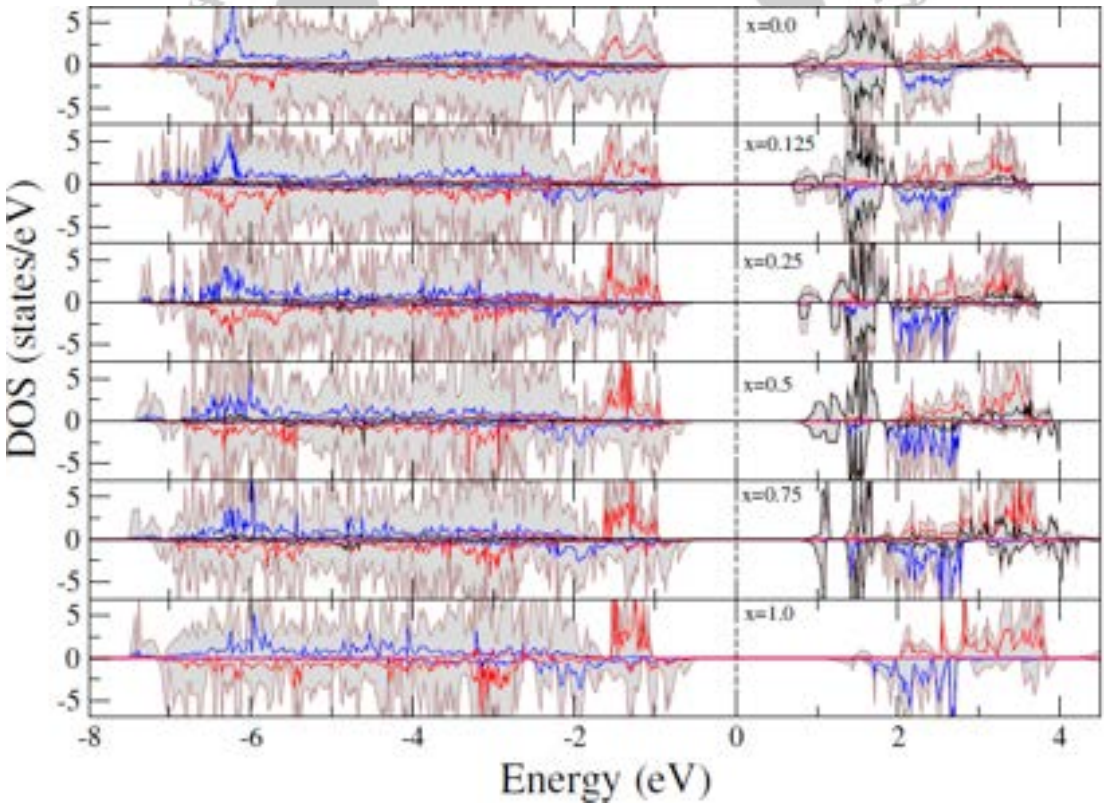

Fig. 6.4: Calculated Density of States (DOS) for different compositions for y = 0.0. The total density of states is represented using the brown shade. The blue and red lines represent the density of states of Co present in A- and B-site, respectively. The solid black colour plots represent the B-site Ti. Dotted vertical lines at E = 0 depicts the Fermi level (E_F). The partial density of states of Ge is not visible due to low intensity.

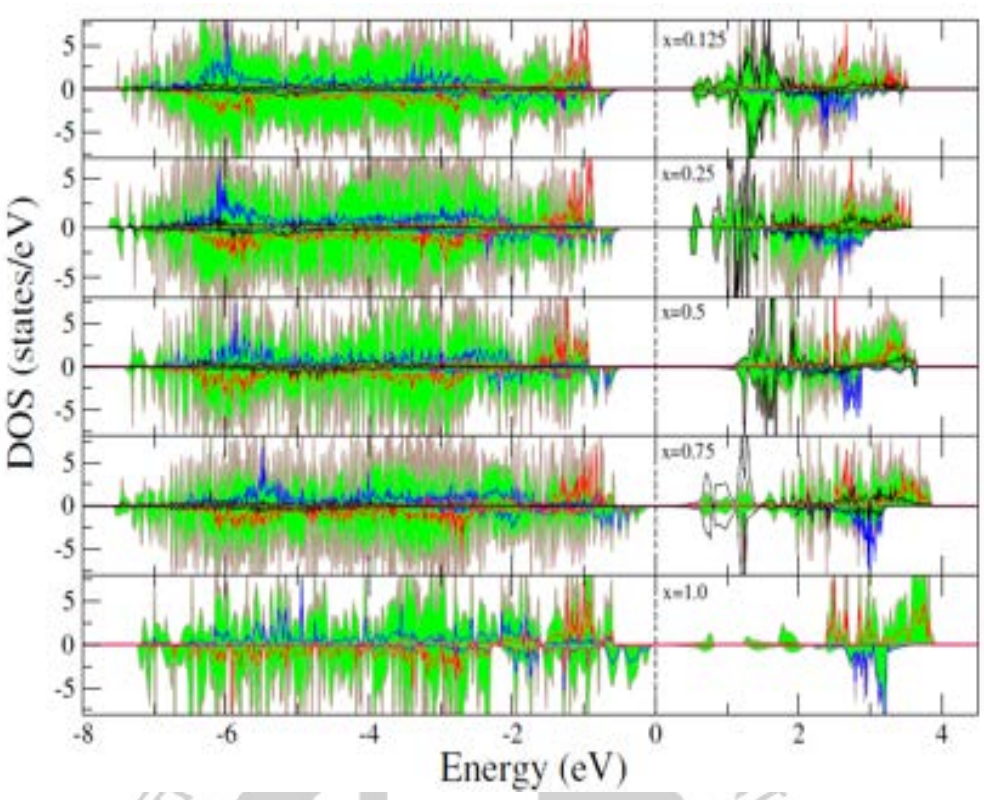

Fig. 6.5: Calculated Density of States (DOS) for different compositions for y = 0.5. The total density of states is represented using the green shade. The blue and red lines represent the density of states of Co present in A- and B-site, respectively. The solid black color represent the B-site Ti. Dotted vertical lines at E = 0 depicts the Fermi level (E_F). The partial density of states of Ge is not visible due to low intensity.

that the hybridization between the O-2*p* and Co-3*d* orbitals is evident across the valence band (at ~ -2.5 eV). In general, for any combination of x and y of the investigated system, the splitting in t_{2g} and e_g symmetries due to the crystal field is clearly noticeable in the density of states versus energy plots (Figs. 6.4-6.6). Although the contribution of Ge density of states is minimal but incorporating it in the Co_2TiO_4 matrix makes noticeable change in the shift of the orbital energies which creates non-degenerate states and is linked to the degree of tetragonality of the system. For all x, Co exhibit high spin (S = 3/2) configuration with divalent oxidation state for both tetrahedral A- and octahedral B-sites, therefore the behaviour of DOS is nearly similar except that for few compositions, noticeable shift in both t_{2g} and e_g states is palpable. For y = 0, x = 0.125 the splitting of majority t_{2g} states of B-site Co is very clear and for higher compositions the splitting in the t_{2g} band is much prominent. Also, the splitting in minority spin e_g states of B-site Co (~ 6 eV, due to non-degenerate *d* orbitals) is also observed for all the combination of x and y. Close examination of the DOS reveals that the $d_{x^2-y^2}$ and d_{z^2} orbitals of e_g states in B-site Co have become non-degenerate while $d_{x^2-y^2}$ exhibits lower energy than the d_{z^2} orbitals implying the presence of tetragonal distortion of the system with c/a ratio greater than 1. For y = 0, for all the values of x we observed non-degenerate orbitals in e_g states, although, the splitting in t_{2g} is most significantly visible for x > 0.25 only. Similar behaviour is observed in case of the t_{2g} states of Ti atoms in the conduction band (~1eV). For low compositions, the sub-bands are suppressed but on increasing the Ge substitution ($x \geq 0.75$) the electronic states gradually populate-up and the splitting is substantial (see Fig. 6.4). This feature clearly suggests that Ti ions equally contribute to the

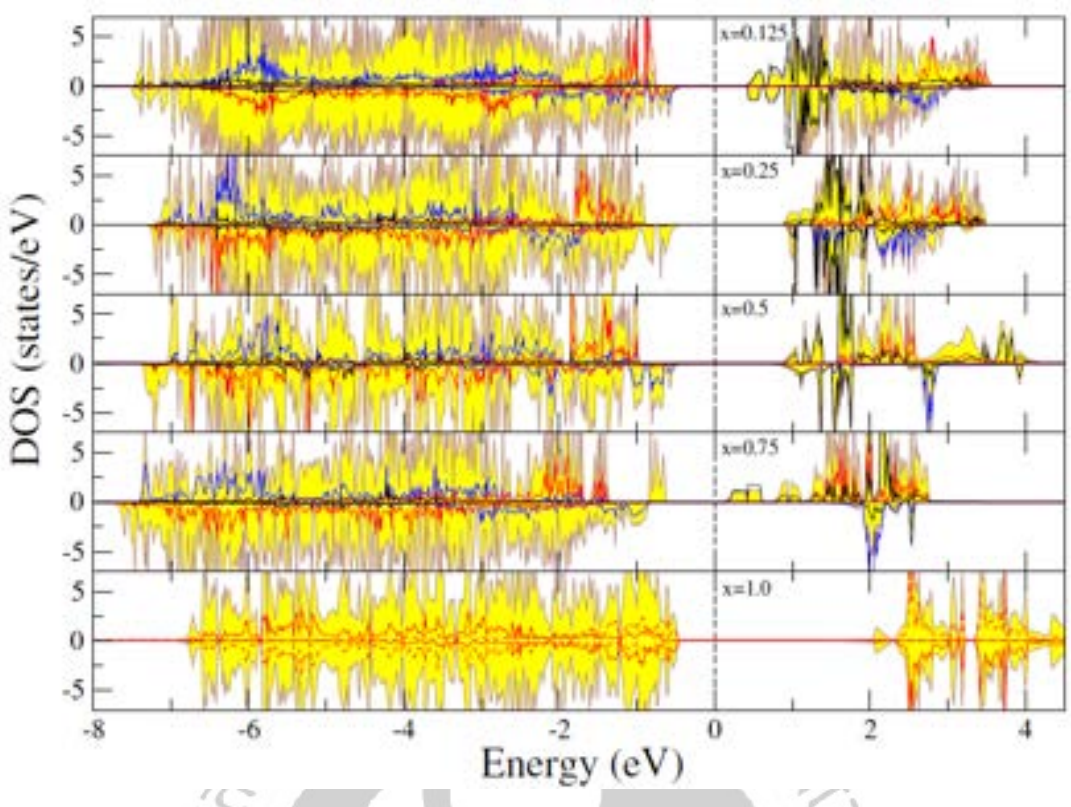

Fig. 6.6: Calculated Density of States (DOS) for different compositions for y = 1.0. The total density of states is represented using the yellow shade. The blue and red lines represent the density of states of Co present in A- and B-site, respectively. The solid black color represent the B-site Ti. Dotted vertical line at E = 0 depicts the Fermi level (E_F). The partial density of states of Ge is not visible due to low intensity.

tetragonal distortion along with the octahedral Co and they also play an important role in deciding the crystal structure. For y = 0.5, the overall DOS of the system exhibits delocalization behaviour of different wave functions which is evident from the Fig. 6.5 as compared to the ordered situation (y = 0) which has clearly distinguishable total DOS. Similar features have been observed in case of atom projected DOS of Co ions located at tetrahedral A-sites and octahedral B-sites. However, the majority t_{2g} states of A-site Co ions shifted towards the lower energy side with the incorporation of Ge: for y = 0.5, E ~ −6 eV and −5.5 eV for x = 0.125 and 0.75, respectively. Similarly, a small shift in energy levels for majority t_{2g} states of B-site Co ions is observed across −1eV. Nevertheless, in the case of Ti atoms an interesting feature of the DOS is observed for x = 0.25 and 0.75; that is the electronic states of Ti atoms dominating at the top of the valence band (~ 0.8eV) and the splitting of $d(t_{2g})$ orbitals is quite clearly visible. However, for x = 0.50, the Ti states are situated deep into the conduction band (~ 1.5 eV from E_F). Similar behaviour has been observed in case of completely disordered system (i.e. all the Ge atoms are in tetrahedral sites y = 1.0) for different compositions except for complete substitution of Ge atoms at Ti. Moreover, for x = 1.0, the up-spin and down-spin states of the Co atoms are symmetric to each other indicating perfect antiferromagnetic (↑↓) arrangement of spins which is consistent with the previously reported experimental observations [167]. All the compositions for y = 0.5 and y = 1.0 (except x = 1.0), the DOS clearly reveals the delocalization of the different atomic wave functions which indicate the instability of the compositions (Figs. 6.5 and 6.6). Due to this reason the entropy of the systems show higher value with respect to y = 0 case. Consequently, the calculated configurational

free energy is relatively high. Therefore, we can conclude that experimentally the formation of the solid solutions with disorder parameters y = 0.5 and y =1.0 is not possible and these remarks are in-line with the formation energy calculations as discussed.

Figure 6.7 shows the DOS associated with the d_{z^2} and $d_{x^2-y^2}$ of e_g orbitals of octahedral Co for x = 1 for different cationic disorder. It is important to depict this figure because the octahedral Co ions are the main source of tetragonal distortion present in the system because of its electronic configuration ($(t_{2g})^5(e_g)^2$). For y = 0, the down spin of d_{z^2} orbitals in the valence band exhibits lower energy with respect to the down spin state of $d_{x^2-y^2}$ orbitals, due to which c/a > 1. While for the y = 0.5 case, it is hard to differentiate between the degenerate states of d_{z^2} and $d_{x^2-y^2}$. As a result, the system stabilizes in the cubic structure, however, the system exhibits weak tetragonal distortion for y = 1.0. But, in this case the c/a < 1 has the energy level corresponding to the non-degenerate d-states with higher energy of d_{z^2} than that of $d_{x^2-y^2}$. Thus, switching of c/a ratio between less than 1 and/or greater than 1 suggest the crucial role of Ge atom in deciding the tetragonal distortion of the investigated system (for $0 \leq y \leq 1$). Similarly, the splitting of d_{z^2} and $d_{x^2-y^2}$ orbitals controls the c/a ratio for different compositions $0 \leq x \leq 1$ for specific y. Figure 6.8 shows the exchange splitting (Δ_{EX}) and crystal field splitting (Δ_{CF}) parameters for the energetically favourable compositions of the CTGO system. We evaluated both the parameters Δ_{EX} and Δ_{CF} from the density of states calculations using the following equations: (a) $\Delta_{EX}^{e_g} = e_{g\uparrow} - e_{g\downarrow}$, ($b$) $\Delta_{EX}^{t_{2g}} = t_{2g\uparrow} - t_{2g\downarrow}$, ($c$)$\Delta_{CF}^{\uparrow} = e_{g\uparrow} - t_{2g\uparrow}$, and ($d$) $\Delta_{CF}^{\downarrow} = e_{g\downarrow} - t_{2g\downarrow}$ as discussed in Chapter 3. In case of A-site Co the exchange splitting linked to the

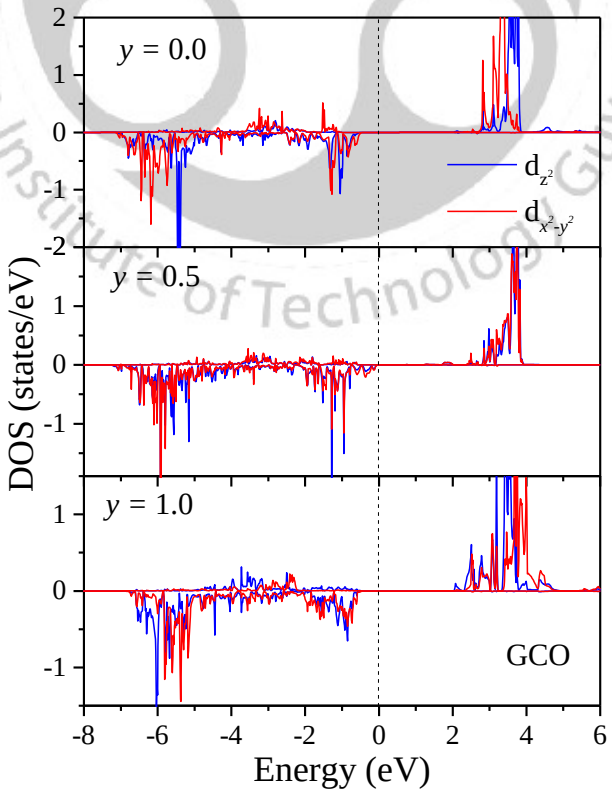

Fig. 6.7: Calculated Density of States (DOS) versus energy (E) plots for octahedral Co in GCO system for different values of y.

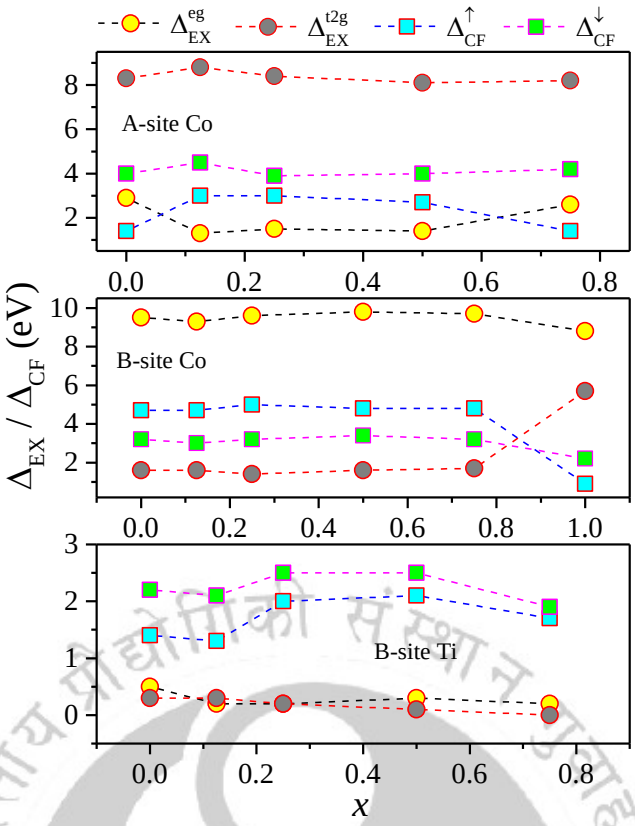

Fig. 6.8: The calculated Exchange splitting (Δ_{EX}) and Crystal field splitting (Δ_{CF}) for different compositions (x) of CTGO.

t_{2g} states are much stronger than the e_g states and the low crystal field splitting (~4 eV) causes the high spin state of Co. On the contrary, for the octahedral Co we noticed the opposite feature ($\Delta_{EX}^{e_g} > \Delta_{EX}^{t_{2g}}$). Nonetheless, the magnitude of Δ_{EX} and Δ_{CF} almost remains same due to the localization of the *d* orbitals. In case of the octahedral Co, the crystal field splitting decreases for x = 1.0 and this occurs due to the increase of bond-length of Co_{oct}-O. It is well known that the crystal field of the octahedral site is inversely proportional to the distance between the cation and anion ($\Delta \sim 1/(B\text{-}O)^5$). For the octahedral Ti, Δ_{EX} is nearly negligible as the up spin and down spin of t_{2g} and e_g states are degenerate, as a consequence the centres of this state lie approximately the same energy level, hence the Δ_{CF} is always greater than Δ_{EX}. Importantly, this analysis leads to the inference that different magnitude of exchange splitting and crystal-field splitting in CTGO system does not have any significant change in the profile of $\Delta_{EX}^{e_g}(x)$ and $\Delta_{EX}^{t_{2g}}(x)$.

Generally, due to the inclusion of the effective coulomb interaction term all the compositions possess semiconductor energy band-gap and exhibits metallic character if we neglect U_{eff}. In general, in the GGA calculations, the density of states of B-sites Co would lie at the Fermi level, however, incorporation of GGA+U calculation breaks the symmetry of the *d*-orbitals and distribute the states on both the sides of the Fermi level which creates the valence and conduction band [119]. Additionally, the tetragonal distortion present in the system is quite small. This happens because the local symmetry barely brakes and as a result the localization of *d*-states is observed in the density of states plots. Thus, the incorporation of suitable U_{eff} would give the precise semiconductor band-gap along with appropriate localization of the states. In order to

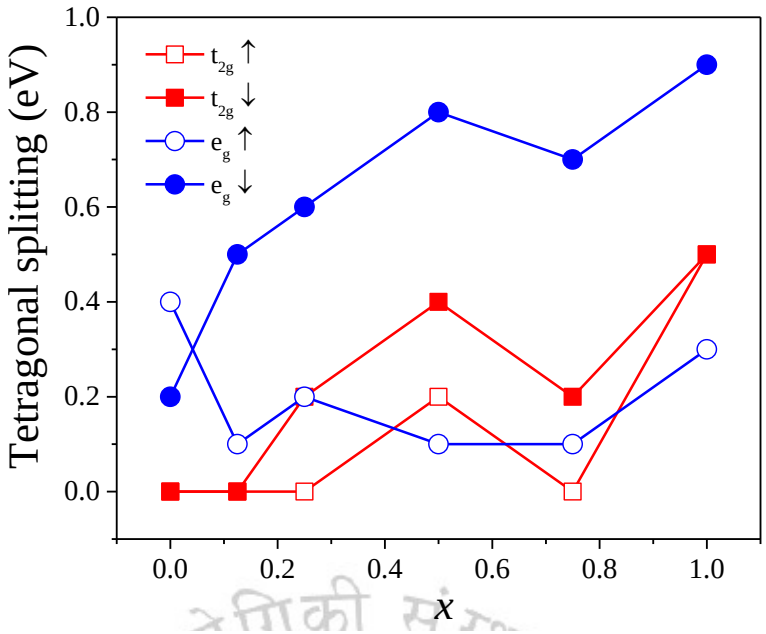

Fig. 6.9: The tetragonal splitting for different compositions (x) obtained from the DOS calculations for the B-site Co in CTGO system.

determine the Jahn-teller elongation Δ_{JT} at t_{2g} and e_g states for the octahedral Co we adopted the following relations [303]: (i) $\Delta_{JT}^{e_g\uparrow} = \left|d_{x^2-y^2}^{\uparrow} - d_{z^2}^{\uparrow}\right|$, (ii)$\Delta_{JT}^{e_g\downarrow} = \left|d_{x^2-y^2}^{\downarrow} - d_{z^2}^{\downarrow}\right|$, (iii) $\Delta_{JT}^{t_{2g}\uparrow} = \left|d_{xy}^{\uparrow} - d_{xz/yz}^{\uparrow}\right|$, and (iv) $\Delta_{JT}^{t_{2g}\downarrow} = \left|d_{xy}^{\downarrow} - d_{xz/yz}^{\downarrow}\right|$. Figure 6.9 shows the Δ_{JT} plot as a function of composition for the octahedral Co ions which is mainly responsible for the tetragonal distortion. From the plot it is clearly evident that $\Delta_{JT}^{e_g\downarrow}$ increases with composition and shows a hump across x = 0.5 ($\Delta_{JT}^{e_g\downarrow}$ = 0.8 eV) and for x = 1.0, $\Delta_{JT}^{e_g\downarrow}$ is maximum with 0.9 eV. The maximum (~0.4 eV) and minimum (0.1 eV) value of $\Delta_{JT}^{e_g\uparrow}$ occur at x = 0.0 and 0.75, respectively. For $x \leq 0.125$ case both the parameters $\Delta_{JT}^{t_{2g}\uparrow}$ and $\Delta_{JT}^{t_{2g}\downarrow}$ exhibit negligibly small magnitude, but for x = 1.0 both the quantities gradually increase and reaches 0.5 eV. For antiferromagnetic GCO the magnitude of Δ_{JT} is significantly high (~ 0.9 eV). Such enhanced crystal field splitting controls the energy band gap (E_g) of the system which is main reason that this pyrochlore system exhibits the maximum E_g than the remaining compositions of the series. Furthermore, the splitting of the *d*-orbitals significantly influences the interaction between the spins and as a result we obtain high exchange interaction between the B-site Co ions (J_{BB} ~ -22.3 meV) value for x =1.0.

In our calculations we used three distinct magnitudes of U_{eff} = 4, 2 and 0 eV for the cations Co, Ti and Ge atoms, respectively and performed the band structure calculation across different symmetry points in the Brillouin zone by considering the ground states configurations of different compositions as shown in Fig. 6.10. Consequently, our calculation results reveal the direct energy band-gap values at Γ(X) symmetry point: E_g ~ 1.7 eV (2.2 eV) and 1.8 eV (3.3 eV) for Co_2TiO_4 (x = 0) and GCO (x = 1), respectively. These results are in good agreements with our experimental results and theoretical findings based on *ab initio* studies discussed in Section 3.3.4. While incorporating Ge in Co_2TiO_4 matrix, the X-X direct band gap does

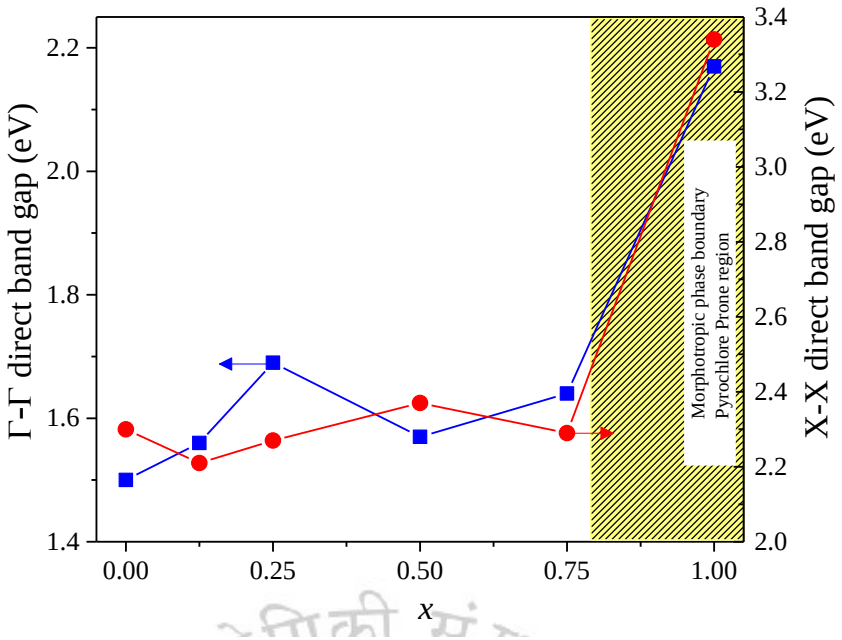

Fig. 6.10: The magnitude of energy direct band gap (E_g) along symmetry directions Γ and X for different compositions of CTGO.

not show any major change except a small increase across x = 0.25 and 0.75 with 1.9 eV and 1.8 eV. In case of Γ-Γ direct band gap, the magnitude of E_g varies between 2.2 eV (for x = 0) and 2.3 eV (for x = 0.875). Nevertheless, for x = 1.0 the X-X direct band gap increases significantly to 3.3 eV. The main origin of such sudden surge in the band gap energy can be clearly understood from the density of states plots. For x = 1, the direct band gap occurs due to the charge transfer between O(2p) and Co^{2+} (e_g) states, while, for the remaining compositions Ti-t_{2g} states emerges near the Fermi level in the conduction band and initiate the charge transfer between O(2p) and Ti^{4+} (t_{2g}) states. On the other hand, the magnetic properties of the system are quite interesting in the sense that for all the values of x and y overall system exhibits FiM behaviour except for the case of x = 1.0 and y = 1.0 (i.e., GCO) in which the system exhibits a perfect AFM ordering. These features are clearly visible in the density of states calculations. In Table 6.3 we present the magnitude of all the individual and total magnetic moments (μ_B) for various combinations of x and y in CTGO lattice. Our calculations suggest that the magnitude of Co moment at A- and B-sites are nearly same in magnitude, but with opposite spin orientations 2.70μ_B and -2.71μ_B, respectively. For y = 0.0, for different compositions the number of Co atoms in A- and B-sites is constant and as a result the total moment ($\Delta\mu$) remains nearly similar. However, this behaviour is not continued for y = 0.5 and 1.0. For y = 0.5, $\Delta\mu$ changes from -0.4μ_B (x = 0.125) to -2.96μ_B (x = 1.0) and in the case of y = 1.0, the total moment increases from -1.50μ_B (x = 0.125) to -4.43μ_B (x = 0.75). The $\Delta\mu$ gradually increases with x due to the imbalance of Co atoms between the A- and B-sites. On the other hand, for any composition, for y = 1.0 the number of Co occupying the B-sites are always higher than for y = 0.5 as results the μ_{Total} is always larger for y = 1.0 as compared to the other two configurations. Another interesting finding is that for any composition the magnetic moment corresponding to A-site Co reduces with increasing 'y', because of the substitution of non-magnetic Ge^{4+} at the A-site and such dilution causes significant increase of Co^{2+} ions migrating to octahedral sites. This feature is quite significant for all the compositions greater than 0.5. On the other hand, the experimental studies on

Table 6.3: List of site dependent magnetic moments of cations in CTGO for different combinations of *x* and *y*.

x	*y*	A-site		B-site			$\Delta\mu$ (μ_B)
		μ_{Co} (μ_B)	μ_{Ge} (μ_B)	μ_{Co} (μ_B)	μ_{Ti} (μ_B)	μ_{Ge} (μ_B)	
0	0.0	2.70	-	-2.71	0.04	-	-0.03
0.125	0.0	2.70	-	-2.70	0.04	0.02	-0.03
	0.5	2.69	-0.02	-2.71	0.05	0.02	-0.40
	1.0	2.69	-0.02	-2.71	0.04	-	-1.50
0.25	0.0	2.70	-	-2.70	0.04	0.02	-0.03
	0.5	2.69	-0.02	-2.70	0.04	0.02	-0.77
	1.0	2.69	-0.02	-2.71	0.05	-	-1.50
0.5	0.0	2.71	-	-2.70	0.04	0.02	-0.03
	0.5	2.69	-0.02	-2.71	0.04	0.02	-1.50
	1.0	2.65	-0.02	-2.71	0.06	-	-2.96
0.75	0.0	2.71	-	-2.70	0.04	0.02	-0.04
	0.5	2.67	-0.02	-2.70	0.03	0.02	-2.23
	1.0	2.61	-0.03	-2.71	0.03	-	-4.43
1.0	0.0	2.71	-	-2.71	-	0.02	-0.04
	0.5	2.66	-0.02	-2.70	-	0.02	-2.96
	1.0	2.74	0.00	-2.74	-	-	0.00

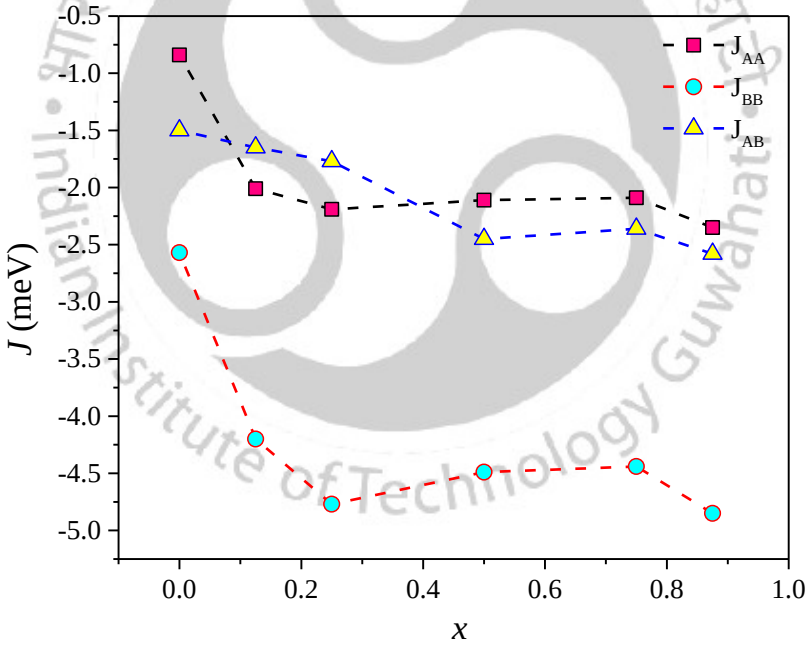

Fig. 6.11: Compositional variation of the magnetic exchange parameters (J_{ij}) for $y = 0$ of CTGO.

this series was first reported way back in 1976 by Strooper *et al.* [243]. These authors reported detailed magnetic properties for different compositions up to $x = 0.4$ ($Ti_{0.6}Ge_{0.4}Co_2O_4$) in which they noticed significant reduction in the ordering temperatures (53 K±2 to 39 K±2 for $x = 0$ to 0.4, respectively) and mean exchange interactions J_{AB} (−6.3 K±0.3 to −5.8 K±0.3 for $x = 0$ to 0.4, respectively) without any major changes in J_{AA} and J_{BB}. The temperature dependence of magnetization studies reported by Strooper *et al.* show no systematic variation of the sub-lattice magnetization ($M_A(0)$ and $M_B(0)$) and Curie-constant (C) as a function of composition of the system: C ($=N_A\mu^2/3k_B$) for $x = 0$ is C= 5.4 cc/mol K and $M_A(0)$ ($= M_B(0)$) ~

20450 G/mol cm^3 and these quantities remain constant with increasing x up till 0.4 [243]. It is important to note that Strooper *et al*. considered that Ge atoms are favourable to occupy the B-sites which in our calculations correspond to the structure for $y = 0$. Accordingly, our calculation results for $y = 0$ yield constant magnetic moment for different compositions of x which is consistent with the results of Strooper *et al.* [243]. In the present case we evaluated the exchange interaction using the Heisenberg Hamiltonian (Eq. 1.19): $H = -\sum_{ij} J_{ij} S_i . S_j$. In the present case we considered the collinear spin configuration and calculated the total energies of the system for four different spin state configurations. Further, this calculated energy was substituted in Eq. (1.19) and first nearest neighbour exchange interactions: J_{AA}, J_{BB} and J_{AB} were computed. Figure 6.11 depicts the variation of J_{AA}, J_{BB} and J_{AB} for different compositions of x (y = 0) which are antiferromagnetic in nature. For x = 0.0, $J_{AA} = -0.8$ meV and it increases with increasing the composition up to -2.01 meV till x reaches 0.125, beyond this composition, no significant increase in J_{AA} is noticed (it reaches maximum value -2.4 meV for x = 0.875). Almost similar trend has been noticed in case of J_{BB} except very high magnitude ~ -4.9 meV for x = 0.875 and comparable to J_{AA}, J_{BB} does not vary much beyond x = 0.125. However, $J_{AB}(x)$ shows a different variation altogether with a maximum value of ~ -2.6 meV for x = 0.875. These variations in exchange interactions are not in consonance with the variation of bond length as a function of x. As we substitute the Ge atoms in place of Ti atoms, the size mismatch between the ions may tilt and/or rotate the CoO_6 oxygen octahedral as a result small local distortion occurs which in turn play a key role on the exchange interactions. In case of GCO, the exchange interaction is significantly high ($J_{BB} = -22.3$ meV) due to its unique pyrochlore antiferromagnetic structure. Previous experimental studies by Diaz *et al.* reported very high magnetic (orbital) frustration in this system due to the competing exchange interactions acting between the triangular and kagome planes [160]. Nevertheless, using the DFT+U techniques we have been able to obtain only the first nearest neighbour interaction and the calculated J_{ij} (at T = 0K) values in the present case are nearly one order higher in magnitude than the previously reported experimental results [177,243].

6.4 Conclusions:

In conclusion, we have demonstrated that Ge substituted Co_2TiO_4 displays disorder driven weak tunable tetragonal distortion due the alteration in the energy levels of non-degenerate d_{z^2} and $d_{x^2-y^2}$ orbitals (with $c/a < 1$, for $E(d_{z^2}) > E(d_{x^2-y^2})$ and $c/a > 1$, for $E(d_{z^2}) < E(d_{x^2-y^2})$) of B-site Co and large exchange splitting $\Delta_{EX-Tet.}^{t_{2g}}$ ($\Delta_{EX-Oct.}^{e_g}$) for Co^{2+} than the crystal field splitting (Δ_{CF}). Ge atoms prefer to occupy at the octahedral B-site for lower and intermediate substitution levels and forms energetically favourable ground state. However, on approaching the morphotropic phase boundary ($x > 0.75$), Ge atoms start occupying the tetrahedral A-site. The Jahn-Teller distortion, Δ_{JT} in these solid-solutions are linked with the large e_g majority spin splitting (Δ_{JT}-e_g) driven by the enhanced crystal field splitting which essentially controls the energy band-gap (1.7eV ($E_{g\text{-}\Gamma\Gamma}$) $\leq E_g \leq$ 3.3eV ($E_{g\text{-}XX}$)) of the investigated system for all the combinations of x and y. For $x = y$ =1, the $E_{g\text{-}XX}$ ~ 3.3eV is associated with the inter-band charge transfer transition, $O(2p) \rightarrow Co^{+2}$ (e_g). Yet, for the remaining compositions, Ti-t_{2g} states emerge near the Fermi-level (E_F) in the conduction

band and thus the E_g departs from 1.7 eV as the charge transfer takes place between O(2*p*) and Ti^{+4} (t_{2g}) states. The magnetic structure is mainly determined by the high spin configuration of Co^{2+} ions, and for any combinations of *x* and *y* the system is ferrimagnetic in nature, except for $x = 1.0$ and $y = 1.0$ the system (GCO) possesses perfect AFM ordering. Under no disorder case ($y = 0$), the net magnetic moment ($\Delta\mu$) remains constant, whereas, for non-zero values of *y* the magnitude of $\Delta\mu$ increases with *x* due to the imbalance of number density of Co atoms between the A- and B-sites. The antiferromagnetic exchange interaction J_{BB} dominates over J_{AA} and J_{AB} for all the compositions except for $x = y = 1.0$. However, for $x > 0.125$, the strength of J_{AA} and J_{BB} does not change significantly whereas J_{AB} gradually rises with *x*.

Chapter 7
Conclusions and future work

This chapter summarize the important theoretical and experimental results obtained in this work and describes an outlook for the possibility of future research work. In the thesis work we successfully probed the role of dilution on the electronic structure and magnetic properties of few spinel oxides by means of DFT+U calculations, neutron scattering experiments and standard magnetization measurements. This thesis also explored the reentrant spin-glass behavior, tetragonal distortion, giant exchange splitting and glassy antiferromagnetic properties in the investigated system. Below we provide chapter wise summary of all the key results presented in the individual chapters and complete this section by discussing the possible future research work on cobalt spinels from theoretical and experimental point of view.

7.1 Conclusions:

Chapter 3 demonstrates the role of dilution on the structural, magnetic, electronic, and optical properties of the antiferromagnetic Co_3O_4. As the octahedral cobalt site of spinel-lattice is diluted with Ge, Al, Ti, Ru and Sn cations, we detected a substantial increase in the size of the unit cell as well as the destruction of long-range magnetic ordering with a spin-orbit compensation effect. The ferrimagnetic ordering in diluted inverse-spinels such as $Co_2\Sigma O_4$ (Σ = Ti and Sn) emerges due to the different magnetic moments of the two-sublattices A ($3.87\mu_B$) and B ($4.16\mu_B$ for Co_2SnO_4 and $5.19\mu_B$ for Co_2TiO_4). Different temperature dependence of these magnetic ions at A- and B-site gives unusual low-temperature compensation behavior, exchange bias and spin-liquid state in Co_2TiO_4 and Co_2SnO_4. Experiments and DFT calculations indicate AFM configuration for Co_3O_4, Co_2AlO_4 (T_N ~ 4.8 K) spinels with an equal and opposite moment of ~ $2.60\mu_B$ at tetrahedral sites of divalent Co ions and negligible contribution from trivalent B-site Co due to complete filling of t_{2g} levels having giant crystal field ~ 2.5 eV and 1.8 eV, respectively. However, in Co_2GeO_4 (T_N ~ 20.4 K) case AFM behavior originates due to the opposite spins at octahedral sites of divalent Co ions. The remaining spinels Co_2TiO_4 (T_N ~ 47.8 K), Co_2SnO_4 (T_N ~ 41 K) and Co_2RuO_4 (T_N ~ 16 K) are more favorable to ferrimagnetic structure as evident from our magnetization measurements with a different temperature dependence of magnetic moments A(T) and B(T) at tetrahedral-A and octahedral-B sites, respectively. The variation in the energy band-gap (E_g = 1.68→3.28eV for Co_2RuO_4→Co_2GeO_4) obtained from DFT+U calculations are in good agreement with our experimental results (E_g = 1.52→3.16eV) obtained from the Kulbelka-Munk analysis of diffusive reflectance spectroscopy data. The extent of exchange splitting, $\Delta_{EX}^{e_g}$ of tetrahedral Co^{2+} varies between 1.8 eV and 1.3 eV for Co_3O_4 and Co_2AlO_4, respectively. Nevertheless, $\Delta_{EX}^{t_{2g}}$ exhibits decreasing trend (5.2 eV→3.6 eV for Co_3O_4→Co_2SnO_4) with increasing the lattice parameter, except Co_2GeO_4.

In Chapter 4 we examined the glassy antiferromagmetic characteristics of Co_2RuO_4 using the dc-magnetic measurements (M-T and M-H) and frequency (f) dependence of the ac-magnetic susceptibilities. These studies reveal that Co_2RuO_4 exhibits an AFM ordering with $T_N \sim 15.2$K, along with a spin-glass state at slightly lower temperature (14.2 K). In this system AFM ordering is mainly governed by the orientation of Co^{2+}spins occupying the A-site, whereas the exchange interaction between the Co^{2+} ions on the A-site and randomly distributed Ru^{3+} on the B-site activates the spin-glass phase (while the Co^{3+} ions on the B-site being in the low-spin non-magnetic state). Analysis of M (H, T) data measured below T_N are used to construct the H-T phase diagram showing that T_{SG} shifts to lower temperatures exhibiting $H^{2/3}$ variation as expected for spin-glass state while T_N is nearly independent of field. Above T_N, the paramagnetic susceptibility data are perfectly fitted to the modified Curie–Weiss law, $\chi = \chi_o + C/(T+\theta)$, with best fit parameters $\chi_o = 0.0015$ emu/mol-Oe yielding $\theta = 53$ K and $C = 2.16$ emu-K/mol-Oe. Using these values we evaluated the effective magnetic moment $\mu_{eff} = 4.16\ \mu_B$ which is comparable to the expected theoretical value of $\mu_{eff} = 4.24\mu_B$ per Co_2RuO_4. By means of high temperature series expansion for χ and using the magnitudes of T_N and θ, dominant exchange constant $J_1/k_B \sim 6$ K between the Co^{2+} on the A-sites is evaluated. Analysis of the ac magnetic susceptibilities near T_{SG} yields the dynamical critical exponent $zv = 5.2$ and microscopic spin relaxation time $\tau_o \sim 1.16\times10^{-10}$ sec characteristic of cluster spin glasses and the observed time-dependence of M(t) are indicating the presence of the spin-glass state. Large M-H loop asymmetry at low temperatures with giant exchange bias effect ($H_{EB} \sim 1.8$ kOe) and coercivity ($H_C \sim 7$ kOe) for a field cooled sample further support the mixed magnetic phase nature of this interesting spinel. It is argued that the observed change from positive MCE (magnetocaloric effect) for $T > T_N$ to inverse MCE for $T < T_N$ observed in Co_2RuO_4 (and reported previously in other systems also) is related to the change in sign of $(\partial M/\partial T)$ vs. T data.

Next we extended our study to the neutron diffraction of the single crystals of Co_2TiO_4 and Co_2SnO_4 to probe their spin structures in the ground state. Both the compounds exhibits strongest magnetic intensity of $(111)_M$ reflection due to ferrimagnetic ordering, which sets in below $T_N = 48.6$ K and 41 K for Co_2TiO_4 and Co_2SnO_4, respectively. An additional low intensity magnetic reflection $(200)_M$ was noticed in Co_2TiO_4 due to the presence of an additional weak antiferromagnetic component. Remarkably, a significant broadening of the magnetic $(111)_M$ reflection was noticed from both the powder and the single-crystal neutron data of Co_2TiO_4 due to the disordered character of Ti and Co atoms on the B site. Practically, the same peak broadening was found for the neutron powder data of Co_2SnO_4. On the other hand, from our single-crystal neutron diffraction data of Co_2TiO_4 we found a spontaneous increase of particular nuclear Bragg reflections below the magnetic ordering temperature. Our analysis showed that this unusual peak broadening effect can be ascribed to the presence of anisotropic extinction, which is associated to a change of the mosaicity of the crystal. In this case it can be expected that competing Jahn-Teller effects act along different crystallographic axes can induce anisotropic local strain. In fact, for both ions Ti^{3+} and Co^{3+} the t_{2g} levels split into a lower d_{xy} level and

yields a higher two-fold degenerate d_{xz}/d_{yz} level. As a consequence, one can expect a tetragonal distortion in Co_2TiO_4 with $c/a < 1$, which could not be significantly detected in the present work. The neutron diffraction study of Co_2TiO_4 single-crystals also showed that some nuclear reflections exhibit a strong increase in their peak intensity below the ordering temperature of about 50 K which is associated to a change of the mosaicity of the crystal. The cause of anisotropic local strain effects in the crystal appears due to the competing Jahn-Teller effects acting along different crystallographic axes in which the t_{2g} levels of both the trivalent cations Ti^{3+} and Co^{3+} split into a lower d_{xy} level resulting to a higher two fold degenerate d_{xz}/d_{yz} level. As a consequence, one can expect a tetragonal distortion in Co_2TiO_4 with a c/a ratio less than 1. However, our powder diffraction data could not show evidence of any peak splitting, which could indicate a transition into a tetragonal structure. Based on the dynamic scaling analysis of ac-susceptibility and the heat-capacity measurements, it is suggested that Co_2TiO_4 first goes through a ferrimagnetic ordering across 48.6 ± 1 K, and then subsequently goes through a reentrant spin-glass transition across 46.8 K with critical exponent 'zv' = 12.04 ± 0.05 as determined from the frequency dependence of real-component of ac-magnetic susceptibility $\chi'(T)$. From the temperature dependence of heat-capcity $C_P(T)$ data we estimated the Debye temperature Θ_D = 554.16 K for the single crystalline Co_2TiO_4 which is significantly higher than the Θ_D = 525 K for polycrystalline Co_3O_4 reported by Roth [87]. A weak hump across 18 K was noticed from the C_PT^{-1} vs. T data indicating further change in the magnetic ordering which is independent of the external applied magnetic field.

In Chapter 6 we studied the electronic structure and magnetic properties of $Co_2Ti_{1-x}Ge_xO_4$ ($0 \leq x \leq 1$) spinel by means of the first-principles methods of DFT involving generalized gradient approximation (GGA) along with the on-site Coulomb interaction (U_{eff}) in the exchange-correlation energy functional. In this study emphasis has been given to explore the site occupancy of Ge atoms in the spinel lattice by introducing the cationic disorder parameter (y) which is done in such a way that one can tailor the Pyrochlore geometry of $GeCo_2O_4$ and determine the electronic/magnetic structure quantitatively. For all the compositions (x), the system exhibits weak tetragonal distortion ($c/a \neq 1$) due to the non-degenerate states of d_{z^2} and $d_{x^2-y^2}$ (e_g orbitals) of the B-site Co. We observe large exchange splitting (Δ_{EX} ~ 9 eV) between the up and down spin bands of t_{2g} and e_g states, respectively, of tetrahedral and octahedral Co^{+2} ($^4A_{2(g)}$(F)) and moderate crystal-field splitting (Δ_{CF} ~ 4 eV) and the Jahn-Teller distortion (Δ_{JT} ~ 0.9 eV). These features indicate a strong intra-atomic interaction of $Co_2Ti_{1-x}Ge_xO_4$ system which is also responsible for the energy band-gap (1.7 eV ≤ E_g ≤ 3.3 eV). The exchange interaction (J_{BB} ~−4.8 meV, for (x,y) = (0.25, 0)) between the Co^{2+} ions dominate the overall AFM behavior of the system for all 'x' as compared to the interactions J_{AA} (~−2.2 meV, for (x,y) = (0.25, 0)) and J_{AB} (~−1.8 meV, for (x,y) = (0.25, 0)). The net FiM moment ($\Delta\mu$) remains constant for all the compositions without any disoderness, however, $\Delta\mu$ increases progressively with x due to the imbalance of Co atoms between the A- and B-sites.

7.2 Prospective for Future Work:

The results reported in this thesis embody almost all the characteristics features of the cobalt based insulating oxide spinels based on extensive DFT+U (GGA), magnetometry, heat-capacity measurements, neutron scattering and UV-Vis-NIR spectroscopy measurements. Nevertheless, some extensions of the current work are possible which are listed below.

(i) In Chapter 3, we have discussed the magnetic ground state of several spinel systems and determined the band structure including the DOS and exchange interactions in detail. However, one can study the phonon dynamics and optical properties at low temperatures because these systems exhibit unusual spin liquid state and weak tetragonal distortion. Hence, in our future work we plan to study a detailed temperature dependence of Phonon dynamics.

(ii) In Chapter 4, we studied the spin-glass and AFM characteristics of Co_2RuO_4, however a detailed XPS analysis including the dielectric spectroscopy, dc-resistivity and magnetoresistance measurements at low temperatures are not investigated in the literature till now. Thus, one can plan these studies in future along with a detailed temperature dependence of specific-heat, Raman and FTIR measurements.

(iii) In Chapter 6, all the studies are related to the DFT+U based calculations only, so one can plan the experimental counterpart of the $Co_2Ti_{1-x}Ge_xO_4$ solid-solutions and explore a detailed ac- and dc-magnetometry along with the charge transport studies using the impedance spectroscopy. In addition, one can plan to synthesize the nanostructures of these spinels and explore their catalytic activity for potential applications in fuel-cells and renewable energy sources.

References

1. V. G. Harris, A. Geiler, Y. Chen, S. D. Yoon, M. Wu, A. Yang, Z. Chen, P. He, P. V. Parimi, Zuo, C. E. Patton, and C. Vittoria, *J. Magn. Magn. Mater.* **321**, 2035 (2009).
2. P. Saha, M. K. Datta, O. I. Velikokhatnyi, A. Manivannan, D. Alman, and P. N. Kumta, *Materials Science* **66**, 1 (2014).
3. F. S. Galasso, "Structure and Properties of Inorganic Solids: International Series of Monographs in Solid State Physics", Elsevier, January 26 (2016).
4. P. W. Anderson, *Phys. Rev.* **102**, 1008 (1956).
5. B. Antic, G. F. Goya, H. R. Rechenberg, V. Kusigerski, N. Jovic and M. Mitric, *J. Phys.: Condens. Matter* **16**, 651 (2004).
6. L. Zhou, H. B. Wu, T. Zhu and X.W. Lou, *J. Mater. Chem.* **52**, 7986 (2012).
7. J. Zhang, J. Liang, Y. Zhu, D. Wei, L. Fan, and Y. Qian, *J. Mater. Chem. A* **2**, 2728 (2014).
8. R. E. Newnhan, "Properties of Materials: Anisotropy, Symmetry, Structure", Oxford University Press, New York (2005).
9. D. C. Kim, S. K. Ihm, *Environ. Sci.* **35**, 222 (2001).
10. S. Thota, B. Prasad and J. Kumar, *Mat. Sci. Eng. B* **167**,153 (2010).
11. L. Zhou, H. B. Wu, T. Zhu and X.W. Lou, *J. Mater. Chem.* **52**, 7986 (2012).
12. F. Basiri and M. Taei, *Microchim Acta* **184**, 155 (2017).
13. A. Zeleňáková, V. Zeleňák, Š. Michalík, J. Kováč, and M. W. Meisel, *Phys. Rev. B* **89**, 104417 (2014).
14. V. Fung, F. Taob and D.-e. Jiang, *Catal. Sci. Technol.* **6**, 6861 (2016).
15. A. Diallo, T. B. Doyle, B. M. Mothudi, E. Manikandan, V. Rajendran, and M. Maaza, *J. Magn. Magn. Mater.* **424**, 251 (2017).
16. Y. Lin, H. Ji, Z. Shen, Q. Jia, and D. Wang, *J. Mater. Sci: Mater. Electron* **27**, 2086 (2016).
17. P. Sahoo, H. Djieutedjeu and P. F. P. Poudeu, *J. Mater. Chem. A* **1**, 15022 (2013).
18. M. S. Niasari, N. Mir, and F. Davar, *J. Phys. Chem. Solids* **70**, 847 (2009).
19. D. De, Ò. Iglesias, S. Majumdar, and S. Giri, *Phys. Rev. B* **94**, 184410 (2016).
20. M. Matsuda, T. Hoshi, H. Aruga Katori, M. Kosaka, and H. Takagi, *Phys. Soc. Jpn.* **80**, 034708 (2011).
21. D. Mandrus, V. Keppens, B. C. Chakoumakos, *Mater. Res. Bull.* **34**, 1013 (1999).
22. S. Nayak, S. Thota, D. Joshi, M. Krautz, A. Waske, A. Behler, J. Eckert, T. Sarkar, M. S. Andersson, R. Mathieu, V. Narang, and M. Seehra, *Phys. Rev. B* **92**, 214434 (2015).
23. S. Thota and M. Seehra, *J. Appl. Phys.* **113**, 203905 (2013).
24. S. Thota, V. Narang, S. Nayak, S. Sambasivam, B. Choi, T. Sarkar, M. S. Andersson, R. Mathieu, and M. Seehra, *J. Phys.: Condens. Matter* **27**, 166001 (2015).
25. W. H. Bragg, *Philos. Mag.* **30**, 305 (1915).
26. S. Nishikawa, *Proc. Math. Phys. Soc. Tokyo* **8**, 199 (1915).
27. N. F. M. Henry and K. Lonsdale (eds.), "International Tables for X-ray Crystallography", Vol. I. Kynoch Press, England (1952).
28. K. E. Sickafus, and J. M. Wills, *J. Am. Ceram. Soc.* **82**, 3279 (1999).
29. S. Blundell, "Magnetism in Condensed Matter", Oxford University Press, Oxford (2001).
30. D. McMorrow, "Order and excitations in condensed matter", Course notes (2006).
31. R. A. Serway and R. J. Beichner, "Physics for Scientists and Engineers with Modern Physics", Saunders College Publishing, Orlando, 5th edition (2000).
32. A. H. Morrish, "The Physical Principles of Magnetism", Wiley-IEEE Press; 1 edition (2001).
33. N. D. Mermin and N. W. Ashcroft, "Solid State Physics", Holt, Rinehart and Winston, New York, (1976).
34. L. B. Mendelsohn, F. Biggs, and J. B. Mann, *Phys. Rev. A* **2**, 1130 (1970).
35. P. Burgardt and M. S. Seehra, *Solid State Commun.* **22**, 153 (1977).
36. J. B. Goodenough, *Phys. Rev.* **100**, 564 (1955).

37. J. Kanamori, *Prog. Theoret. Phys.* **17**, 177 (1957).
38. J. B. Goodenough, *J. Phys. Chem. Solids* **6**, 287 (1958).
39. J. Kanamori, J. Phys. Chem. Solids **10**, 87 (1959).
40. J. Kanamori, *J. Appl. Phys. Suppl.* **31**, 145 (1960).
41. R. C. O' Handley, "Modern Magnetic Materials: Principles and Applications", New York: John Wiley, (2000).
42. S. Nayak, D. C. Joshi, M. Krautz, A. Waske, J. Eckert, and S. Thota, *J. Appl. Phys.* **119**, 043901 (2016).
43. S. Nayak, K. Dasari, D. C. Joshi, P. Pramanik, R. Palai, A. Waske, R. N. Chauhan, N. Tiwari, T. Sarkar and S. Thota, *J. Appl. Phys.* **120**, 163905 (2016).
44. L. Néel, *Ann. Phys.* (Paris) **3**, 137 (1948).
45. T. Nagata, "Rock Magnetism", second ed., Maruzen, Tokyo (1961).
46. A. Kumar and S.M. Yusuf, *Phys. Rep.* **556**, 1 (2015).
47. S. Thota, Q. Zhang, F. Guillou, U. Lüders, N. Barrier, W. Prellier, A. Wahl and P. Padhan, *Appl. Phys. Lett.* **97**, 112506 (2010).
48. W. H. Meiklejohn, C. P. Bean, *Phys. Rev.* **105**, 904 (1957).
49. J. Hong, J. Kane, J. Hashimoto, M. Yamagishi, K. Noma and H. Kanai, *IEE Trans. Magn.* **38**, 15 (2002).
50. K. Stoev, F. Liu, Y. Chen, X. Dang, P. Luo, J. Chen, J. Wang, K. Kung, M. Lederman and M. Re, *J. Appl. Phys.* **93**, 6552 (2003).
51. C. Tsang, T. Lin, S. MacDonald, M. Pinarbasi, N. Robertson, H. Santini, M. Doerner, T. Reith, L. Vo, T. Diola and P. Arnett, *IEEE Trans. Magn.* **33**, 2866 (1977).
52. C. Tsang, M. Pinarbasi, H. Santini, E. Marinero, P. Amett, R. Olson, R. Hsiao, M. Williams, R. Payne, R. Wang, J. Moore, B. Gurney, T. Lin and R. Fontana, *IEEE Trans. Magn.* **35**, 689 (1999).
53. T. Lin, D. Mauri and Y. Luo, *IEEE Trans. Magn.* **36**, 2563 (2000).
54. F. H. Liu, K. Stoev, X. Shi, H. C. Tong, C. Chien, Z. W. Dong, X. Yan, M. Gibbons, S. Funada, Y. Liu, P. Prabhu, S. Dey, M. Schultz, S. Malhotra, B. Lal, J. Kimmal, M. Russak and P. Kern, *IEEE Trans. Magn.* **36**, 2140 (2000).
55. A. M. Mack, K. Subramanian, L. R. Pust, Senior Member, IEEE, C. J. Rea, N. Amin, M. A. Seigler, S. Mao, Member, IEEE, S. Xue, and S. Gangopadhyay, Member, *IEEE Trans. Magn.* **37**, 1727 (2001).
56. A. Matsuzono, S. Terada, H. Ono, A. Furukawa, T. Sone, S. Sasaki, Y. Kakihara, Y. Takeda, N. Chiyokubo and H. Matsuki, *J. Appl. Phys.* **91**, 7267 (2002).
57. J. Zhang, Y. Huai and M. Lederman, *J. Appl. Phys.* **91**, 7285 (2002).
58. A. Tanaka, Y. Shimizu, Y. Seyama, K. Nagasaka, R. Kondo, H. Oshima, S. Eguchi and H. Kanai, *IEEE Trans. Magn.* **38**, 84 (2002).
59. J. Sort, S. Suriñach, J. S. Muñoz, M. D. Baró, J. Nogués, G. Chouteau, V. Skumryev and G. C. Hadjipanayis, *Phys. Rev. B* **65**, 174420 (2002).
60. J. Sort, J. Nogués, X. Amils, S. Suriñach, J. S. Muñoz and M. D. Baró, *Appl. Phys. Lett.* **75**, 3177 (1999).
61. E. Y. Chen, S. Tehrani, T. Zhu, M. Durlam and H. Goronkin, *J. Appl. Phys.* **81**, 3992 (1997).
62. S. S. P. Parkin, X. Jiang, C. Kaiser, A. Panchula, K. Roche and M. Samant, *Proc. IEEE* **91**, 661 (2003).
63. G. A. Prinz, *Science* **282**, 1660 (1998).
64. G. A. Prinz, *J. Magn. Magn. Mater.* **200**, 57 (1999).
65. S. A. Wolf, D. D. Awschalom, R. A. Buhrman, J. M. Daughton, S. von Molnár, M. L. Roukes, A. Y. Chtchelkanova and D. M. Treger, *Science* **294**, 1488 (2001).
66. B. Dieny, V. S. Speriosu, S. S. P. Parkin, B. A. Gurney, D. R. Wilhoit and D. Mauri, *Phys. Rev. B* **43**, 1297 (1991).
67. J. C. S. Kools, *IEEE Trans. Magn.* **32**, 3165 (1996).
68. E. P. Wohlfarth, *Adv. Phys.* **8**, 87 (1959).
69. J. S. Kouvel, *J. Phys. Chem. Solids* **24**, 795 (1963).
70. N. H. March, P. Lambin and F. Herman, *J. Magn. Magn. Mater.* **44**, 1 (1984).
71. J. Nogués and I. K. Schuller, *J. Magn. Magn. Mater.* **192**, 203 (1999).

72. J. F. Bobo, L. Gabillet and M. Bibes, *J. Phys.: Condens. Matter* **16**, S471 (2004).
73. J. Nogués, J. Sort, V. Langlais, V. Skumrye, S. Suriñach, J. S. Muñoz and M. D. Baró, *Phys. Rep.* **422**, 65 (2005).
74. O'. Iglesias, A. Labarta and X. Batlle, *J. Nanosci. Nanotechnol.* **8**, 2761 (2008).
75. J. S. Kouvel, *J. Phys. Chem. Solids* **21**, 57 (1961).
76. G. Toulouse, *Commun. Phys.* **2**, 115 (1977).
77. J. Villain, *J. Phys.* **C10**, 1717 (1977).
78. J. A. Mydosh, "Spin glasses: an experimental introduction", Taylor & Francis, London, Washington, DC (1993).
79. K. Binder and A. P. Young, *Rev. Mod. Phys.* **58**, 801 (1986).
80. S. F. Edwards and P. W. Anderson, *J. Phys.* **F5**, 965 (1975).
81. P. Nordblad, L. Lundgren, L. Sandlund, *J. Magn. Magn. Mater.* **54**, 185 (1986).
82. C. A. Mulder, A. J. van Duyyneveldt and J. A. Mydosh, *Phys. Rev. B* **23**, 1384 (1981).
83. B. V. B. Sarkissian, *J. Phys. F: Metal Phys.* **11**, 2191 (1981).
84. C. Dekker, A. F. M. Arts and H. W. de Wjn, *J. Appl. Phys.* **63**, 4334 (1988).
85. H. Yoshizawa, S. Mistuda, H. Aruga and A. Ito, *Phys. Rev. Lett.* **59**, 2364 (1987).
86. S. Thota, S. K. Das, A. Kumar, S. Sangaraju and B. C. Choi, *IEEE Trans. Magn.* **49**, 1020 (2013).
87. W. L. Roth, *J. Phys. Chem. Solids* **25**, 1 (1964).
88. W. L. Roth, *J. Phys. France* 25, 507 (1964).
89. W. Moffitt and C. J. Ballhausen, *Annu. Rev. Phys. Chem* **7**, 107 (1956).
90. J. Dunitz and L. Orgel, *J. Phys. Chem. Solids* **3**, 20 (1957).
91. G. Kresse and J. Furthmüller, *Phys. Rev. B* **54**, 11169 (1996).
92. G. Kresse and D. Joubert, *Phys. Rev.* **59**, 1758 (1999).
93. R. M. Martin, "Electronic Structure: Basic Theory and Practical Methods", Cambridge University Press (2003).
94. M. Born and R. Oppenheimer, *Annalen der Physik* **389**, 457 (1927).
95. P. Hohenberg and W. Kohn, *Phys. Rev.* **136**, B864 (1964).
96. W. Kohn and L. J. Sham, *Phys. Rev.* **140**, A1133 (1965).
97. L. H. Thomas, *Math. Proc. Cambridge Philos. Soc.* **23**, 542548 (1927).
98. E. Fermi, *Zeitschrift für Physik* **48**, 73 (1928).
99. H. Eschrig, "The Fundamentals of Density Functional Theory", Teubner Verlag: Stuttgart, Germany (1996).
100. J. G. Lee, "Computational materials science: An Introduction", CRC press (2016).
101. P. A. M. Dirac, *Math. Proc. Camb. Philos. Soc.* **26**, 376385 (1930).
102. J. P. Perdew and Y. Wang, *Phys. Rev. B* **45**, 13244 (1992).
103. R. O. Jones and O. Gunnarsson, *Rev. Mod. Phys.* **61**, 689 (1989).
104. J. P. Perdew, K. Burke, and M. Ernzerhof, *Phys. Rev. Lett.* **77**, 3865 (1996).
105. J. Hubbard, *Proc. Roy. Soc. Lond.* **A276**, 238 (1963).
106. J. Hubbard, *Proc. Roy. Soc. Lond.* **A277**, 237 (1964).
107. J. Hubbard, *Proc. Roy. Soc. Lond.* **A281**, 401 (1964).
108. J. Hubbard, *Proc. Roy. Soc. Lond.* **A285**, 542 (1965).
109. J. Hubbard, *Proc. Roy. Soc. Lond.* **A296**, 82 (1966).
110. J. Hubbard, *Proc. Roy. Soc. Lond.* **A296**, 100 (1966).
111. S. L. Dudarev, G. A. Botton, S. Y. Savrasov, C. J. Humphreys, and A. P. Sutton, *Phys. Rev. B* **57**, 1505 (1998).
112. C. Kittel, P. McEuen, and P. McEuen, "Introduction to solid state physics", Wiley New York (1996).
113. M. Cardona and Y. Y. Peter, "Fundamentals of semiconductors", Springer (2005).
114. H. J. Monkhorst and J. D. Pack, *Phys. Rev. B* **13**, 5188, (1976).
115. D. J. Chadi and M. L. Cohen, *Phys. Rev. B* **8**, 5747, (1973).
116. H. Hellmann, *J. Chem. Phys.* **3**, 61, (1935).
117. J. C. Phillips and L. Kleinman, *Phys. Rev.* **116**, 287 (1959).

118. P. E. Blöchl, *Phys. Rev. B* **50**, 17953 (1994).
119. A. J. Dekker, "Solid State Physics", Macmillan Education, Limited (1969).
120. J. Rodríguez-Carvajal, Lab. Léon Brillouin (CEA-CNRS), CEA/Sacley, 91191 Gif Sur Yvette Cedex, France (2015).
121. W. Kraus and G. Nolze, *J. Appl. Crystallogr.* **29**, 301 (1996).
122. J. Clarke and A. I. Braginski, The SQUID Handbook (2005).
123. R. L. Fagaly, *Rev. Sci. Instrum.* **77**, 101101 (2006).
124. S. Ran, Gravity Probe B: Exploring Einstein's Universe with Gyroscopes-Einstein NASA p. 26 (2004).
125. S. Shapiro, *Phys. Rev. Lett.* **11**, 80 (1963).
126. M. Buchner, K. Höfler, B. Henne, V. Ney and A. Ney, *J. Appl. Phys.* **124**, 161101 (2018).
127. S. H. Liao and Y. K. Su, Sens. *Actuator B-Chem.* **238**, 66 (1997).
128. Physical Property Measurement System, Heat Capacity Option User's Manual (Quantum Design, 2010).
129. J. S. Hwang, K. J. Lin and C. Tein, *Rev. Sci. Instrum.* **68**, 94 (1997).
130. G. L. Squires, "Introduction to the Theory of Thermal Neutron Scattering", Cambridge University Press, Cambridge, U.K. (1978).
131. S. W. Lovesey, "Theory of Neutron Scattering from Condensed Matter", vol. 2, Clarendon Press, Oxford (1984).
132. T. Chatterji, "Neutron scattering from magnetic materials", Elsevier (2005).
133. G. Shirane, S. M. Shapiro and J. M. Tranquada, "Neutron scattering with a triple-axis spectrometer", Cambridge, Great Britain (2002).
134. P. Pramanik, "Magnetic and electronic structure of frustrated Antiferro/Ferrimagnetic Pyrochlore spinels", PhD. Thesis, IIT Guwahati (2020).
135. T. Nakamura, M. Misono, and Y. Yoneda, *J. Catal.* **83**, 151 (1983).
136. L. Peter and K. Wijayantha, *Electrochem. commun.* **1**, 576 (1999).
137. E. Iglesia, S. L. Soled, R. A. Fiato, and G. H. Via, *J. Catal.* **143**, 345 (1993).
138. J. Xu, P. Gao, and T. Zhao, *Energy Environ. Sci.* **5**, 5333 (2012).
139. Z. Wu, W. Ren, L. Wen, L. Gao, J. Zhao, C. Zhao, Z. Chen, G. Zhou, F. Li, and H. M. Cheng, *ACS nano* **4**, 3187 (2010).
140. S. Thota and S. Singh, "Magnetic Spinels-Synthesis, Properties and Applications", InTech (2017).
141. P. Pramanik, S. Thota, S. Singh, D. C. Joshi, B. Weise, A. Waske, and M. S. Seehra, *J. Phys. Condens. Matter* **29**, 425803 (2017).
142. T. Suzuki, H. Nagai, M. Nohara and H. Takagi, *J. Phys.: Condens. Matter* **19**, 145265 (2007)
143. P. Dutta, M. Seehra, S. Thota, and J. Kumar, *J. Phys. Condens. Matter* **20**, 015218 (2007).
144. S. Thota, A. Kumar, and J. Kumar, *Mater. Sci. Eng. B* **164**, 30 (2009).
145. A. Walsh, S.-H. Wei, Y. Yan, M. Al-Jassim, J. A. Turner, M. Woodhouse, and B. Parkinson, *Phys. Rev. B* **76**, 165119 (2007).
146. T. Gibb, R. Greatrex, N. Greenwood, D. Puxley, and K. Snowdon, *Chem. Phys. Lett.* **20**, 130 (1973).
147. J. Hubsch and G. Gavoille, *Phys. Rev. B* **26**, 3815 (1982).
148. J. Hubsch and G. Gavoille, *J. Magn. Magn. Mater.* **66**, 17 (1987).
149. S. Thota, M. Reehuis, A. Maljuk, A. Hoser, J. -U. Hoffmann, B. Weise, A. Waske, M. Krautz, D. C. Joshi, S. Nayak, S. Ghosh, P. Suresh, K. Dasari, S. Wurmehl, O. Prokhnenko, B. Büchner, *Phys. Rev. B* **96**, 144104 (2017).
150. J. Chen, X. Wu, and A. Selloni, *Phys. Rev. B* **83**, 245204 (2011).
151. Lima, *J. Phys. Chem. Solids* **75**, 148 (2014).
152. Lima, *J. Phys. Chem. Solids* **91**, 86 (2016).
153. S. Selcuk and A. Selloni, *J. Phys. Chem. C* **119**, 9973 (2015).
154. X.-L. Xu, Z.-H. Chen, Y. Li, W.-K. Chen, and J.-Q. Li, *Surf. Sci* **603**, 653 (2009).
155. T. Roisnel, J. Rodrguez-Carvajal, Mater. Sci. Forum, Proceedings of the Seventh European Powder Diffraction Conference **7**, 118 (2000).
156. D. Das, R. Biswas, and S. Ghosh, *J. Phys. Condens. Matter* **28**, 446001 (2016).
157. G. L. Stamokostas and G. A. Fiete, *Phys. Rev. B* **97**, 085150 (2018).
158. L. Khriplovich, E. Kholopov, and I. Paukov, *J. Chem. Thermodyn.* **14**, 207 (1982).

159. V. Singh, M. Kosa, K. Majhi, and D. T. Major, *J. Chem. Theory Comput.* **11**, 64 (2014).
160. S. Diaz, S. Brion, G. Chouteau, B. Canals, V. Simonet, and P. Strobel, *Phys. Rev. B* **74**, 092404 (2006).
161. S. Singh, P. Pramanik, S. Sangaraju, A. Mallick, L. Giebeler, and S. Thota, *J. Appl. Phys* **121**, 194303 (2017).
162. P. Kubelka and F. Munk, *Z. Tech. Phys* **12**, 593 (1931).
163. A. P. Ramirez, *Nature* **421**, 483 (2003).
164. H. T. Diep, ed. "Frustrated spin systems", World Scientific, (2013).
165. V. A. M. Brabers, "Handbook of Magnetic Materials", edited by K. H. J. Buschow (North-Holland, Amsterdam, 1995), Vol. **8**, p.189.
166. J. Dulac, *Bull. Soc. Fr. Miner. Crist.* **92**, 487 (1969).
167. S. Ghosh, S. Singh, D. C. Joshi, P. Pramanik, S. Ghosh, P. K. Mishra, S. Thota, *Phys. Rev. B* **98**, 235119 (2018).
168. B. Krutzsch, S. Kemmler-Sack, *Mater. Res. Bull.* **18**, 647 (1983).
169. T. Kawano, J. Takahashi, T. Okutani, T. Yamada, and H, Yamane, *J. Alloys Compd.* **468**, 447 (2009).
170. G. E. Granroth, D. Mandrus, V. Keppens, and S. E. Nagler, *J. Magn. Magn. Mater.* **272**, 1306 (2004).
171. R. N. Bhowmik and R. Ranganathan, Phys. Rev. B **74**, 214417 (2006).
172. M. H. Mendonça, M. R. Nunes, F. M. A. Costa, A. Carvalho, and M. M. Godinho, *J. Mater. Chem.* **4**, 515 (1994).
173. P. D. Battle, S. K. Bollen, and A.V. Powell, *J. Solid State Chem.* **99**, 267 (1992).
174. B. Koteswararao, T. Chakrabarty, T. Basu, B. K. Hazra, P. V. Srinivasarao, P. L. Paulose and S. Srinath, *Sci. Rep.* **7**, 8300 (2017).
175. H.-J. Schmidt, A. Lohmann, and Johannes Richter, *Phys. Rev. B* **84**, 104443 (2011).
176. M. E. Fisher, *Philosophical Magazine* **7**, 1731 (1962).
177. P. Pramanik, S. Ghosh, P. Yanda, D. C. Joshi, S. Pittala, A. Sundaresan, P. K. Mishra, S. Thota, and M. S. Seehra, *Phys. Rev. B* **99**, 134422 (2019).
178. V. Narang, D. Korakakis, M. S. Seehra, *J. Magn. Magn. Mater.* **368**, 353 (2014).
179. Y. Shapira, and S. Foner. *Phys. Rev. B* **1**, 3083 (1970).
180. P. Bag, P. R. Baral, and R. Nath, *Phys. Rev. B* **98**, 144436 (2018).
181. Y. Tabata, T. Waki, and H. Nakamura, *Phys. Rev. B* **96**, 184406 (2017).
182. P. M. Shand, T. Rash, M. Streicher, T. E. Kidd, K. R. Boyle and L. H. Strauss, *Phys. Rev. B* **82**, 214413 (2010).
183. F. Wang, J. Zhang, Y. Chen, G. Wang, J. Sun, S. Zhang, and B. Shen, *Phys. Rev. B* **69**, 094424 (2004).
184. P. M. Shand, A. L. Meyer, M. Streicher, A. Wilson, T. Rash, M. W. Roth, T. E. Kidd and L. H. Strauss, *Phys. Rev. B* **85**, 144432 (2012).
185. S. D. Tiwari and K. P. Rajeev, *Phys. Rev. B* **72**, 104433 (2005).
186. T. Sarkar, V. Duffort, V. Pralong, V. Caignaert, and B. Raveau, *Phys. Rev. B* **83**, 094409 (2011).
187. M. D. Mukadam, S. M. Yusuf, P. Sharma, S. K. Kulshreshtha, *J. Magn. Magn. Mater.* **269**, 317 (2004).
188. M. K. Singh, R. S. Katiyar, W. Prellier and J. F. Scott, *J. Phys.: Condens. Matter* **21**, 042202 (2009).
189. A. Truong, A. O. Watanabe, P. A. Mortemousque, K. Ando, T. Sato, T. Taniyama, and K. M. Itoh, *Phys. Rev. B* **91**, 214425 (2015).
190. L. E. Wenger, and J. A. Mydosh, *Phys. Rev. B* **29**, 4156 (1984).
191. V. K. Anand, D. T. Adroja, and A. D. Hillier, *Phys. Rev. B* **85**, 014418 (2012).
192. G. V. Lecomte, H.v. Löhneysen, and E. F. Wassermann, *Z. Physik B - Condensed Matter* **50**, 239 (1983).
193. T. Sarkar, V. Pralong, V. Caignaert, and B. Raveau, *Chem. Mater.* **22**, 2885 (2010).
194. P. Singh, M. Shukla and C. Upadhyay, *Nanoscale* **10**, 22583 (2018).
195. V. Singh, M. S. Seehra and J. Bonevich, *J. Appl. Phys.* **105**, 07B518 (2009).
196. J. L. Dormann, L. Bessais and D. Fiorani, *J. Phys. C: Solid State Phys.* **21**, 2015 (1988).
197. M. S. Seehra and K. L. Pisane, *J. Phys. Chem. Solids* **93,** 79 (2016).
198. A. Malinowski, V. L. Bezusyy, R. Minikayev, P. Dziawa, Y. Syryanyy, and M. Sawicki, *Phys. Rev. B* **84**, 024409 (2011).
199. S. Pakhira, C. Mazumdar, R. Ranganathan, S. Giri, and M. Avdeev, *Phys. Rev. B* **94**, 104414 (2016).
200. D. N. H. Nam, R. Mathieu, P. Nordblad, N. V. Khiem, and N. X. Phuc, *Phys. Rev. B* **62**, 8989 (2000).

201. S. Ghara, B. G. Jeon, K. Yoo, K. H. Kim, and A. Sundaresan, *Phys. Rev. B* **90**, 024413 (2014).
202. J. Lago, S. J. Blundell, A. Eguia, M. Jansen, and T. Rojo, *Phys. Rev. B* **86**, 064412 (2012).
203. T. Mori and H. Mamiya, *Phys. Rev. B* **68**, 214422 (2003).
204. M. D. Mukadam, S. M. Yusuf, P. Sharma, S. K. Kulshreshtha, and G. K. Dey, *Phys. Rev. B* **72**, 174408 (2005).
205. J. D. Rall and M. S. Seehra, *J. Phys.: Condens. Matter* **24**, 076002 (2012).
206. C. B. R. Jesus, E. C. Mendonça, L. S. Silva, W. S. D. Folly, C. T. Meneses, J. G. S. Duque, *J. Magn. Magn. Mater.* **350**, 47 (2014)
207. M. S. Seehra, V. Singh, S. Thota, B. Prasad, and J. Kumar, *Appl. Phys. Lett.* **97**, 112507 (2010).
208. M. S. Seehra, V. Singh, and S. Thota, *J. Appl. Phys.* **110**, 113907 (2011).
209. A. C. Pebley, P. E. Fuks, T. M. Pollock, M. J. Gordon, *J. Magn. Magn. Mater.* **419**, 29 (2016).
210. J. Nogués, J. Sort, V. Langlais, S. Doppiu, B. Dieny, J. S. Muñoz, S. Suriñach, M. D. Baró, S. Stoyanov, Y. Zhang, *Int. J. Nanotechnol.* **2**, 23 (2005).
211. M. Artus, S. Ammar, L. Sicard, J. Piquemal, F. Herbst, M. Vaulay, F. Fievet, V. Richard, *Chem. Mater.* **20**, 4861 (2008).
212. Z. M. Tian, S. L. Yuan, S. Y. Yin, L. Liu, J. H. He, H. N. Duan, P. Li, C. H. Wang, *Appl. Phys. Lett.* **93**, 222505 (2008).
213. L. Del Bianco, D. Fiorani, A. M. Testa, E. Bonetti, L. Signorini, *Phys. Rev. B* **70**, 052401 (2004).
214. Q. Zhang, S. Thota, F. Guillou, P. Padhan, V. Hardy, A. Wahl and W. Prellier, *J. Phys.: Condens. Matter*. **23**, 052201 (2011).
215. J. Shi, S. Yin, M. S. Seehra, and M. Jain, *J. Appl. Phys.* **123**, 193901 (2018).
216. M. H. Phan and S. C. Yu, *J. Magn. Magn. Mater.* **308**, 325 (2007).
217. T. P. Rashid, K. Arun, I. Curlik, S. Ilkovic, M. Reiffers, A. Dzubinska, R. Nagalakshmi, *J. Magn. Magn. Mater.* **466**, 283 (2018).
218. X. Liu, C. Feng, F. Xiao, S. W. Or, Y. Sun, C. Jin, and A. Xia, *Materials Research*, **17**, 186 (2014).
219. H. Zhang, Y. J. Sun, L. H. Yang, E. Niu, H. S. Wang, F. X. Hu, J. R. Sun, and B. G. Shen, *J. Appl. Phys.* **115**, 063901 (2014).
220. L. V. B. Diop and O. Isnard, *J. Appl. Phys.* **119**, 213904 (2016).
221. S. Chandra, A. Biswas, S. Datta, B. Ghosh, A. K. Raychaudhuri and H. Srikanth, *Nanotechnology* **24**, 505712 (2013).
222. A. Chaturvedi, J. N. Duggan, C. B. Roberts, and T. Suzuki, *IEEE Trans. Magn*, **51**, 1 (2015).
223. A. Ali, Y. Singh, *J. Magn. Magn. Mater.* **499**, 166253 (2020).
224. C. Li, T. Yan, G. Zerihun, Q. Fu, R. Zhang, X. C. S. Huang, S. Yuan, *J. Am. Ceram. Soc.* **101**, 5571(2018).
225. A. Biswas, S. Chandra, T. Samanta, M. H. Phan, I. Das, and H. Srikanth, *J. Appl. Phys.* **113**, 17A902 (2013).
226. V. B. Naik and R. Mahendiran, *J. Appl. Phys.* **110**, 053915 (2011).
227. Q. S. Fu, X. H. Chen, C. Chakrabarti, C. L. Li, J. Zheng, P. J. Wang, H. X. Yin, Y. Qiu, B. Meng and S. L. Yuan, *Phys. Chem. Chem. Phys.* **22**, 7058 (2020).
228. Q. Zhang, F. Guillou, A. Wahl, Y. Bréard, and V. Hardy, *Appl. Phys. Lett.* **96**, 242506 (2010).
229. A. M. Alieva, A. G. Gamzatova, A. B. Batdalov, V. S. Kalitka, A. R. Kaul, *J. Alloys and Compounds* **509**, L1 (2011).
230. S. Thota, F. Guillou, V. Hardy, A. Wahl, W. Prellier, and J. Kumar, *J. Appl. Phys.* **109**, 053902 (2011).
231. F. Guillou, S. Thota, W. Prellier, J. Kumar, and V. Hardy, *Phys. Rev. B* **83**, 094423 (2011).
232. T. Zou, Y.-Q. Cai, C. R. dela Cruz, V. O. Garlea, S. D. Mahanti, J.-G. Cheng, and X. Ke, *Phys. Rev. B* **94**, 214406 (2016).
233. A. Miyata, S. Takeyama and H. Ueda, *Phys. Rev. B* **87**, 214424 (2013).
234. S. Abiko, S. Niidera, and F. Matsubara, *Phys. Rev. Lett.* **94**, 227202 (2005)
235. S. B. Roy and M. K. Chattopadhyay, *Phys. Rev. B* **79**, 052407 (2009)
236. S. Niidera and F. Matsubara, *Phys. Rev. B* **75**, 144413 (2007).
237. T. Sato, T. Ando, and T. Ogawa, S. Morimoto and A. Ito, *Phys. Rev. B* **64**, 184432 (2001).
238. R. Padam, T. Sarkar, R. Mathieu, S. Thota, and D. Pal, *J. Appl. Phys.* **122**, 073908 (2017).

239. R. Padam, S. Pandya, S. Ravi, A. K. Nigam, S. Ramakrishnan, A. K. Grover, D. Pal, *Appl. Phys. Lett.* **102**, 112412 (2013).
240. I. Fita, A. Wisniewski, R. Puzniak, V. Markovich, G. Gorodetsky. *Phys. Rev. B* **93**, 184432 (2016).
241. R. Kumar, R. Padam, S. Rayaprol, Vasudeva Siruguri, D. Pal, *J. Appl. Phys.* **119**, 12 (2016).
242. S. Thota and M. Seehra, *J. Appl. Phys.* **118**, 129901 (2015).
243. K. De Strooper, A. Govaert, C. Dauwe, and G. Robbrecht, *Phys. Status Solidi A* **37**, 127 (1976).
244. K. De Strooper, *Phys. Status Solidi A* **39**, 431 (1977).
245. G. Gavoille, J. Hubsch, and S. Koutani, *J. Magn. Magn. Mater.* **102**, 283 (1991).
246. J. Srivastava, S. Ramakrishnan, V. Marathe, G. Chandra, R. Vijayaraghavan, J. Kulkarni, V. Darshane and S. Singh, *J. Appl. Phys.* **61**, 3622 (1987).
247. J. Srivastava, J. Kulkarni, S. Ramakrishnan, S. Singh, V. Marathe, G. Chandra, V. Darshane, and R. Vijayaraghavan, *J. Phys. C: Solid State Phys.* **20**, 2139 (1987).
248. K. De Strooper, A. van Alboom, C. Henriet-Iserentant, R. Vanleerberghe, R. Vandenberghe, *phys. stat. sol.* (a) **44**, 215 (1977).
249. S. Nayak, K. Dasari, D. C. Joshi, P. Pramanik, R. Palai, V. Sathe, R. N. Chauhan, N. Tiwari, S. Thota, *physica status solidi* (b) **253**, 2270 (2016).
250. M. Inagaki and S. Naka, *J. Solid State Chem.* **13**, 365 (1975).
251. M. A. Prosnikov, A. D. Molchanova, R. M. Dubrovin, K. N. Boldyrev, A. N. Smirnov, V. Yu. Davydov, A. M. Balbashov, M. N. Popova, R. V. Pisarev, *Phys. Solid State* **58**, 2516 (2016) [Fiz. Tverd. Tela **58**, 2427 (2016)].
252. N. Sakamoto and Y. Yamaguchi, *J. Phys. Soc. Jpn.* **17**, 276 (1962).
253. S. Ogawa and S. Waki, *J. Phys. Soc. Jpn.* **20**, 540 (1965).
254. S. Kirkpatrick and D. Sherrington, *Phys. Rev. B* **17**, 4384 (1978).
255. D. Sherrington, *physica status solidi (b)* **251**, 1967 (2014), D. Sherrington and S. Kirkpatrick, Phys. *Rev. Lett.* **35**, 1792 (1975).
256. J. Jayaprakash and S. Kirkpatrick, *Phys. Rev. B* **21**, 4072 (1980).
257. M. Gabay and G. Toulouse, *Phys. Rev. Lett.* **47,** 201(1981).
258. R. R. Galazka, S. Nagata, and P. H. Keesom, *Phys. Rev. B* **22**, 3344 (1980).
259. D. M. Cragg, D. Sherrington, and M. Gabay, *Phys. Rev. Lett.* **49**, 158 (1982).
260. J. A. Mydosh, *Hyperfine Interact.* **31,** 347 (1986).
261. J. Villain, *Z. Phys. B* **33**, 31 (1979).
262. J. Villain, R. Bidaux, J.-P. Carton, R. Conte, *J. Phys. France* **41**, 1263 (1980).
263. J. Rodríguez-Carvajal, *Physica B* (Amsterdam) **192**, 55 (1993).
264. S. R. Hall, G. S. D. King, and J. M. Stewart, eds., The Xtal3.4 User's Manual (Lamb Print, University of Western, Australia, Perth, 1995).
265. V. F. Sears, in International Tables for Crystallography edited by A. J. C. Wilson (Kluwer Academic Publishers, Dordrecht/Boston/London, 1995), C, 383.
266. P. J. Brown, in International Tables for Crystallography edited by A. J. C. Wilson (Kluwer Academic Publishers, Dordrecht/Boston/London, 1995), C, 391.
267. M. Reehuis, M. Tovar, D. M. Többens, P. Pattison, A. Hoser, and B. Lake, *Phys. Rev. B* **91**, 024407 (2015).
268. J. K. Kwak, K. H. Park, D. Y. Yun, D. U. Lee, T.W. Kim, D. I. Son, J. H. Han, and J. Y. Lee, *J. Korean Phys. Soc.* **57**, 1803 (2010).
269. J. G. Kim, D. L. Pugmire, D. Bhattagila, and M. A. Langell, *Appl. Surf. Sci.* **165**, 70 (2000).
270. S. C. Petitto, E. M. Marsh, G. A. Carson, and M. A. Langell, *J. Mol. Catal. A: Chem.* **281**, 49 (2008).
271. E. McCafferty and J. P.Wightman, *Surf. Interface Anal.* **26**, 549 (1998).
272. M.C. Biesinger, L.W.M. Lau, A. Gerson and R. St. C. Smart, *Appl. Surf. Sci.* **257**, 887 (2010).
273. Y. Fu, H. Du, S. Zhang, and W. Huang, *Mater. Sci. Eng. A* **403**, 25 (2005).

274. P. N. Shelke, Y. B. Khollam, K. R. Patil, S. D. Gunjal, S. R. Jadkar, M. G. Takwale, and K. C. Mohite, *J. Nano. Electron. Phys*. **3**, 486 (2011).
275. L. Aswaghosh, D. Manoharan, and N. V. Jaya, *Phys. Chem. Chem. Phys.* **18**, 5995 (2016).
276. Z. Zhou, Y. Zhang, Z. Wang, W. Wei, W. Tang, J. Shi, and R. Xiong, *Appl. Surf. Sci.* **254**, 6972 (2008).
277. Y. Yamasaki, S. Miyasaka, Y. Kaneko, J. P. He, T. Arima, and Y. Tokura, Phys. Rev. Lett. **96**(20), 207204 (2006).
278. J. Souletie and J. Tholence, *Phys. Rev. B* **32**, 516 (1985).
279. A. Harris and R. Fisch, *Phys. Rev. Lett.* **38**, 796 (1977).
280. R. Mathieu, P. Nordblad, D. Nam, N. Phuc, and N. Khiem, *Phys. Rev. B* **63**, 174405 (2001).
281. R. Mathieu, P. Svedlindh, and P. Nordblad, *Europhys. Lett.* **52**, 441(2000).
282. R. Brand, H. Georges-Gibert, J. Hubsch, and J. Heller, *J. Phys. F: Met. Phys.* **15**, 1987 (1985).
283. C. P. Poole, Jr. and H. A. Farach, *Z. Phys. B: Condens. Matter* **47**, 55 (1982).
284. R. Mathieu, J. He, Y. Kaneko, H. Yoshino, A. Asamitsu, and Y. Tokura, *Phys. Rev. B* **76**, 014436 (2007).
285. E. Gopal, "Specific heats at low temperatures", New York: Plenum Press (1966). F
286. X. Fabrèges, E. Ressouche, F. Duc, S. de Brion, M. Amara, C. Detlefs, L. Paolasini, E. Suard, L.-P. Regnault, B. Canals, P. Strobel, and V. Simonet, *Phys. Rev. B* **95**, 014428 (2017).
287. T. Watanabe, S. Hara, and S.-I. Ikeda, *Phys. Rev. B* **78**, 094420 (2008).
288. G. Sim and S. Lee, *Phys. Rev. B* **98**, 014423 (2018).
289. T. Hoshi, H. A. Katori, M. Kosaka, and H. Takagi, *J. Magn. Magn. Mater.* **310**, e448 (2007).
290. J. C. Lashley, R. Stevens, M. K. Crawford, J. Boerio-Goates, B. F. Woodfield, Y. Qiu, J. W. Lynn, P. A. Goddard, and R. A. Fisher, *Phys. Rev. B* **78**, 104406 (2008).
291. P. T. Barton, M. C. Kemei, M. W. Gaultois, S. L. Moffitt, L. E. Darago, R. Seshadri, M. R. Suchomel, and B. C. Melot, *Phys. Rev. B* **90**, 064105 (2014).
292. S. Jin, G. Yang, H. Song, H. Cui, and C. Wang, *ACS Appl. Mater. Interfaces* **7**, 24932 (2015).
293. S. Yuvaraj, M. S. Park, V. G. Kumar, Y. S. Lee, and D. W. Kim, *J. Electrochem. Sci. Technol.* **8**, 323 (2017).
294. F. C. Romeijn, *Phil. Res. Rep.* **8**, 304 (1953).
295. D. Reinen, *Z. anorg. Chem.* **366**, 172 (1968).
296. A. Zunger, S.-H.Wei, L. Ferreira, and J. E. Bernard, *Phys. Rev. Lett.* **65**, 353 (1990).
297. D. E. Vanpoucke, P. Bultinck, S. Cottenier, V. Van Speybroeck, and I. Van Driessche, *Phys. Rev. B* **84**, 054110 (2011).
298. D. Das and S. Ghosh, *J. Phys.: Condens. Matter* **29**, 055805 (2017).
299. D. Das, S. Ganguly, B. Sanyal, S. Ghosh, *Mater. Res. Express* **3** 106106 (2016).
300. S. Diaz, S. de Brion, M. Holzapfel, G. Chouteau, and P. Strobel, *Physica B* **346**, 146 (2004)
301. A. Navrotsky and O. Kleppa, *J. Inorg. Nucl. Chem.* **29**, 2701 (1967).
302. C. J. Kriessman, and Harrison, *Phys. Rev.* **103**, 857 (1956).
303. R. D. Wulandari, S. Muhammady, Y. Darma, *J. Phys. Chem. Solids* **137**, 109225 (2020).